DOCTOR OF SCIENCES

Diverging from the beaten track

rational design of thermally activated delayed fluorescence emitters inspired by different fields of organic electronics

Cardeynaels, Tom

Award date:
2020

Awarding institution:
University of Namur

Diverging from the beaten track - rational design of thermally activated delayed fluorescence emitters inspired by different fields of organic electronics

Chairman:	Prof. Dr Marc Gyssens
Promoters:	Prof. Dr Benoît Champagne
	Prof. Dr Wouter Maes
Copromoters:	Prof. Dr Dirk Vanderzande
Members of the jury:	Prof. Dr Andy P. Monkman, Durham University
	Prof. Dr Juan-Carlos Sancho-García, Universidad de Alicante
	Prof. Dr Anitha Ethirajan, Hasselt University
	Prof. Dr Guillaume Berionni, Université de Namur
	Dr Vincent Liégeois, Université de Namur

Acknowledgements

The beginning and the end: the beginning of this thesis and yet the end of my time as a PhD student, but also the beginning of the next step in my life. The past years have been a major learning experience and I would like to thank some people for helping me and guiding me along the way (even though some of them will likely never read this).

First and foremost, Jan Jaco, my high school chemistry teacher, is the one who got me on this road. His PowerPoint presentations were so on point and his classes that entertaining that I immediately fell in love with chemistry and from that point on, I knew I wanted to pursue a career in chemistry.

During my masters, I got the opportunity to work in the group of Prof. dr. Bert Meijer together with Prof. dr. Anja Palmans on polymeric self-assembling nanoparticles with catalysing properties. This was a very challenging research topic and despite not obtaining the results that we had hoped for (they didn't catalyse very well), I was able to learn a lot of synthesis techniques and further develop my presentation and writing skills. Therefore, I would like to thank both of them as well as my master thesis supervisors dr. Yiliu Liu and dr. Müge Artar for their support and guidance.

I would like to thank my promoters Prof. dr. Wouter Maes and Prof. dr. Benoît Champagne for giving me the opportunity to do this research. It was a daunting task, being the first person in both research groups to take on this multifaceted research. But with the freedom to do what I wanted and their guidance, I was able to deliver high-end research. Special thanks to Benoît for teaching me the fundamentals of quantum mechanics and computational chemistry which I was completely new to.

Both in Hasselt and in Namur, I had the pleasure to work with many awesome colleagues. I would like to thank all of them for making the past four years fun and full of joy. Whether it was singing and dancing in the lab, helping each other with synthesis and computational challenges or having fun at the team buildings and activities outside of work. Special thanks to my colleagues Jean

Quertinmont and Pierre Beaujean in Namur for helping me out with all my questions regarding the computational aspect of this work. Many thanks to my partner in crime Simon Paredis who joined the TADF project two years ago and has been working with me on the development of novel emitters. Our discussions were always fruitful and together we came up with a lot of ideas, most of which are yet to come to fruition. I would also like to thank Jasper Deckers for allowing me to invade his research on BODIPY dyes with my ideas, which has already led to one publication (and at least one more to come). Our collaboration has proven that the principles shown in this thesis are much more widely applicable than just the field of TADF.

Apart from my lab and office colleagues, I would like to thank the technical staff in Namur and Hasselt. Namely Laurent Demelenne (UNamur), Huguette Penxten, Gunther Reekmans and Koen Van Vinckenroye (UHasselt) for their help with either computer- or network-related issues, the UV-VIS and fluorescence measurements and the NMR measurements. Special thanks to Gunther and Koen for measuring my NMR samples so swiftly and always being there for assistance. I would also like to thank the didactic team Hilde, Iris, Linda and Eugène for helping out with the practical lab courses with the students and making sure everything was running smoothly.

I would also like to thank the Consortium des Équipements de Calcul Intensif (CÉCI) and in particular the Technological Platform of High-Performance Computing on which my calculations were performed.

Additionally, I would like to thank Laurence Lutsen for supporting the organic chemistry research groups at Hasselt University and keeping track of the finances. Without her proper management, we wouldn't be able to do high-level research.

During my PhD, I had the privilege to go to Durham University (UK) three times: once for a workshop on TADF and two times for a short research stay. Prof. dr. Andy Monkman has been very kind and welcoming and without the work that I have performed in his group, this thesis would have definitely looked entirely different. The expertise in his group and the available equipment made it possible to study the materials designed in this thesis in great detail and allowed me to uncover some of their fascinating properties. Therefore, I would like to thank him very much. I have thoroughly enjoyed being in Durham, because of

the research but also because of how nice of a city it is with all of its heritage. Additionally, I would like to thank dr. Andrew Danos. His relentless sarcasm and cynicism have made me laugh on many occasions but more importantly, without his help with the equipment and data processing, I wouldn't have been able to perform all the measurements in such a short notice. I would also like to thank dr. Marc Etherington for engaging in many interesting discussions and helping me around in the lab and during the TADF workshop when I didn't know anybody yet, Patrycja Stachelek for helping out with the measurements and Kleitos Stavrou for helping me with the sublimation setup.

Not to forget the help and support that I have received from my parents and my family during my studies and PhD. They have always been there supporting me, rooting for me, and allowing me to pursue my dreams.

Last but not least, I would like to thank the members of the jury for accepting my invitation to be a part of the conclusion of my PhD and for reading and reviewing this thesis. The private defence was a fruitful discussion and I really enjoyed it.

The past four years have been quite the ride (quite literally in fact). Driving to Namur and back more times than I can remember and undertaking many adventures, like the conferences and workshops that I have attended, but most notably my trips to Durham. The last of these trips to the UK, I did by taking the long road via the English Channel with my car and coming back just in time before the borders were closed because of the COVID-19 lockdowns in Europe. During this PhD I was also lucky enough to meet my girlfriend, Karen Driesen, who has supported me through the last year and a half and also joined me on my adventures to the UK. Together we make a great team and I'm looking forward to whatever comes next with her by my side.

To conclude these acknowledgements, it was a pleasure working on this research for the past four years and I am very satisfied with what I have been able to accomplish. In fact, I think I'm quite ready for another adventure.

Happy reading,

Tom Cardeynaels

List of publications

T. Cardeynaels, S. Paredis, J. Deckers, S. Brebels, D. Vanderzande, W. Maes and B. Champagne, Finding the optimal exchange-correlation functional to describe the excited state properties of push-pull organic dyes designed for thermally activated delayed fluorescence, *Phys. Chem. Chem. Phys.*, 2020, **22**, 16387-16399.

J. Deckers, **T. Cardeynaels**, H. Penxten, A. Ethirajan, M. Ameloot, M. Kruk, B. Champagne and W. Maes, Near-Infrared BODIPY-Acridine Dyads Acting as Heavy-Atom-Free Dual-Functioning Photosensitizers, *Chem. Eur. J.*, 2020, DOI: 10.1002/chem.202002549.

G. Pirotte, J. Kesters, **T. Cardeynaels**, P. Verstappen, J. D'Haen, L. Lutsen, B. Champagne, D. Vanderzande and W. Maes, The Impact of Acceptor–Acceptor Homocoupling on the Optoelectronic Properties and Photovoltaic Performance of PDTSQx_{ff} Low Bandgap Polymers, *Macromol. Rapid Commun.*, 2018, **39**, 1800086.

R. Lenaerts, **T. Cardeynaels**, I. Sudakov, J. Kesters, P. Verstappen, J. Manca, B. Champagne, L. Lutsen, D. Vanderzande, K. Vandewal, E. Goovaerts and W. Maes, All-Polymer Solar Cells Based on Photostable Bis(Perylene Diimide) Acceptor Polymers, *Sol. Energy Mater. Sol. Cells*, 2019, **196**, 178-184.

R. Lenaerts, D. Devisscher, G. Pirotte, S. Gielen, S. Mertens, **T. Cardeynaels**, B. Champagne, L. Lutsen, D. Vanderzande, P. Adriaensens, P. Verstappen, K. Vandewal and W. Maes, The effect of halogenation on PBDTT-TQxT based non-fullerene polymer solar cells – chlorination vs fluorination, *Dyes Pigm.*, 2020, **181**, 108577.

Table of contents

Chapter 7: Summary, conclusions and outlook

List of acronyms

A	acceptor
AO	atomic orbital
BHJ	bulk heterojunction
MS-CASPT2	CASSCF corrected with second-order perturbation theory
CCD	charge-coupled device
CT	charge-transfer
CC2	coupled cluster approximate singles and doubles
CC3	coupled cluster approximate singles, doubles and triples
CCSDT	coupled cluster singles, doubles and triples
CV	cyclic voltammetry
DF	delayed fluorescence
DFT	density functional theory
D	donor
EPR	electron paramagnetic resonance
ETL	electron transport layer
eV	electron volt
XC	exchange-correlation
XCF	exchange-correlation functional
EQE	external quantum efficiency
GTO	Gaussian-type orbital
GGA	generalized gradient approximation
HF	Hartree-Fock
HOMO	highest occupied molecular orbital
HLCT	hybridized local and charge-transfer
HFI	hyperfine interaction
IT	integration time
iCCD	intensified charge-coupled device
IC	internal conversion
IQE	internal quantum efficiency
ISC	intersystem crossing

LED	light-emitting diode
LCAO	linear combination of atomic orbitals
LDA	local density approximation
LE	localized excited (state)
LUMO	lowest unoccupied molecular orbital
MALDI	matrix-assisted laser desorption/ionization
MAE	mean absolute error
MSE	mean signed error
MO	molecular orbital
CASSCF	multi-state complete active space self-consistent field
NIR	near-infrared
NMR	nuclear magnetic resonance
OLED	organic light-emitting diode
OPD	organic photodetector
OPV	organic photovoltaic
OSC	organic solar cell
ppm	parts per million
PDT	photodynamic therapy
PL	photoluminescence
PLQY	photoluminescence quantum yield
PCM	polarizable continuum model
PF	prompt fluorescence
RGB	red, green and blue
riCC2	resolution-of-the-identity CC2
rISC	reverse intersystem crossing
ROMP	ring-opening metathesis polymerization
rt	room temperature
RTP	room temperature phosphorescence
STA	single transition approximation
SEC	size-exclusion chromatography
SSSE	solid-state solvation effect
SOC	spin-orbit coupling
SI	supporting information
TDA	Tamm-Dancoff approximation

TADF	thermally activated delayed fluorescence
TD	time delay
TDDFT	time-dependent density functional theory
ToF	time-of-flight
TIPS	triisopropylsilyl
TF	triplet fusion
TTA	triplet-triplet annihilation
UV-VIS	ultraviolet-visible
VC	vibronic coupling
VLC	visible light communication

Chapter 1

Introduction

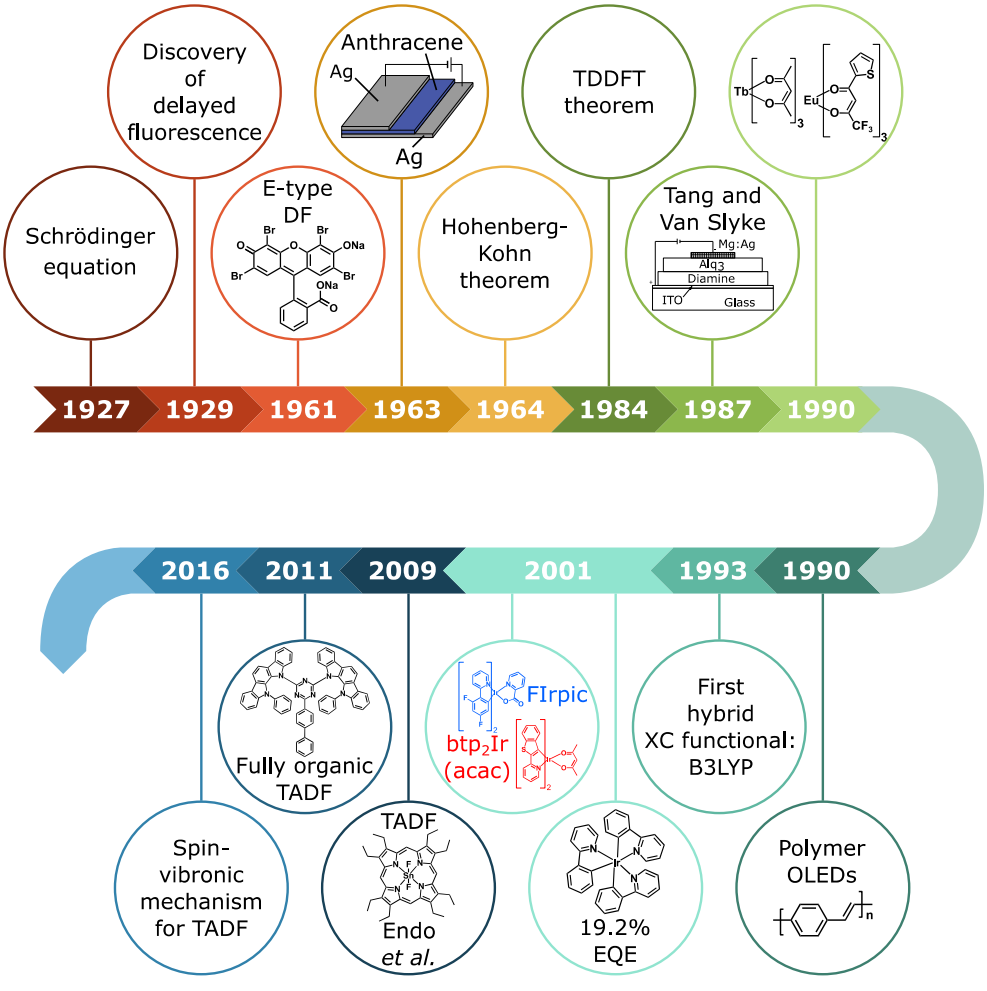

Organic light-emitting diodes (OLEDs) have entered our everyday life as we can nowadays find them in smartphone and television screens. Their widespread use can be attributed to their ability to outperform technologies based on classical semiconductors, whereas this is not possible or not yet achieved in other fields of optoelectronics such as solar cells. Current OLED efficiencies (i.e. the light output versus the power input) match or even surpass those of inorganic LEDs. Furthermore, the ability for ultra-thin processing and direct color emission (instead of having to rely on liquid crystals) makes them very successful in display technologies. In the following sections, a brief historic overview of the development of OLEDs is given.

1.1. *1st Generation OLEDs*

OLEDs have come a long way since the discovery of electroluminescence in 1936.[1] Destriau was the first to show that ZnS is able to show emission when an electric field is applied. In 1953, Bernanose *et al.* for the first time observed electroluminescence in organic materials by introducing acridine orange (Figure 1.1) in a cellulose matrix and applying an alternating electric field.[2] 10 years later, Pope *et al.* placed a layer of single crystal anthracene between two silver electrodes and applied a voltage to this (Figure 1.1).[3] At over 400 V, the result was a faint, but typical emission for anthracene. When anthracene was mixed with tetracene, the fluorescence emission of tetracene was observed.

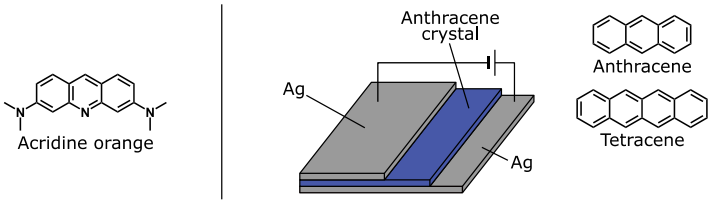

Figure 1.1: Molecular structure of acridine orange (left) and device architecture and active materials used by Pope *et al.*[3] (right).

In 1987, Tang and VanSlyke created the first electroluminescent device that paved the way for modern day OLEDs at the Eastman Kodak Company (Figure 1.2).[4] They described their device as being a double layer diode, wherein two organic layers consisting of Alq_3 and a diamine were used. Alq_3 acts as a green emitter, whereas the diamine layer is used for monopolar charge carrier (hole)

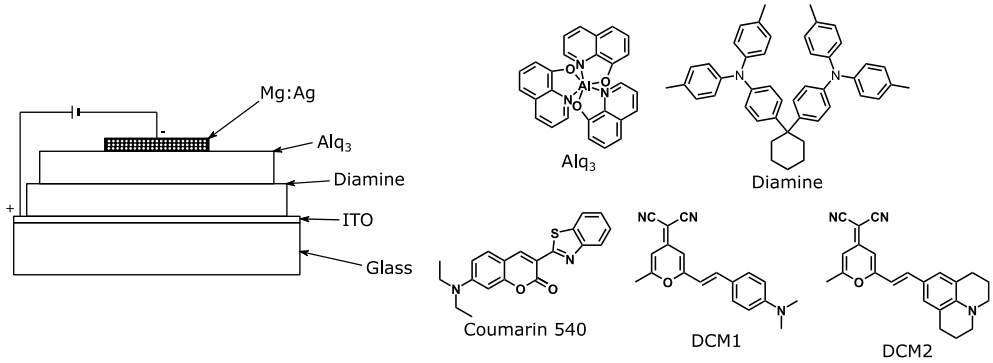

Figure 1.2: Device architecture applied by Tang and VanSlyke and molecular structures of Alq_3, the diamine layer and the colored emitters coumarin 540, DCM1 and DCM2.[4, 5]

transport. Around the same time, Adachi *et al.* published a series of papers in which they expanded the device structure to three layers, including hole transport (HTL) and electron transport layers (ETL) between which the emitting layer is sandwiched.[6, 7] Various emitter materials such as anthracene, coronene and perylene[6] and a 12-phthaloperinone derivative[7] were used. The two-layer architecture from Tang and VanSlyke worked rather well because the emitters have relatively good electron-transporting properties. Switching to the three-layer architecture removed this need as both barrier layers provide enhanced charge carrier transport and so the pool of emitter materials could be expanded. Adachi and coworkers further illustrated this by incorporating a hole transport layer with emitting properties, effectively combining the emitter and hole-transporting layer into one.[8]

In 1989, Tang *et al.* were able to reach substantial device efficiencies by sandwiching an Alq_3 layer doped with green and orange-red emitters between two layers of pure Alq_3 (Figure 1.2).[5] The higher photoluminescence quantum yield (PLQY), i.e. the ratio of emitted to absorbed photons, of the doped films, 3 to 5 times larger with respect to that of pure Alq_3 (PLQY = 8%), was expected to afford an increased device performance. Whereas devices using Alq_3 as the sole emitter afforded an efficiency of 1%, the new sensitized devices reached up to 3%. The device efficiency is defined here as the ratio the number of photons emitted by the device to the number of charges injected into the device.

In these types of sensitized devices, electrons and holes that are injected from the anode and cathode move through the device until they encounter each other and recombine to form excitons (i.e. bound electron-hole pairs). Device tuning,

making use of additional layers such as the hole and electron transporting layers, ensures that the electrons and holes recombine in the so-called active layer. This active layer usually consists of a 'host' material, i.e. a large gap semiconducting material capable of transporting the charge carriers to their destination, and an emitting material, on which the charges recombine.

Soon afterwards, in 1990, Burroughes *et al.* took a different route with the advent of organic conjugated polymers.[9] Their work involved the synthesis of a poly(*p*-phenylene vinylene) (PPV) conjugated polymer (Figure 1.3). The main advantage foreseen for a polymer emitter would be an improvement of the device stability as small molecule devices often suffer from recrystallization and other structural changes. However, due to the insolubility of the final polymer, a precursor polymer had to be processed from solution onto the bottom electrode, which itself was deposited on a suitable substrate, followed by a thermal annealing step in vacuum in which the final PPV polymer was formed. Indium tin oxide (ITO) was chosen as the bottom contact because of its semi-transparency, whereas a thin layer of aluminum was used as the top contact. In this device architecture, the polymer acts as the host and emitter at the same time, allowing charge recombination to occur on the polymer chains, followed by exciton diffusion until they decay and light is emitted. Unfortunately, the device efficiencies only reached up to 0.05%, which was attributed to failures at the polymer/thin metal interface.

Since then, several strategies have been used to synthesize soluble, and thus readily processable, polymers for OLED applications. These strategies often

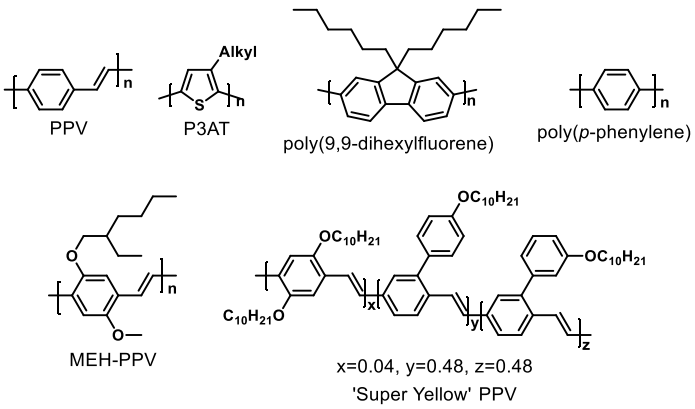

Figure 1.3: Polymer structures used in OLED devices.

encompass the incorporation of large, sometimes branched, aliphatic chains as these prevent stacking (and thereby emission quenching) between the conjugated polymer backbones. Other aromatic motifs such as thiophene, fluorine and phenylene have been used. Changing the polymer backbone leads to a variation in emission color, but could also lead to changes in device stability and processability. Ohmori *et al.* (1991) made devices with poly(3-alkylthiophene) (P3AT)[10] and poly(9,9-dihexylfluorene)[11] as the active materials because both polymers are well soluble with emission in the orange-red and blue, respectively (Figure 1.3). Unfortunately, efficiencies have not been reported for these devices. In 1992, Grem *et al.* prepared a poly(*p*-phenylene) based device, similar to that of Burroughes *et al.*, in which a precursor polymer was processed and the final polymer was obtained after thermal annealing (Figure 1.3).[12] With blue emission, the device only managed to reach efficiencies of 0.01–0.05%, similar to the results with unfunctionalized PPV polymers. In the meantime, progress was made using PPV polymers and D. Braun and A.J. Heeger went on to functionalize the original PPV polymer with methoxy and 2'-ethylhexyloxy side chains to create poly(2-methoxy-5-(2'-ethylhexyloxy)-1,4-phenylene vinylene) or MEH-PPV (Figure 1.3).[13] This functionalized PPV polymer has the benefit of being soluble in organic solvents, allowing facile processing without a thermal annealing step.

Development in the field of polymer OLEDs has continued, although polymers such as MEH-PPV are still being used as prototypical reference materials. One notable example is the PDY-132 developed by Merck Gmbh, which is also dubbed "super-yellow" (Figure 1.3).[14] This PPV-based copolymer has a high PLQY in the yellow region and devices with 5.3% efficiency have been obtained, which is among the highest values reported for polymer-based OLEDs. Early incorporations of polymer OLEDs can be found in for example the Norelco electric shaver by Philips (Figure 1.4).

In addition to polymer OLEDs, researchers have investigated different ways of combining facile solution processing with excellent photophysical properties. Dendrimers can be designed to have extended π-conjugated structures, giving them semiconducting properties, but because of their branched nature, they are far more soluble than their polymer counterparts. Early designs were based on an emissive core surrounded by either a fully conjugated or partially saturated

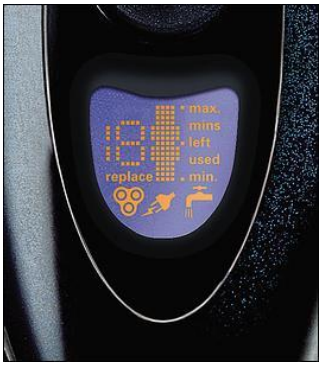

Figure 1.4: Norelco electric shaver by Philips with a polymer OLED screen.[15]

periphery. Using conjugated or partially conjugated branches, the charge transport from the electrodes to the active material could be improved. In 1996, Wang *et al.* built a dendrimer around an anthracene unit using phenylene

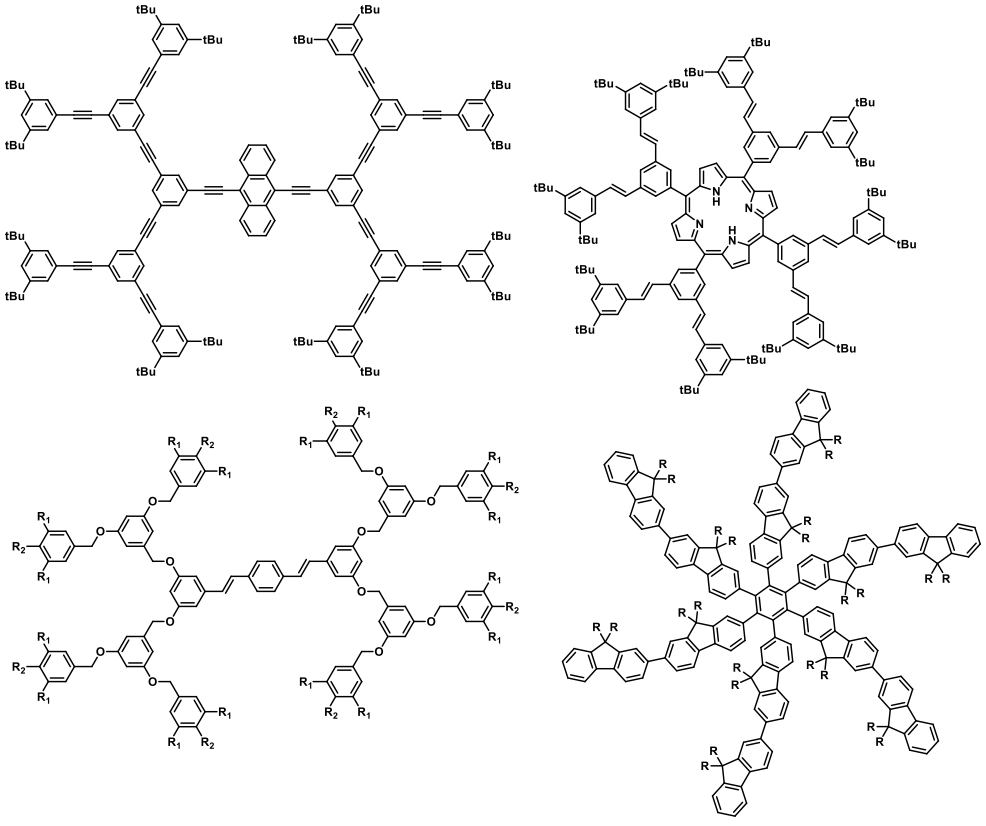

Figure 1.5: Dendritic active materials studied by Wang *et al.*[16] (top left), Pillow *et al.*[17] (top right), Kwok and Wong[18] (bottom left) and Zou *et al.*[19] (bottom right).

ethynylene units to create the branches (Figure 1.5).[16] Unfortunately, the devices suffered from solid-state aggregation and self-quenching. Pillow *et al.* designed a dendrimer with a porphyrin core and stilbene branches (Figure 1.5), resulting in red emission.[17] Kwok and Wong used distyrylbenzenes with poly(benzyl ether) type dendritic wedges (Figure 1.5).[18] Their dendrimer showed blue emission and despite its non-conjugated periphery, it was found that energy transfer does occur between the branches and the core. In 2003, six-arm star-shaped oligofluorenes were synthesized by Zou *et al.* (Figure 1.5), affording blue emission and a maximum device efficiency of 6.8%.[19]

Despite substantial efforts towards solution-processable polymer and dendrimer OLEDs, small molecule OLEDs have remained the main area of interest. This is mainly due to the lower device efficiencies obtained using polymer and dendrimer active materials, which themselves are a result of device defects that are introduced via solution processing and defects in the polymer backbones introduced during their synthesis. Device defects occur as the hole/electron transporting/blocking layers are often small molecule organic materials, which can partially redissolve during the addition of novel layers, making pin-holes more likely and leading to a poor active layer morphology. In contrast to polymers, small molecule emitters can be readily purified using sublimation techniques and they allow device fabrication via vapor deposition techniques, affording a higher degree of control over the layers and their morphology in multi-layer device stacks.

In the above section, a brief summary of the history of the first generation OLEDs, based on simple fluorescent emitters, is provided. While some historically important studies are mentioned, the overview on fluorescent OLEDs given here is far from exhaustive.

1.2. 2nd Generation OLEDs

Shortly after the initial discovery by Tang and VanSlyke,[4] an alternative emission mechanism in the form of phosphorescence was used to develop OLED devices. Phosphorescence is the emission from the triplet state and is not commonly observed in organic fluorophores (e.g. in the materials from the previous section) (Figure 1.6). The underlying mechanism can be explained using

quantum mechanics. For most organic materials, the ground state is of singlet nature. Absorption of a photon leads to excitation from the singlet ground state to one of the singlet excited states, depending on the energy of that photon. Because the excited triplet states have a different spin configuration, a change of spin is required to go from the singlet to the triplet state. Because of the laws of conservation of momentum, the change in spin angular momentum should be paired with a change of momentum elsewhere, typically in the orbital angular momentum. Hence, the term spin-orbit coupling (SOC) is coined to describe the connection between the spin and orbital angular momentum in systems ranging from atoms to large organic compounds. Large SOC values are typically observed when heavy atoms such as lead (Pb), platinum (Pt) or iridium (Ir) are introduced, whereas intermediate values can be found for the heavy halogens

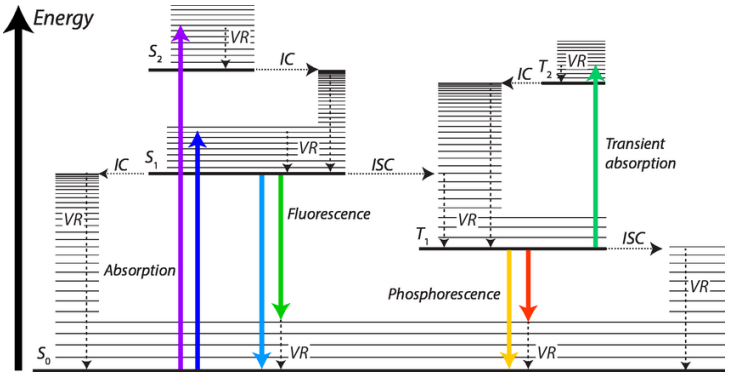

Figure 1.6: Jablonski diagram showing possible transitions. VR = vibrational relaxation; IC = internal conversion; ISC = intersystem crossing.

iodine (I) and bromine (Br). To achieve direct absorption into the triplet state and subsequent emission back to the ground state, a certain amount of SOC is needed. The lack of SOC in common organic molecules, however, makes them unable to show phosphorescence. Furthermore, when an electron and a hole recombine in an OLED device, the formed exciton can be either of singlet or triplet nature. Because there is only one possible singlet and three possible triplet configurations, the excitons are formed in a ratio of 25% singlets and 75% triplets. Since phosphorescence is not possible for the 1st generation OLED emitters, the maximum internal quantum efficiency (IQE) can only be around 25%. The IQE is defined as the proportion of charge carriers that are converted into photons. The external quantum efficiency (EQE), so far simply referred to as the device efficiency, is expressed as the number of photons leaving the device

with respect to the number of charge carriers injected into the device.[20] The EQE is subjected to the light outcoupling efficiency, in which nearly 75% of all emitted light is lost. Light outcoupling is mainly diminished by internal reflection and destructive interference.[21]

The second generation of OLED materials was designed to overcome these issues by the incorporation of heavy atoms. As they lead to an increase in spin-orbit coupling, giving rise to phosphorescence, intersystem crossing (ISC) becomes viable (Figure 1.6). The same SOC that leads to phosphorescence also enables ISC from the singlet to the triplet excited state. In an OLED device with such a heavy metal containing emissive material, the 75% of triplet excitons that are inherently formed during charge recombination can now be exploited through the phosphorescent pathway. Subsequently, the 25% singlet excitons can be converted to the triplet state via ISC, leading to a maximal IQE of 100%. Nevertheless, even with an IQE of 100%, light-outcoupling efficiencies of around 25% prevent EQE's of more than 25%.

In 1990, Kido *et al.* used a terbium (Tb^{3+}) complex of acetylacetonate to construct a two-layer device with TPD as the hole-transporting layer (Figure 1.7).[22] The device emitted green light with a very narrow spectral width, another advantage of using heavy-metal complexes making them ideally suitable for display applications. In 1993, Kido *et al.* reported on a red-emitting tris(thienyltrifluoroacetylacetonato)Eu^{3+} complex which was spin-coated in a poly(methylphenylsilane) film because it was not possible to evaporate this complex (Figure 1.7).[23] These two complexes are among the first examples of heavy-metal complexes being applied to the field of OLEDs with the intent of boosting the device performance in terms of EQE and color purity. Baldo *et al.*

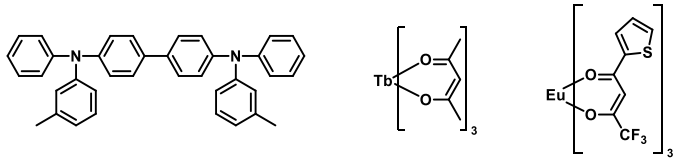

TPD Tb(acac)$_3$ Eu(ttfa)$_3$

Figure 1.7: Terbium and Europium complexes used by Kido *et al.*, with TPD as the hole-transporting material.[22, 23]

used a phosphorescent 2,3,7,8,12,13,17,18-octaethyl-21*H*,23*H*-porphyrine platinum(II) (PtOEP) dye as the emitter doped in Alq_3 (Figure 1.8).[24] With this

combination, more than 90% energy transfer from the Alq_3 host to the porphyrin emitter was obtained, leading to an IQE and EQE of 23% and 4%, respectively. At the time, this was a record efficiency for a red-emissive OLED. The same research groups then reported two more red-emitting porphyrin-based OLEDs, again using Alq_3 as the host material (Figure 1.8).[25] 2,7,13,17-Tetraethyl-3,8,12,18-tetramethyl-21*H*,23*H*-porphyrine platinum(II) (PtOX) and 5,15-diphenyl-21*H*,23*H*-porphyrine platinum(II) (PtDPP) showed similar red-shifted emission as PtOEP, but with varying photoluminescence quantum yields. PtOX and PtOEP have quantum yields of 0.44 and 0.55, respectively, as is expected due to the minimal structural change. PtDPP has a QY of only 0.16 as the phenyl groups on the porphyrin *meso*-positions likely lead to more non-radiative losses. As a result, the devices obtained with PtOX and PtOEP showed similar EQEs, whereas the devices containing PtDPP lagged behind.

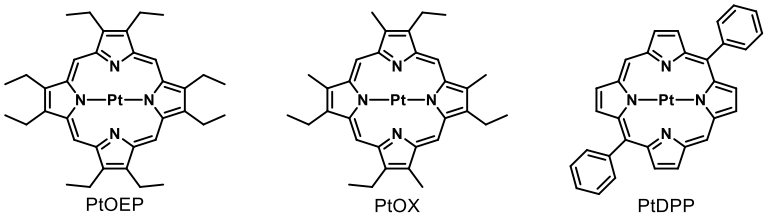

Figure 1.8: Phosphorescent Pt(II)-porphyrin emitters used by Baldo *et al.*[24] and Kwong *et al.*[25]

Introduction of a dopant into a host material was already described by Pope *et al.* as they showed doping of tetracene in anthracene gave predominant emission of the former.[3] Tang and VanSlyke used Alq_3 as a host for various fluorescent emitters[5] and the same host material was used for the porphyrin-based OLEDs by Baldo *et al.* and Kwong *et al.* Doping of an emitter material in a suitable host has, in these examples, been shown to be advantageous for the overall efficiency of the devices. One of the key factors in achieving good efficiencies is the proper energy level alignment of the emitter and host molecules.[26] Ideally, the energy levels of the host encompass those of the emitter to ensure exciton formation on the dye molecule. In the case of exciton formation on the host molecules, exciton diffusion can occur and they will migrate to the dye, which essentially acts as an exciton trap (Figure 1.9). The emitter can therefore achieve higher IQE values as emission from the host or other device layers is minimized. Additionally, energy transfer from the host to

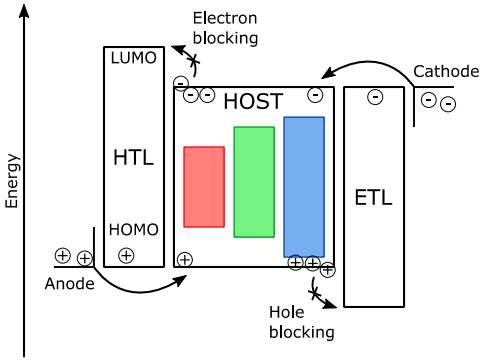

Figure 1.9: Simplified schematic of the energy levels in an OLED, ensuring exciton formation in the emitting layer.

the emitter should be as high as possible and ideally approach 100%. Another advantage of using doping is that doped devices often give narrower electroluminescence than non-doped devices.[26] This is particularly interesting when looking at full color displays where mixing of the primary colors red, green and blue (RGB) is necessary to obtain white light. A lower color purity (i.e. broad emission) leads to washed out colors. Doping also enhances stability as the emitter is no longer crystalline and the ETL and HTL have less tendency to crystallize. As doping is typically done in low amounts (<20%), the emitter molecules experience less self-quenching and ultimately less material is needed to construct efficient devices. This is particularly useful as the emitter is usually the most expensive component of an OLED device.

The next important improvement on the device architecture came with the introduction of additional layers to enhance charge carrier confinement in the emitting layer and thereby improve the overall device efficiencies. Up until this point, only two-layer (hole-transporting and emitting) or three-layer (hole and electron-transporting and emitting layer) architectures were used. Ikai *et al.* introduced a hole and exciton-blocking layer consisting of perfluorinated compounds in a four-layer architecture (Figure 1.10).[27] The device consisted of electron (Alq_3) and hole (α-NPD) transporting layers between which the hole/exciton-blocking layer and emitting layer are sandwiched. The hole/exciton-blocking layer is deposited between the emitting and electron-transporting layer to ensure that either holes or excitons are not able to migrate into the electron-transporting layer for charge recombination or relaxation (Figure 1.10). This is

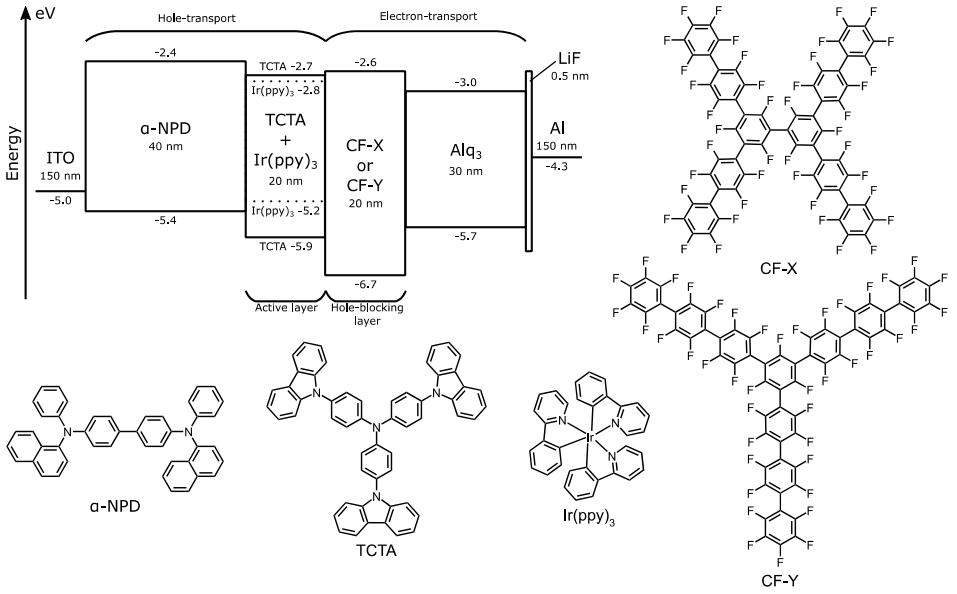

Figure 1.10: Device architecture and materials used in the work of Ikai *et al.*[27]

possible due to the low-lying HOMO and LUMO which are necessary for effective blocking of holes and injection of electrons, respectively. The green emitter tris[2-phenylpyridinato-C2,N]iridium(III), better known as $Ir(ppy)_3$, was doped in 4,4',4"-tri(*N*-carbazolyl)triphenylamine (TCTA), which also has hole-transporting properties. Additional layers include an aluminum cathode, a lithium fluoride (LiF) electron injection layer and an ITO anode (Figure 1.10). EQEs of up to 19.2% were obtained using this device architecture.

Iridium arose as one of the most suitable heavy metals to obtain highly emissive complexes with color tuneability, owing to the strong SOC of the iridium atom and strong metal-ligand charge transfer. In 2001, Adachi *et al.* reported three novel iridium complexes with modified ligands to obtain blue-emissive complexes.[28] Due to the requirement of having high-energy singlet and triplet states, blue-emissive complexes are more difficult to obtain than their green or red counterparts. By gradually making the ligands more electron poor ($Ir(ppy)_2(acac)$ to $Ir(Fppy)_2(acac)$) and by switching an acetylacetonato ligand for a picolinate (FIrpic), the emission was shifted from 516 to 465 nm in dilute chloroform solution (Figure 1.11). Using FIrpic, an EQE of 5.7 ± 0.3% was obtained, which was a significant improvement over existing technologies at that time for a blue emitter. In the same year, Adachi *et al.* also reported on the

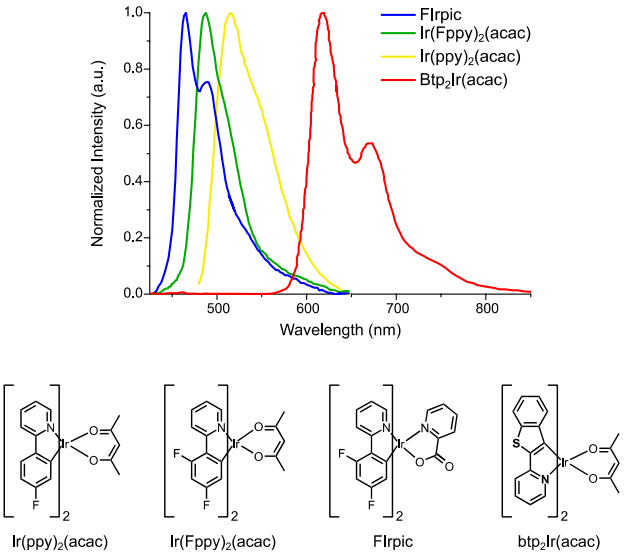

Figure 1.11: Iridium complexes and their emission reported by Adachi *et al.*[28, 29]

highly efficient red-emitting complex bis(2-(2'-benzo[4,5-α]thienyl)pyridinato-*N*,C$^{3'}$)iridium(acetylacetonate) [btp$_2$Ir(acac)] (Figure 1.11).[29] With an electroluminescence maximum at 616 nm, it comes close to the ideal color coordinates for video display standards. A maximum EQE of 7.5% was achieved, which is a significant increase over the 4% reported for the red-emitting PtOEP porphyrin (*vide supra*). Tuning of the emission color was further exploited by Tsuboyama *et al.*, who reported on a large number of red-emitting iridium complexes in which the ligand character was made more donating or accepting depending on the addition of specific functional groups such as methyl or CF_3.[30] Varying the ligand strength not only changes the emission color, but also has implications on the phosphorescence quantum yield (Φ_{Ph}), as it changes the positions of the singlet and triplet energy levels (Figure 1.12). Ir(piq)$_3$ was found to give very efficient red emission ($\lambda_{max,Ph}$ = 603 nm, Φ_p = 0.26) and a maximum EQE of 10.3 %.

Next to platinum and iridium-based complexes, other heavy metals such as ruthenium, osmium and rhenium have also been used.[31] Due to the higher oxidation potentials of these materials with respect to iridium, the prerequisites for the ligands are more strict and less design freedom is available. In combination with the (generally) higher EQEs for iridium-based devices, iridium has received most attention.[32-35]

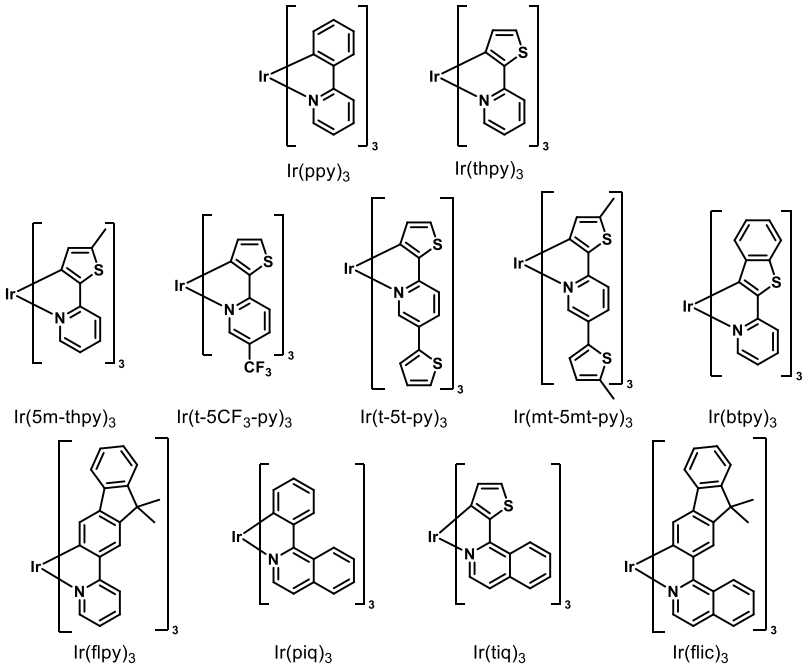

Figure 1.12: Iridium complexes synthesized by Tsuboyama *et al.*[30]

1.3. 3rd Generation OLEDs

The commercial success of the second generation OLEDs has inspired researchers to further investigate the possibilities to further improve the device performance in terms of stability, lifetime and sustainability. One of the possible ways to do so is to apply the concept of thermally activated delayed fluorescence (TADF).

1.3.1. The history of TADF

The discovery of TADF dates back to the beginning of the 20th century. In 1929, Delorme and Perrin discovered delayed fluorescence emission from certain uranium salts both in the solid state and in solution.[36] Measuring the salts at room temperature and at -180 °C (liquid oxygen), they observed a decrease in the emission lifetime, whereas the phosphorescence lifetime would go up upon decreasing the temperature. They therefore attributed the emission to some kind of delayed fluorescence. More than a decade later, Lewis *et al.* investigated the fluorescein molecule (Figure 1.13) in a solid state boric acid glass medium

and found delayed emission by carefully looking at the emission and its lifetime at various temperatures.[37] In 1961, Parker *et al.* measured the time-resolved emission of eosin (Figure 1.13) in glycerol and ethanol and found the first example of temperature dependent delayed emission in solution.[38] They found

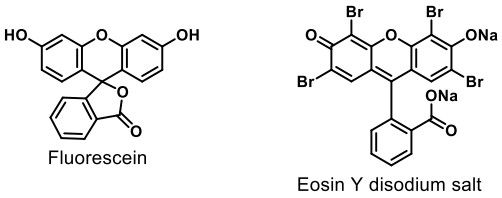

Figure 1.13: Chemical structures of fluorescein and eosin Y.

evidence for thermally activated ISC as well as direct ISC from an upper vibrational energy level of the singlet state to the triplet state. A prerequisite for these processes to occur efficiently is the proximity of the lowest excited singlet and triplet states, so that a small thermal barrier is left for either the ISC or the reverse ISC (rISC) process. The term E-type (E for eosin) delayed fluorescence was coined to describe the phenomenon. A year later, when investigating solutions of anthracene and phenanthrene (Figure 1.14), they observed similar delayed emission, but from singlet and triplet states that were further apart in energy. Therefore, a thermally activated process was ruled out. Instead, Parker *et al.* found that triplet-triplet quenching (also known as triplet-triplet annihilation or TTA) was most likely responsible for the formation of singlet excitons at very long lifetimes.[39] This phenomenon occurs when two excited

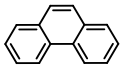

Figure 1.14: Chemical structure of phenanthrene.

molecules in the triplet state are in close proximity and energy transfer from one molecule to the other takes place. Two triplet excited states are converted to one singlet excited state and one molecule in the ground state, after which the singlet excited state can decay as delayed fluorescence. The process of TTA was originally named P-type delayed fluorescence after the molecule phenanthrene for which it was first discovered. TTA is here only mentioned because of its historical relevance. The detailed mechanism will be discussed later on when comparing the various triplet upconversion strategies.

Nishikawa *et al.* found E-type delayed fluorescence when trying to analyze porphyrinoid materials (Figure 1.15) based on their phosphorescence, but

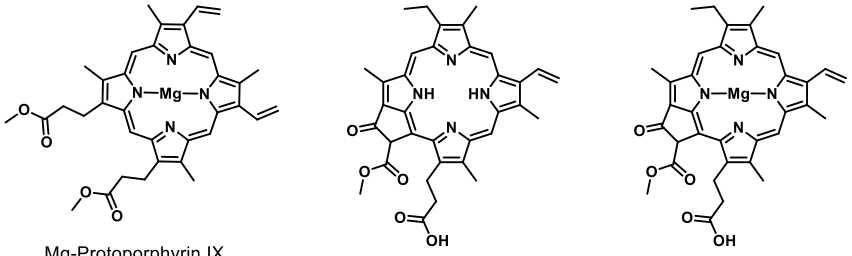

Figure 1.15: Porphyrinoids used by Nishikawa *et al.*[40, 41]

instead discovered delayed emission with a similar spectral position as the regular fluorescence.[40, 41] On top of the thermally activated nature, they postulated that the energy gap between the first excited singlet and triplet states should be less than 11 kcal mol^{-1} (0.5 eV) as compounds exhibiting a larger singlet-triplet gap would not show delayed fluorescence.[41] Substituting the free-base porphyrins with a metal ion influences the rate of ISC and rISC according to the atomic number of the substituted metal ion, affording increased rates when going from H to Mg^{2+} and Zn^{2+}. While E-type or thermally activated delayed fluorescence was found in numerous small molecules, such as the aforementioned ones but also in C70 fullerenes,[42] benzophenones[43] and aromatic thiones,[44] a suitable application was not found.

1.3.2. The theory of TADF

In 2009, Endo *et al.* discovered TADF in tin(IV)-porphyrins and decided to implement them in OLED devices (Figure 1.16).[45] Their results were in line with the findings of Nishikawa *et al.*[41] that substituting the free-base porphyrins can lead to a significant increase in the observed TADF intensity. Although the compounds still contained a "heavy" metal atom, this report sparked the interest in the field and the search for new TADF materials began as scientists started to understand the design principles behind TADF in fully organic molecules.

Following Endo's 2009 work on tin-porphyrins,[45] the amount of literature on TADF increased significantly and fully organic emitters for OLED applications were reported soon thereafter. In 2011, the Adachi group published 2-biphenyl-4,6-bis(12-phenylindolo[2,3-*a*]carbazole-11-yl)-1,3,5-triazine (PIC-TRZ) as the

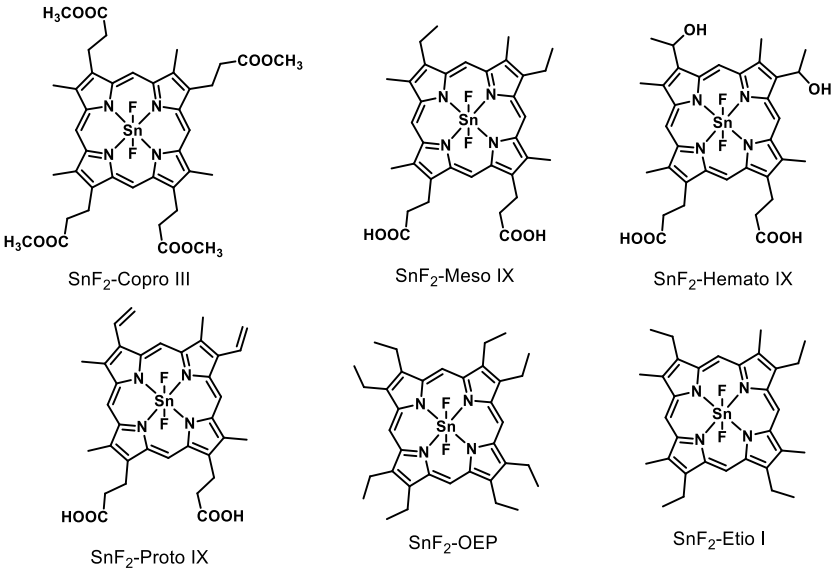

Figure 1.16: SnF_2-porphyrins used by Endo *et al*. to construct TADF-based OLEDs.[45]

first metal-free TADF compound for OLED applications, affording an EQE of 5.3% when doped in 1,3-bis(*N*-carbazolyl)benzene (mCP, 6 wt%).[46] In the next two years, 10 reports with new emitters were published, of which 9 having Adachi as the corresponding author[47-55] and 1 from the Monkman group[56]. The best performing compounds from these reports are displayed in Figure 1.17 and some experimental data are listed in Table 1.1. Although these data were obtained through varying methods for the different compounds, they provide a preliminary means of comparison. With EQEs ranging from 4.4% for the earliest work to >13% in the later works, a huge improvement in OLED efficiency was already achieved. With emission maxima between 485 and 553 for most of the materials, the compounds were largely green-yellow emitting and only one blue OLED device had been reported until this point, with red TADF OLEDs not being reported at all.

As was found by Parker *et al.*[38] and Nishikawa *et al.*[41], the mechanism of thermally activated delayed fluorescence relies on a series of excited state processes (Figure 1.18). When talking in terms of photoluminescence, a photon is absorbed and an electron is promoted from the (generally) singlet ground state to a singlet excited state according to the energy of the absorbed photon and the position of the singlet energy levels of the molecule in question. The

Table 1.1: Overview of fully organic TADF reports from 2011-2013.

Compound	$\lambda_{max,em}$ [a]	ΔE_{ST} (meV)[b]	Max EQE (%)	Date	Reference
PIC-TRZ	466	110	5.3	01/2011	46
Spiro-CN	540	57	4.4	04/2012	47
CC2TA	490	—[c]	11.0	08/2012	48
SDB-tBuCbz	424	—[c]	9.9	08/2012	49
PXZ-TRZ	544	—[c]	12.5	09/2012	50
ACRFLCN	485	100	10.1	10/2012	51
4CzIPN	508	83	19.3	12/2012	52
2PXZ-OXD	517	150	14.9	05/2013	53
DBTDO-tBuCbz	416	350	—[c]	05/2013	56
tri-PXZ-TRZ	553	—[c]	13.3	09/2013	54
ACRSA	494	30	16.5	09/2013	55

[a] Estimated from electroluminescence or doped-film photoluminescence spectra. [b] Calculated from the onset of prompt fluorescence and phosphorescence or via an Arrhenius plot. [c] These values were not reported.

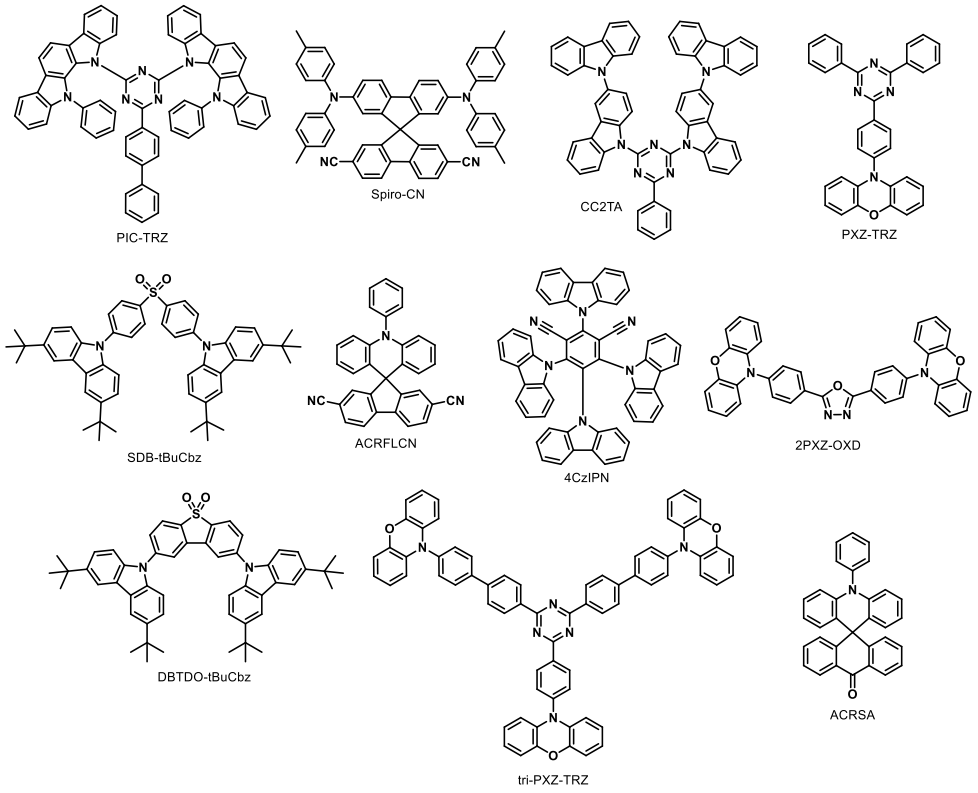

Figure 1.17: Chemical structures of the TADF emitters listed in Table 1.1.

excited state rapidly decays to the first excited singlet state in accordance to Kasha's rule,[57] which states that internal conversion (IC) from a higher energy

excited state to the lowest energy excited state of the same multiplicity occurs faster than any other excited state pathway. After the IC step, ISC from the singlet to the triplet state can occur. As previously discussed for the 2nd generation OLEDs, a change in the spin angular momentum has to be overcome by a change of orbital angular momentum through spin-orbit coupling. The use of heavy-metal atoms facilitates this transition due to their inherently larger SOC effect. However, the compounds used by Parker *et al.*[38] and Nishikawa *et al.*[41] did not contain heavy-metal atoms. The intersystem crossing rate (k_{ISC}) is dependent on both the energy difference between the respective singlet and triplet states as well as the amplitude of SOC. A smaller energy difference between the singlet and triplet states leads to a larger k_{ISC}. Following the initial intersystem crossing, reverse ISC (rISC) can occur, whereupon the exciton goes from the triplet state back to the singlet state. Because the triplet configuration is generally lower in energy than the singlet configuration for a given state in organic compounds, this rISC process is endoenergetic and an energy barrier

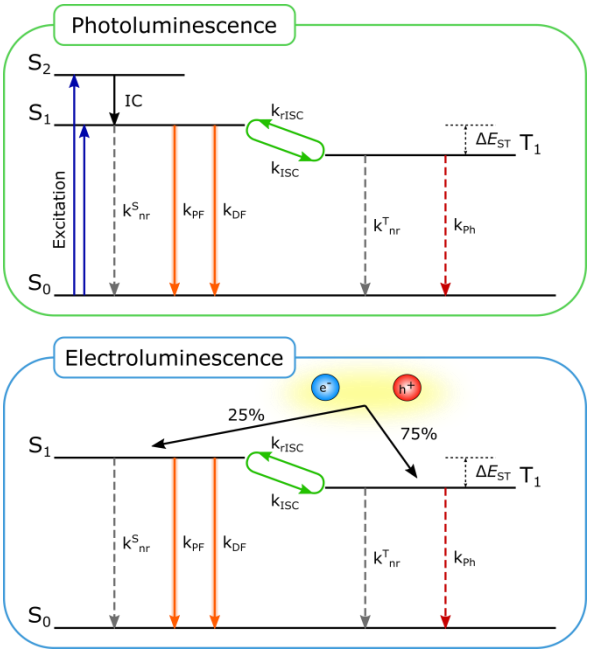

Figure 1.18: Schematic representation of the photophysical processes occurring upon photon absorbtion (top) or electrical excitation (bottom). IC = internal conversion, k^S_{nr}/k^T_{nr} = rate of non-radiative relaxation from the singlet or triplet state, k_{PF} = rate of prompt fluorescence, k_{DF} = rate of delayed fluorescence, k_{ISC}/k_{rISC} = rate of (reverse) intersystem crossing, k_{Ph} = rate of phosphorescence.

needs to be overcome. As the name TADF implies, this barrier is overcome using thermal energy. This also means the barrier cannot be too large. Whereas Nishikawa *et al.* postulated a barrier of approximately 0.5 eV,[41] it should be at least below 0.2 eV for efficient rISC.[58] Once the exciton returns to its singlet configuration, there are two options: either the exciton decays radiatively through fluorescence or it undergoes a second cycle of ISC/rISC. All these processes are dependent on their mutual rates. As was briefly touched upon, IC is typically very fast ($\ll 10^{-9}$ s), while fluorescence occurs at $\sim 10^{-9}$ s. ISC and rISC take place on much slower timescales of around 10^{-7} s and 10^{-6} – 10^{-5} s, respectively. The latter is especially slow due to the endoenergetic nature of the process. While phosphorescence is spin-forbidden, it is not entirely impossible. However, due to the SOC dependence, it occurs only at around 10^{-3} s. Given these rates, the rate of TADF is effectively governed by the rate of rISC, as it is the slowest step. Delayed emission in TADF emitters is therefore often observed in the microsecond domain.[58] As the singlet state from which radiative decay occurs is the same for the prompt ($\sim 10^{-9}$ s) and the delayed ($\sim 10^{-6}$ s) emission, their spectral shape should be identical, as was observed by Parker *et al.*[38] and Nishikawa *et al.*[41] and led them to believe the observed delayed emission could not be coming from phosphorescence.

Moving to OLEDs, where excitons are formed by recombination of electrons and holes rather than via absorption of a photon, the processes involved are the same, with the exception that ISC is no longer a prerequisite for rISC to occur as the excitons are formed in a 25/75 ratio of singlets/triplets (Figure 1.18). Upconversion of the 75% formed triplet excitons via rISC gives TADF OLEDs the possibility to achieve up to 100% IQE. The former method of analysis via photon absorption rather than electrical excitation still plays a crucial role as potential emitters are typically characterized in this way before being tested in actual OLED devices. While we discussed the crucial excited state processes for efficient TADF, these are not the only possible pathways for the excitons to traverse along. Non-radiative transitions, such as IC, can also occur between the lowest excited singlet or triplet states and the ground state, resulting in a loss of the exciton energy without the irradiation of visible light. These non-radiative transitions are often coupled with vibrations, rotations of specific functional groups or the molecules as a whole and collisions with other molecules (e.g. in

solution) need to be minimized. The key to avoiding them is making the molecule very rigid, so that the possibility for the vibrations and rotations to occur is very low. Therefore, in TADF design, as can be seen in Figure 1.17, the emitters generally consist of large conjugated and often heteroaromatic systems.

Next to being rigid, the key to designing efficient TADF emitters is to minimize the energy difference between the first excited singlet (S_1) and triplet (T_1) states. From quantum mechanics within the single transition approximation (STA), the singlet (ΔE_S) and triplet (ΔE_T) state energies can be written as Eq. 1.1 and 1.2, in which subscripts i and a are used to describe the occupied (often the highest, i.e. HOMO) and unoccupied (often the lowest, i.e. LUMO) molecular orbitals (MOs), respectively. J_{ai} is the Coulomb interaction and K_{ai} is the exchange interaction between the occupied and unoccupied MOs. The energy difference ΔE_{ST} can then be written as Eq. 1.3. The value of K_{ia} is related to the overlap between φ_i and φ_a, as indicated in Eq. 1.4. Spatial separation of φ_i and φ_a should therefore lead to a small K_{ia} and hence a small ΔE_{ST}.

$$\Delta E_S = {}^1\Delta E_{ai} = (\varepsilon_a - \varepsilon_i) - J_{ai} + 2K_{ai} \quad \text{Eq. 1.1}$$

$$\Delta E_T = {}^3\Delta E_{ai} = (\varepsilon_a - \varepsilon_i) - J_{ai} \quad \text{Eq. 1.2}$$

$$\Delta E_{ST} = {}^1\Delta E_{ai} - {}^3\Delta E_{ai} = 2K_{ai} \quad \text{Eq. 1.3}$$

$$K_{ai} = \iint dr\, dr' \varphi_a(r)\varphi_i(r) \frac{1}{|r-r'|} \varphi_a(r')\varphi_i(r') \quad \text{Eq. 1.4}$$

While the single-transition approximation presents limitations that are corrected using TDDFT calculations (most excited states have contributions from several single-particle transitions), it served as a first design criterion for novel TADF emitters.

In organic materials, the HOMO is typically located on the electron rich parts of the molecule, whereas the LUMO is typically located on the electron poor parts. By connecting an electron-rich moiety (often called electron-donating group or donor "D") to an electron-deficient unit (often called electron-accepting group or acceptor "A") via a covalent bond, localization of the frontier orbitals is only achieved to a given extent so that overlap remains present, leading to relatively large values of ΔE_{ST}. By spatially twisting the D and A groups in a molecule, the conjugation between them will decrease as the π-orbital overlap diminishes (Figure 1.19). This also leads to a better separation of the HOMO and LUMO.[58]

Therefore, the most used strategy to obtain a small ΔE_{ST} is to provide sufficient steric hindrance between the D and A parts of a molecule to ensure a large dihedral angle between the two moieties.[59] Alternatively, sp^3-hybridized linkages such as a spiro conjugation can be applied as the lack of non-hybridized p-orbitals in an sp^3-hybridized atom breaks the conjugation between its connecting atoms and also leads to HOMO-LUMO separation (Figure 1.19).[60] Unfortunately, a trade-off exists between the frontier orbital overlap and the rate of fluorescence (k_{PF}).[58] The oscillator strength determines the strength of the coupling between the singlet ground and excited state. Excitations with a smaller oscillator strength show weaker absorption and emission intensity than excitations with a large oscillator strength. The size of the oscillator strength is determined by the overlap between the orbitals that are involved in the given transition. For a HOMO->LUMO transition for example, a large overlap between the HOMO and LUMO will lead to a large oscillator strength, if the symmetry conditions are also fulfilled, and a localized excited state (^{1}LE state, superscript 1 for singlet and 3 for triplet states), whereas a small overlap leads to a charge-transfer state (^{1}CT state, superscript 1 for singlet and 3 for triplet states) with a small oscillator strength. As the requirements for TADF include a small orbital

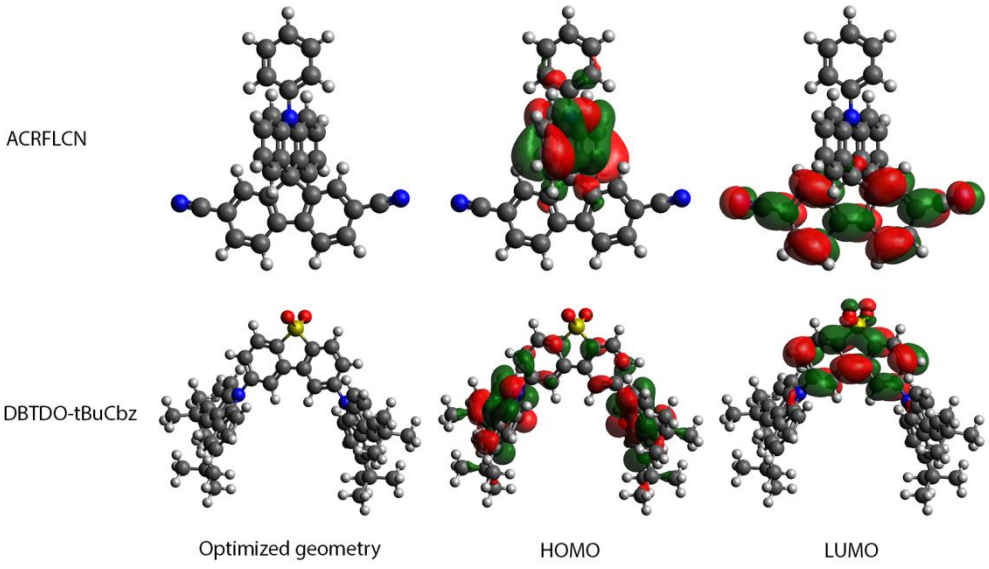

Figure 1.19: Optimized geometries, HOMO and LUMO topologies for a spiro conjugated (ACRFLCN) and a D-A based (DBTDO-tBuCbz) TADF emitter obtained using DFT (M06/6-311G(d)) (Structures in Figure 1.17).

overlap, typically for the HOMO and LUMO, these transitions are paired with a small oscillator strength, which is unfavorable for the fluorescence efficiency. Luckily, TADF emitters with a high k_{PF} and fluorescence quantum yield have been reported, indicating a less straightforward relationship between ΔE_{ST} and k_{PF}.

1.3.3. The spin-vibronic mechanism of TADF

Due to the structural design of TADF emitters, they often exhibit charge-transfer character in their transitions. Initially, the mechanism of TADF was therefore expected to result from direct (r)ISC between the first singlet and triplet excited CT states (i.e. ^{1}CT and ^{3}CT). However, the law of conservation of momentum forbids a change in spin angular momentum without a corresponding change in orbital angular momentum, or in other words, a ^{1}CT->^{3}CT transition between states of the same nature is not possible as there is no change in orbital angular momentum,[61, 62] which is also known as El-Sayed's rule.[62] Hyperfine coupling induced ISC was proposed as an alternative mechanism based on time-resolved electron paramagnetic resonance (EPR) methods,[63] but due to the small values for hyperfine interactions (HFI), usually in the range of 10^{-4} meV, it is unlikely that HFI alone can induce strong (r)ISC in these systems.[64] Furthermore, two experimental reports showed that the rate of reverse intersystem crossing (k_{rISC}) is not directly related to the size of ΔE_{ST}[65] and that, in some systems, it is possible to tune the excited states involved in the rISC step independently by changing the surrounding of the emitter.[56, 66] These findings lead to a more dynamic rISC process, which is not strictly governed by ΔE_{ST} and not strictly occurring between CT states.

Chen *et al.* tried to calculate k_{rISC} occurring via SOC, but found a significant deviation from experimental values, even for the ^{1}CT->^{3}LE transition, which is allowed according to El-Sayed's rule.[67] Marian used multi-reference methods to show that direct SOC was too small to explain the efficient rISC observed in TADF, in agreement with the work by Chen et al.[67] Instead, she proposed vibrational mixing between the ^{3}CT and an energetically close ^{3}LE state to be responsible for the efficient rISC.[68-70] Gibson *et al.* further elaborated on this and showed, through quantum dynamics simulations, the role of vibrational-electronic (vibronic) coupling of excited triplet states on k_{ISC} and k_{rISC}.[64] For the

molecule PTZ-$DBTO_2$ (Figure 1.20), time-dependent density functional theory (TDDFT) calculations (M06-2X/def2-TZVP under the Tamm-Dancoff approximation) showed the lowest singlet excited state to be of CT character (^{1}CT), whereas the lowest triplet excited state is of LE character, localized on the donor unit (^{3}LE). The second excited triplet state is of CT character (^{3}CT) and is of the same nature as ^{1}CT. The vibrational modes in the molecule were calculated using DFT and the vibrations that are eligible for thermal activation (<500 cm^{-1}, 62 meV) and of the correct symmetry to couple the triplet states were selected to construct a Hamiltonian which was used in the dynamics simulations to account for spin-vibronic interactions. The vibrational analysis yielded 3 possible vibrational modes for coupling: a D-A bond rocking, an A torsion and a D-A torsion mode. Figure 1.20 shows the results of their dynamics simulations for the relative ^{1}CT population associated with rISC over time after populating the ^{3}LE state. In black is the result from their unaltered Hamiltonian. Removing the HFI (green) does not lead to a significant change and is therefore also ruled out as the dominant factor. Removing the vibronic coupling (VC, blue) entirely kills the rISC process, while increasing the VC by 10% slightly increases the k_{rISC} (red). Decreasing the ^{3}LE-^{3}CT energy gap by half increases k_{rISC}, indicating that both VC and $\Delta E_{T1\text{-}T2}$ are crucial for efficient (r)ISC to occur. These findings show the need for two triplet states to be in close energetic proximity. In the aforementioned work,[64] they are of CT and LE

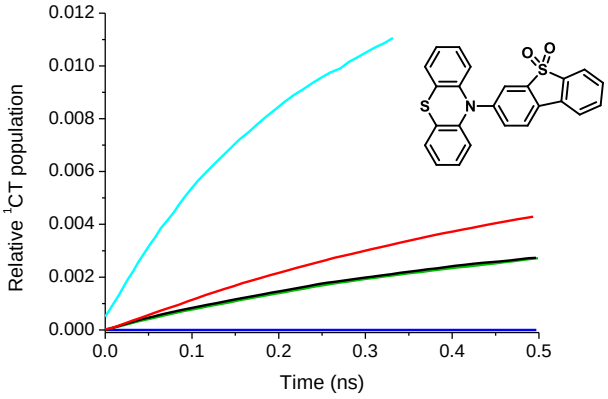

Figure 1.20: Relative populations of the ^{1}CT state associated with rISC after initially populating the ^{3}LE state of PTZ-$DBTO_2$ as simulated in the work by Gibson and co-workers.[64] Black: full model Hamiltonian, green: no HFI, blue: no VC, red: VC increased by 10%, cyan: energy gap between ^{3}LE and ^{3}CT halved. The molecular structure of PTZ-$DBTO_2$ is given in the graph insert.

nature, but they can well be both of CT nature if the two CT transitions have different orbital character. Furthermore, the vibronic mechanism helps to explain why compounds with an apparently large ΔE_{ST} can still show TADF. ΔE_{ST} is typically obtained from the onset of the prompt fluorescence (singlet energy) at room temperature and delayed phosphorescence (triplet energy) at 80 K, both occurring from the lowest energy excited state for each multiplicity. The phosphorescence spectra are taken at 80 K because this transition is spin-forbidden and non-radiative losses dominate at room temperature. Decreasing

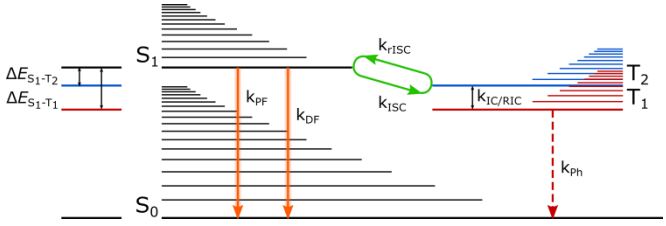

Figure 1.21: Overview of the spin-vibronic mechanism for TADF. Vibronic coupling (VC) between T_1 and T_2 ensures population of the T_2 state regardless of the available thermal energy, resulting in a smaller effective ΔE_{ST}.

the thermal energy and locking the conformation in a solid matrix allows the generally weak and red-shifted phosphorescence to be observed. The vibronic mechanism, however, couples the lowest excited triplet state to a higher energy excited triplet state to create 'mixed' states which are closer in energy to ^{1}CT. The energy gap that triplet excitons need to overcome to undergo rISC is therefore smaller than the experimental ΔE_{ST} (Figure 1.21).[59]

1.3.4. TADF emitters

In the previous sections, the most important design criteria for TADF emitters have already been addressed, such as a large dihedral angle between the D and A parts to afford a good HOMO/LUMO separation and a small ΔE_{ST}, a rigid structure to minimize non-radiative losses and a high fluorescence quantum yield (Figure 1.18). From the spin-vibronic mechanism, it became clear that molecular vibrations, such as the D-A rocking vibration for D-A type compounds (Figure 1.22), play a crucial role in increasing the rISC efficiency.[64,70] In compounds with spiro-conjugation or planar TADF emitters, other low energy vibrations fulfill this role, although their origin is not well understood yet. Therefore, most TADF emitters are constructed via a C-N bond connecting the D

and A parts of the molecule, as already seen in Figure 1.17. Color tuning is done by combining weaker or stronger donor or acceptor units to obtain more blue or red-shifted emission, respectively.[71] The electron-donating or accepting strength can be gauged by looking at the HOMO energy for electron donors and the LUMO

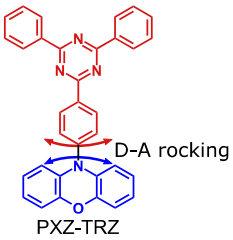

Figure 1.22: D-A rocking vibration indicated by the arrows in which the D and A units rotate independently around the D-A bond.

energy for electron acceptors. Donor units with a higher HOMO energy are more electron-donating, whereas acceptor units with a lower LUMO energy are more electron-accepting. These values are not readily available from experimental measurements, but DFT calculations can be performed on the individual building blocks to have an idea of their energy level positioning. The results of such DFT calculations (M06/6-311G(d)), performed by myself, are given in Table 1.2 for a number of commonly used donor and acceptor units. The chemical structures of these units are shown in Figure 1.23. The color of the emitter is largely determined by the acceptor unit because of the wider spread in LUMO energies (-1.40 to -3.28 e V) with respect to the spread in HOMO energies (-6.02 to -5.26) for the donor units.[†] The donor unit has a minor influence based on its electron-donating strength. However, the steric hindrance between the donor and acceptor units is largely determined by the donor. Looking at Figure 1.24,

Table 1.2: HOMO and LUMO energies (in eV) for various donor and acceptor units commonly used in TADF emitters as obtained by DFT calculations using M06/6-311G(d).

Donor			Acceptor		
Name	HOMO (eV)	LUMO (eV)	Name	HOMO (eV)	LUMO (eV)
Cbz	-6.02	-0.81	TXO2	-7.62	-1.40
*t*BuCbz	-5.81	-0.81	DBTDO	-7.67	-1.51
DPA	-5.67	-0.30	TRZ	-8.07	-1.56
PTZ	-5.51	-0.53	DBTO2	-7.22	-1.93
DMAC	-5.47	-0.27	IPN	-8.40	-2.31
TPA	-5.38	-0.24	BT	-7.12	-2.34
PXZ	-5.26	-0.37	HAP	-7.66	-3.16
DHP	-4.72	-0.22	CNQxP	-7.15	-3.28

[†] Although DHP has a much lower HOMO energy than PXZ, it is not regarded as a typical TADF donor.

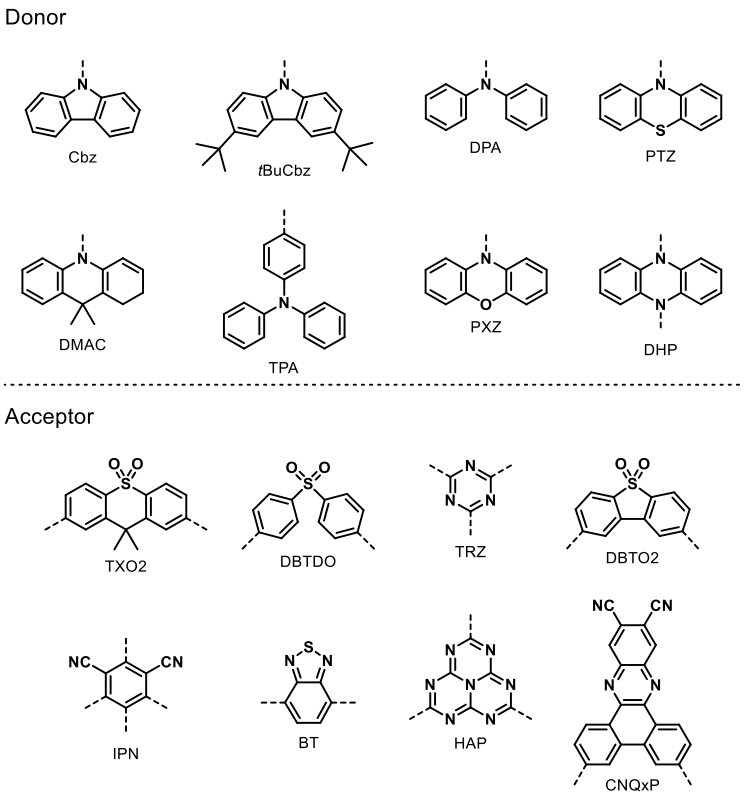

Figure 1.23: Chemical structures of the donor and acceptor units listed in Table 1.2. The D-A connection sites are indicated by dashed bonds.

for the donor units TPA, Cbz and DMAC, the distance between the proton and the adjacent connection point (indicated by a dashed bond) becomes smaller, leading to reduced rotational freedom around the D-A bond. DPA is a special case because the two phenyl rings will form a propeller shape by which the steric hindrance is reduced with respect to the other donor units. When connected to an acceptor, for instance CNQxP, the D-A dihedral angles using these donor units were calculated using M06/6-311G(d) and vary from DPA (25°) < TPA (36°) < Cbz (49°) < DMAC = PTZ = PXZ (90°). Changes to the dihedral angles can occur when the molecular structure of the acceptor forces the donor units in a more perpendicular orientation, as is the case for 4CzIPN (Figure 1.17), which is formed by connecting 4 carbazole units to one isophthalonitrile. As the dihedral angle determines the overlap between the HOMO and LUMO orbitals, DMAC, PTZ and PXZ are more likely to give well-

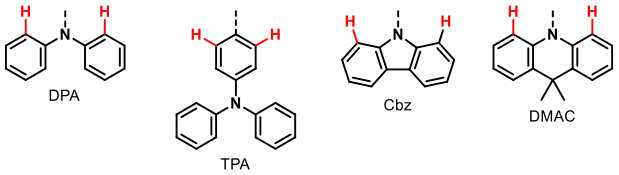

Figure 1.24: Influence of donor geometry on the dihedral angle of D-A compounds.

separated frontier orbitals than Cbz or *t*BuCbz.

In TADF literature, most reports deal with the design of novel (efficient) blue emitters. While 2nd generation phosphorescent OLEDs are commercially viable for green and red emission, blue phosphorescent emitters suffer from instability due to the relatively weak metal-ligand bond and the inherently high triplet energy needed for blue emission. Blue TADF emitters might be able to overcome these issues, but their design is not straightforward. As mentioned before, blue CT emission can be achieved when relatively weak donor and acceptor units are coupled together. However, as their electron-donating and accepting properties become weaker, so does the CT character of their transitions and hence ΔE_{ST} becomes larger. Another issue is the use of DMAC, PTZ or PXZ as the electron-donating groups. While these groups provide large steric hindrance and good HOMO/LUMO separation, their strong electron-donating properties red-shift the emission, often leading to blueish/green emission. Similarly, when the acceptor unit is too strong, the emission is also red-shifted and becomes green or even yellow. This explains why the first reported TADF materials were predominantly green or yellow emitters (Table 1.1, Figure 1.17). Nonetheless, the design of blue emitters has been successful, as demonstrated by the large amount of entries in review articles, some of them affording OLEDs with EQEs above 20%.[33, 71-75] Unfortunately, blue TADF emitters still suffer from rapid and significant roll-off of the device efficiency and more research to find stable, blue emitters is required.[76, 77]

On the other end of the spectrum are the red TADF emitters. These have received less initial interest because there were sufficient red-emitting phosphorescent complexes available (Figure 1.12), affording OLEDs with decent EQEs. While red emitters do not suffer so much from instability issues, their PLQY is often much lower due to the so-called energy gap law.[86, 87] As the energy gap between the ground and excited state becomes smaller, non-

radiative transitions become more plausible as the upper vibrational states of the electronic ground state start to overlap with those of the electronic excited states. Because of this, the highest EQEs reported are in the range of 10–20%, with a few outliers above 20%.[71, 88] In 2018, Chen *et al.* reported a summary of red emitters with a maximum electroluminescence wavelength of 600 nm or larger.[89] Additionally, due to their fully organic, and thus non-toxic nature, they have found application in other fields outside of OLEDs as well. In 2014, Xiong *et al.* showed that a fluorescein derivative showing delayed fluorescence could be used for time-resolved fluorescence imaging in biological cells. Due to the long-lived nature, the cell autofluorescence dies out before the fluorescein delayed emission has, enabling to enhance the imaging contrast.[78] Furthermore, the red-shifted emission of such materials makes them viable for operation in the so-called phototherapeutic window (600-1200 nm). Several other reports using TADF emitters for time-resolved imaging have been made since.[79-85] Although the generally reported TADF emitters are not water-soluble, several solubilizing strategies have been developed for *in vivo* studies with organic dyes and therapeutics, and these can be readily applied here as well.

Similar to the first generation OLEDs, researchers have tried to incorporate the principles of TADF in other types of molecules such as dendrimers and polymers. The main advantages of dendrimer and polymer structures include facile processing via spin- or spray-coating for large area applications such as television screens and solid-state lighting.[74] Both fully and partially conjugated dendrimers have been made (Figure 1.25). In both cases, the dendrimer core consists of a TADF emitter which is responsible for the photophysical properties. The dendrons in conjugated dendrimers often consist of extended carbazole networks,[90-93] whereas in partially conjugated dendrimers a short aliphatic chain connects the core with the conjugated dendrons.[94, 95] In both architectures, the dendrons serve effectively as the 'host' material for the dendrimer core and facilitate charge recombination and charge transfer to the TADF core. Despite their advantages for solution processable OLEDs, the EQEs have remained much lower in comparison to vacuum deposited small molecule OLEDs. For a more extensive overview of dendritic TADF materials, several reviews can be consulted.[72, 74, 96]

For polymer-based TADF OLEDs, several design strategies are available. First, a

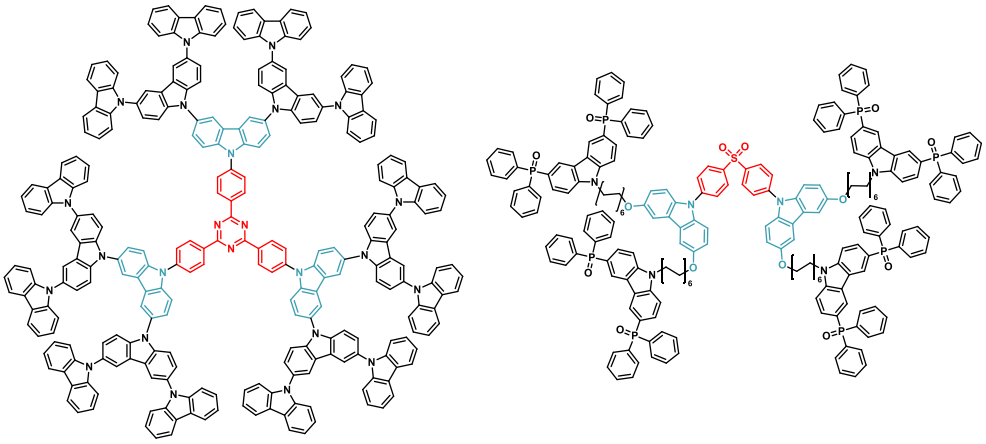

Figure 1.25: Molecular structures of two types of dendritic TADF emitters based on fully[90] (left) and partially[95] (right) conjugated dendrons. The acceptor and donor units are indicated in red and blue, respectively.

division between non-conjugated and conjugated backbones can be made (Figure 1.26). Within the polymers with a conjugated backbone, a second division can be made between polymers in which the backbone consists of alternating D and A units (Figure 1.26b) and polymers in which the backbone consists of (a single or alternating) D units to which the A unit is grafted as a side chain (Figure 1.26c). The opposite case in which the backbone is constructed of A units is less straightforward as the reactive sites used for polymerization are the same as those used for the construction of the D-A bond. In non-conjugated polymers, (Figure 1.26) the backbone is formed by polymerization of styrene-like[97-100] or acrylate[101] monomers via controlled free-radical polymerization techniques or functionalized norbornenes[102] for ring-opening metathesis polymerization (ROMP). A TADF emitter is incorporated in the monomer structure and is copolymerized with another monomer containing a hole-transporting functionality such as carbazole. Conjugated D-A alternating copolymers are often used in other fields of organic electronics such as organic photovoltaics (OPVs) and organic photodetectors (OPDs), but they are not suitable for TADF applications as the overlap between the HOMO (typically located on the D) and The LUMO (typically located on the A) is significant and thus ΔE_{ST} is large. A twist in the backbone is needed, similar to the design of small molecule TADF emitters, leading to a breakup of the conjugation along the polymer backbone. The main consequence is that charge transport along the

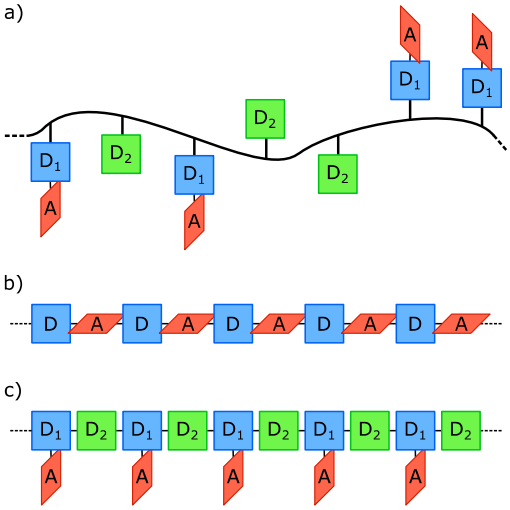

Figure 1.26: Design motifs for TADF-based polymers.

polymer backbone is severely reduced and therefore these polymers need to have an additional charge-transporting host material in which they are imbedded.[103] To reduce self-quenching and to improve the charge carrier mobility, either a non-conjugated spacer was incorporated between the various D-A blocks[104] or the D-A TADF emitters were copolymerized with an additional donor unit which acts as a kind of host material.[105] The most employed strategy is copolymerization of multiple, typically one or two, donor units to one of which an acceptor unit is grafted. The other donor unit in the backbone then acts as a kind of host material, improving charge carrier mobility, and is sometimes functionalized to further improve these properties.[72, 74, 103, 106-112]

1.3.5. Hyperfluorescence

In 2014, an alternative OLED design strategy was reported by combining a TADF emitter with a fluorescent emitter in the active layer.[113] This strategy is sometimes called generation 3.5 and was termed hyperfluorescence™ by Kyulux. The main advantages of hyperfluorescence are the optimal usage of excitons (up to 100% IQE) utilising the TADF emitter and the narrow emission with high PLQY and large k_{PF} for the fluorescent emitter. Because an additional energy transfer step is required for the fluorescent emitter, the design of these systems requires even more tuning of the energy levels of the OLED layers and active materials.

1.4. Alternative triplet upconversion strategies

1.4.1. Triplet-triplet annihilation (TTA)

Since the discovery of TTA, sometimes called triplet fusion (TF), in 1962 by Parker *et al.*[39] (*vide supra*), it is well known as an upconversion mechanism to form singlet excited states. Proceeding via a Dexter energy transfer mechanism (Figure 1.27), two molecules with excited triplet configurations need to be in close proximity to form one de-excited molecule and one molecule with an excited singlet configuration. As twice the triplet excitation energy is generally larger than the first singlet excitation energy, it can occur that a higher singlet

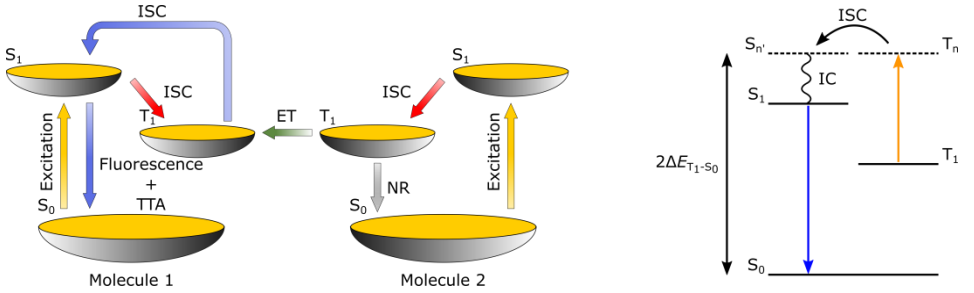

Figure 1.27: Schematic overview of Dexter energy transfer in TTA (left) and how it leads to singlet emission by combining 2 excited triplet states (right). ET = energy transfer, NR = non-radiative relaxation.

state (S_n) is formed first, after which IC takes place to arrive at the first excited singlet state (S_1), followed by fluorescence (Figure 1.27). In time-resolved emission spectroscopy, TTA can be distinguished from other types of delayed emission by varying the laser power and looking at the delayed emission intensity. When the emission intensity increases linearly with a slope of 2 in a log-log plot versus the laser power, the emission is coming from TTA, whereas a slope of 1 indicates TADF. This is because the likelihood of two triplet excitons being in close proximity increases with high exciton formation. The TTA mechanism is especially prevalent under electrical excitation where, according to spin statistics, 75% of the excitons are formed in the triplet configuration. However, because two triplet states are converted to one singlet state, the IQE of a resulting OLED can only be 62.5% (initial 25% plus half of the triplet states formed), which is significantly lower than the 100% IQE achievable via phosphorescent or TADF OLEDs. Nevertheless, TTA has played a significant role

in the development of early OLED devices, and to this day remains an attractive prospect for the fabrication of blue-emitting OLEDs. As early fluorescent devices were only able to effectively use 25% of the formed excitons, the device EQEs were theoretically limited to ~5%, taking into account a device outcoupling efficiency of approximately 20% into account. However, reports of fluorescent based OLEDs with EQEs higher than the theoretical limit of 5% do exist. While other effects such as increased device outcoupling or improved selectivity for the generation of singlet excitons upon electrical excitation are possible, they are unable to account for the large increase in EQE. In 1998, Kido and Iizumi were the first to suggest TTA as the plausible pathway for their record EQE (at the time) of 7.1%.[114] In 1999 and 2003, Partee *et al.*[115] and Sinha and Monkman[116] reported TTA as an efficiency boosting mechanism in PPV and MEH–PPV based OLEDs, respectively. In many other reports throughout the beginning of the 21st century, TTA is the likely candidate to explain EQEs above 5% for traditional fluorescent OLEDs. However, with the advent of phosphorescent and TADF-based OLEDs, research in this area has slowed down, with the exception of blue-emitting materials.[117-119] Despite the promise and achievement of higher EQEs for blue-emitting OLEDs using either phosphorescent iridium or TADF-based emitters, they both lack in device lifetime, while color purity is also an issue for the latter.[117-119] Poor electrochemical stability as a result of the fluorine substituents typically used for blue Ir-complexes (Figure 1.11) and instability of the metal-ligand bonds due to the high triplet energy (>2.7 eV) causes the blue phosphorescent OLEDs to have poor operation lifetimes.[119] While TADF emitters do not suffer from the same metal-ligand related issues, the inherently high triplet energy still causes deterioration of the emitter, with relatively short lifetimes as a result.[119] Furthermore, the CT character of the emission leads to broad emission peaks, affording inferior color purity with respect to the phosphorescent or fluorescent competitors. Blue fluorescent emitters suffer less from these instability issues due to their simpler molecular structures and as such are only hindered by the maximal attainable IQE of 25%. An upconversion mechanism such as TTA is able to boost this to 62.5% and hence can make blue emitters based on TTA viable, as apparent in recent literature.[120-122]

1.4.2. Hybridized local and charge-transfer states

Proposed in 2013 by Ma and co-workers, hybridized local and charge-transfer (HLCT) poses an alternative but similar mechanism to that of TADF (Figure 1.28).[123] The HLCT mechanism relies on intersystem crossing between an upper excited triplet state (T_n, n > 1) and an excited singlet state (S_n, n > 0). HLCT emitters rely on significant LE character in their first excited singlet state to ensure efficient coupling to the singlet ground state for a high PLQY. Two upper excited states of singlet and triplet multiplicity have to be in close energetic proximity for (r)ISC to occur. The lowest excited triplet state T_1, typically of LE nature, has to be significantly below T_2, typically of CT nature, and S_1 to reduce IC from T_2 to T_1 and to prevent TADF from happening from T_1 as large energy gaps reduce the coupling between the various states. ISC is enhanced when the upper states show hybrid LE/CT character,[124] which circumvents El-Sayed's rule, but is not a prerequisite for the HLCT mechanism to occur. Time-resolved emission measurements show that these emitters only have a single lifetime, instead of two as for TADF, indicating a k_{ISC} larger than k_{PF}. The HLCT mechanism thus indirectly increases the amount of excitons in the singlet

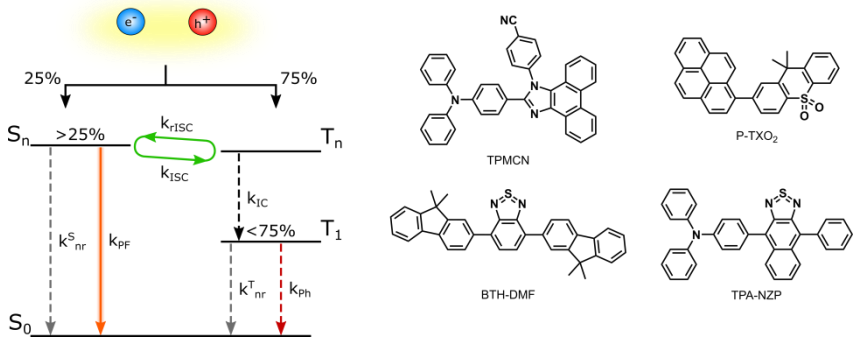

Figure 1.28: Simplified schematic overview of the HLCT triplet upconversion mechanism (left) and chemical structures of some highly efficient HLCT emitters: TPMCN,[122] P-TXO2,[124] BTH-DMF[125] and TPA-NZP[123] (right).

configuration beyond the statistical 25%, while HLCT materials act as regular fluorescent emitters beyond the initial ISC step. To obtain excited states with hybrid LE/CT character, twisted D-A structures are designed (Figure 1.28) and (TD)DFT calculations are performed to assess the character and the position of the upper excited states as these are difficult to determine experimentally. IC is

the favored transition according to Kasha's rule (*vide supra*) and the HLCT ISC mechanism is therefore not as efficient as the (r)ISC pathways of TADF can be. This means a significant portion of the 75% formed triplet excitons will still decay non-radiatively to T_1 (k_{IC}) where they are effectively trapped until they can further decay non-radiatively to the ground state (k^T_{nr}). As a result, EQEs using this approach have only been around 10%.[125, 126] Because of its heavy reliance on quantum chemical calculations, lack of structure-property relationships that can be deduced and non-ideal working conditions, the HLCT mechanism is currently of less interest to obtain high-efficiency OLEDs.

1.5. Quantum chemistry in TADF

1.5.1. Introduction to quantum chemical methods

Quantum chemical methods are often divided in two groups: Wavefunction methods and density functional theory (DFT). Hartree-Fock (HF) based methods rely on solving the Schrödinger equation for a given wavefunction, whereas in density functional theory, the electron density, denoted as ρ, occupies a central position. Since the exact wavefunction (Ψ_0) for a multi-electron system is out of reach, it is approximated by a single Slater determinant (Eq. 1.5).[127] The Slater determinant is built from occupied spinorbitals ($\Theta_i(\vec{x}_i)$) (Eq. 1.6) and each

$$\Psi(\vec{x}_1, \vec{x}_2, \dots, \vec{x}_N) = \frac{1}{\sqrt{N!}} \begin{vmatrix} \Theta_i(\vec{x}_1) & \Theta_j(\vec{x}_1) & \cdots & \Theta_k(\vec{x}_1) \\ \Theta_i(\vec{x}_2) & \Theta_j(\vec{x}_2) & \cdots & \Theta_k(\vec{x}_2) \\ \vdots & \vdots & \ddots & \vdots \\ \Theta_i(\vec{x}_N) & \Theta_j(\vec{x}_N) & \cdots & \Theta_k(\vec{x}_N) \end{vmatrix} \quad \text{Eq. 1.5}$$

$$\Theta_i(\vec{x}_i) = \varphi_i(\vec{r}_i)\sigma_i(\omega_i) \quad \text{Eq. 1.6}$$

spinorbital consists of a spatial orbital ($\varphi_i(\vec{r}_i)$) and a spin function $\sigma_i(\omega_i)$ ($\alpha_i(\omega_i)$ or $\beta_i(\omega_i)$ for spin up or spin down, respectively).

To arrive at the best approximation for the exact wavefunction of the system, a trial wavefunction (Ψ) with an energy larger than the exact ground-state wavefunction ($E(\Psi) > E_0(\Psi_0)$) is constructed and, using the variational principle,[128] its energy is minimized.[129-131] The molecular orbitals (MOs; φ_i) are constructed by introducing the linear combination of atomic orbitals (LCAO) approximation (Eq. 1.7), in which a weighted sum of a predefined set of atomic orbitals (AOs, χ_μ) is used.[132] In Eq. 1.7, the $c_{\mu i}$ are the LCAO coefficients and K is

the total number of atomic orbitals. From the optimized trial wavefunction (Ψ), the energy and other properties of the system can be derived. Alternatively, DFT

$$\varphi_i(\vec{r}) = \sum_{\mu=1}^{K} c_{\mu i}\chi_u(\vec{r}) \qquad \text{Eq. 1.7}$$

focusses on the electron density of the multi-electron system. The first theorem by Hohenberg and Kohn shows that the ground-state properties of a system are fully determined by the electron density ($\rho(\vec{r})$, Eq. 1.8,1.9).[133] Instead of describing the energy as a functional of the wavefunction in HF theory, it is now

$$\rho(\vec{r}_1) = N \int \dots \int |\Psi(\vec{x}_1, \vec{x}_2, \cdots, \vec{x}_N)|^2 d\omega_1 d\vec{x}_1 \cdots d\vec{x}_N \qquad \text{Eq. 1.8}$$

$$\text{with } N = \int \rho(\vec{r})\, d\vec{r} \qquad \text{Eq. 1.9}$$

a functional of the electron density, E(ρ). Similarly to the use of the variational principle within in the HF scheme, a trial electron density (ρ) is constructed which has an energy higher than the exact ground-state electron density (ρ_0). Within that frame, Hohenberg and Kohn divided the energy functional into several contributions (Eq. 1.10):[133]

$$E[\rho] = T[\rho] + V_{ee}[\rho] + V_{eN}[\rho] \qquad \text{Eq. 1.10}$$

With T[ρ] the kinetic energy functional, V_{ee}[ρ] the electron-electron (repulsion) potential energy functional, and V_{eN}[ρ] the electron-nucleus (attraction) potential energy functional. V_{eN}[ρ] can be calculated for each electron and the remaining terms are gathered in the Hohenberg and Kohn functional (F_{HK}) (Eq. 1.11,1.12). In Eq. 1.12, the electron-electron repulsion term is split into two

$$E[\rho] = V_{eN}[\rho] + F_{HK}[\rho] \qquad \text{Eq. 1.11}$$

$$\text{with } F_{HK}[\rho] = T[\rho] + J[\rho] + E_{ncl}[\rho] \qquad \text{Eq. 1.12}$$

parts: the Coulomb functional J[ρ] and the non-classical functional E_{ncl}[ρ], which accounts for self-interaction, correlation and exchange. Kohn and Sham then rearranged the equation for the Hohenberg and Kohn functional (F_{HK}), now F_{KS} (Eq. 1.13,1.14):[134]

$$F_{KS}[\rho] = T_S[\rho] + J[\rho] + E_{XC}[\rho] \qquad \text{Eq. 1.13}$$

$$\text{so that } E_{XC}[\rho] = T[\rho] - T_S[\rho] + E_{ncl}[\rho] \qquad \text{Eq. 1.14}$$

The Kohn-Sham functional (Eq. 1.13) consists of the kinetic energy of non-interacting electrons (T_S[ρ]), the Coulomb energy of the system (J[ρ]) and the

exchange-correlation functional ($E_{XC}[\rho]$). Whereas the first two terms can be calculated exactly, the exchange-correlation functional (XCF) consists of the kinetic energy of the whole system minus that of the non-interacting electrons and the non-classical functional, $E_{ncl}[\rho]$, which in itself accounts for self-interaction, correlation and exchange and its form is unknown. Kohn and Sham then expressed the electron density from a wavefunction that takes the form of a single Slater determinant (Eq 1.15) and using the LCAO approximation, Kohn-Sham spinorbitals (Θ_i) can be constructed.

$$\left[-\frac{1}{2}\nabla^2 + V_{eff}(\vec{r})\right]\Theta_i(x) = \varepsilon_n\Theta_i(x) \qquad \text{Eq. 1.15}$$

Since the form of the XCF is unknown, many researchers have developed various XCFs with different strategies and objectives in mind. The simplest strategy is the local density approximation (LDA) where E_{XC} only depends on the electron density ($E_{XC}[\rho]$). The generalized gradient approximation (GGA) functionals improve the LDA functionals by introducing a dependence on the gradient of ρ ($E_{XC}[\rho,\nabla\rho]$). Both consist of a separate exchange and correlation part with some well-known GGA functionals being BLYP (consisting of Becke's B88 exchange functional[135] and the Lee-Yang-Parr (LYP) correlation functional[136]), BPW91 (consisting of Becke's B88 exchange functional[135] and the PW91 correlation functional[137]) and PBE (technically PBEPBE as it consists of the PBE exchange and correlation functionals[138]). The third class of XC functionals are called meta-GGA functionals as they include both the dependence on the gradient of the density as well as a dependence on the kinetic energy density ($\nabla^2\rho \sim \tau$): $E_{XC}[\rho,\nabla\rho,\tau]$. Notable examples are M06L[139] and TPSS[140]. Mixing Hartree-Fock exchange with GGA exchange functionals leads to the formation of hybrid functionals. This is based on the ansatz that the exact exchange energy is situated between the GGA exchange energy functional and the Hartree-Fock exchange integral.[141] As a result, a fixed percentage of HF exchange is included. B3LYP,[142] the most used functional in DFT, belongs to this category. This functional uses 3 parameters for the mixing ratios between the HF exchange integral (20%) and LDA exchange functional and between the LYP-GGA and LDA correlation functionals, and is combined with the B88 exchange functional. In PBE0, 25% of the PBE exchange functional is replaced by the HF exchange integral.[143] Furthermore, in 2007, Zhao and Trular proposed two new hybrid

functionals M06 (27% exact exchange) and M06-2X (54% exact exchange) which have been parametrized including both transition metals and nonmetals for M06 and only nonmetals for M06-2X, respectively.[144] Additionally, The M06 and M06-2X functionals have been parametrized to implicitly account for London dispersion interactions, making them very suitable for the geometry optimizations of organic molecules. Other hybrid functionals used in this work are B971[145] (a re-parameterization of the semiempirical B97[146] functional containing 21% HF exchange) and TPSSh[147] (an expansion of the TPSS functional using 10% HF exchange). The next improvement can be made by the introduction of range-separated HF exchange in these hybrid functionals. Incorrect asymptotic behavior of the exchange can lead to large errors on the calculation of excitation energies for charge-transfer and Rydberg states. In these functionals, the contribution of the exact exchange depends on the distance between the interacting electrons and is done by splitting the $^1/_r$ function into two parts (eq. 1.16):

$$\frac{1}{r_{12}} = \frac{1 - erf(\mu r_{12})}{r_{12}} + \frac{erf(\mu r_{12})}{r_{12}} \qquad \text{Eq. 1.16}$$

where erf is the standard error function and μ is a parameter determining the division ratio. Chai and Head-Gordon introduced the ωB97 and ωB97X functionals as range-separated variants of the semiempirical B97 functional with HF exchange varying from 0-100 and 16-100, respectively.[148] Additionally, they added empirical dispersion corrections to account for van der Waals interactions, to obtain their ωB97X-D functional.[149] The CAM-B3LYP functional was introduced as a range separated version of the famous B3LYP functional to improve on the charge transfer excitation energies with respect to the original functional, with a mixture of HF exchange and B88 exchange of 19/81% at short range and 65/35% at long range, respectively, and a range separating parameter of 0.33 $bohr^{-1}$.[150] Other examples of range-separating functionals are LC-ωPBE[151] (with HF exchange going from 0-100% with a range-separating parameter of 0.4 $bohr^{-1}$) and LC-BLYP (with HF exchange going from 0-100% with a range-separating parameter of 0.47 $bohr^{-1}$)[152].

Both HF and DFT methods rely on the construction of MO's via the LCAO approximation. In practice this is done by the choice of a basis set of AOs. A basis set is typically a collection of contractions of Gaussian-type orbitals

(GTOs), which effectively are Gaussians. Since the product of a Gaussian is another Gaussian, their implementation into the Hartree-Fock or Kohn-Sham equations is facile. A large number of basis sets have been developed over the years. In this work, the basis set 6-311G(d) has mostly been used and was initially defined by Pople and coworkers:[153-160]

"6": 1 contraction of 6 Gaussians for the core electrons

"311": 3 contractions for the valence electrons: the first of 3 Gaussians and the second and third of 1 Gaussian each

"G": stands for Gaussian

"(d)": the addition of a set of polarization d functions for the 2nd and 3rd row elements. Sometimes also denoted as "*". Subsequently, "(d,p)" or "**" adds a set of polarization p functions to hydrogen atoms.

"+": adds a set of diffuse s and p functions for the 2nd and 3rd row elements.

In the next chapter, a different family of basis sets by Ahlrichs and coworkers was used for the calculations using the Turbomole package as these were specifically designed for this package.[161-164] Their basis sets are named "def2-" followed by an acronym matching the description of the basis set. We used the def2-TZVP basis set which is also of the triple-ζ split-valence type, similar to the 6-311G(d) basis set, with sets of polarization functions. The size of the basis set can have a large influence on the accuracy of the calculation (if the size is too small) but can also lead to extended calculation times (when it is too large). The choice of whether to incorporate double, triple or even higher split-valence, polarization or diffusion functions needs to be weighed against the accuracy and time that is needed for the calculations to complete. Similarly, a larger system (i.e. a system containing more or heavier atoms and thus more electrons) requires more atomic orbitals to be computed and therefore will also lead to a longer calculation time.

In order to probe the excited state properties, a time-dependent perturbation is applied to the ground-state wavefunction or electron density for HF or DFT based methods, respectively. Runge and Gross showed that for time-dependent DFT (TDDFT), the density is still uniquely defined by the external potential.[165] The time-dependent Kohn-Sham equation can be written as Eq. 1.17:[166, 167]

$$\left[-\frac{1}{2}\nabla^2 + V_{eff}(\vec{r},t)\right]\theta_i(\vec{r},t) = i\frac{\delta}{\delta t}\theta_i(\vec{r},t) \qquad \text{Eq. 1.17}$$

with $V_{eff}(\vec{r},t) = V(t) + V_{SCF}(\vec{r},t)$ Eq. 1.18

and $V_{SCF}(\vec{r},t) = \int \frac{\rho(\vec{r},t)}{|\vec{r}-\vec{r}'|} d\vec{r}' + V_{XC}(\vec{r},t)$ Eq. 1.19

assuming the existence of a potential $V_{eff}(\vec{r},t)$, for an independent particle system whose orbitals $\theta_i(\vec{r},t)$ yield the same charge density $\rho(\vec{r},t)$ as for the interacting system. $V_{XC}(\vec{r},t)$ (Eq. 1.18) is the exchange-correlation potential and is given as the functional derivative of the exchange-correlation action A_{XC} (Eq. 1.20):[168]

$$V_{XC}[\rho](\vec{r},t) = \frac{\delta A_{XC}[\rho]}{\delta \rho(\vec{r},t)} \approx \frac{\delta E_{XC}[\rho_t]}{\delta \rho_t(\vec{r})} = V_{XC}[\rho_t](\vec{r}) \quad \text{Eq. 1.20}$$

The unknown functional A_{XC} of ρ over both space and time is approximated by E_{XC} (the exchange-correlation functional of time-independent Kohn-Sham theory) which is a function of ρ_t at fixed t. This local approximation in time is commonly referred to as the adiabatic approximation and allows the use of the same exchange-correlation functionals as described above.[168]

The linear response of the density matrix after applying a time-dependent perturbation can be rewritten as Eq. 1.21:[169]

$$\left[\begin{pmatrix} A & B \\ B^* & A^* \end{pmatrix} - \omega \begin{pmatrix} 1 & 0 \\ 0 & -1 \end{pmatrix}\right] \begin{pmatrix} \delta P \\ \delta P^* \end{pmatrix} = \begin{pmatrix} -\delta V \\ -\delta V^* \end{pmatrix} \quad \text{Eq. 1.21}$$

where the elements of matrices A and B are defined as

$$A_{ai,bj} = \delta_{ab}\delta_{ij}(\epsilon_a - \epsilon_i) + K_{ai,bj} \quad \text{Eq. 1.22}$$

and

$$B_{ai,bj} = K_{ai,jb} \quad \text{Eq. 1.23}$$

with i,j for occupied and a,b for virtual molecular orbitals, ϵ_a and ϵ_i are the orbital energies for the virtual and occupied orbitals, respectively, $K_{ai,bj}$ is the coupling matrix $[(ai|bj) + (ai|f_{XC}|bj)]$ with f_{XC} being the first order exchange-correlation kernel and $\delta P(\omega)$ is the linear response of the KS/HF density matrix in the basis of the unperturbed molecular orbitals. The excitation energies are determined as the poles of the response functions, leading to zero eigenvalues on the left hand side of Eq. 1.21. Therefore, the problem can be rewritten as a non-Hermitian eigenvalue problem for which the solutions are the excitation energies:[169, 170]

$$\begin{bmatrix} A & B \\ B & A \end{bmatrix}\begin{bmatrix} X \\ Y \end{bmatrix} = \omega \begin{bmatrix} 1 & 0 \\ 0 & -1 \end{bmatrix}\begin{bmatrix} X \\ Y \end{bmatrix} \quad \text{Eq. 1.24}$$

With $X_{ai} = \delta P_{ai}(\omega)$ and $Y_{ai} = \delta P_{ia}(\omega)$. *X* is associated to the excitation and *Y* is associated with the de-excitation. Each excitation is characterized by an energy and one or multiple electronic transitions (e.g. 70% HOMO→LUMO and 30% HOMO-1→LUMO). By computing the transition dipole moment ($\vec{\mu}_{eg}$) from the ground state (g) to the excited state (e), the oscillator strength (f_{eg}) is available:

$$f_{eg} = \frac{2}{3}\frac{m_e}{e^2\hbar^2}\left\|\vec{\mu}_{eg}\right\|^2 \Delta E_{eg} \quad \text{Eq. 1.25}$$

$$\text{with } \vec{\mu}_{eg} = \langle \Psi_e | \hat{\mu} | \Psi_g \rangle \quad \text{Eq. 1.26}$$

From the results of the TDDFT calculations, information regarding the CT character of a given transition can be obtained by analyzing the ground and excited state densities. Le Bahers *et al.* showed that by taking the difference between the excited and ground state densities, regions of increasing (Figure 1.29, purple) and decreasing (Figure 1.29, cyan) electron density can be determined.[171] When these regions are localized on the acceptor and donor units of the molecule, respectively, the transition is more likely of CT character. To quantify this, several figures of merit are used. The distance over which charge is transferred (d_{CT}) is derived by taking the barycenters of positive and negative electron density change and calculating the distance between them. The change in dipole moment (Δμ) is calculated by taking the difference of the dipole moments of the ground and excited states. Larger d_{CT} and Δμ values are characteristic of CT transitions as the regions of increased and decreased electron density are localized on different parts of the molecule for these transitions. However, they need to be considered independently for each

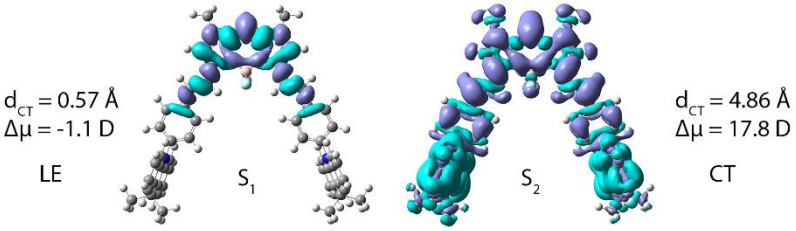

Figure 1.29: Excited-ground state electron density differences as obtained by the method of Le Bahers *et al.*, indicating the LE character (S_1) and CT character (S_2) of a BODIPY compound used in Chapter 6. The smaller d_{CT} and Δμ values for S_1 than for S_2 indicate LE and CT character for the former and the latter, respectively.

molecule as the size of the molecule and possible symmetry in D-A-D systems can lead to small d_{CT} and Δμ values while still having CT character. Therefore, careful investigation of the observed excited-ground state electron density differences in conjunction with the d_{CT} and Δμ values is required to have a good understanding of the CT character of a given transition.

Unfortunately, the TDDFT calculations can lead to triplet instabilities. The stability of the Kohn-Sham wave function with respect to symmetry breaking can be tested by considering an arbitrary unitary transformation of orbitals (Eq. 1.27):[172]

$$\varphi_r^{\lambda}(\vec{r}) = e^{i\lambda(\hat{R}+i\hat{I})}\varphi_r(\vec{r}) \qquad \text{Eq. 1.27}$$

where $\hat{R}$ and $\hat{I}$ are real operators. With some algebra, the energy expression can be derived:

$$E_{\lambda} = E_0 + \lambda^2[R^*(A-B)R + I^*(A+B)I] + \Omega(\lambda^3) \qquad \text{Eq. 1.28}$$

The $\Omega(\lambda^3)$ term disappears because the energy has already been minimized before considering symmetry-breaking. The (A±B) term indicates the connection with Eq. 1.24, which can now be written as the eigenvalue equation:

$$(A+B)(A-B)Z_I = \omega_I^2 Z_I \qquad \text{Eq. 1.29}$$

For pure DFT, the matrix (A-B) is always positive definite, however, the matrix (A+B) may have some negative eigenvalues, in which case the energy E_λ will fall below E_0 for some value of I.[172] This also corresponds to a negative value for ω_I^2 and, subsequently, an imaginary value of ω_I. This mathematical relationship is the triplet instability. The Tamm-Dancoff approximation overcomes this problem by setting the matrix B equal to 0.[173, 174] This decouples the linear response TDDFT excitation energy problem from the ground state stability problem and reduces Eq. 1.24 to

$$\begin{bmatrix} A & 0 \\ 0 & A \end{bmatrix}\begin{bmatrix} X \\ Y \end{bmatrix} = \omega \begin{bmatrix} 1 & 0 \\ 0 & -1 \end{bmatrix}\begin{bmatrix} X \\ Y \end{bmatrix} \qquad \text{Eq. 1.30}$$

which is further simplified to

$$AX = \omega X \qquad \text{Eq. 1.31}$$

Lastly, calculations are often performed on a single molecule in vacuo. However, for comparison to experimental results, insertion of the molecule into a suitable

medium might be necessary. Several strategies have been employed of which the polarizable continuum model (PCM) has been the most used.[175-177] The model implicitly accounts for a solvent by enveloping the molecule inside a charged cavity (Figure 1.30). The PCM assumes that the most dominant interactions between the surrounding and solute are Coulomb interactions and it is therefore not suitable to investigate the influence of hydrogen-bonding interactions between the solvent and solute. The solvent "cage" is built to reproduce the empty space between the solute and the "would-be" solvent molecules and is dependent on the chosen solvent (Figure 1.30). The charge density at the surface of the cavity is dependent on the dielectric constant of the chosen solvent.

These methods have been implemented in a variety of quantum chemical packages such as Gaussian,[178] Turbomole[179] and Dalton.[180]

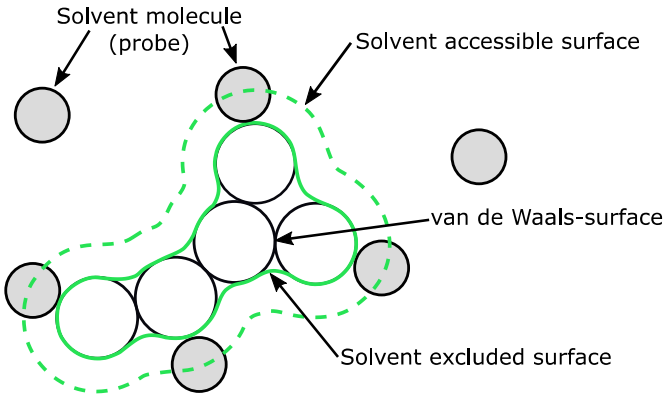

Figure 1.30: Simplified representation of the PCM in which the solvent cage is constructed by probing the outer edges of the molecule using a solvent molecule, reproduced from ref [177].

1.5.2. Application of (TD)DFT to TADF

While DFT is able to achieve similar accuracy to HF-based methods for ground-state properties, its main merit is the reduced computational effort (computation time and hardware requirements) that is needed for time-dependent properties such as excited-state energies or excited-state geometry optimizations. This is especially true when using higher level HF-based methods such as the second-order approximate coupled cluster singles and doubles model CC2, for which the computational cost increases rapidly (as N^x, with N a measure of the size of the compound; x = 5 for CC2). While their accuracy exceeds that of TDDFT, these

methods are inviable to calculate the excited-state properties of larger systems (>50 atoms) for screening purposes.[25]

For TADF applications, DFT has been widely applied to optimize the ground-state geometries and TDDFT to calculate the first singlet and triplet excitation energies, and then to estimate ΔE_{ST}. The process starts with a chemical structure that is drawn in a software package such as ChemDraw. Using visualisation software such as Chem3D, Avogadro, GaussView or DrawMole, the Lewis structure is transformed into a 3D representation which can preliminarily be optimized using simple force-field optimization to speed up the calculations that are performed using Gaussian (for example). The coordinates are then inserted into a Gaussian input file and using several keywords, the required task is specified. The first calculation typically run is an optimization of the ground-state geometry. Using the non-optimized coordinates, the Gaussian package constructs a trial density based on the specified basis set (6-311G(d) in this work). Using the Kohn-Sham method, the total energy of the system is minimized until a minimum (characterized by negligeable forces and the absence of imaginary frequencies) and convergence for the energy of this state is reached. Special care needs to be taken that the input geometry is close enough to the expected final geometry as local minima on the potential energy surface are possible. Molecules with multiple possible conformers can be pushed toward a higher energy conformer by changing the starting geometry appropriately. The XCF (in this work, M06[144] for geometry optimizations) that is used in the DFT theorems is also specified in the input file and will have a significant influence on the value of the total energy of the system. Typically the influence of the used XCF on the geometrical parameters is relatively small when suitable XCFs are used. The optimized geometry can be analyzed using the same visualization softwares as described before, with the exception of Chem3D. From the geometry optimization, all structural parameters such as bond lengths and dihedral angles as well as the orbital energies and topologies can be extracted. This gives a first insight into the potential for TADF by looking at the localization of the HOMO and LUMO. Using the coordinates of the optimized geometry, the next calculations can be performed, such as a vibrational analysis, typically performed to verify that a minimum on the potential energy surface is obtained, or TDDFT. With TDDFT the ground-state geometry is taken and the excited-state

density is optimized. From this density, the singlet or triplet states can be calculated and properties such as their energy, the oscillator strengths in the case of singlet states and their single-particle transition natures can be determined. With this information, the energy levels of the various singlet and triplet states can be compared and an estimate of ΔE_{ST} is given. The excited-state properties of organic molecules are even more prone to influences by the choice of the XCF. The next chapter delves deeper into the choice of the correct XCF by comparing different types of XCFs for various D-A compounds.

1.6. References

1. G. Destriau, *J. Chim. Phys.*, 1936, **33**, 587-625.
2. A. Bernanose, M. Comte and P. Vouaux, *J. Chim. Phys.*, 1953, **50**, 64-68.
3. M. Pope, H. P. Kallmann and P. Magnante, *J. Chem. Phys.*, 1963, **38**, 2042-2043.
4. C. W. Tang and S. A. VanSlyke, *Appl. Phys. Lett.*, 1987, **51**, 913-915.
5. C. W. Tang, S. A. VanSlyke and C. H. Chen, *J. Appl. Phys.*, 1989, **65**, 3610-3616.
6. C. Adachi, S. Tokito, T. Tsutsui and S. Saito, *Jpn. J. Appl. Phys.*, 1988, **27**, L269-L271.
7. C. Adachi, S. Tokito, T. Tsutsui and S. Saito, *Jpn. J. Appl. Phys.*, 1988, **27**, L713-L715.
8. C. Adachi, T. Tsutsui and S. Saito, *Appl. Phys. Lett.*, 1989, **55**, 1489-1491.
9. J. H. Burroughes, D. D. C. Bradley, A. R. Brown, R. N. Marks, K. Mackay, R. H. Friend, P. L. Burns and A. B. Holmes, *Nature*, 1990, **347**, 539-541.
10. Y. Ohmori, M. Uchida, K. Muro and K. Yoshino, *Jpn. J. Appl. Phys.*, 1991, **30**, L1938-L1940.
11. Y. Ohmori, M. Uchida, K. Muro and K. Yoshino, *Jpn. J. Appl. Phys.*, 1991, **30**, L1941-L1943.
12. G. Grem, G. Leditzky, B. Ullrich and G. Leising, *Adv. Mater.*, 1992, **4**, 36-37.
13. D. Braun and A. J. Heeger, *Appl. Phys. Lett.*, 1991, **58**, 1982-1984.
14. Merck, https://www.merckgroup.com/business-specifics/performance-materials/Optoelectronics/global/Datasheet-Livilux-PDY-132-Super-Yellow-EN.pdf).
15. J. K. Borchardt, *Mater. Today*, 2004, **7**, 42-46.
16. P.-W. Wang, Y.-J. Liu, C. Devadoss, P. Bharathi and J. S. Moore, *Adv. Mater.*, 1996, **8**, 237-241.
17. J. N. G. Pillow, M. Halim, J. M. Lupton, P. L. Burn and I. D. W. Samuel, *Macromolecules*, 1999, **32**, 5985-5993.
18. C. C. Kwok and M. S. Wong, *Macromolecules*, 2001, **34**, 6821-6830.
19. Y. Zou, J. Zou, T. Ye, H. Li, C. Yang, H. Wu, D. Ma, J. Qin and Y. Cao, *Adv. Funct. Mater.*, 2013, **23**, 1781-1788.

20. S. R. Forrest, D. D. C. Bradley and M. E. Thompson, *Adv. Mater.*, 2003, **15**, 1043-1048.
21. W. Brütting, J. Frischeisen, T. D. Schmidt, B. J. Scholz and C. Mayr, P*hys. Status Solidi (a)*, 2013, **210**, 44-65.
22. J. Kido, K. Nagai and Y. Ohashi, *Chem. Lett.*, 1990, **19**, 657-660.
23. J. Kido, K. Nagai and Y. Okamoto, *J. Alloys Compd.*, 1993, **192**, 30-33.
24. M. A. Baldo, D. F. O'Brien, Y. You, A. Shoustikov, S. Sibley, M. E. Thompson and S. R. Forrest, *Nature*, 1998, **395**, 151-154.
25. R. C. Kwong, S. Sibley, T. Dubovoy, M. Baldo, S. R. Forrest and M. E. Thompson, *Chem. Mater.*, 1999, **11**, 3709-3713.
26. A. A. Shoustikov, Y. Yujian and M. E. Thompson, *IEEE J. Sel. Top. Quantum Electron.*, 1998, **4**, 3-13.
27. M. Ikai, S. Tokito, Y. Sakamoto, T. Suzuki and Y. Taga, *Appl. Phys. Lett.*, 2001, **79**, 156-158.
28. C. Adachi, R. C. Kwong, P. Djurovich, V. Adamovich, M. A. Baldo, M. E. Thompson and S. R. Forrest, *Appl. Phys. Lett.*, 2001, **79**, 2082-2084.
29. C. Adachi, M. A. Baldo, S. R. Forrest, S. Lamansky, M. E. Thompson and R. C. Kwong, *Appl. Phys. Lett.*, 2001, **78**, 1622-1624.
30. A. Tsuboyama, H. Iwawaki, M. Furugori, T. Mukaide, J. Kamatani, S. Igawa, T. Moriyama, S. Miura, T. Takiguchi, S. Okada, M. Hoshino and K. Ueno, *J. Am. Chem. Soc.*, 2003, **125**, 12971-12979.
31. C. Bizzarri, F. Hundemer, J. Busch and S. Bräse, *Polyhedron*, 2018, **140**, 51-66.
32. J. Hyocheol, S. Hwangyu, L. Jaehyun, K. Beomjin, P. Young-Il, Y. Kyoung Soo, A. Byeong-Kwan and P. Jongwook, *J. Photonics Energy*, 2015, **5**, 1-23.
33. Q. Wei, N. Fei, A. Islam, T. Lei, L. Hong, R. Peng, X. Fan, L. Chen, P. Gao and Z. Ge, *Adv. Opt. Mater.*, 2018, **6**, 1800512.
34. J.-H. Jou, S. Kumar, A. Agrawal, T.-H. Li and S. Sahoo, *J. Mater. Chem. C*, 2015, **3**, 2974-3002.
35. H. Xu, R. Chen, Q. Sun, W. Lai, Q. Su, W. Huang and X. Liu, *Chem. Soc. Rev.*, 2014, **43**, 3259-3302.
36. R. Delorme and F. Perrin, *J. Phys. Radium*, 1929, **10**, 177-186.
37. G. N. Lewis, D. Lipkin and T. T. Magel, *J. Am. Chem. Soc.*, 1941, **63**, 3005-3018.
38. C. A. Parker and C. G. Hatchard, *T. Faraday Soc.*, 1961, **57**, 1894-1904.
39. C. A. Parker, C. G. Hatchard and E. J. Bowen, *Proc. Math. Phys. Eng. Sci.*, 1962, **269**, 574-584.
40. Y. Onoue, K. Hiraki and Y. Nishikawa, *Bull. Chem. Soc. Jpn.*, 1981, **54**, 2633-2635.
41. Y. Nishikawa, K. Hiraki, Y. Onoue, K. Nishikawa, Y. Yoshitake and T. Shigematsu, *Bunseki kagaku*, 1983, **32**, E115-E122.
42. M. N. Berberan-Santos and J. M. M. Garcia, *J. Am. Chem. Soc.*, 1996, **118**, 9391-9394.
43. M. W. Wolf, K. D. Legg, R. E. Brown, L. A. Singer and J. H. Parks, *J. Am. Chem. Soc.*, 1975, **97**, 4490-4497.
44. A. Maciejewski, M. Szymanski and R. P. Steer, *J. Phys. Chem.*, 1986, **90**, 6314-6318.
45. A. Endo, M. Ogasawara, A. Takahashi, D. Yokoyama, Y. Kato and C. Adachi, *Adv. Mater.*, 2009, **21**, 4802-4806.

46. A. Endo, K. Sato, K. Yoshimura, T. Kai, A. Kawada, H. Miyazaki and C. Adachi, *Appl. Phys. Lett.*, 2011, **98**, 083302.
47. T. Nakagawa, S.-Y. Ku, K.-T. Wong and C. Adachi, *Chem. Commun.*, 2012, **48**, 9580-9582.
48. S. Youn Lee, T. Yasuda, H. Nomura and C. Adachi, *Appl. Phys. Lett.*, 2012, **101**, 093306.
49. Q. Zhang, J. Li, K. Shizu, S. Huang, S. Hirata, H. Miyazaki and C. Adachi, *J. Am. Chem. Soc.*, 2012, **134**, 14706-14709.
50. H. Tanaka, K. Shizu, H. Miyazaki and C. Adachi, *Chem. Commun.*, 2012, **48**, 11392-11394.
51. G. Méhes, H. Nomura, Q. Zhang, T. Nakagawa and C. Adachi, *Angew. Chem. Int. Ed.*, 2012, **51**, 11311-11315.
52. H. Uoyama, K. Goushi, K. Shizu, H. Nomura and C. Adachi, *Nature*, 2012, **492**, 234-238.
53. J. Lee, K. Shizu, H. Tanaka, H. Nomura, T. Yasuda and C. Adachi, *J. Mater. Chem. C*, 2013, **1**, 4599-4604.
54. H. Tanaka, K. Shizu, H. Nakanotani and C. Adachi, *Chem. Mater.*, 2013, **25**, 3766-3771.
55. K. Nasu, T. Nakagawa, H. Nomura, C.-J. Lin, C.-H. Cheng, M.-R. Tseng, T. Yasuda and C. Adachi, *Chem. Commun.*, 2013, **49**, 10385-10387.
56. F. B. Dias, K. N. Bourdakos, V. Jankus, K. C. Moss, K. T. Kamtekar, V. Bhalla, J. Santos, M. R. Bryce and A. P. Monkman, *Adv. Mater.*, 2013, **25**, 3707-3714.
57. M. Kasha, *Discuss. Faraday Soc.*, 1950, **9**, 14-19.
58. T. J. Penfold, F. B. Dias and A. P. Monkman, *Chem. Commun.*, 2018, **54**, 3926-3935.
59. J. Gibson and T. J. Penfold, *Phys. Chem. Chem. Phys.*, 2017, **19**, 8428-8434.
60. X. Liang, Z.-L. Tu and Y.-X. Zheng, *Chem. Eur. J.*, 2019, **25**, 5623-5642.
61. M. Baba, *J. Phys. Chem. A*, 2011, **115**, 9514-9519.
62. M. A. El - Sayed, *J. Chem. Phys.*, 1963, **38**, 2834-2838.
63. T. Ogiwara, Y. Wakikawa and T. Ikoma, *J. Phys. Chem. A*, 2015, **119**, 3415-3418.
64. J. Gibson, A. P. Monkman and T. J. Penfold, *ChemPhysChem*, 2016, **17**, 2956-2961.
65. J. S. Ward, R. S. Nobuyasu, A. S. Batsanov, P. Data, A. P. Monkman, F. B. Dias and M. R. Bryce, *Chem. Commun.*, 2016, **52**, 2612-2615.
66. P. L. Santos, J. S. Ward, P. Data, A. S. Batsanov, M. R. Bryce, F. B. Dias and A. P. Monkman, *J. Mater. Chem. C*, 2016, **4**, 3815-3824.
67. X.-K. Chen, S.-F. Zhang, J.-X. Fan and A.-M. Ren, *J. Phys. Chem. C*, 2015, **119**, 9728-9733.
68. C. M. Marian, *J. Phys. Chem. C*, 2016, **120**, 3715-3721.
69. F. B. Dias, J. Santos, D. R. Graves, P. Data, R. S. Nobuyasu, M. A. Fox, A. S. Batsanov, T. Palmeira, M. N. Berberan-Santos, M. R. Bryce and A. P. Monkman, *Adv. Sci.*, 2016, **3**, 1600080.
70. T. J. Penfold, E. Gindensperger, C. Daniel and C. M. Marian, *Chem. Rev.*, 2018, **118**, 6975-7025.
71. W. Che, Y. Xie and Z. Li, *Asian J. Org. Chem.*, 2020, **n/a**.
72. Z. Yang, Z. Mao, Z. Xie, Y. Zhang, S. Liu, J. Zhao, J. Xu, Z. Chi and M. P. Aldred, *Chem. Soc. Rev.*, 2017, **46**, 915-1016.

73. T.-T. Bui, F. Goubard, M. Ibrahim-Ouali, D. Gigmes and F. Dumur, *Beilstein J. Org. Chem.*, 2018, **14**, 282-308.
74. Y. Liu, C. Li, Z. Ren, S. Yan and M. R. Bryce, *Nat. Rev. Mater.*, 2018, **3**, 18020.
75. M. Y. Wong and E. Zysman-Colman, *Adv. Mater.*, 2017, **29**, 1605444.
76. J. Sohn, D. Ko, H. Lee, J. Han, S.-D. Lee and C. Lee, *Org. Electron.*, 2019, **70**, 286-291.
77. J. U. Kim, I. S. Park, C.-Y. Chan, M. Tanaka, Y. Tsuchiya, H. Nakanotani and C. Adachi, *Nat. Comm.*, 2020, **11**, 1765.
78. X. Xiong, F. Song, J. Wang, Y. Zhang, Y. Xue, L. Sun, N. Jiang, P. Gao, L. Tian and X. Peng, *J. Am. Chem. Soc.*, 2014, **136**, 9590-9597.
79. W. Hu, L. Guo, L. Bai, X. Miao, Y. Ni, Q. Wang, H. Zhao, M. Xie, L. Li, X. Lu, W. Huang and Q. Fan, *Adv. Healthc. Mater.*, 2018, **7**, 1800299.
80. Z. Zhu, D. Tian, P. Gao, K. Wang, Y. Li, X. Shu, J. Zhu and Q. Zhao, *J. Am. Chem. Soc.*, 2018, **140**, 17484-17491.
81. F. Ni, Z. Zhu, X. Tong, W. Zeng, K. An, D. Wei, S. Gong, Q. Zhao, X. Zhou and C. Yang, *Adv. Sci.*, 2019, **6**, 1801729.
82. F. Ni, N. Li, L. Zhan and C. Yang, *Adv. Opt. Mater.*, 2020, **8**, 1902187.
83. W. Zhao, H. Wei, F. Liu and C. Ran, *Photodiagnosis Photodyn. Ther.*, 2020, **30**, 101744.
84. C. I. C. Crucho, J. Avó, A. M. Diniz, S. N. Pinto, J. Barbosa, P. O. Smith, M. N. Berberan-Santos, L.-O. Pålsson and F. B. Dias, *Front. Chem.*, 2020, **8**, 404.
85. S. Xu, Q. Zhang, X. Han, Y. Wang, X. Wang, M. Nazare, J.-D. Jiang and H.-Y. Hu, *ACS Sensors*, 2020, **5**, 1650-1656.
86. M. Bixon, J. Jortner, J. Cortes, H. Heitele and M. E. Michel-Beyerle, *J. Phys. Chem.*, 1994, **98**, 7289-7299.
87. R. Englman and J. Jortner, *Mol. Phys.*, 1970, **18**, 145-164.
88. J. H. Kim, J. H. Yun and J. Y. Lee, *Adv. Opt. Mater.*, 2018, **6**, 1800255.
89. Z. Chen, Z. Wu, F. Ni, C. Zhong, W. Zeng, D. Wei, K. An, D. Ma and C. Yang, *J. Mater. Chem. C*, 2018, **6**, 6543-6548.
90. K. Albrecht, K. Matsuoka, K. Fujita and K. Yamamoto, *Angew. Chem. Int. Ed.*, 2015, **54**, 5677-5682.
91. K. Albrecht, K. Matsuoka, D. Yokoyama, Y. Sakai, A. Nakayama, K. Fujita and K. Yamamoto, *Chem. Commun.*, 2017, **53**, 2439-2442.
92. Y. Li, G. Xie, S. Gong, K. Wu and C. Yang, *Chem. Sci.*, 2016, **7**, 5441-5447.
93. J. Luo, S. Gong, Y. Gu, T. Chen, Y. Li, C. Zhong, G. Xie and C. Yang, *J. Mater. Chem. C*, 2016, **4**, 2442-2446.
94. K. Sun, Y. Sun, T. Huang, J. Luo, W. Jiang and Y. Sun, *Org. Electron.*, 2017, **42**, 123-130.
95. X. Ban, W. Jiang, K. Sun, B. Lin and Y. Sun, *ACS Appl. Mater. & Interfaces*, 2017, **9**, 7339-7346.
96. J.-L. Wu, Y.-T. Lee, C.-T. Chen and C.-T. Chen, *J. Chin. Chem. Soc.*, 2018, **65**, 87-106.
97. C. Li, Z. Ren, X. Sun, H. Li and S. Yan, *Macromolecules*, 2019, **52**, 2296-2303.
98. C. Li, Y. Wang, D. Sun, H. Li, X. Sun, D. Ma, Z. Ren and S. Yan, *ACS Appl. Mater. Interfaces*, 2018, **10**, 5731-5739.
99. J. Hu, Q. Li, S. Shao, L. Wang, X. Jing and F. Wang, *Adv. Opt. Mater.*, 2020, **8**, 1902100.

100. Z. Ren, R. S. Nobuyasu, F. B. Dias, A. P. Monkman, S. Yan and M. R. Bryce, *Macromolecules*, 2016, **49**, 5452-5460.
101. C. J. Christopherson, D. M. Mayder, J. Poisson, N. R. Paisley, C. M. Tonge and Z. M. Hudson, *ACS Appl. Mater. Interfaces*, 2020, **12**, 20000-20011.
102. X. Zeng, J. Luo, T. Zhou, T. Chen, X. Zhou, K. Wu, Y. Zou, G. Xie, S. Gong and C. Yang, *Macromolecules*, 2018, **51**, 1598-1604.
103. B. Zhang and Y. Cheng, *Chem. Rec.*, 2019, **19**, 1624-1643.
104. A. E. Nikolaenko, M. Cass, F. Bourcet, D. Mohamad and M. Roberts, *Adv. Mater.*, 2015, **27**, 7236-7240.
105. S. Y. Lee, T. Yasuda, H. Komiyama, J. Lee and C. Adachi, *Adv. Mater.*, 2016, **28**, 4019-4024.
106. Y. Liu, Y. Wang, C. Li, Z. Ren, D. Ma and S. Yan, *Macromolecules*, 2018, **51**, 4615-4623.
107. Y. Liu, L. Hua, S. Yan and Z. Ren, *Nano Energy*, 2020, **73**, 104800.
108. Y. Liu, G. Xie, Z. Ren and S. Yan, *ACS Appl. Polym. Mater.*, 2019, **1**, 2204-2212.
109. Q. Wei, P. Kleine, Y. Karpov, X. Qiu, H. Komber, K. Sahre, A. Kiriy, R. Lygaitis, S. Lenk, S. Reineke and B. Voit, *Adv. Funct. Mater.*, 2017, **27**, 1605051.
110. Y. Wang, Y. Zhu, X. Lin, Y. Yang, B. Zhang, H. Zhan, Z. Xie and Y. Cheng, *J. Mater. Chem. C*, 2018, **6**, 568-574.
111. Y. Yang, K. Li, C. Wang, H. Zhan and Y. Cheng, *Chem. Asian J.*, 2019, **14**, 574-581.
112. D. M. E. Freeman, A. J. Musser, J. M. Frost, H. L. Stern, A. K. Forster, K. J. Fallon, A. G. Rapidis, F. Cacialli, I. McCulloch, T. M. Clarke, R. H. Friend and H. Bronstein, *J. Am. Chem. Soc.*, 2017, **139**, 11073-11080.
113. H. Nakanotani, T. Higuchi, T. Furukawa, K. Masui, K. Morimoto, M. Numata, H. Tanaka, Y. Sagara, T. Yasuda and C. Adachi, *Nat. Commun.*, 2014, **5**, 4016.
114. J. Kido and Y. Iizumi, *Appl. Phys. Lett.*, 1998, **73**, 2721-2723.
115. J. Partee, E. L. Frankevich, B. Uhlhorn, J. Shinar, Y. Ding and T. J. Barton, *Phys. Rev. Lett.*, 1999, **82**, 3673-3676.
116. S. Sinha and A. P. Monkman, *Appl. Phys. Lett.*, 2003, **82**, 4651-4653.
117. D. Y. Kondakov, *Philos. Trans. R. Soc. A*, 2015, **373**, 20140321.
118. A. P. Monkman, *ISRN Mater. Sci.*, 2013, **2013**, 670130.
119. J.-H. Lee, C.-H. Chen, P.-H. Lee, H.-Y. Lin, M.-k. Leung, T.-L. Chiu and C.-F. Lin, *J. Mater. Chem. C*, 2019, **7**, 5874-5888.
120. N. A. Kukhta, T. Matulaitis, D. Volyniuk, K. Ivaniuk, P. Turyk, P. Stakhira, J. V. Grazulevicius and A. P. Monkman, *J. Phys. Chem. Lett.*, 2017, **8**, 6199-6205.
121. H. W. Bae, G. W. Kim, R. Lampande, J. H. Park, I. J. Ko, H. J. Yu, C. Y. Lee and J. H. Kwon, *Org. Electron.*, 2019, **70**, 1-6.
122. Y. Takita, K. Takeda, N. Hashimoto, S. Nomura, T. Suzuki, H. Nakashima, S. Uesaka, S. Seo and S. Yamazaki, *J. Soc. Inf. Disp.*, 2018, **26**, 55-63.
123. S. Zhang, W. Li, L. Yao, Y. Pan, F. Shen, R. Xiao, B. Yang and Y. Ma, *Chem. Commun.*, 2013, **49**, 11302-11304.
124. W. Li, Y. Pan, R. Xiao, Q. Peng, S. Zhang, D. Ma, F. Li, F. Shen, Y. Wang, B. Yang and Y. Ma, *Adv. Funct. Mater.*, 2014, **24**, 1609-1614.

125. C. Fu, S. Luo, Z. Li, X. Ai, Z. Pang, C. Li, K. Chen, L. Zhou, F. Li, Y. Huang and Z. Lu, *Chem. Commun.*, 2019, **55**, 6317-6320.
126. J. Liu, Z. Li, T. Hu, X. Wei, R. Wang, X. Hu, Y. Liu, Y. Yi, Y. Yamada-Takamura, Y. Wang and P. Wang, *Adv. Opt. Mater.*, 2019, **7**, 1801190.
127. J. C. Slater, *Phys. Rev.*, 1929, **34**, 1293-1322.
128. R. Walter, *J. für die Reine und Angew. Math.*, 1909, **1909**, 1-61.
129. D. R. Hartree, *Math. Proc. Cambridge Philos. Soc.*, 1928, **24**, 89-110.
130. V. Fock, *Z. Phys.*, 1930, **61**, 126-148.
131. V. Fock, *Z. Phys.*, 1930, **62**, 795-805.
132. J. E. Lennard-Jones, *Proc. Math. Phys. Eng. Sci.*, 1949, **198**, 1-13.
133. P. Hohenberg and W. Kohn, *Phys. Rev.*, 1964, **136**, B864-B871.
134. W. Kohn and L. J. Sham, *Phys. Rev.*, 1965, **140**, A1133-A1138.
135. A. D. Becke, *Phys. Rev. A*, 1988, **38**, 3098-3100.
136. C. Lee, W. Yang and R. G. Parr, *Phys. Rev. B*, 1988, **37**, 785-789.
137. J. P. Perdew and Y. Wang, *Phys. Rev. B*, 1992, **45**, 13244-13249.
138. J. P. Perdew, K. Burke and M. Ernzerhof, *Phys. Rev. Lett.*, 1996, **77**, 3865-3868.
139. Y. Zhao and D. G. Truhlar, *J. Chem. Phys.*, 2006, **125**, 194101.
140. J. Tao, J. P. Perdew, V. N. Staroverov and G. E. Scuseria, *Phys. Rev. Lett.*, 2003, **91**, 146401.
141. T. Tsuneda, *Density Functional Theory in Quantum Chemistry*, Springer Japan, 1st edn., 2014.
142. A. D. Becke, *J. Chem. Phys.*, 1993, **98**, 5648-5652.
143. C. Adamo and V. Barone, *J. Chem. Phys.*, 1999, **110**, 6158-6170.
144. Y. Zhao and D. G. Truhlar, *Theor. Chem. Acc.*, 2008, **120**, 215-241.
145. F. A. Hamprecht, A. J. Cohen, D. J. Tozer and N. C. Handy, *J. Chem. Phys.*, 1998, **109**, 6264-6271.
146. A. D. Becke, *J. Chem. Phys.*, 1997, **107**, 8554-8560.
147. V. N. Staroverov, G. E. Scuseria, J. Tao and J. P. Perdew, *J. Chem. Phys.*, 2003, **119**, 12129-12137.
148. J.-D. Chai and M. Head-Gordon, *J. Chem. Phys.*, 2008, **128**, 084106.
149. J.-D. Chai and M. Head-Gordon, *Phys. Chem. Chem. Phys.*, 2008, **10**, 6615-6620.
150. T. Yanai, D. P. Tew and N. C. Handy, *Chem. Phys. Lett.*, 2004, **393**, 51-57.
151. O. A. Vydrov, J. Heyd, A. V. Krukau and G. E. Scuseria, *J. Chem. Phys.*, 2006, **125**, 074106.
152. H. Iikura, T. Tsuneda, T. Yanai and K. Hirao, *J. Chem. Phys.*, 2001, **115**, 3540-3544.
153. J. D. Dill and J. A. Pople, *J. Chem. Phys.*, 1975, **62**, 2921-2923.
154. J. S. Binkley and J. A. Pople, *J. Chem. Phys.*, 1977, **66**, 879-880.
155. J. S. Binkley, J. A. Pople and W. J. Hehre, *J. Am. Chem. Soc.*, 1980, **102**, 939-947.
156. M. M. Francl, W. J. Pietro, W. J. Hehre, J. S. Binkley, M. S. Gordon, D. J. DeFrees and J. A. Pople, *J. Chem. Phys.*, 1982, **77**, 3654-3665.
157. M. S. Gordon, J. S. Binkley, J. A. Pople, W. J. Pietro and W. J. Hehre, *J. Am. Chem. Soc.*, 1982, **104**, 2797-2803.
158. J.-P. Blaudeau, M. P. McGrath, L. A. Curtiss and L. Radom, *J. Chem. Phys.*, 1997, **107**, 5016-5021.
159. V. A. Rassolov, J. A. Pople, M. A. Ratner and T. L. Windus, *J. Chem. Phys.*, 1998, **109**, 1223-1229.

160. V. A. Rassolov, M. A. Ratner, J. A. Pople, P. C. Redfern and L. A. Curtiss, *J. Comput. Chem.*, 2001, **22**, 976-984.
161. A. Schäfer, H. Horn and R. Ahlrichs, *J. Chem. Phys.*, 1992, **97**, 2571-2577.
162. F. Weigend, M. Häser, H. Patzelt and R. Ahlrichs, *Chem. Phys. Lett.*, 1998, **294**, 143-152.
163. F. Weigend and R. Ahlrichs, *Phys. Chem. Chem. Phys.*, 2005, **7**, 3297-3305.
164. D. Rappoport and F. Furche, *J. Chem. Phys.*, 2010, **133**, 134105.
165. E. Runge and E. K. U. Gross, *Phys. Rev. Lett.*, 1984, **52**, 997-1000.
166. E. K. U. Gross and W. Kohn, *Advances in Quantum Chemistry*, ed. P.-O. Löwdin, Academic Press, 1990, vol. 21, pp. 255-291.
167. R. E. Stratmann, G. E. Scuseria and M. J. Frisch, *J. Chem. Phys.*, 1998, **109**, 8218-8224.
168. C. A. Ullrich, U. J. Gossmann and E. K. U. Gross, *Phys. Rev. Lett.*, 1995, **74**, 872-875.
169. M. E. Casida, *Recent Advances in Density Functional Methods*, WORLD SCIENTIFIC, 1995, vol. Volume 1, pp. 155-192.
170. R. Bauernschmitt and R. Ahlrichs, *Chem. Phys. Lett.*, 1996, **256**, 454-464.
171. T. Le Bahers, C. Adamo, I. Ciofini, *J. Chem. Theory Comput.*, 2011, ***7*** (8), 2498-506.
172. M. A. L. Marques, C. A. Ullrich, F. Nogueira, A. Rubio, K. Burke and E. K. U. Gross, *Time-Dependent Density Functional Theory*, Springer, Berlin, Heidelberg, 2006.
173. S. Hirata and M. Head-Gordon, *Chem. Phys. Lett.*, 1999, **314**, 291-299.
174. M. E. Casida, *Low-Lying Potential Energy Surfaces*, American Chemical Society, 2002, vol. 828, ch. 9, pp. 199-220.
175. S. Miertuš, E. Scrocco and J. Tomasi, *Chem. Phys.*, 1981, **55**, 117-129.
176. E. Cancès, B. Mennucci and J. Tomasi, *J. Chem. Phys.*, 1997, **107**, 3032-3041.
177. J. Tomasi, B. Mennucci and R. Cammi, *Chem. Rev.*, 2005, **105**, 2999-3094.
178. G. W. Trucks, M. J. Frisch, H. B. Schlegel, G. E. Scuseria, M. A. Robb, J. R. Cheeseman, G. Scalmani, V. Barone, G. A. Petersson, H. Nakatsuji, X. Li, M. Caricato, A. V. Marenich, J. Bloino, B. G. Janesko, R. Gomperts, B. Mennucci, H. P. Hratchian, J. V. Ortiz, A. F. Izmaylov, J. L. Sonnenberg, D. Williams-Young, F. Ding, F. Lipparini, F. Egidi, J. Goings, B. Peng, A. Petrone, T. Henderson, D. Ranasinghe, V. G. Zakrzewski, J. Gao, N. Rega, G. Zheng, W. Liang, M. Hada, M. Ehara, K. Toyota, R. Fukuda, J. Hasegawa, M. Ishida, T. Nakajima, Y. Honda, O. Kitao, H. Nakai, T. Vreven, K. Throssell, J. A. Montgomery, Jr., J. E. Peralta, F. Ogliaro, M. J. Bearpark, J. J. Heyd, E. N. Brothers, K. N. Kudin, V. N. Staroverov, T. A. Keith, R. Kobayashi, J. Normand, K. Raghavachari, A. P. Rendell, J. C. Burant, S. S. Iyengar, J. Tomasi, M. Cossi, J. M. Millam, M. Klene, C. Adamo, R. Cammi, J. W. Ochterski, R. L. Martin, K. Morokuma, O. Farkas, J. B. Foresman, and D. J. Fox, Gaussian, Inc., Wallingford CT, 2016.
179. Turbomole v7.3.1, University of Karlsruhe and Forschungszentrum Karlsruhe GmbH, 1989−2007, TURBOMOLE GmbH, Since 2007.2019.

180. K. Aidas, C. Angeli, K. L. Bak, V. Bakken, R. Bast, L. Boman, O. Christiansen, R. Cimiraglia, S. Coriani, P. Dahle, E. K. Dalskov, U. Ekström, T. Enevoldsen, J. J. Eriksen, P. Ettenhuber, B. Fernández, L. Ferrighi, H. Fliegl, L. Frediani, K. Hald, A. Halkier, C. Hättig, H. Heiberg, T. Helgaker, A. C. Hennum, H. Hettema, E. Hjertenæs, S. Høst, I.-M. Høyvik, M. F. Iozzi, B. Jansík, H. J. A. Jensen, D. Jonsson, P. Jørgensen, J. Kauczor, S. Kirpekar, T. Kjærgaard, W. Klopper, S. Knecht, R. Kobayashi, H. Koch, J. Kongsted, A. Krapp, K. Kristensen, A. Ligabue, O. B. Lutnæs, J. I. Melo, K. V. Mikkelsen, R. H. Myhre, C. Neiss, C. B. Nielsen, P. Norman, J. Olsen, J. M. H. Olsen, A. Osted, M. J. Packer, F. Pawlowski, T. B. Pedersen, P. F. Provasi, S. Reine, Z. Rinkevicius, T. A. Ruden, K. Ruud, V. V. Rybkin, P. Sałek, C. C. M. Samson, A. S. de Merás, T. Saue, S. P. A. Sauer, B. Schimmelpfennig, K. Sneskov, A. H. Steindal, K. O. Sylvester-Hvid, P. R. Taylor, A. M. Teale, E. I. Tellgren, D. P. Tew, A. J. Thorvaldsen, L. Thøgersen, O. Vahtras, M. A. Watson, D. J. D. Wilson, M. Ziolkowski and H. Ågren, *WIREs Comput. Mol. Sci.*, 2014, **4**, 269-284.

Chapter 2

Finding the optimal exchange-correlation functional to describe the excited state properties of push-pull organic dyes designed for thermally activated delayed fluorescence

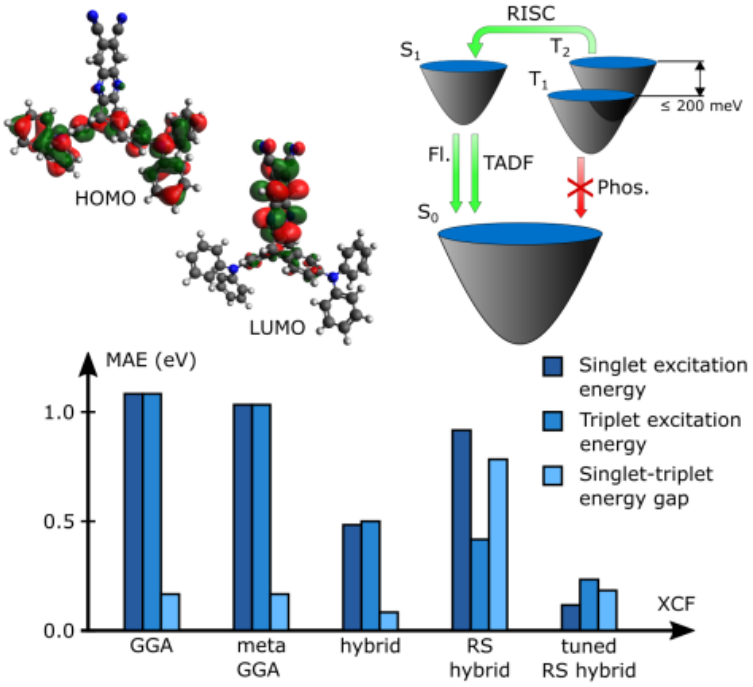

This chapter is based on a manuscript published in Physical Chemistry Chemical Physics:
T. Cardeynaels, S. Paredis, J. Deckers, S. Brebels, D. Vanderzande, W. Maes, and B. Champagne, *Phys. Chem. Chem. Phys.*, 2020**, *22*** (28), 16387-16399.

Contributions:
T. Cardeynaels: All riCC2 and (TD)DFT calculations, synthesis of compounds **1-7**, structural characterization of compounds **1-9** and preparation of the manuscript.
S. Paredis: Synthesis of compound **9** and discussion.
J. Deckers: UV-VIS and fluorescence analysis of all compounds.
S. Brebels: Synthesis of compound **8**.
D. Vanderzande, W. Maes and B. Champagne: Project management, discussion of the results and revision of the manuscript.

Abstract

To gauge the suitability of an organic dye for thermally activated delayed fluorescence (TADF), its excited state properties are often calculated using density functional theory. For this purpose, the choice of the exchange-correlation (XC) functional is crucial as it heavily influences the quality of the obtained results. In this work, 19 different XC functionals with various amounts of Hartree-Fock (HF) exchange and/or long-range correction parameters are benchmarked versus resolution-of-the-identity second-order coupled cluster (riCC2) calculations for a set of 10 prototype intramolecular donor-acceptor compounds. For the time-dependent density functional theory (TD-DFT) calculations, LC-BLYP(ω=0.20) and M06-2X are the better performing XC functionals when looking at singlet and triplet excitation energies, respectively. For the singlet-triplet energy gap, LC-BLYP(ω=0.17), LC-ωPBE(ω=0.17) and a hybrid LC-BLYP(ω=0.20)/M06-2X method give the smallest mean average errors (MAEs). Using the Tamm-Dancoff approximation (TD-DFT/TDA), the MAEs are further reduced for the triplet vertical excitation energies and the singlet-triplet energy gaps.

2.1. Introduction

Computational chemistry has been instrumental to help resolving the mechanism behind thermally activated delayed fluorescence (TADF).[1-7] Although higher level theoretical calculations do exist, such as the second-order approximate coupled cluster singles and doubles model CC2, the computational cost increases rapidly, as N^x with N a measure of the size of the compound (x = 5 for CC2), making these methods inviable to calculate the excited state properties of larger systems for screening purposes. Density functional theory (DFT) is often applied to determine the dihedral angle between the donor and acceptor units, as well as the spatial separation of the frontier orbitals. Adiabatic linear-response time-dependent DFT (TDDFT) can be used to investigate the excitation energies of the singlet and triplet states, from which the singlet-triplet energy gap (ΔE_{ST}) can be deduced at a much lower cost than with higher-level theories such as CC2. However, the choice of the exchange-correlation (XC) functional in (TD)DFT calculations is of crucial importance to obtain accurate and reliable results. Several papers have already described the use of TDDFT or the Tamm-Dancoff approximation to TDDFT (TDDFT/TDA)[8] to obtain accurate results for the first singlet and triplet vertical excitation energies of small organic conjugated compounds[9, 10] and larger organic dyes for solar cell applications.[11] In the work of Jacquemin *et al.*,[9] 34 different XC functionals (XCFs) were investigated and benchmarked versus excitation energies obtained using high level methods such as MS-CASPT2 [*i.e.* multi-state complete active space self-consistent field (CASSCF) corrected with second-order perturbation theory], CC2, and CC3 (*i.e.* approximate coupled cluster singles, doubles, and triples model). Among the best performing functionals in their study are BMK (42% HF exchange) and M06-2X (54% HF exchange). Brückner *et al.*[12] investigated the singlet and triplet excitation energies for the application of singlet fission in organic solar cells using 14 different XC functionals benchmarked against MS-CASPT2 calculations. On top of regular TDDFT calculations, the Tamm-Dancoff approximation was also assessed. The M06-2X XCF was found to give the best results when TDDFT singlet excitations are combined with TDA triplet values. Wong *et al.*[11] investigated the behavior of the long-range corrected functional LC-BLYP for different values of the range-separating parameter ω on a series of

coumarin dyes for dye-sensitized solar cells. Their results using the B3LYP and modified LC-BLYP functionals were benchmarked versus CC2 calculations and the authors concluded that the modified LC-BLYP functional significantly improves the accuracy of the singlet excitation energies with respect to B3LYP. Of particular interest are the works of Huang *et al.*[13], Penfold[14], Sun *et al.*[15], and Moral *et al.*[16], who investigated the behavior of various functionals for TADF active materials and host materials. The earliest investigation by Huang *et al.*[13] benchmarks a series of XCFs to experimental values. The investigation includes long-range separated functionals, but these were found to severely overestimate the S_1 vertical excitation energy due to the lack of tuning of the range-separated parameters. Moral *et al.*[16] used PBE0 within the TDA to evaluate the S_1 vertical excitation energies with respect to experimental values, not aiming to provide a benchmark, but rather to deduce structure-property relationships. Additionally, they employed the so-called double hybrids B2-PLYP and B2GP-PLYP to investigate the effects of non-local exchange and correlation on the excitation energies. Although the double hybrid functionals are noted to have a higher computational cost with similar overall results to their calculations with PBE0, they present a slight improvement for the compounds with a larger charge transfer character. Sun *et al.*[15] and Penfold[14] opted to modify the range-separating parameter in LC-ωPBE and LC-BLYP, respectively. In both works, the calculated excitation energies were benchmarked against experimental values for the singlet excitation energies and singlet-triplet energy gaps. With ω values from 0.14 to 0.20 (given in $bohr^{-1}$ units throughout the paper) for LC-ωPBE and 0.15 to 0.19 for LC-BLYP, the authors found very small errors (MAE < 0.15 eV) with respect to the experimental values for both properties under investigation.

In this work, the TDDFT method is employed to evaluate the first singlet and triplet excitation energies and the corresponding singlet-triplet energy gaps for a set of 10 compounds (Figure 2.1) and a number of functionals from different rungs of a ladder leading to quantum chemical accuracy[17] are tested. Our goal is to find a method with a good trade-off between computational cost and accuracy while being applicable to an as large as possible set of compounds. The 10 compounds were chosen from TADF literature or devised from ongoing work within our groups. They were selected because they span a broad range of experimental (and theoretical) singlet-triplet energy splitting values, together

with fluorescence characteristics going all the way from blue to red. Furthermore, the compounds were designated to consist of varying donor and acceptor groups to allow generalization. For compounds **1**, **4**, **5**, **6**, **9**, and **10**, TADF properties have been observed experimentally. For compound **3**, it was shown that no TADF is present. To our knowledge, compounds **2**, **7**, and **8** have not been investigated yet in literature and no experimental data on their

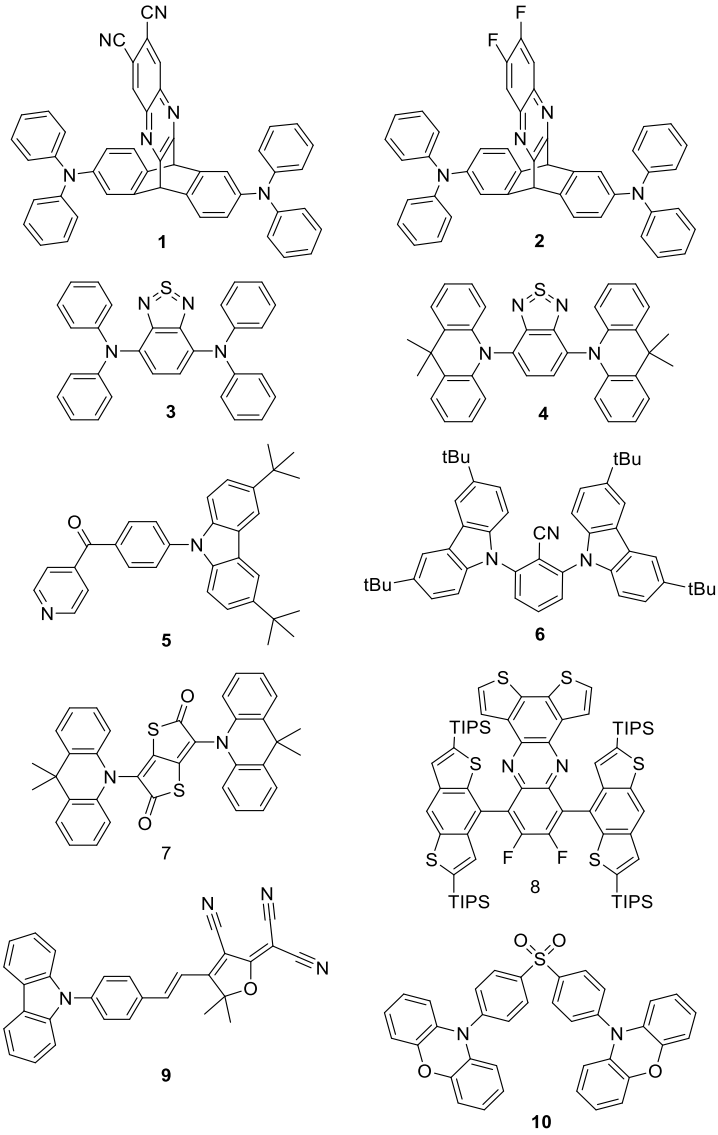

Figure 2.1: Overview of the donor-acceptor compounds studied in this work.

TADF behavior are available. The synthesis of compounds **2**, **7**, and **8** is therefore reported, together with their UV-VIS absorption and emission spectra. For the sake of consistency, we carried out similar optical characterizations for the other compounds to provide a data set for comparison with the quantum chemical predictions. Our set of XCFs includes those that were already previously tested with good results, such as M06-2X, LC-BLYP(ω = 0.17), and LC-ωPBE(ω = 0.17), the two latter with modified range-separating parameters. We opted for averages of the optimal ω values obtained by Sun *et al.*[15] and Penfold[14], because this is more convenient for screening purposes than having to optimize this parameter for every compound, either to get the smallest errors on the excitation energies or to satisfy Koopmans' theorem.[18] These XC functionals are benchmarked against resolution-of-the-identity second-order coupled cluster (riCC2)[19] calculations. Furthermore, this work expands the investigation on the accurate determination of the singlet and triplet excitation energies beyond the first excited states. This could lead to useful insights in other fields outside that of TADF such as upper state photophysics,[20] singlet fission,[21] and photodynamic therapy (PDT).[22-24] Accurate determination of the second triplet excitation energy could be particularly useful for (image-guided) PDT applications[24-26] or when screening materials for their potential as efficient TADF emitters according to the vibronic mechanism, without going as far as calculating the spin-orbit coupling or vibronic interactions.

2.2. Results and discussion

2.2.1. Synthesis and optical characterizations

Compounds **1**,[27] **3-6**,[28-30] and **9**[31] were synthesized according to their respective literature procedures. Compound **10** was obtained from Lumtech Inc (LT-N545). Syntheses of **2**, **7**, and **8** were performed following the procedures presented in Scheme 2.1. TPA-DK[27] and 1,4-dibromo-2,3-difluoro-5,6-dinitrobenzene[32] were synthesized according to their respective literature procedures. Details with respect to the synthesis and characterization of these compounds are provided in the Supporting Information (SI).

All electronic absorption spectra were measured on a Varian Cary 5000 UV-Vis-NIR spectrophotometer from Agilent Technologies. Corrected steady-state

emission spectra were recorded on a Horiba-Jobin Yvon Fluorolog-3 spectrofluorometer equipped with a 450 W Xenon lamp as light source, with excitation at the ascending slope of the charge transfer absorption band. Freshly prepared samples in 1 cm quartz cells were used to perform all UV-Vis-NIR absorption and fluorescence measurements. Fluorescence measurements were performed using 10 mm optical path length cuvettes under a right-angle arrangement. All spectroscopic measurements were done in non-degassed samples at 20 °C in spectroscopic grade toluene.

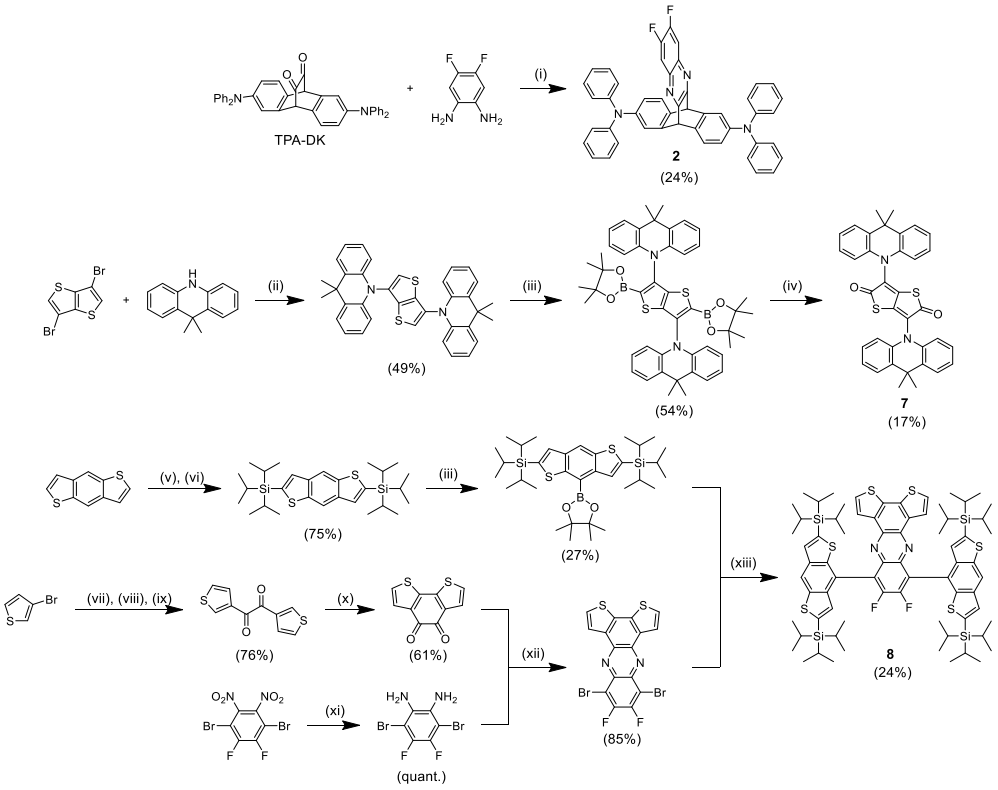

Scheme 2.1: Synthesis procedures for compounds **2**, **7**, and **8**: (i) ethanol/acetic acid (19/1) at reflux for 1 h; (ii) $Pd(OAc)_2$, XPhos and Na(O*t*Bu) in toluene at 110 °C for 24 h; (iii) bis(pinacolato)diboron, $[Ir(OMe)(COD)]_2$, 4,4'-di-*tert*-butyl-2,2'-bipyridine in dry cyclohexane at 80 °C for 24 h; (iv) Oxone™ in THF/H_2O (10/1) at room temperature for 3 h; (v) *n*-BuLi, dry THF at 0 °C for 1 h, (vi) TIPSCl, dry THF at 65 °C for 16 h; (vii) *n*-BuLi, dry THF at −78 °C for 1 h; (viii) CuBr, LiBr in dry THF at 0 °C for 1 h; (ix) oxalyl chloride at 0 °C for 1 h; (x) $FeCl_3$, CH_3NO_2 in CH_2Cl_2 at room temperature for 3 h; (xi) iron powder in acetic acid at 45 °C for 6 h; xii) acetic acid at 75 °C for 16 h; (xiii) $Pd(PPh_3)_4$, K_2CO_3 in DMF/H2O (4/1) at 130 °C for 24 h.

2.2.2. Theoretical and computational details

The ground-state geometries of all compounds were fully optimized at the M06/6-311G(d) level.[33] All vibrational frequencies are real, demonstrating the optimized geometries correspond to minima on the potential energy surface. For compound **8**, the triisopropysilyl (TIPS) groups were substituted by H atoms to reduce the computational cost. TDDFT calculations were performed using a variety of XC functionals (Table 2.1), ranging from GGA, meta-GGA and global hybrid to range-separated hybrid XC functionals using the 6-311G(d) basis set. For the LC-BLYP and LC-ωPBE range-separated hybrids, the range-separating parameter ω was modified. The modified versions of LC-BLYP and LC-ωPBE are henceforth denoted with the respective value of ω in the name: LC-BLYP33 [which is a condensed notation for LC-BLYP(ω=0.33)], LC-BLYP20, LC-BLYP17, and LC-ωPBE17. All excited state calculations were performed using the PCM model (cyclohexane) to account for an apolar environment. In addition to TDDFT calculations, its Tamm-Dancoff approximation was also applied for all functionals and all compounds, allowing the assessment of its performance with respect to TDDFT. From the excited state calculations, the vertical excitation energies to the S_1 ($\Delta E_{S_0-S_1} = E_{S_1} - E_{S_0}$), S_2 ($\Delta E_{S_2-S_0} = E_{S_2} - E_{S_0}$), T_1 ($\Delta E_{T_1-S_0} = E_{T_1} - E_{S_0}$) and T_2 ($\Delta E_{T_2-S_0} = E_{T_2} - E_{S_0}$) states, the oscillator strengths of the corresponding $S_0 \rightarrow S_1$ and $S_0 \rightarrow S_2$ transitions ($f_{S_0-S_1}$ and $f_{S_0-S_2}$), and the dominant one-electron transitions (molecular orbital pairs) for $S_0 \rightarrow S_1$ and $S_0 \rightarrow T_1$ transitions were obtained. From these values, $\Delta E_{S_1-T_1} = \Delta E_{S_1-S_0} - \Delta E_{T_1-S_0}$ (also referred to as ΔE_{ST}) and $\Delta E_{T_2-T_1} = \Delta E_{T_2-S_0} - \Delta E_{T_1-S_0}$ were calculated. All DFT and TDDFT/TDA calculations were performed using the Gaussian09 program.[34]

The vertical excitation properties obtained with TDDFT and TDDFT/TDA were benchmarked using the resolution-of-the-identity approximation of the second-order approximated coupled-cluster model[19] using the Turbomole program (Version 7.3.1)[35]. The resolution of the identity approximation for two-electron integrals reduces the CPU time needed to calculate these integrals. In addition, the method uses a partitioned form of the CC2 equations, eliminating the need to store double excitation cluster amplitudes. Using the riCC2 method allows computation of much larger systems such as the ones used in this work, whereas they would be difficult to perform with the unaltered CC2 method. Schreiber *et al.*[36] showed that the vertical excitation energies obtained with CC2

are in good agreement with those obtained with even higher levels of approximation such as the third-order approximation of the coupled cluster (CC3) and coupled cluster singles, doubles and triples (CCSDT) when the excitations exhibit a single excitation nature. Similarly, for the oscillator strengths, CC2 gives similar values to CC3 and CASPT2 calculations and allows at least for a qualitatively consistent picture. Indeed, in these benchmarks on small- and medium-size closed-shell organic molecules, for singlet excitation energies, the mean absolute errors (MAEs) with respect to the CASPT2 reference data amount to 0.32 eV, 0.50 eV, and 0.22 eV for the CC2, CCSD, and CC3 methods, whereas for the triplet excitation energies, the MAEs given in the same order are 0.19 eV, 0.16 eV, and 0.08 eV, respectively. An alternative choice for the benchmark calculations might have been the spin-scaled-component version of CC2, SCS-CC2,[37] but recent investigations on the prediction of the valence excitation energies of closed-shell organic chromophores did not demonstrate an advantage for employing or not the spin-scaled-component scheme.[12, 37-39] The same ground-state geometries were used for the riCC2 calculations as for the TDDFT and TDDFT/TDA calculations to exclude any geometry dependent differences. For these Turbomole calculations, def2-TZVP was chosen both as the main and auxiliary basis set as it also comprises split-valence triple zeta basis functions with polarization functions for the second- and third-row atoms. Additional TDDFT/def2-TZVP calculations were performed to demonstrate that the use of different basis sets for the riCC2 and TDDFT calculations has a negligible impact. Indeed, at the TDDFT/LC-BLYP17 level, differences of excitation energies between the def2-TZVP and 6-311G* basis sets are always smaller than 0.08 eV and the mean absolute difference amounts to 0.03 eV. Moreover, the impact of the ground state geometries on the first singlet and triplet excitation energies has been assessed by performing additional TDDFT/LC-BLYP17 excitation energy calculations on geometries optimized at the ωB97X-D/6-311G(d) level of approximation. The ωB97X-D[40] XC functional accounts explicitly for London dispersion forces by using empirical expressions, whereas M06 was parameterized to account, implicitly, for London dispersion interactions. The differences of TDDFT/LC-BLYP17 excitation energies between the M06 and ωB97X-D optimized geometries is negligible, with a mean absolute difference of 0.04 eV.

The mean absolute errors (MAEs), mean signed errors (MSEs), and standard deviations are calculated for all XCFs and for both TDDFT and TDDFT/TDA schemes in comparison to the reference riCC2 results (difference = TDDFT – riCC2). The absolute average errors help to objectively determine the most accurate XC functional, whereas the sign-dependent average errors yield some insight to whether the chosen XC functional tends to over- or underestimate the given property.

Table 2.1: Overview of the selected XC functionals grouped by their position on Jacob's ladder.

	XC functional	% HF exchange[a]	Range-separating parameter ω ($bohr^{-1}$)[b]
GGA	BLYP		
	BPW91		
	PBE		
meta-GGA	M06L		
	TPSS		
Global hybrid GGA	B3LYP	20	
	B971	21	
	PBE0	25	
Global hybrid meta-GGA	TPSSh	10	
	M06	27	
	M06-2X	54	
Long-range separated hybrid GGA/meta-GGA	ωB97	0-100	0.40 (1.323)
	ωB97X	16-100	0.30 (1.764)
	CAM-B3LYP	19-65	0.33 (1.604)
	LC-ωPBE17	0-100	0.17 (3.113)
	LC-BLYP17	0-100	0.17 (3.113)
	LC-BLYP20	0-100	0.20 (2.646)
	LC-BLYP33	0-100	0.33 (1.604)
	LC-BLYP	0-100	0.47 (1.126)

[a] For long-range corrected functionals, the % HF exchange is given at interelectronic distance $r_{12} = 0$ and ∞. [b] corresponding length L = 1/ω (Å) in parentheses

2.2.3. Experimental spectroscopic results and earlier theoretical data

Results from the literature are summarized in Table 2.2 for the electronic and optical properties of compounds **1**, **3**-**6**, and **9**-**10**. These include experimental data as well as TDDFT results related to the first singlet and triplet excited states. Our experimental UV-VIS absorption and emission data are also given for the whole list of compounds. Compound **7** was found to be non-emissive. Although the differences between literature results and ours are generally small

Table 2.2: Experimental and theoretical properties of the selected compounds.

	ΔE_{max}, eV (λ_{max}, nm) abs.[a]	ΔE_{max}, eV (λ_{max}, nm) em.[a]	ΔE_{max}, eV (λ_{max}, nm) abs.[b]	ΔE_{max}, eV (λ_{max}, nm) em.[b]	$\Delta E_{T_1-S_0}$, eV[d]	ΔE_{ST}, eV[d]	Calc. ΔE_{ST}, eV[e]	XC functional and basis set[e]
1[27]	2.95 (420)	2.25 (552)	2.95 (421)	2.15 (578)	—	—	0.11	B3LYP/6-31G(d)
2	—	—	3.37 (368)	2.55 (486)	—	—	—	—
3[29]	2.43 (510)	1.91 (648)	2.43 (510)	1.86 (668)	—	—	0.69	LC-ωPBE/6-31G(d)[f]
4[29]	2.57 (482)	1.94 (638)	2.58 (481)	1.92 (645)	2.12	0.11	0.02	LC-ωPBE/6-31G(d)[f]
5[30]	3.32 (373)	2.65 (467)	3.31 (375)	2.62 (473)	2.84	0.13	0.32	B3LYP/6-31G
6[28]	3.38 (367)	2.99 (414)	3.43 (362)	2.99 (414)	2.97	0.26	0.13	B3LYP/6-31G(d,p)
7	—	—	2.02 (613)	—[c]	—	—	—	—
8	—	—	2.88 (430)	2.24 (553)	—	—	—	—
9[31]	3.67 (338)	2.10 (590)	2.58 (480)	2.06 (602)	1.95	0.10	0.68	B3LYP/6-31G(d)
10[41]	~3.18 (~390)	2.45 (507)	3.14 (395)	2.39 (519)	2.65	0.08	0.03	B3LYP/6-31G(d)

[a] Experimental ΔE_{max} (λ_{max}) for the absorption ($S_0 \rightarrow S_1$) and emission ($S_1 \rightarrow S_0$) in toluene as taken from the respective references. [b] Experimental ΔE_{max} (λ_{max}) for the absorption ($S_0 \rightarrow S_1$) and emission ($S_1 \rightarrow S_0$) in toluene as measured in this work. [c] No fluorescence observed. [d] Experimental values obtained from the corresponding literature. [e] TDDFT values taken from the respective references. [f] The authors make no reference to modification of the range-separating parameter, which is therefore expected to be default (ω = 0.33).

(a few tenths of eV), the ΔE_{max} of absorption of **9** differs by more than one eV. As discussed below, the new value is much more consistent with the quantum-chemical calculations. This new experimental value of **9** substantiates the fact that we enacted our own set of optical characterizations.

2.2.4. Reference riCC2 calculations

The benchmark riCC2 values used to reference the TDDFT and TDDFT/TDA calculations are given in Table 2.3. The agreement between the first vertical singlet excitation energies ($\Delta E_{S_0-S_1}$) calculated using riCC2 and the experimental absorption maxima was verified by constructing a correlation plot between the two properties (Figure 2.2). The slope of the correlation plot is slightly larger than 1, indicating that the riCC2 vertical excitation energy increases more rapidly with increasing absorption maximum. The R^2 value of 0.95 points to a very good correlation between the two properties, proving the high level of predictability of riCC2 calculations in comparison to experimental values. Although the number of points is reduced, a similarly good correlation between riCC2 and experiment is observed for the $S_0 \rightarrow T_1$ transition energies. For ΔE_{ST} no valid correlation could be drawn, probably because the experimental values are not obtained from the difference between $\Delta E_{S_0-S_1}$ and $\Delta E_{S_0-T_1}$, but rather from the onsets of the fluorescence (at room temperature) and phosphorescence (at 77 K) CT emission peaks.

Table 2.3: riCC2 excitation energies, oscillator strengths, and energy gaps for compounds **1-10**.

	$\Delta E_{S_0-S_1}$ (eV)	$\Delta E_{S_0-S_2}$ (eV)	$f_{S_0-S_1}$	$f_{S_0-S_2}$	$\Delta E_{S_0-T_1}$ (eV)	$\Delta E_{S_0-T_2}$ (eV)	$\Delta E_{T_1-T_2}$ (eV)	$\Delta E_{S_1-T_1}$ (eV)
1	2.969	2.996	0.170	0.098	2.903	2.948	0.045	0.067
2	3.468	3.496	0.157	0.131	3.337	3.354	0.016	0.130
3	2.474	3.355	0.231	0.008	2.081	3.256	1.175	0.393
4	2.456	2.525	0.000	0.000	2.457	2.527	0.069	-0.001
5	3.524	3.718	0.396	0.004	3.227	3.411	0.185	0.297
6	3.565	3.646	0.207	0.001	3.494	3.502	0.009	0.071
7	1.923	1.882	0.094	0.002	1.852	1.853	0.001	0.029
8	3.076	3.150	0.083	0.005	2.575	2.961	0.386	0.501
9	2.692	3.488	1.011	0.585	2.159	2.809	0.651	0.534
10	3.022	3.031	0.032	0.010	3.010	3.019	0.009	0.012

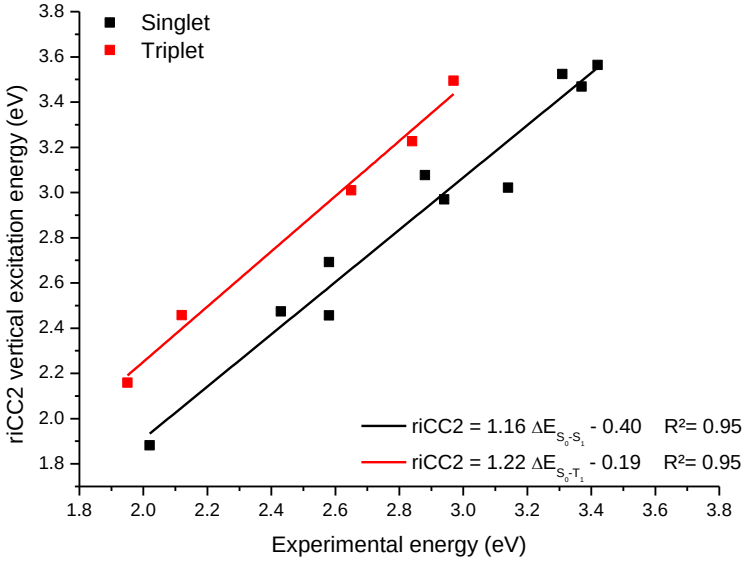

Figure 2.2: Correlation plots between the riCC2 vertical excitation energies and the experimental values for maximum absorption $\Delta E_{S_0-S_1}$ and $\Delta E_{S_0-T_1}$.

2.2.5. TDDFT and TDDFT/TDA versus riCC2 calculations

2.2.5.1. Singlet excitation energies and oscillator strengths

For the vertical singlet excitation energies and the corresponding oscillator strengths, the choice was made to only consider states that have the same nature in both the riCC2 and the TDDFT or TDDFT/TDA calculations. With the exception of compound **7** (HOMO-1→LUMO), the dominant nature of the first excited state of all compounds is of HOMO→LUMO character for the riCC2 calculations. Given the near degeneracy (Table 2.3) of the first and second vertical excitation energies, and to have the comparison between the compounds more in line with each other, we have chosen to take the HOMO→LUMO transition as the first state and the HOMO-1→LUMO transition as the second state for compound **7**. In a few compound-functional combinations, the nature of the first singlet excited state calculated with TDDFT or TDDFT/TDA does not correspond to a HOMO→LUMO transition. We then opted to use the second (HOMO→LUMO) excited state to compare states of the same nature. Indeed, comparison between two states of different nature may lead to faulty conclusions about the XCFs ability to correctly predict the targeted properties. These statistical analyses are provided in Table 2.4 for TDDFT values and in

Table 2.5 for the TDDFT/TDA ones. The full list of all compounds and their excited state data for the first two states can be found in the SI.

In Figure 2.3, each colored line represents a single XCF and the sign-dependent error with respect to the riCC2 calculation is plotted for every compound. For the first singlet excitation energy (Figure 2.3a), we can clearly see some functionals heavily overestimating (LC-BLYP, ωB97, ωB97X, LC-BLYP33) and some functionals underestimating (PBE, BPW91, BLYP, TPSS, M06L, TPSSh, B3LYP, B971, PBE0, M06) the singlet excitation energy. Overestimation of the singlet excitation energy typically occurs when there is too much HF exchange, *i.e.* for range-separated hybrids when the range-separating parameter is not properly tuned (ω is too large). Underestimation happens when there is not enough HF exchange present, as is the case for the GGA and meta-GGA functionals, but even for some of the hybrid functionals. This originates from the ultra-locality of the XCF and the related self-interaction error, leading to a poor description of the CT excitations.[42, 43] We also observe some variations of the errors as a function of the nature of the compounds, but most XC functionals seem to follow the same trend. The absolute values of the errors depicted in Figure 2.3 are averaged per functional in Table 2.4 and are provided together with their standard deviation. From Table 2.4, the functionals that show a relatively small error are CAM-B3LYP (0.311 eV) and M06-2X (0.283 eV), but they are outperformed by LC-ωPBE17 (0.141 eV), LC-BLYP17 (0.157 eV) and LC-BLYP20 (0.141 eV). From the difference between the signed and absolute errors (Table S2.1), it is also clear that LC-BLYP20 tends to either slightly over- or underestimate the singlet excitation energy for a given compound. This is likely due to the small size of the error, as the other functionals all show the same amplitudes for the signed and absolute errors. Taking the LC-BLYP XCFs, the signed errors range from -0.157 eV (ω = 0.17, the amount of HF exchanges grows the least rapidly with r_{12}) to 0.056 eV (ω = 0.20), 0.650 eV (ω = 0.33), and 0.978 eV (ω = 0.47, the amount of HF exchanges grows the fastest with r_{12}), demonstrating the key role of long-range exchange. Using the Tamm-Dancoff approximation has a minor impact in the sense that large underestimations or overestimations of $\Delta E_{S_0-S_1}$ remain when employing that approximation.

The second vertical singlet energy, $\Delta E_{S_0-S_2}$, follows the same trend as the first vertical singlet energy. A decrease in the MAE is observed with increasing HF exchange until a minimum is reached and the error increases again as the amount of HF exchange becomes too high. The most notable XC functionals are the same as for the first vertical singlet energy, LC-ωPBE17 (0.182 eV), LC-BLYP17 (0.192 eV) and LC-BLYP20 (0.182 eV). Again, there is little difference between the TDDFT and TDDFT/TDA results. For both singlet excitation energies, LC-BLYP20 gives the smallest MAEs. The standard deviations on the MAEs for both properties are related to the MAEs themselves. If the MAE decreases, so does the standard deviation and *vice versa*. A slight exception to this is M06-2X (0.102 eV), which has relatively small standard deviations, still comparable to LC-BLYP17 (0.106 eV) and LC-ωPBE17 (0.102), despite having a MAE that is nearly twice as large.

For the oscillator strengths, the analysis is less straightforward because their amplitudes cover more than one order of magnitude [even after neglecting those states with very small (f < 0.05) values]. Moreover, as shown in Table 2.3 (riCC2 values), with exception of compound **9**, all compounds show relatively small to very small oscillator strengths. This is most definitely true for the oscillator strength of the $S_0 \rightarrow S_2$ transition. As a matter of fact, for these very small oscillator strengths, most XCFs perform well because they reproduce the dominant character of the transition, which determines the negligible *f* values. This is illustrated by compound **4**, where the $S_0 \rightarrow S_1$ and $S_0 \rightarrow S_2$ transitions have a CT character, between the donor and acceptor groups that are perpendicular to each other (and therefore of different symmetry). To a given extent, the same trend as for the first singlet excitation energies roughly holds. This is expected as a good representation of the excitation energy should give a good description of its oscillator strength. Then, as already observed for benzene derivatives, XCFs with a small amount of HF exchange underestimate both the excitation energies and oscillator strengths.[44] For the $S_0 \rightarrow S_1$ transition, a large number of functionals are within 0.2 of each other and give relatively consistent results. Functionals such as LC-BLYP17 (0.050), LC-ωPBE17 (0.051), LC-BLYP20 (0.086), M06-2X (0.084), CAM-B3LYP (0.101), M06 (0.050), PBE0 (0.053), B971 (0.068), B3LYP (0.074 eV) and TPSSh (0.095) all have errors below 0.1, albeit their standard deviations are larger than the errors themselves (since the

errors originate from a few excited states only). Using the Tamm-Dancoff approximation again barely changes these general conclusions, although, in more detail, its impact depends on the XCF and on the excited state (S_1 or S_2). Indeed, the absolute average error decreases slightly for most functionals, except for M06-2X and the range-separated functionals when looking at the $S_0 \rightarrow S_1$ transition. For the $S_0 \rightarrow S_2$ transition, the MAEs decrease slightly for all functionals except for LC-ωPBE17 and LC-BLYP. The best performing functionals for both transitions are M06-2X, LC-BLYP17, LC-ωPBE17, and LC-BLYP20.

2.2.5.2. First and second triplet excitation energies

To achieve efficient intersystem crossing, the ^{3}CT and ^{3}LE state (or ^{3}CT state of a different nature) need to be close in energy for efficient vibronic coupling to take place. Therefore, this work not only focuses on calculating the first, but also the second vertical triplet excitation energies (Figure 2.3, Tables 2.4 and 2.5). Looking at the data obtained using the TDDFT approach, the error on the first triplet excitation energy, $\Delta E_{S_0-T_1}$, is the smallest for M06-2X (0.162 eV). This is consistent with the results of Brückner *et al.*[9a] in their report on the singlet-triplet gap for triplet-triplet annihilation. When looking at the other functionals that perform well, LC-BLYP20 (0.215 eV), LC-BLYP33 (0.231 eV), ωB97X (0.311 eV), LC-BLYP17 (0.314 eV), CAM-B3LYP (0.332 eV), and LC-ωPBE17 (0.344 eV) all have absolute average errors within 0.35 eV. It is apparent that a substantially high amount of HF exchange is necessary to accurately describe the triplet energy as is observed for the LC-BLYP functionals with ω = 0.20 and 0.33 which outperform those with ω = 0.17 and LC-ωPBE17. On the other hand, the unmodified LC-BLYP has a much higher MAE, indicating a too large value for ω. The MAEs for the second vertical triplet excitation energy, $\Delta E_{S_0-T_2}$, follow the same trend as for the first excitation energy and are even a bit smaller for all functionals.

When comparing TDDFT with TDDFT/TDA, all functionals show a more consistent behavior throughout the series (Figure S2.1). The accuracy of all functionals increases as can be seen by a decrease of the absolute average error for all functionals. Most notable are CAM-B3LYP (0.332 eV -> 0.151 eV) and LC-BLYP (0.623 eV -> 0.199 eV), which gain significant accuracy and have smaller standard deviations when using the TDDFT/TDA approach. Upon using the TDA,

a number of functionals, comprising M06-2X (0.144 eV), CAM-B3LYP (0.151 eV), LC-BLYP20 (0.149 eV), LC-BLYP33 (0.175 eV), and LC-BLYP (0.199 eV), have absolute average errors within 200 meV. The sudden decrease in MAE for the vertical triplet excitation energies using functionals such as CAM-B3LYP and LC-BLYP is attributed to the ground state triplet instability problem for these systems, which is known to occur when using XCFs with a large amount of HF exchange.[42, 43, 45, 46] In the TDA, only excitation between occupied-virtual orbital pairs is allowed as opposed to conventional TDDFT, where virtual-occupied de-excitation contributions are also allowed. The form of the TDA eigenvalue equation precludes the occurrence of imaginary excitation energies and hence circumvents the triplet instability issues that can arise.

The error on the second triplet excitation energy is the smallest for M06-2X (0.133 eV) and furthermore it has also the smallest standard deviation. Second best is LC-BLYP20 (0.157 eV), which, despite its relatively poor accuracy with respect to M06-2X, has a similar standard deviation and is closely followed by CAM-B3LYP (0.234 eV). Other functionals that are noteworthy are (0.302 eV), LC-BLYP17 (0.287 eV), and LC-BLYP33 (0.248 eV), all having absolute average errors within 0.3 eV. The overall performance is enhanced when using the TDA, except for M06-2X, in which the absolute average error goes up by 25% (0.133 -> 0.177 eV). Using TDA, LC-BLYP20 (0.123 eV) and CAM-B3LYP (0.127 eV) perform similarly.

Due to the vibronic enhancement, the T_1-T_2 energy gap can help to explain a compound's potential for TADF (Figure 2.3, Tables 2.4 and 2.5). The largest absolute average error is 0.400 eV (LC-BLYP), meaning that the errors are generally smaller than when looking at the energies of the individual states. This leads us to conclude that a large number of functionals benefit from a cancellation of two relatively large errors. Therefore, the discussion will mainly focus on the functionals that did well in estimating the transition energies to T_1 and T_2. The best performing functional is LC-BLYP17 (0.039 eV), followed by LC-ωPBE17 (0.050 eV), LC-BLYP20 (0.072 eV), and M06-2X (0.081 eV). Applying the Tamm-Dancoff approximation, the absolute average errors have significantly decreased further for the aforementioned functionals. Furthermore, CAM-B3LYP (0.213 -> 0.067 eV) performs a whole lot better under the TDA, as was also shown for the T_1 and T_2 energies.

Table 2.4 Statistical analysis including mean absolute errors (MAEs, eV) and standard deviations (eV) obtained from the comparison between TDDFT calculations with different XCFs and riCC2 reference values.

	$\Delta E_{S_0-S_1}$ (eV)		$f_{S_0-S_1}$		$\Delta E_{S_0-S_2}$ (eV)		$f_{S_0-S_2}$		$\Delta E_{S_0-T_1}$ (eV)		$\Delta E_{S_0-T_2}$ (eV)		$\Delta E_{T_1-T_2}$ (eV)		$\Delta E_{S_1-T_1}$ (eV)	
	MAE	Std Dev	MAE	Std Dev	MAE	Std Dev	MAE	Std Dev	MAE	Std Dev	MAE	Std Dev	MAE	Std Dev	MAE	Std Dev
BLYP	1.242	0.213	0.116	0.144	1.329	0.231	0.072	0.173	1.153	0.265	1.224	0.190	0.139	0.161	0.113	0.144
BPW91	1.236	0.216	0.113	0.143	1.322	0.230	0.072	0.173	1.153	0.266	1.220	0.193	0.138	0.160	0.111	0.142
PBE	1.238	0.216	0.113	0.143	1.322	0.229	0.072	0.173	1.153	0.268	1.225	0.195	0.144	0.168	0.112	0.142
M06L	1.021	0.202	0.109	0.138	1.102	0.237	0.072	0.173	0.952	0.224	1.005	0.178	0.130	0.145	0.100	0.130
TPSS	1.166	0.204	0.110	0.139	1.244	0.223	0.069	0.173	1.090	0.251	1.151	0.188	0.137	0.155	0.105	0.138
TPSSh	0.850	0.149	0.095	0.119	0.904	0.191	0.072	0.173	0.820	0.158	0.845	0.157	0.115	0.137	0.078	0.083
B3LYP	0.596	0.110	0.074	0.089	0.628	0.172	0.070	0.173	0.610	0.086	0.605	0.112	0.076	0.090	0.054	0.048
B971	0.555	0.102	0.068	0.083	0.583	0.169	0.070	0.173	0.566	0.083	0.563	0.105	0.072	0.084	0.053	0.046
PBE0	0.430	0.089	0.053	0.064	0.445	0.164	0.119	0.229	0.526	0.068	0.482	0.080	0.049	0.059	0.096	0.070
M06	0.379	0.106	0.050	0.057	0.399	0.179	0.068	0.173	0.460	0.089	0.430	0.091	0.035	0.037	0.081	0.068
M06-2X	0.283	0.102	0.084	0.107	0.257	0.109	0.024	0.050	0.162	0.081	0.133	0.095	0.081	0.081	0.239	0.112
ωB97	0.882	0.239	0.254	0.233	0.850	0.238	0.088	0.150	0.388	0.196	0.351	0.243	0.362	0.311	1.263	0.161
ωB97X	0.740	0.215	0.225	0.224	0.713	0.203	0.060	0.135	0.311	0.184	0.300	0.221	0.332	0.287	1.044	0.142
CAM-B3LYP	0.311	0.124	0.101	0.145	0.316	0.118	0.047	0.084	0.332	0.177	0.234	0.133	0.213	0.162	0.643	0.119
LC-ωPBE17	0.141	0.102	0.051	0.101	0.182	0.086	0.048	0.117	0.344	0.099	0.302	0.086	0.050	0.057	0.209	0.127
LC-BLYP17	0.157	0.106	0.050	0.098	0.192	0.085	0.042	0.115	0.314	0.089	0.287	0.079	0.039	0.042	0.156	0.102
LC-BLYP20	0.107	0.074	0.086	0.138	0.075	0.074	0.052	0.128	0.215	0.129	0.157	0.076	0.072	0.072	0.270	0.136
LC-BLYP33	0.650	0.192	0.210	0.211	0.600	0.195	0.058	0.137	0.231	0.161	0.248	0.179	0.245	0.220	0.868	0.125
LC-BLYP	0.978	0.264	0.270	0.236	0.956	0.262	0.117	0.204	0.623	0.239	0.492	0.248	0.400	0.354	1.601	0.187
LC-BLYP20-M06-2X	—	—	—	—	—	—	—	—	—	—	—	—	—	—	0.155	0.090

Table 2.5: Statistical analysis including mean absolute errors (MAEs, eV) and standard deviations (eV) obtained from the comparison between TDDFT/TDA calculations with different XCFs and riCC2 reference values.

	$\Delta E_{S_0-S_1}$ (eV)		$f_{S_0-S_1}$		$\Delta E_{S_0-S_2}$ (eV)		$f_{S_0-S_2}$		$\Delta E_{S_0-T_1}$ (eV)		$\Delta E_{S_0-T_2}$ (eV)		$\Delta E_{T_1-T_2}$ (eV)		$\Delta E_{S_1-T_1}$ (eV)	
	MAE	Std Dev	MAE	Std Dev	MAE	StdDev	MAE	Std Dev	MAE	Std Dev	MAE	Std Dev	MAE	Std Dev	MAE	Std Dev
BLYP	1.220	0.226	0.098	0.118	1.318	0.242	0.071	0.173	1.148	0.269	1.222	0.191	0.142	0.165	0.112	0.137
BPW91	1.214	0.229	0.096	0.117	1.310	0.242	0.071	0.173	1.146	0.272	1.217	0.194	0.141	0.164	0.111	0.136
PBE	1.215	0.229	0.096	0.116	1.311	0.241	0.071	0.173	1.147	0.273	1.218	0.196	0.142	0.165	0.112	0.136
M06L	1.001	0.213	0.093	0.117	1.092	0.245	0.072	0.173	0.932	0.240	0.992	0.184	0.135	0.153	0.105	0.136
TPSS	1.144	0.216	0.094	0.114	1.236	0.236	0.071	0.173	1.079	0.259	1.143	0.193	0.138	0.160	0.108	0.135
TPSSh	0.828	0.160	0.076	0.097	0.894	0.198	0.070	0.173	0.784	0.190	0.818	0.171	0.129	0.151	0.094	0.116
B3LYP	0.574	0.120	0.055	0.071	0.618	0.177	0.069	0.173	0.560	0.122	0.580	0.122	0.102	0.108	0.074	0.081
B971	0.533	0.113	0.050	0.065	0.573	0.173	0.068	0.173	0.520	0.116	0.540	0.115	0.097	0.101	0.072	0.077
PBE0	0.407	0.099	0.036	0.047	0.435	0.168	0.067	0.173	0.436	0.079	0.444	0.082	0.068	0.064	0.064	0.056
M06	0.356	0.113	0.035	0.045	0.389	0.182	0.067	0.173	0.372	0.079	0.371	0.113	0.080	0.083	0.061	0.062
M06-2X	0.322	0.088	0.100	0.137	0.289	0.116	0.017	0.026	0.144	0.127	0.177	0.101	0.052	0.045	0.187	0.104
ωB97	0.966	0.208	0.287	0.274	0.903	0.234	0.051	0.118	0.236	0.183	0.385	0.269	0.155	0.172	0.731	0.103
ωB97X	0.812	0.187	0.255	0.265	0.758	0.199	0.047	0.114	0.210	0.166	0.322	0.213	0.129	0.135	0.612	0.100
CAM-B3LYP	0.356	0.105	0.119	0.171	0.351	0.109	0.037	0.047	0.151	0.090	0.127	0.103	0.067	0.074	0.303	0.127
LC-ωPBE17	0.128	0.087	0.065	0.125	0.153	0.089	0.064	0.120	0.273	0.078	0.264	0.089	0.043	0.038	0.171	0.109
LC-BLYP17	0.141	0.092	0.066	0.123	0.164	0.090	0.026	0.069	0.262	0.075	0.261	0.079	0.036	0.021	0.137	0.090
LC-BLYP20	0.118	0.097	0.107	0.171	0.088	0.072	0.036	0.088	0.149	0.066	0.123	0.052	0.044	0.040	0.226	0.130
LC-BLYP33	0.721	0.168	0.241	0.254	0.645	0.194	0.047	0.113	0.175	0.149	0.255	0.184	0.100	0.098	0.563	0.127
LC-BLYP	1.073	0.230	0.305	0.280	1.030	0.254	0.061	0.119	0.199	0.181	0.351	0.307	0.171	0.186	0.883	0.125
LC-BLYP20-M06-2X	—	—	—	—	—	—	—	—	—	—	—	—	—	—	0.146	0.097

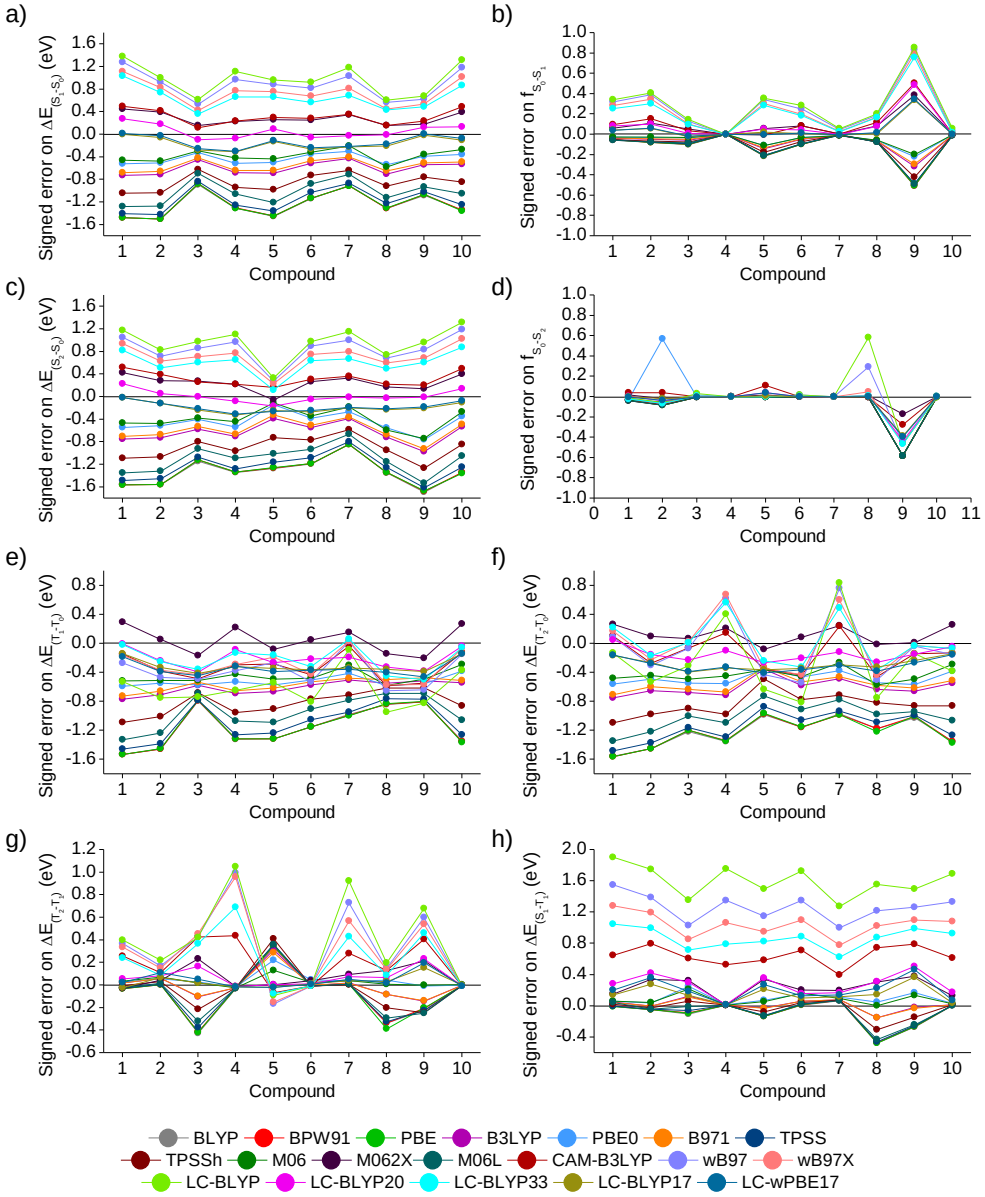

Figure 2.3: Signed errors on each property for each individual XC functional for all 10 compounds obtained using TDDFT. a) First vertical singlet excitation energy, $\Delta E_{S_0-S_1}$. b) Oscillator strength for the first singlet excitation, $f_{S_0-S_1}$. c) Second vertical singlet excitation energy, $\Delta E_{S_2-S_0}$. d) Oscillator strength for the second vertical singlet excitation, $f_{S_0-S_2}$. e) First vertical triplet excitation energy, $\Delta E_{T_1-S_0}$. f) Second vertical triplet excitation energy, $\Delta E_{T_2-S_0}$. g) Triplet-triplet energy gap for the first two triplet excited states, $\Delta E_{T_2-T_1}$. h) Singlet-triplet gap for the first singlet and triplet excited states, $\Delta E_{S_1-T_1}$.

2.2.5.3. Singlet-triplet energy gap

The first property that is typically considered when analyzing a compound for TADF, is the singlet-triplet energy gap. Its amplitude is correlated, with good approximation, to the spatial overlap between the HOMO and LUMO because the first singlet and triplet transitions are dominated by the HOMO-to-LUMO configuration. This is evidenced in Figure S2.2 at the representative M06/6-311G(d) level of approximation. One would expect that the XC functionals that are accurately describing both the singlet and triplet excitation energies also perform well at describing the energy gap between them. Therefore, from the previous sections, it follows that LC-ωPBE17 (0.209 eV), LC-BLYP17 (0.156 eV), LC-BLYP20 (0.270 eV) and M06-2X (0.239 eV) are reliable functionals to use under the regular TDDFT formalism, despite not having the smallest absolute errors or standard deviations. Ideally, TDDFT/TDA is used and the error on the energy gaps for LC-ωPBE17 (0.171 eV), LC-BLYP17 (0.137 eV), LC-BLYP20 (0.226 eV), and M06-2X (0.187 eV) is reduced. CAM-B3LYP (0.643 -> 0.303 eV) still shows a relatively large error on ΔE_{ST} due to its larger average error on the singlet excitation energy than the other two functionals.

Surprisingly, most functionals, including the GGA and meta-GGA functionals without HF exchange (BLYP, BPW91, PBE, TPSS, M06L), perform well for the singlet-triplet energy gap. These data also explain why one of the most used functionals in literature (B3LYP), has not been found to give erroneous results, despite its poor ability to describe both the singlet and triplet excitation energies. The same goes for the other functionals. When looking at the singlet and triplet energies individually, they fail dramatically in predicting accurate values. The corresponding underestimations of both types of excitation energies have the same origin, which is related to the CT character of the excitations.[58] Therefore, their ability to accurately predict ΔE_{ST} is due to the compensation of two large errors, as was also seen for the T_1-T_2 energy gap. Ultimately, since they are obtained with the wrong underlying quantities, these functionals are not recommended, even though they might give a quantitatively correct answer for a certain set of compounds. Because of the large errors on the singlet and triplet excitation energies when using these functionals, one can never be sure that the calculated singlet-triplet energy gap is trustworthy, nor whether related

quantities like the spin-orbit couplings could be accurate since they depend on the nature of the excited state.

Lastly, the possibility to use a 'hybrid' approach in which the vertical singlet and triplet excitation energies are calculated using two different functionals can be taken into consideration, *i.e.* i) LC-BLYP20 that gives the best results for the singlet excitation energies and ii) M06-2X that provides the best results for the triplet excitation energies. Combining the results from both functionals shows mean absolute errors on the singlet-triplet energy gap of 0.155 eV using TDDFT and 0.146 eV using TDDFT/TDA (Tables 2.4 and 2.5). These values are comparable to those obtained with single functional calculations such as LC-BLYP17, but give better performance than functionals such as M06-2X and LC-BLYP20 separately.

2.2.5.4. Further discussion on the performance of the TDDFT scheme with respect to riCC2

To further evaluate the XC functionals used in this work, the consistency of the TDDFT and TDDFT/TDA results versus the results obtained using riCC2 for the first excited singlet and triplet states was checked by constructing correlation plots. In Figure 2.4, the correlation is given for LC-BLYP20, which is the best performing functional for the vertical singlet excitation energies and also performs well for the triplet vertical excitation energies. In Figure S2.3, the correlation plots for all functionals used in this work can be found. While each of the functionals shows a linear correlation, the slopes vary widely from 0.66 to 1.07, with R^2 values varying from 0.73 to 0.98. XC functionals without HF exchange (BLYP, BPW91, PBE, M06L, and TPSS) reproduce the riCC2 values poorly, with slopes much smaller than 1 and R^2 values below 0.85. The group of functionals with a small percentage of HF exchange (TPSSh, B3LYP, B971, PBE0, M06, and M062X) performs significantly better, especially with increasing amount of HF exchange. Apart from TPSSh (with only 10% of HF exchange), these functionals are showing correlations with R^2 values above 0.95, but with slopes that are still only around 0.9. As the amount of HF exchange increases to 54% for M06-2X, slopes of around 1.0 with R^2 values of around 0.95 are found. Finally, the group of range-separated functionals (ωB97, ωB97X, CAM-B3LYP, LC-ωPBE17, LC-BLYP17, LC-BLYP20, LC-BLYP33, and LC-BLYP) shows varying behavior, depending on their range-separated parameter. Due to the, generally,

higher amount of HF exchange, the slopes of the correlation plots are all in the range of 0.95 – 1.07, but the R^2 values change heavily. In the cases where the range-separating parameter is too large, the amount of HF exchange increases rapidly and the R^2 values get smaller, as is the case for ωB97, ωB97X, CAM-B3LYP, LC-BLYP33, and LC-BLYP. For the tuned range-separating functionals such as LC-ωPBE17, LC-BLYP17, and LC-BLYP20, both the slopes and R^2 values obtained are close to 1.0. Utilizing the Tamm-Dancoff approximation shows little influence on the correlation of the vertical singlet excitation energies, as was also shown above. For the correlation on the triplet excitation energies, the TDDFT/TDA approach leads to a slight decrease in the slope and R^2 values for the hybrid and non-hybrid functionals and leads to a slight increase or decrease in the slope depending on whether the slope was smaller or larger than 1.0 and a slight increase in the R^2 values for the range-separated functionals. Overall, it means the TDA approach gives a better correlation (closer to 1) for the range-separated functionals with an increased R^2. It is further interesting to analyze the intercepts at the origin for the different first singlet and triplet excitation energies, which are directly related to a comparison of the regression lines. For GGA, mGGA, and hybrids with small amount of HF exchange, these intercepts vary little from the singlet to triplet excitation energies or from the TDDFT to the TDDFT/TDA calculations (typically by less than 0.2 eV). This gives a kind of impression (at the scale of the plots) that a unique regression line might describe the 4 sets of data. On the other hand, with large amount of HF exchange (global or range-separated hybrids), the intercepts at the origin are systematically larger for the $\Delta E_{S_0-S_1}$ values than the $\Delta E_{S_0-T_1}$ ones. In addition, for the triplets, there is a difference between the TDDFT and TDDFT/TDA results, with smaller intercepts at the origin using the TDDFT scheme.

These results substantiate our findings in the previous sections. The functionals that tend to predict the vertical singlet and triplet excitation energies better, give better correlations to the riCC2 results. The Tamm-Dancoff approximation again gives improved results for the vertical triplet excitation energies, proving that, owing to correcting for the errors related to triplet instabilities,[42] it is a very useful approximation to get the most accurate results from the TDDFT calculations.

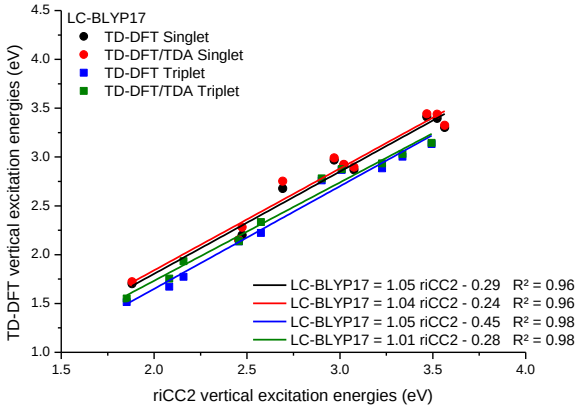

Figure 2.4: Correlation between the LC-BLYP17 and riCC2 calculations for the first vertical singlet and triplet excitations.

2.3. Conclusions

In this work, the TDDFT method has been employed to evaluate the first singlet and triplet excitation energies and the corresponding singlet-triplet energy gaps on a set of 10 compounds that were designed to exhibit thermally activated delayed fluorescence. These compounds have been selected because they cover a broad range of singlet-triplet energy splitting values, together with fluorescence characteristics going from blue to red, while presenting a clear chemical diversity in terms of donor and acceptor units. By using a broad variety of XC functionals, our goal was to highlight the best ones in comparison to benchmark results evaluated at the resolution-of-the-identity second-order coupled cluster (riCC2) level, while the performance of the latter method against experimental data was preliminarily demonstrated.

We have shown that two functionals stand out when aiming at predicting the vertical singlet and triplet excitation energies, being LC-BLYP20 and M06-2X. These functionals show steady behavior and minimal errors on the excited state energies in comparison to riCC2 calculations. LC-BLYP20 tends to predict the singlet energies more accurately than the triplet energies, whereas the opposite is true for M06-2X. Therefore, the singlet-triplet energy gaps that follow from these calculations have similar errors for a given compound. Furthermore, when looking at the singlet-triplet energy gaps, LC-ωPBE17 and LC-BLYP17

outperform LC-BLYP20 and M06-2X. The question of which functional is best to use then falls back to the primary focus of the investigation. If the focus is on the singlet state energies, LC-BLYP20 followed by LC-ωPBE17 and LC-BLYP17 would be the optimal functionals. If the focus is rather on the position of the triplet states and their mutual energy difference, M06-2X would be the optimal functional. Using the Tamm-Dancoff approximation has no significant influence on the singlet excitation energies. It does, however, decrease the errors obtained using LC-BLYP20, LC-BLYP17, LC-ωPBE17, and M06-2X for the triplet excitation energies and consequently for the singlet-triplet energy gap. Furthermore, using TDA increases the precision of the obtained triplet energy errors within the set of 10 compounds. Although we have shown in this work that small errors for the singlet-triplet energy gap can be obtained with a large number of functionals, their accuracy lies in a cancellation of two large errors. These functionals are therefore not trustworthy.

We therefore propose the use of the Tamm-Dancoff approximation in combination with either LC-BLYP17, LC-ωPBE17, LC-BLYP20, or M06-2X when looking at the ΔE_{ST} quantities for a given compound. Ultimately, a hybrid approach using the TDA approach and taking the ΔE_{ST} from the singlet and triplet excitation energies obtained with LC-BLYP20 and M06-2X, respectively, gives errors on the singlet-triplet gap that are roughly the same as those obtained with the best functional LC-BLYP17, but with better estimates for the singlet and triplet excitation energies respectively.

2.4. References

1. X. K. Chen, D. Kim and J. L. Brédas, *Acc. Chem. Res.*, 2018, **51**, 2215-2224.
2. J. Gibson, A. P. Monkman and T. J. Penfold, *ChemPhysChem*, 2016, **17**, 2956-2961.
3. T. J. Penfold, F. B. Dias and A. P. Monkman, *Chem. Commun.*, 2018, **54**, 3926-3935.
4. T. J. Penfold, E. Gindensperger, C. Daniel and C. M. Marian, *Chem. Rev.*, 2018, **118**, 6975-7025.
5. P. K. Samanta, D. Kim, V. Coropceanu and J. L. Brédas, *J. Am. Chem. Soc.*, 2017, **139**, 4042-4051.
6. J. Sanz-Rodrigo, Y. Olivier and J.-C. Sancho-García, *Molecules*, 2020, **25**, 1006.
7. J.-M. Mewes, *Phys. Chem. Chem. Phys.*, 2018, **20**, 12454-12469.
8. S. Hirata and M. Head-Gordon, *Chem. Phys. Lett.*, 1999, **314**, 291-299.

9. D. Jacquemin, E. A. Perpète, I. Ciofini and C. Adamo, *J. Chem. Theory Comput.*, 2010, **6**, 1532-1537.
10. A. D. Laurent, C. Adamo and D. Jacquemin, *Phys. Chem. Chem. Phys.*, 2014, **16**, 14334-14356.
11. B. M. Wong and J. G. Cordaro, *J. Chem. Phys.*, 2008, **129**, 214703.
12. C. Brückner and B. Engels, *Chem. Phys.*, 2017, **482**, 319-338.
13. S. Huang, Q. Zhang, Y. Shiota, T. Nakagawa, K. Kuwabara, K. Yoshizawa and C. Adachi, *J. Chem. Theory Comput.*, 2013, **9**, 3872-3877.
14. T. J. Penfold, *J. Phys. Chem. C*, 2015, **119**, 13535-13544.
15. H. Sun, C. Zhong and J. L. Brédas, *J. Chem. Theory Comput.*, 2015, **11**, 3851-3858.
16. M. Moral, L. Muccioli, W. J. Son, Y. Olivier and J. C. Sancho-Garcia, *J. Chem. Theory Comput.*, 2015, **11**, 168-177.
17. J. P. Perdew and K. Schmidt, *AIP Conf. Proc.*, 2001, **577**, 1-20.
18. L. Kronik, T. Stein, S. Refaely-Abramson and R. Baer, *J. Chem. Theory Comput.*, 2012, **8**, 1515-1531.
19. C. Hättig and F. Weigend, *J. Chem. Phys.*, 2000, **113**, 5154-5161.
20. Y. Kaizu, H. Maekawa and H. Kobayashi, *J. Phys. Chem.*, 1986, **90**, 4234-4238.
21. W. Ni, G. G. Gurzadyan, J. Zhao, Y. Che, X. Li and L. Sun, *J. Chem. Phys. Lett.*, 2019, **10**, 2428-2433.
22. X. Miao, W. Hu, T. He, H. Tao, Q. Wang, R. Chen, L. Jin, H. Zhao, X. Lu, Q. Fan and W. Huang, *Chem. Sci.*, 2019, **10**, 3096-3102.
23. J. Zhao, K. Xu, W. Yang, Z. Wang and F. Zhong, *Chem. Soc. Rev.*, 2015, **44**, 8904-8939.
24. K. Plaetzer, B. Krammer, J. Berlanda, F. Berr and T. Kiesslich, *Lasers Med. Sci.*, 2009, **24**, 259-268.
25. S. Ji, J. Ge, D. Escudero, Z. Wang, J. Zhao and D. Jacquemin, *J. Org. Chem.*, 2015, **80**, 5958-5963.
26. J. Zhao, K. Chen, Y. Hou, Y. Che, L. Liu and D. Jia, *Org. Biomol. Chem.*, 2018, **16**, 3692-3701.
27. K. Kawasumi, T. Wu, T. Zhu, H. S. Chae, T. Van Voorhis, M. A. Baldo and T. M. Swager, *J. Am. Chem. Soc.*, 2015, **137**, 11908-11911.
28. C. Y. Chan, L. S. Cui, J. U. Kim, H. Nakanotani and C. Adachi, *Adv. Funct. Mater.*, 2018, **28**, 1706023.
29. F. Ni, Z. Wu, Z. Zhu, T. Chen, K. Wu, C. Zhong, K. An, D. Wei, D. Ma and C. Yang, *J. Mater. Chem. C*, 2017, **5**, 1363-1368.
30. P. Rajamalli, N. Senthilkumar, P. Gandeepan, C. C. Ren-Wu, H. W. Lin and C. H. Cheng, *ACS Appl. Mater. Interfaces*, 2016, **8**, 27026-27034.
31. B. Zhao, G. Xie, H. Wang, C. Han and H. Xu, *Chemistry*, 2019, **25**, 1010-1017.
32. H.-Y. Liu, P.-J. Wu, S.-Y. Kuo, C.-P. Chen, E.-H. Chang, C.-Y. Wu and Y.-H. Chan, *J. Am. Chem. Soc.*, 2015, **137**, 10420-10429.
33. Y. Zhao and D. G. Truhlar, *Theor. Chem. Acc.*, 2008, **120**, 215-241.
34. G. W. Trucks, M. J. Frisch, H. B. Schlegel, G. E. Scuseria, M. A. Robb, J. R. Cheeseman, G. Scalmani, V. Barone, B. Mennucci, G. A. Petersson, H. Nakatsuji, M. Caricato, X. Li, H. P. Hratchian, A. F. Izmaylov, J. Bloino, G. Zheng, J. L. Sonnenberg, M. Hada, M. Ehara, K. Toyota, R. Fukuda, J. Hasegawa, M. Ishida, T. Nakajima, Y. Honda, O. Kitao, H. Nakai, T. Vreven, J. A. Montgomery, Jr., J. E. Peralta, F. Ogliaro, M. Bearpark, J. J. Heyd, E. Brothers, K. N. Kudin, V. N. Staroverov, T. Keith, R. Kobayashi,

J. Normand, K. Raghavachari, A. Rendell, J. C. Burant, S. S. Iyengar, J. Tomasi, M. Cossi, N. Rega, J. M. Millam, M. Klene, J. E. Knox, J. B. Cross, V. Bakken, C. Adamo, J. Jaramillo, R. Gomperts, R. E. Stratmann, O. Yazyev, A. J. Austin, R. Cammi, C. Pomelli, J. W. Ochterski, R. L. Martin, K. Morokuma, V. G. Zakrzewski, G. A. Voth, P. Salvador, J. J. Dannenberg, S. Dapprich, A. D. Daniels, O. Farkas, J. B. Foresman, J. V. Ortiz, J. Cioslowski, and D. J. Fox, Gaussian, Inc., Wallingford CT, 2016.

35. Turbomole v7.3.1, University of Karlsruhe and Forschungszentrum Karlsruhe GmbH, 1989−2007, TURBOMOLE GmbH, Since 2007.2019.
36. M. Schreiber, M. R. Silva-Junior, S. P. Sauer and W. Thiel, *J. Chem. Phys.*, 2008, **128**, 134110.
37. A. Hellweg, S. A. Grün and C. Hättig, *Phys. Chem. Chem. Phys.*, 2008, **10**, 4119-4127.
38. D. Jacquemin, I. Duchemin and X. Blase, *J. Chem. Theory Comput.*, 2015, **11**, 5340-5359.
39. A. Tajti and P. G. Szalay, *J. Chem. Theory Comput.*, 2019, **15**, 5523-5531.
40. J.-D. Chai and M. Head-Gordon, *Phys. Chem. Chem. Phys.*, 2008, **10**, 6615-6620.
41. Q. Zhang, B. Li, S. Huang, H. Nomura, H. Tanaka and C. Adachi, *Nat. Photon.*, 2014, **8**, 326-332.
42. M. J. G. Peach and D. J. Tozer, *J. Phys. Chem. A*, 2012, **116**, 9783-9789.
43. B. Moore, H. Sun, N. Govind, K. Kowalski and J. Autschbach, *J. Chem. Theory Comput.*, 2015, **11**, 3305-3320.
44. M. Miura, Y. Aoki and B. Champagne, *J. Chem. Theory Comput.*, 2007, **127**, 084103.
45. M. J. Peach, M. J. Williamson and D. J. Tozer, *J. Chem. Theory Comput.*, 2011, **7**, 3578-3585.
46. B. Moore Ii, R. L. Schrader, K. Kowalski and J. Autschbach, *ChemistryOpen*, 2017, **6**, 385-392.

2.5. *Supporting information*

2.5.1. Signed error plots (TDDFT/TDA)

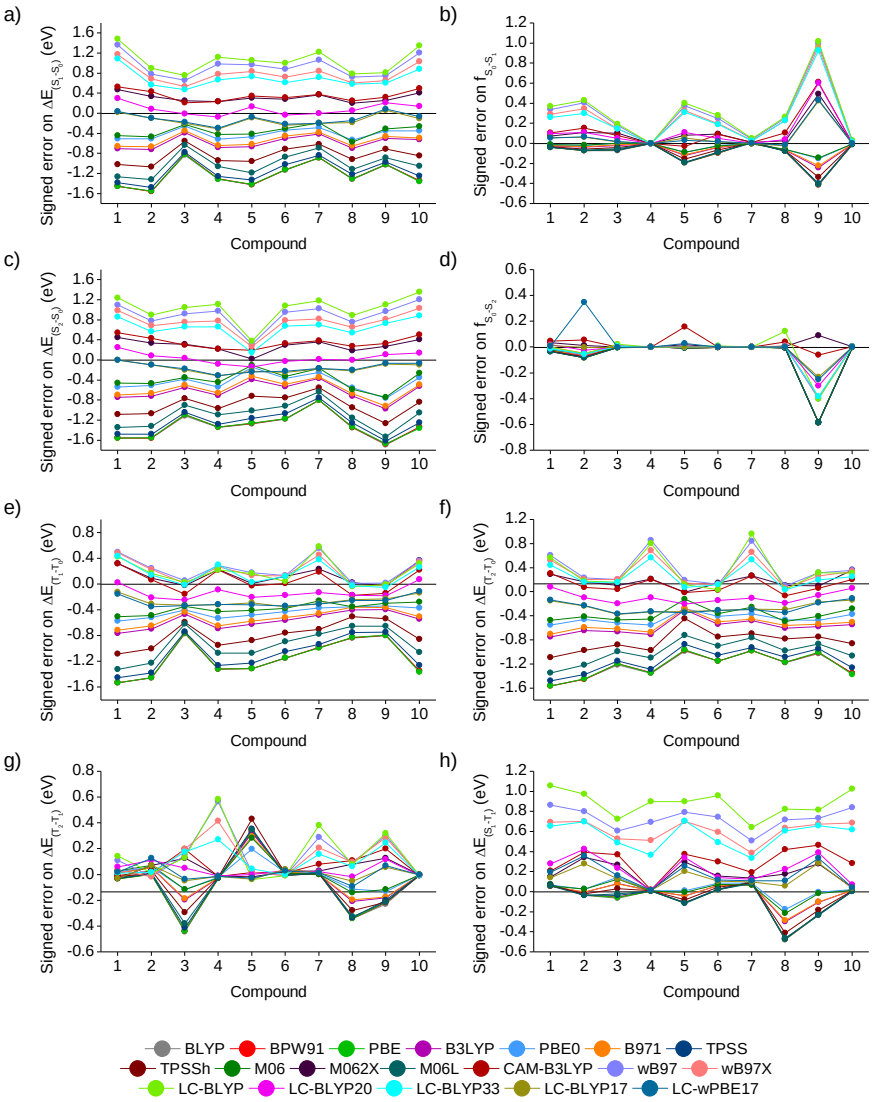

Figure S2.1: Signed errors on each property for each individual XC functional for all 10 compounds obtained using TDDFT/TDA. a) First vertical singlet excitation energy, $\Delta E_{S_0-S_1}$. b) Oscillator strength for the first singlet excitation, $f_{S_0-S_1}$. c) Second vertical singlet excitation energy, $\Delta E_{S_2-S_0}$. d) Oscillator strength for the second vertical singlet excitation, $f_{S_0-S_2}$. e) First vertical triplet excitation energy, $\Delta E_{T_1-S_0}$. f) Second vertical triplet excitation energy, $\Delta E_{T_2-S_0}$. g) Triplet-triplet energy gap for the first two triplet excited states, $\Delta E_{T_2-T_1}$. h) Singlet-triplet gap for the first singlet and triplet excited states, $\Delta E_{S_1-T_1}$.

Table S2.1: Statistical analysis including mean signed errors (MSEs, eV) and standard deviations (eV) obtained from the comparison between TDDFT calculations with different XCFs and riCC2 reference values.

	$\Delta E_{S_0-S_1}$ (eV)		$f_{S_0-S_1}$		$\Delta E_{S_0-S_2}$ (eV)		$f_{S_0-S_2}$		$\Delta E_{S_0-T_1}$ (eV)		$\Delta E_{S_0-T_2}$ (eV)		$\Delta E_{T_1-T_2}$ (eV)		$\Delta E_{S_1-T_1}$ (eV)	
	MSE	Std Dev	MSE	Std Dev	MSE	Std Dev	MSE	Std Dev	MSE	Std Dev	MSE	Std Dev	MSE	Std Dev	MSE	Std Dev
BLYP	-1.242	0.213	-0.116	0.144	-1.329	0.231	-0.072	0.173	-1.153	0.265	-1.224	0.190	-0.070	0.201	-0.094	0.157
BPW91	-1.236	0.216	-0.113	0.143	-1.322	0.230	-0.072	0.173	-1.153	0.266	-1.220	0.193	-0.067	0.201	-0.090	0.157
PBE	-1.238	0.216	-0.113	0.143	-1.322	0.229	-0.072	0.173	-1.153	0.268	-1.225	0.195	-0.072	0.209	-0.090	0.157
M06L	-1.021	0.202	-0.109	0.138	-1.102	0.237	-0.072	0.173	-0.952	0.224	-1.005	0.178	-0.053	0.187	-0.069	0.148
TPSS	-1.166	0.204	-0.110	0.139	-1.244	0.223	-0.069	0.173	-1.090	0.251	-1.151	0.188	-0.062	0.198	-0.081	0.153
TPSSh	-0.850	0.149	-0.095	0.119	-0.904	0.191	-0.072	0.173	-0.820	0.158	-0.845	0.157	-0.025	0.177	-0.032	0.110
B3LYP	-0.596	0.110	-0.074	0.089	-0.628	0.172	-0.070	0.173	-0.610	0.086	-0.605	0.112	0.005	0.118	0.014	0.071
B971	-0.555	0.102	-0.068	0.083	-0.583	0.169	-0.070	0.173	-0.566	0.083	-0.563	0.105	0.003	0.111	0.012	0.069
PBE0	-0.430	0.089	-0.053	0.064	-0.445	0.164	-0.006	0.258	-0.526	0.068	-0.482	0.080	0.043	0.063	0.096	0.070
M06	-0.379	0.106	-0.050	0.057	-0.399	0.179	-0.068	0.173	-0.460	0.089	-0.430	0.091	0.030	0.041	0.081	0.068
M062X	0.283	0.102	0.084	0.107	0.246	0.132	-0.014	0.054	0.044	0.176	0.114	0.117	0.071	0.090	0.239	0.112
ωB97	0.882	0.239	0.254	0.233	0.850	0.238	-0.022	0.173	-0.381	0.208	-0.056	0.423	0.325	0.349	1.263	0.161
ωB97X	0.740	0.215	0.225	0.224	0.713	0.203	-0.047	0.141	-0.304	0.195	-0.006	0.373	0.299	0.321	1.044	0.142
CAM-B3LYP	0.311	0.124	0.100	0.145	0.316	0.118	-0.009	0.096	-0.332	0.177	-0.136	0.232	0.196	0.181	0.643	0.119
LC-ωPBE17	-0.136	0.109	0.045	0.104	-0.182	0.086	-0.039	0.120	-0.344	0.099	-0.302	0.086	0.042	0.063	0.209	0.127
LC-BLYP17	-0.157	0.106	0.044	0.100	-0.192	0.085	-0.039	0.116	-0.314	0.089	-0.287	0.079	0.027	0.051	0.156	0.102
LC-BLYP20	0.056	0.118	0.086	0.138	0.009	0.105	-0.042	0.132	-0.215	0.129	-0.147	0.094	0.068	0.076	0.270	0.136
LC-BLYP33	0.650	0.192	0.210	0.211	0.600	0.195	-0.053	0.139	-0.218	0.178	0.009	0.305	0.227	0.239	0.868	0.125
LC-BLYP	0.978	0.264	0.270	0.236	0.956	0.262	0.010	0.235	-0.623	0.239	-0.244	0.494	0.379	0.377	1.601	0.187
LC-BLYP20-M062X	—	—	—	—	—	—	—	—	—	—	—	—	—	—	0.012	0.179

Table S2.2: Statistical analysis including mean signed errors (MSEs, eV) and standard deviations (eV) obtained from the comparison between TDDFT/TDA calculations with different XCFs and riCC2 reference values.

	$\Delta E_{S_0-S_1}$ (eV)		$f_{S_0-S_1}$		$\Delta E_{S_0-S_2}$ (eV)		$f_{S_0-S_2}$		$\Delta E_{S_0-T_1}$ (eV)		$\Delta E_{S_0-T_2}$ (eV)		$\Delta E_{T_1-T_2}$ (eV)		$\Delta E_{S_1-T_1}$ (eV)	
	MSE	Std Dev	MSE	Std Dev	MSE	Std Dev	MSE	Std Dev	MSE	Std Dev	MSE	Std Dev	MSE	Std Dev	MSE	Std Dev
BLYP	-1.220	0.226	-0.096	0.120	-1.318	0.242	-0.071	0.173	-1.148	0.269	-1.222	0.191	-0.074	0.205	-0.072	0.161
BPW91	-1.214	0.229	-0.093	0.119	-1.310	0.242	-0.071	0.173	-1.146	0.272	-1.217	0.194	-0.071	0.205	-0.067	0.162
PBE	-1.215	0.229	-0.093	0.119	-1.311	0.241	-0.071	0.173	-1.147	0.273	-1.218	0.196	-0.070	0.206	-0.068	0.162
M06L	-1.001	0.213	-0.093	0.118	-1.092	0.245	-0.072	0.173	-0.932	0.240	-0.992	0.184	-0.060	0.195	-0.069	0.157
TPSS	-1.144	0.216	-0.091	0.116	-1.236	0.236	-0.071	0.173	-1.079	0.259	-1.143	0.193	-0.064	0.202	-0.065	0.160
TPSSh	-0.828	0.160	-0.075	0.098	-0.894	0.198	-0.070	0.173	-0.784	0.190	-0.818	0.171	-0.034	0.196	-0.044	0.142
B3LYP	-0.574	0.120	-0.055	0.071	-0.618	0.177	-0.069	0.173	-0.560	0.122	-0.580	0.122	-0.020	0.148	-0.014	0.109
B971	-0.533	0.113	-0.050	0.065	-0.573	0.173	-0.068	0.173	-0.520	0.116	-0.540	0.115	-0.019	0.138	-0.013	0.105
PBE0	-0.407	0.099	-0.035	0.048	-0.435	0.168	-0.066	0.174	-0.436	0.079	-0.444	0.082	-0.008	0.093	0.028	0.080
M06	-0.356	0.113	-0.035	0.045	-0.389	0.182	-0.067	0.173	-0.372	0.079	-0.371	0.113	0.001	0.115	0.015	0.086
M062X	0.322	0.088	0.100	0.137	0.289	0.116	0.017	0.026	0.136	0.135	0.176	0.103	0.040	0.056	0.187	0.104
ωB97	0.966	0.208	0.287	0.274	0.903	0.234	-0.044	0.120	0.236	0.183	0.385	0.269	0.149	0.177	0.731	0.103
ωB97X	0.812	0.187	0.255	0.265	0.758	0.199	-0.041	0.117	0.199	0.179	0.322	0.213	0.123	0.141	0.612	0.100
CAM-B3LYP	0.356	0.105	0.113	0.175	0.351	0.109	0.025	0.054	0.053	0.168	0.113	0.118	0.060	0.080	0.303	0.127
LC-ωPBE17	-0.103	0.116	0.062	0.127	-0.153	0.091	0.014	0.136	-0.273	0.078	-0.264	0.089	0.010	0.056	0.171	0.109
LC-BLYP17	-0.125	0.113	0.061	0.125	-0.164	0.090	-0.022	0.071	-0.262	0.075	-0.261	0.079	0.001	0.042	0.137	0.090
LC-BLYP20	0.096	0.119	0.107	0.171	0.040	0.106	-0.029	0.091	-0.130	0.098	-0.094	0.095	0.036	0.047	0.226	0.130
LC-BLYP33	0.721	0.168	0.241	0.254	0.645	0.194	-0.043	0.115	0.157	0.168	0.255	0.184	0.098	0.101	0.563	0.127
LC-BLYP	1.073	0.230	0.305	0.280	1.030	0.254	-0.029	0.130	0.190	0.191	0.351	0.307	0.160	0.195	0.883	0.125
LC-BLYP20-M062X	—	—	—	—	—	—	—	—	—	—	—	—	—	—	-0.040	0.170

2.5.3. Optimized geometries and HOMO/LUMO topologies

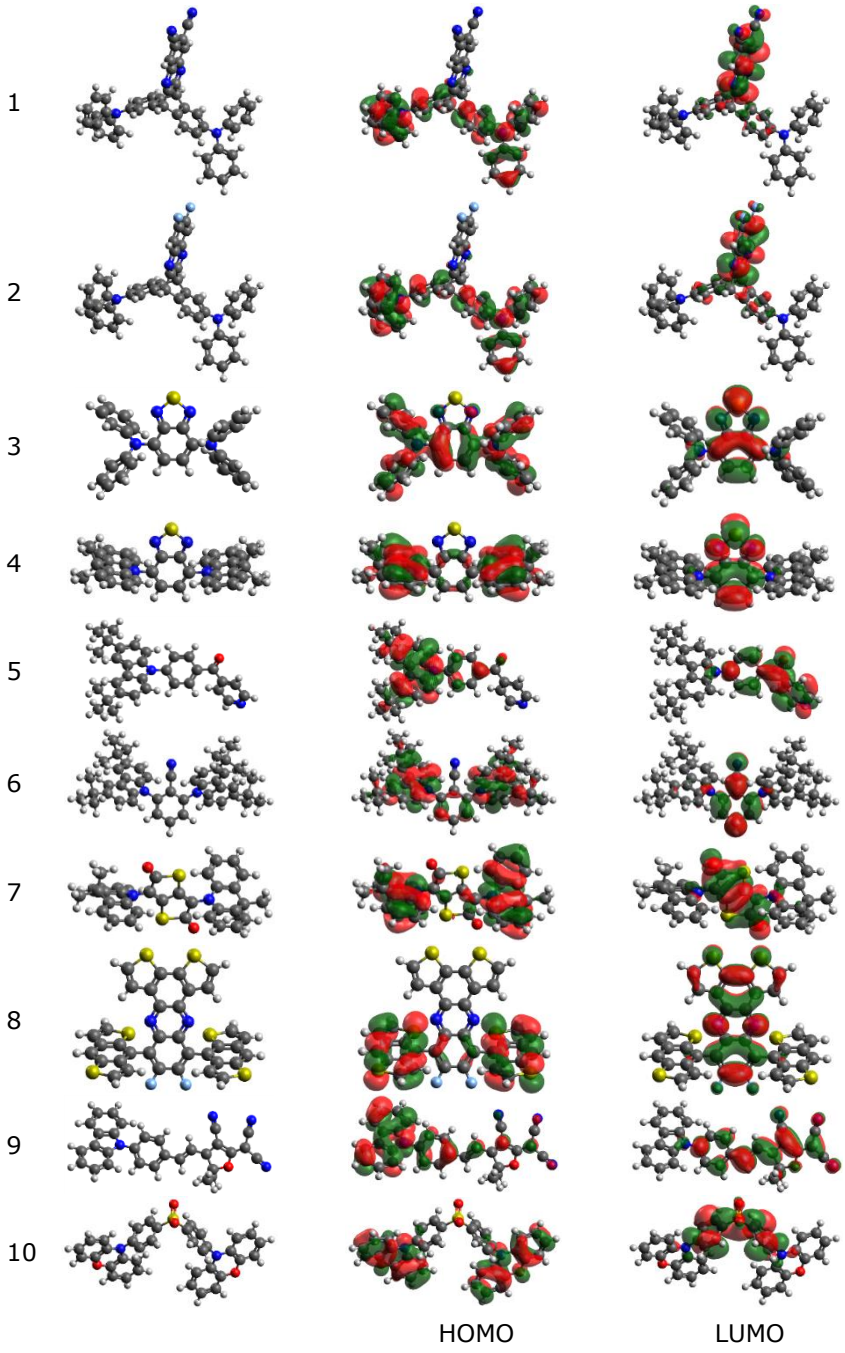

Figure S2.2: Optimized geometries and HOMO and LUMO topologies for all compounds (calculated using M06 and 6-311G(d)). Isocontour value = 0.02 a.u. for all orbitals.

2.5.4. TDDFT versus riCC2 correlation plots

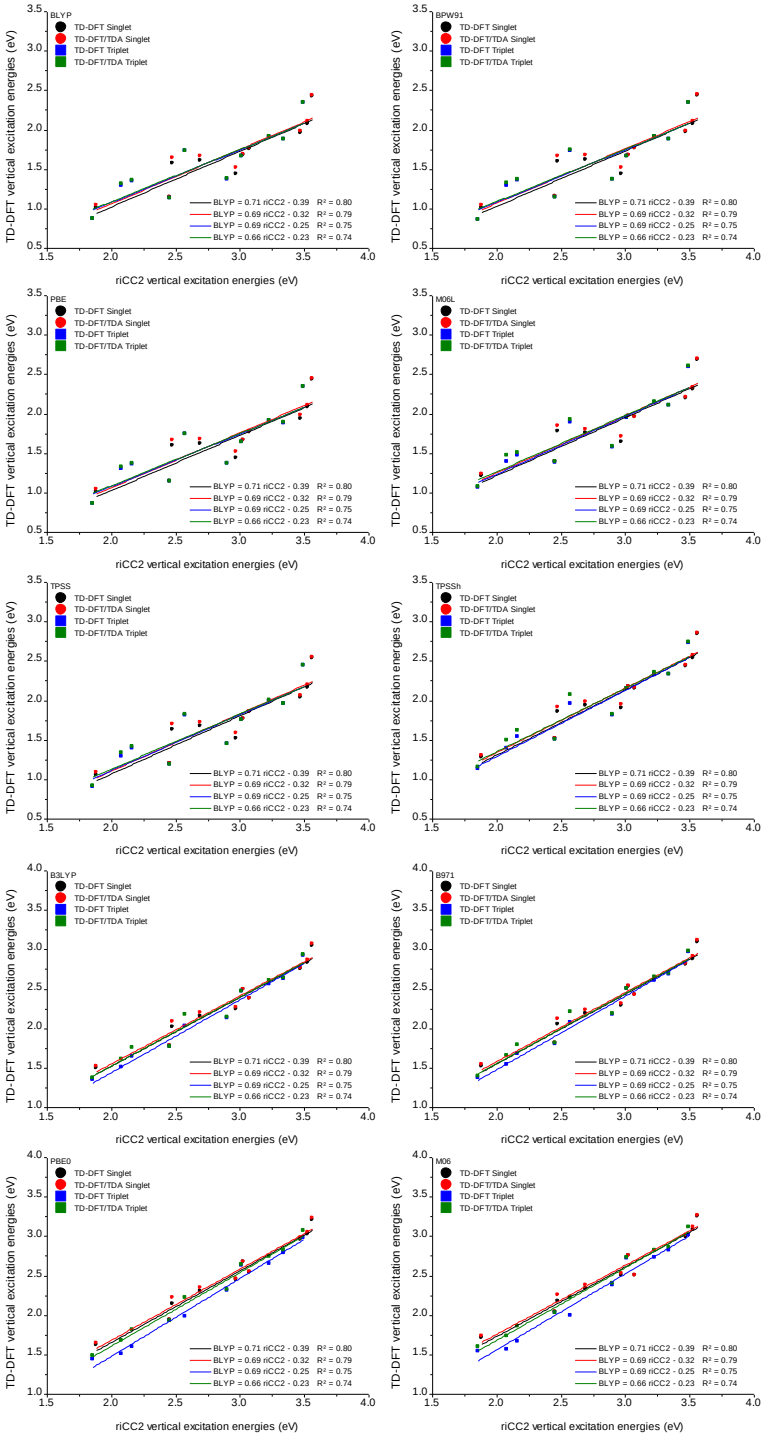

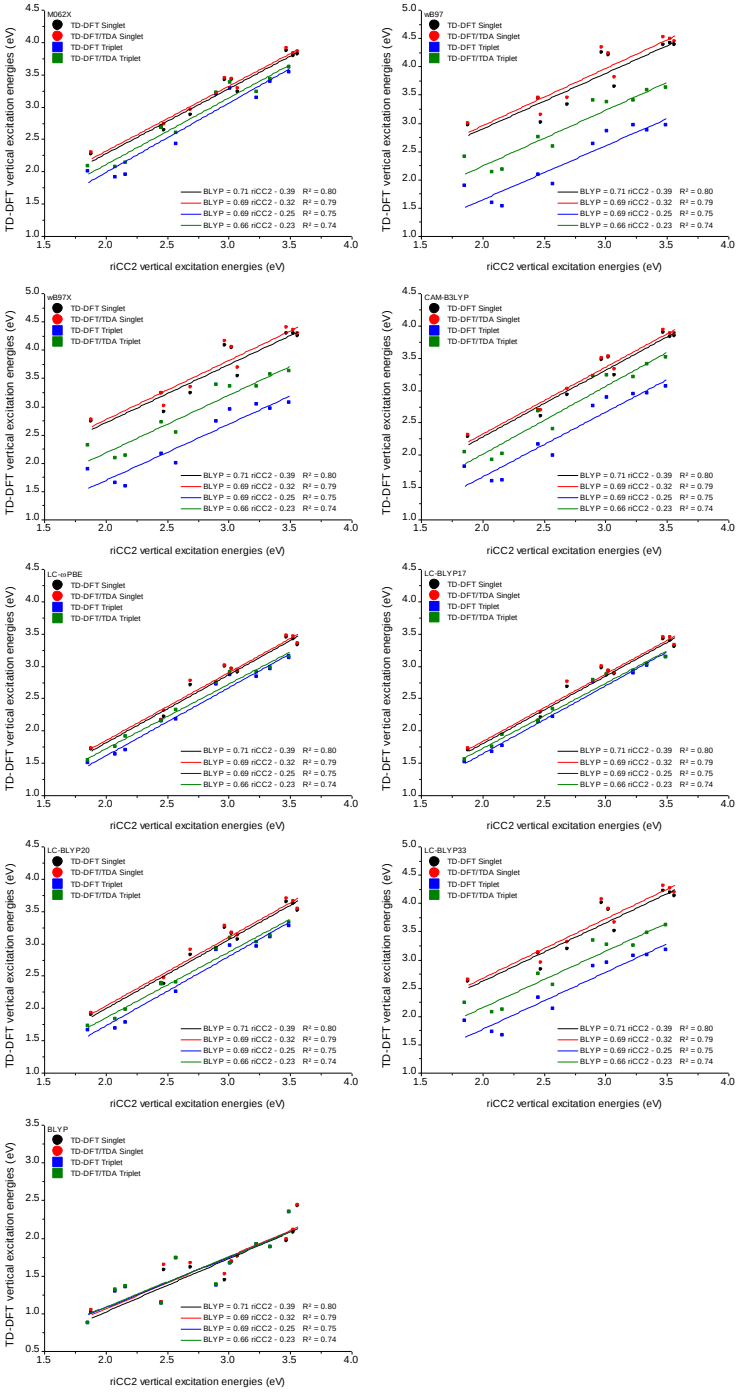

Figure S2.3: TDDFT versus riCC2 excitation energies as determined with different exchange-correlation functionals.

2.5.5. Experimental section

2.5.5.1. Materials and methods

Unless stated otherwise, all reagents and chemicals were obtained from commercial sources and used without further purification. Compounds **1**[1], **3-6**,[2-4] and **9**[5] were synthesized according to their respective literature procedures. Compound **10** was obtained from Lumtech Inc (LT-N545).

Preparative (recycling) size exclusion chromatography (prep-SEC) was performed on a JAI LC-9110 NEXT system equipped with JAIGEL 1H and 2H columns (eluent $CHCl_3$, flow rate 3.5 mL min^{-1}). It was used to purify all synthesized compounds before performing any further analysis. NMR measurements were performed in $CDCl_3$ on 400 MHz instruments (Varian or Jeol). The chemical shifts (δ, in ppm) were determined relative to the residual $CHCl_3$ (7.26 ppm) proton signals. MALDI-ToF mass spectra were recorded on a Bruker Daltonics Ultraflex II Tof/Tof. 1 µL of the matrix solution (16 mg mL^{-1} *trans*-2-[3-(4-*tert*-butylphenyl)-2-methyl-2-propenylidene]malononitrile in $CHCl_3$) was spotted onto an MTP Anchorchip 600/384 MALDI plate. The spot was allowed to dry and 1 µL of the analyte solution (0.5 mg mL^{-1} in $CHCl_3$) was spotted on top of the matrix.

2.5.5.2. Synthesis procedures

Synthesis of TPA-QNX(F)2 (2)

(9*R*,10*R*)-2,6-bis(diphenylamino)-9,10-dihydro-9,10-ethanoanthracene-11,12-dione (TPA-DK) was synthesised according to literature.[1] TPA-DK (68.3 mg, 0.12 mmol) and 4,5-difluoro-1,2-benzenediamine (20.6 mg, 0.14 mmol) were heated to reflux for 1 h in ethanol/acetic acid (10 mL, 19/1). Orange crystals were formed at an early stage of the reaction. After the reaction, the mixture was cooled down to room temperature. The crystals were collected by filtration, washed with ethanol and dried under reduced pressure to obtain TPA-QNX(F)2 (19.7 mg, 24%). ^{1}H NMR (400 MHz, $CDCl_3$): 7.67 (t, *J* = 9.3 Hz, 2H), 7.29 (d, *J* = 8.1 Hz, 2H), 7.25-7.18 (m, 10H), 7.06-6.98 (m, 12H), 6.82 (dd, *J* = 8.1, 2.2 Hz, 2H), 5.34 (s, 2H). ^{13}C NMR (100 MHz, $CDCl_3$): 158.12, 152.90/152.73/150.36/150.19 (dd, *J* = 255.5, 17.3 Hz), 147.56, 146.85, 142.97, 136.29/136.23/136.17 (t, *J* = 5.9 Hz), 134.90, 129.39, 125.64, 124.74, 123.24, 121.19, 119.76, 114.81/114.74/114.68/114.62 (dd, *J* = 12.6, 6.8 Hz), 54.48. MS (ESI+) Calcd. for $C_{46}H_{30}F_2N_4$ [M]+: *m/z* 676.244, found: 676.240.

Synthesis of TTD-DMAC (7)

3,6-bis(9,9-dimethylacridin-10(9H)-yl)thieno[3,2-b]thiophene (DMAC-TT)

3,6-Dibromothieno[3,2-*b*]thiophene (504.8 mg, 1.69 mmol), 9,9-dimethyl-9,10-dihydroacridine (737.1 mg, 3.52 mmol), palladium(II) acetate (22.9 mg, 0.10 mmol), XPhos (84.2 mg, 0.18 mmol) and sodium *tert*-butoxide (339.2 mg, 3.53 mmol) were dissolved in dry toluene under argon atmosphere (12 mL) in a flame-dried Schlenk tube. The mixture was stirred at 110 °C for 24 h and then cooled down to room temperature. The reaction mixture was poured into water and extracted with CH_2Cl_2. The organic phase was dried over anhydrous $MgSO_4$, filtered and concentrated under reduced pressure. The crude product was purified by silica gel column chromatography with CH_2Cl_2/petroleum ether (v/v = 20/80) as the eluent. The obtained solid was further purified by trituration in isopropanol, filtered and washed with CH_2Cl_2. The product was obtained as a white solid (456.7 mg, 49%). ^{1}H NMR (400 MHz, $CDCl_3$): 7.52 (dd, *J* = 7.7, 1.6 Hz, 4H), 7.51 (s, 2H), 7.11 (ddd, *J* = 8.3, 7.3, 1.6 Hz, 4H), 7.03 (td, *J* = 7.5, 1.3 Hz, 4H), 6.64 (dd, *J* = 8.2, 1.3 Hz, 4H), 1.74 (s, 12H). ^{13}C NMR (100 MHz, $CDCl_3$): 139.78, 137.41, 132.43, 131.10, 127.70, 126.80, 125.17, 121.58, 114.02, 36.15, 30.51.

10,10'-(2,5-bis(4,4,5,5-tetramethyl-1,3,2-dioxaborolan-2-yl)thieno[3,2-b]thiophene-3,6-diyl)bis(9,9-dimethyl-9,10-dihydroacridine) (DMAC-TT-pinacol)[6]

DMAC-TT (199.0 mg, 0.36 mmol), bis(pinacolato)diboron (276.7 mg, 1.09 mmol), 4,4'-di-*tert*-butyl-2,2'-bipyridine (22.5 mg, 0.08 mmol), and $[Ir(OMe)(COD)]_2$ (28.1 mg, 0.04 mmol) were added to a flame-dried Schlenk under argon atmosphere and subsequently dry cyclohexane (10 mL) was added. The resulting mixture was stirred at 80 °C for 15 h in the dark. After cooling down to room temperature, the reaction mixture was poured in water and the organic material was extracted using CH_2Cl_2. The organic layer was washed with brine and dried over $MgSO_4$. After removing the solvent under reduced pressure, the residue was purified by silica gel column chromatography with CH_2Cl_2 to afford the product as a beige solid (156.4 mg, 54%). ^{1}H NMR (400 MHz, $CDCl_3$): 7.48 (dd, *J* = 7.7, 1.6 Hz, 4H), 7.02 (ddd, *J* = 8.2, 7.2, 1.6 Hz, 4H), 6.94 (td, *J* = 7.4, 1.3 Hz, 4H), 6.39 (dd, *J* = 8.1, 1.3 Hz, 4H), 1.86 (s, br, 6H), 1.66 (s, br, 6H), 0.99 (s, 24H). ^{13}C NMR (100 MHz, $CDCl_3$): 144.08, 139.98, 134.43 (br),

130.37, 126.52, 125.13, 120.67, 113.75, 84.10, 53.48, 36.05, 33.92 (br), 29.29 (br), 24.39.

3,6-bis(9,9-dimethylacridin-10(9H)-yl)thieno[3,2-b]thiophene-2,5-dione (TTD-DMAC)[6]

To a solution of DMAC-TT-pinacol (152.0 mg, 0.19 mmol) in THF (10 mL) and H_2O (1 mL) was added Oxone (372.8 mg, 0.61 mmol) in one portion at room temperature. The mixture was stirred at room temperature for 3 h in the dark, and then quenched with $Na_2S_2O_3$ (aq.). The organic layer was extracted with hexanes, washed with water and dried over $MgSO_4$. After evaporation of the solvent, the residue was purified by silica gel column chromatography with CH_2Cl_2/petroleum ether (v/v= 20/80) to give TTD-DMAC (18.9 mg, 17%) as a dark green/black solid. ^{1}H NMR (400 MHz, $CDCl_3$): 7.52 (dd, *J* = 7.8, 1.5 Hz, 4H), 7.23 (ddd, *J* = 8.1, 7.3, 1.5 Hz, 4H), 7.11 (td, *J* = 7.5, 1.2 Hz, 4H), 6.76 (dd, *J* = 8.1, 1.2 Hz, 4H), 1.69 (s, 12H). ^{13}C NMR (100 MHz, $CDCl_3$): 183.17, 155.48, 137.69, 133.24, 132.17, 127.12, 125.89, 123.08, 114.18, 36.19, 30.63. MS (MALDI-TOF) Calcd. for $C_{36}H_{28}N_2O_2S_2$ [M]+: *m/z* 584.159, found: 584.165.

Synthesis of DTBQx-BDT-TIPS (8)

2,6-bis(triisopropylsilyl)benzo[1,2-b:4,5-b']dithiophene (BDT-TIPS)[7]

To a solution of benzo[1,2-*b*:4,5-*b*']dithiophene (1.26 g, 6.63 mmol) in THF (10.0 mL), *n*-BuLi (2.5 M in hexane; 8.0 mL, 19.89 mmol) was added dropwise at 0 °C and the mixture was stirred for 1 h at room temperature. Afterwards, triisopropylsilyl chloride (4.2 mL, 19.6 mmol) was slowly added. After the mixture was heated to reflux for 16 h, it was poured out in a beaker containing water (100 mL) and hydrochloric acid (1 M, 100 mL). The resulting precipitate was collected by vacuum filtration and washed with water, methanol and *n*-hexane. The filtrate was then evaporated under reduced pressure and the remaining solid was triturated in *n*-hexane, followed by filtration and subsequent washing with *n*-hexane. BDT-TIPS was obtained as a white solid (2.49 g, 75%). ^{1}H NMR (400 MHz, $CDCl_3$): 8.30 (s, 2H), 7.50 (s, 2H), 1.48-1.37 (m, 6H), 1.16 (d, *J* = 7.4 Hz, 36H). ^{13}C NMR (100 MHz, $CDCl_3$): 140.62, 138.95, 138.31, 131.55, 115.63, 18.66, 11.85.

(4-(4,4,5,5-tetramethyl-1,3,2-dioxaborolan-2-yl)benzo[1,2-b:4,5-b']dithiophene-2,6-diyl)bis(triisopropylsilane) (BDT-TIPS-pinacol)[7]

A mixture of BDT-TIPS (1.635 g 3.25 mmol), bis(pinacolato)diboron (1.48 g, 5.81 mmol), $[Ir(OMe)(COD)]_2$ (107.2 mg, 0.16 mmol), and 4,4'-di-*tert*-butyl-2,2'-bipyridine (94.8 mg, 0.35 mmol) in dry cyclohexane was stirred in the dark at 80 °C for 16 h under nitrogen atmosphere. After cooling down to room temperature, evaporation of the solvent under reduced pressure gave a residue, which was purified by silica gel column chromatography with CH_2Cl_2/petroleum ether (v/v= 20/80) to yield BDT-TIPS-pinacol as a white solid (555.3 mg, 27%). The reaction also yields unreacted BDT-TIPS as well as disubstituted BDT-TIPS-pinacol as the main side products. ^{1}H NMR (400 MHz, $CDCl_3$): 8.39 (s, 1H), 8.35 (s, 1H), 7.52 (s, 1H), 1.47 (s, 12H), 1.50-1.39 (m, 6H), 1.19 (d, *J* = 7.4 Hz, 36H). ^{13}C NMR (100 MHz, $CDCl_3$): 148.3, 144.0, 140.0, 138.7, 138.0, 137.7, 134.1, 130.8, 118.1, 116.0, 83.7, 24.8, 18.4, 11.6.

1,2-di(thiophen-3-yl)ethane-1,2-dione

3-Bromothiophene (2.34 mL, 24.69 mmol) was added dropwise to a solution of *n*-BuLi (2.5 M in *n*-hexane; 11.0 mL, 27.50 mmol) in THF (50 mL) and the resulting mixture was stirred at −78 °C for 1 h. The reaction mixture was subsequently added to a homogeneously stirred suspension of CuBr (3.59 g, 25.03 mmol) and LiBr (4.34 g, 49.98 mmol) in THF (50 mL) at 0 °C and the mixture was stirred for 1 h at this temperature. After dropwise addition of oxalyl chloride (1.1 mL, 12.57 mmol), the reaction mixture was again stirred for 1 h at 0 °C. The reaction was quenched with a saturated aqueous NH_4Cl solution (40 mL). After partial removal of the reaction solvent under reduced pressure, the product was extracted with hexanes and the organic phase was washed with a saturated aqueous NH_4Cl solution, water and brine. The organic phase was dried over $MgSO_4$, filtered and the solvent was removed under reduced pressure. The residue was purified by silica gel column chromatography with CH_2Cl_2/petroleum ether (v/v= 50/50) to give a yellow crystalline product (2.11 g, 76%). ^{1}H NMR (400 MHz, $CDCl_3$): 8.36 (dd, *J* = 2.9, 1.2 Hz, 2H), 7.70 (dd, *J* = 5.1, 1.2 Hz, 2H), 7.40 (dd, *J* = 5.1, 2.9 Hz, 2H).

benzo[2,1-b:3,4-b']dithiophene-4,5-dione

To a stirring solution of 1,2-di(thiophen-3-yl)ethane-1,2-dione (1.00 g, 4.50 mmol) in CH_2Cl_2 (200 mL), a solution of $FeCl_3$ (2.92 g, 18.00 mmol) in nitromethane (25 mL) was added dropwise. The reaction mixture was stirred for at room temperature for 3 h after which the reaction was quenched with a 1 M aqueous HCl solution (50 mL). The product was extracted with chloroform and washed with a 1 M aqueous HCl solution, water and brine. The organic phase dried over $MgSO_4$, filtered and the solvent was removed under reduced pressure. The residue was purified by silica gel column chromatography using chloroform as the eluent and after evaporation of the solvent under reduced pressure, a black crystalline product was obtained (0.60 g, 61%). ^{1}H NMR (400 MHz, $CDCl_3$): 7.50 (d, *J* = 5.2 Hz, 2H), 7.21 (d, *J* = 5.2 Hz, 2H).

3,6-dibromo-4,5-difluorobenzene-1,2-diamine

1,4-Dibromo-2,3-difluoro-5,6-dinitrobenzene[8] (1.00 g, 2.76 mmol) and iron powder (2.25 g, 40.29 mmol) were stirred in acetic acid (40 mL) at 45 °C for 6 h. The solution was cooled down to room temperature and then poured into a cold NaOH solution (5%, 100 mL). The product was extracted with ethyl acetate and washed with a saturated aqueous $NaHCO_3$ solution. The organic phase was collected, dried over $MgSO_4$, filtered and the solvent was removed under reduced pressure to obtain the product in a quantitative yield (0.82 g). ^{1}H NMR (400 MHz, $CDCl_3$): 5.16 (s, 4H).

8,11-dibromo-9,10-difluorodithieno[3,2-a:2',3'-c]phenazine (DTPz)

Benzo[2,1-*b*:3,4-*b'*]dithiophene-4,5-dione (0.50 g, 2.27 mmol) and 3,6-dibromo-4,5-difluorobenzene-1,2-diamine (0.69 g, 2.27 mmol) were dissolved in acetic acid (20 mL) and the resulting solution was stirred at 75 °C for 16 h. The reaction was quenched with a saturated aqueous $NaHCO_3$ solution. The product was extracted with chloroform and washed with a saturated aqueous $NaHCO_3$ solution, water and brine. The organic phase dried over $MgSO_4$, filtered and the solvent was removed under reduced pressure. The product was purified by recrystallization from CH_2Cl_2/MeOH to acquire a yellow crystalline product (0.94 g, 85%). ^{1}H NMR (400 MHz, $CDCl_3$): 8.53 (d, *J* = 5.3 Hz, 2H), 7.65 (d, *J* = 5.3 Hz, 2H).

8,11-bis(2,6-bis(triisopropylsilyl)benzo[1,2-b:4,5-b']dithiophen-4-yl)-9,10-difluorodithieno[3,2-a:2',3'-c]phenazine (DTPz-BDT-TIPS)

DTPz (90.2 mg, 186.5 µmol), BDT-TIPS-pinacol (245.0 mg, 389.6 µmol) and tetrakis(triphenylphosphine)palladium(0) (10.7 mg, 9.3 µmol) were added to a flame-dried Schlenk flask. The flask was evacuated and backfilled with nitrogen three times and pre-degassed anhydrous DMF (16 mL) and a K_2CO_3 solution (2 M, 4 mL) were added. The reaction mixture was heated at 130 °C and stirred for 24 h under a nitrogen atmosphere. The reaction mixture was poured into water, then extracted with dichloromethane and dried over $MgSO_4$, filtered and washed. After evaporation of the solvent under reduced pressure, the product was purified by silica gel column chromatography with CH_2Cl_2/petroleum ether (v/v= 20/80) as the eluent. DTPz-BDT-TIPS was further purified using preparative (recycling) GPC and was obtained as a yellow solid (60.0 mg, 24%). ^{1}H NMR (400 MHz, $CDCl_3$): 8.57 (d, *J* = 2.0 Hz, 2H), 7.70 (d, *J* = 1.9 Hz, 2H), 7.47 (dd, *J* = 5.3, 1.7 Hz, 2H), 7.23 (s, 1H), 7.16 (dd, *J* = 5.3, 2.1 Hz, 2H), 7.12 (s, 1H), 1.45-1.18 (m, 12H), 1.17-0.90 (m, 72H). ^{13}C NMR (100 MHz, $CDCl_3$): 151.72, 151.55, 149.16, 148.97, 142.74, 142.64, 140.86, 140.80, 139.19, 139.16, 138.94, 138.54, 138.48, 138.24, 138.18, 137.07, 137.03, 136.06, 134.61, 131.90, 131.76, 131.62, 131.54, 124.41, 124.34, 124.33, 124.27, 119.24, 119.18, 116.53, 77.38, 18.69, 18.66, 18.60, 18.55, 18.50, 18.46, 18.38, 11.85, 11.82, 11.76, 11.71. MS (ESI+) Calcd. for $C_{72}H_{94}F_2N_2S_6Si_4$ [M]+: *m/z* 1328.479, found: 1328.475.

2.5.6. UV-VIS absorption and emission (fluorescence) spectra

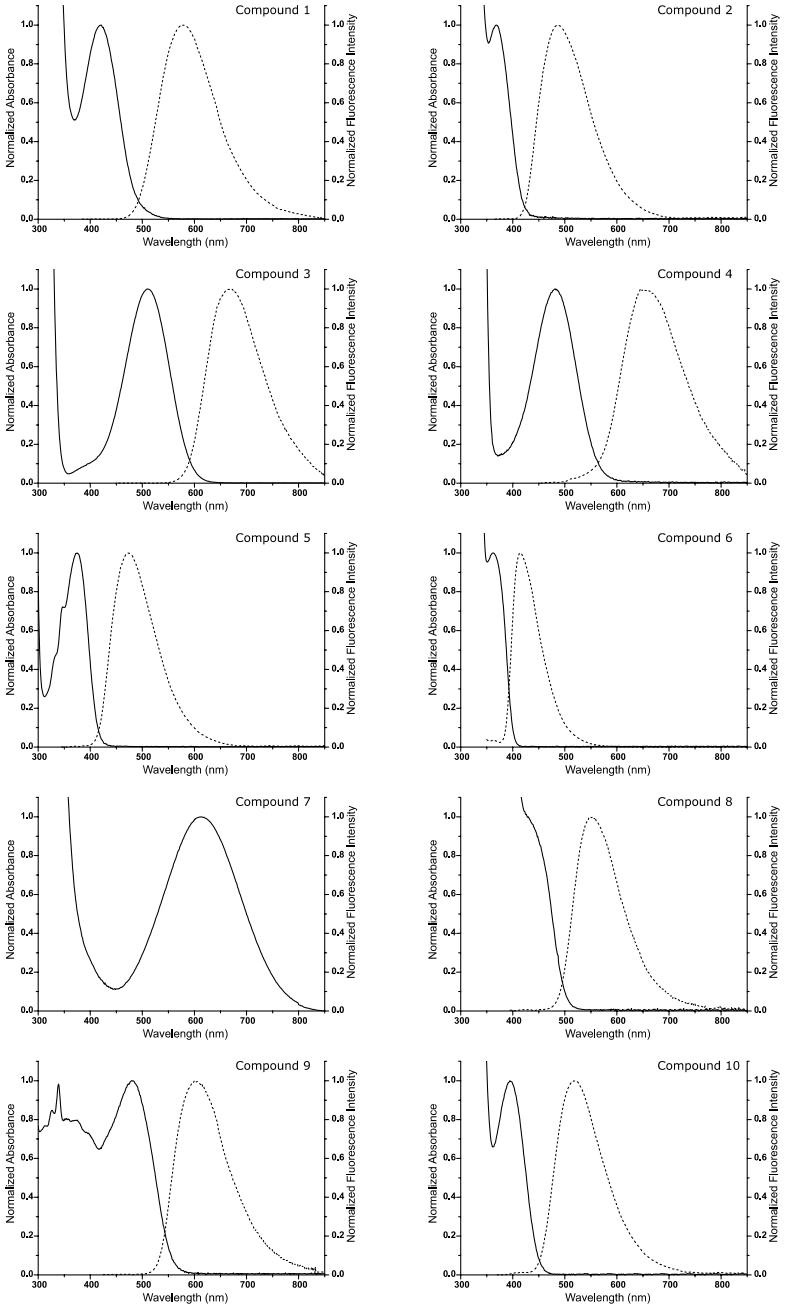

Figure S2.4: Normalized absorption spectra (solid lines) of all compounds and their corresponding normalized fluorescence spectra (dashed lines) in toluene. Spectra are normalized to their charge transfer bands.

Table S2.3: Spectroscopic data for all compounds in toluene.[a]

Compound	λ_{abs} (nm)[b]	λ_{em} (nm)[c]	$\Delta\bar{\nu}$ (cm^{-1})[d]
1	421	578	6452
2	368	486	6598
3	510	668	4638
4	481	645	5286
5	375	473	5525
6	362	414	3470
7	613	—[e]	—[e]
8	430	553	5173
9	480	602	4222
10	395	519	6049

[a] Only data on the charge transfer bands are given. [b] Charge transfer absorption maximum. [c] Charge transfer fluorescence emission maximum. [d] Stokes shift. [e] No fluorescence observed.

2.5.7. NMR spectra

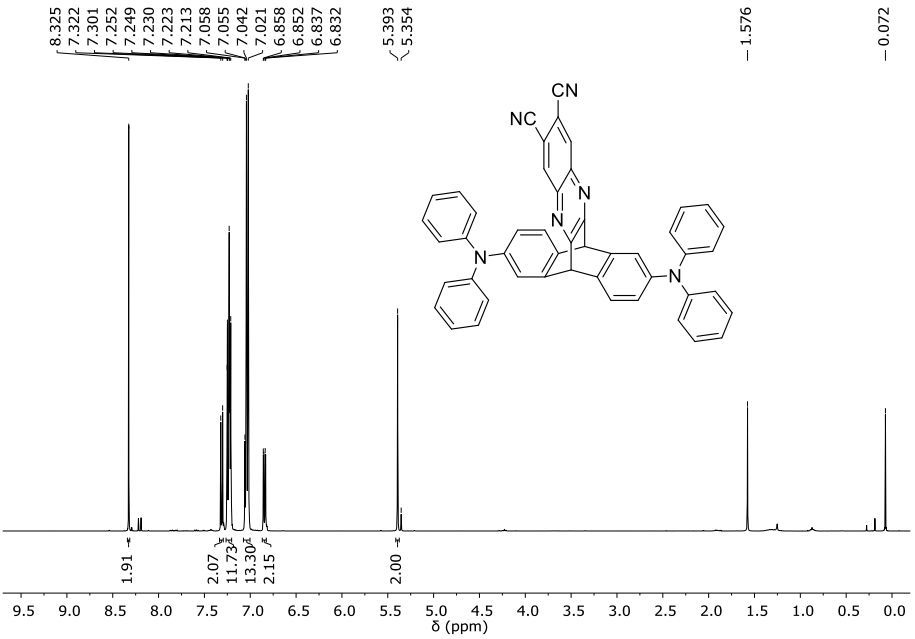

Figure S2.5: ^{1}H NMR spectrum of compound **1** in $CDCl_3$.

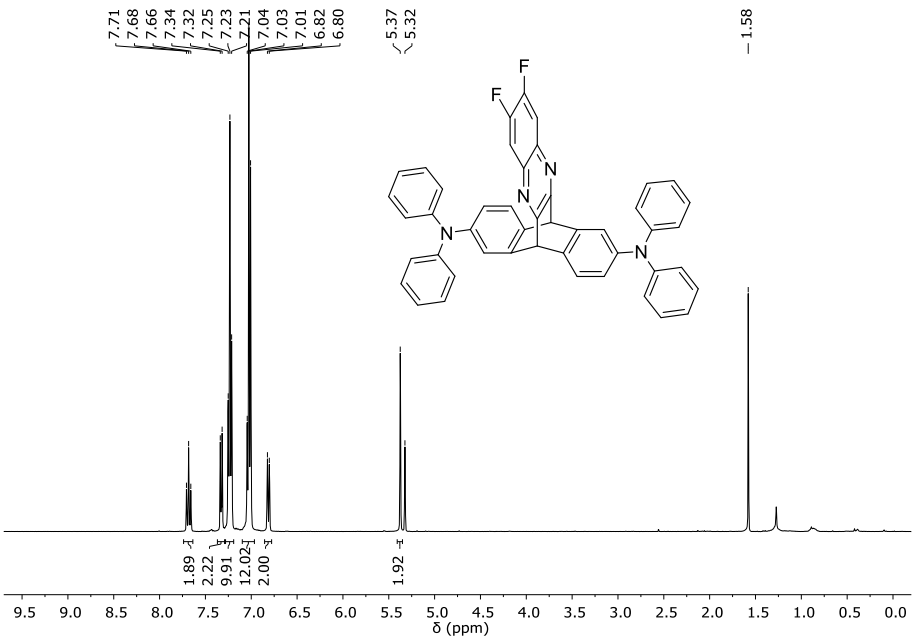

Figure S2.6: ^{1}H NMR spectrum of compound **2** in $CDCl_3$.

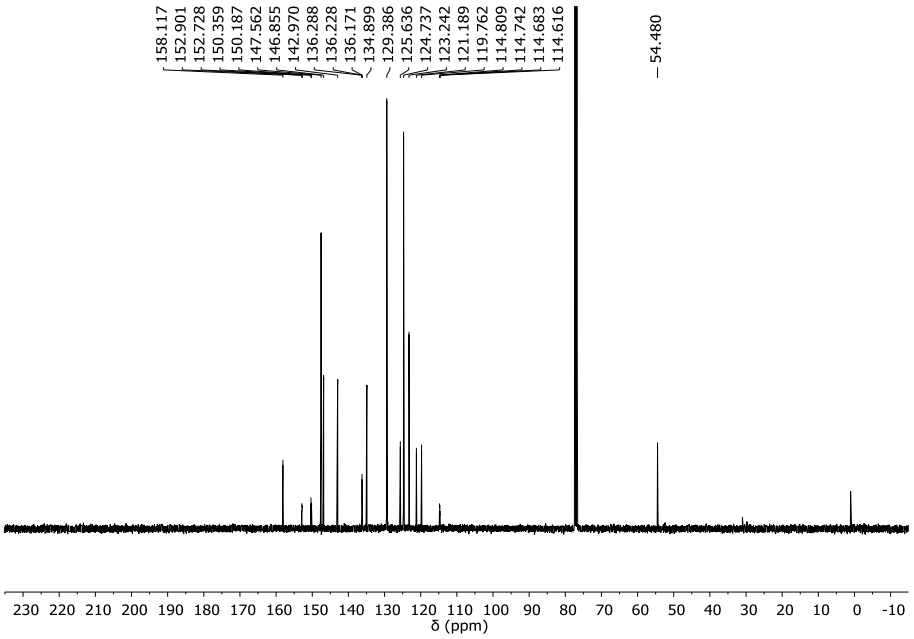

Figure S2.7: ^{13}C NMR spectrum of compound **2** in $CDCl_3$.

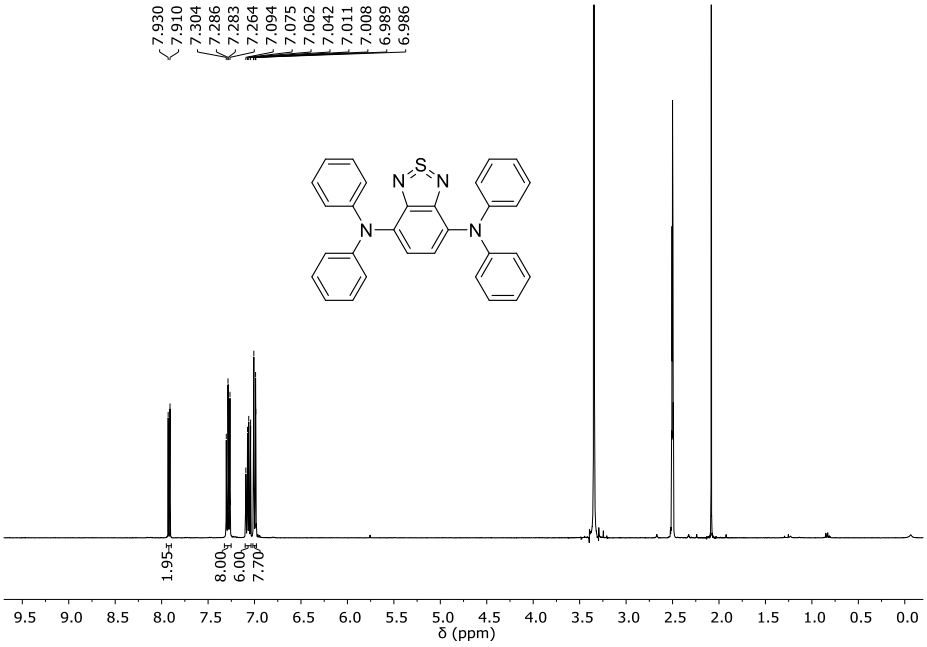

Figure S2.8: ^{1}H NMR spectrum of compound **3** in DMSO-d_6.

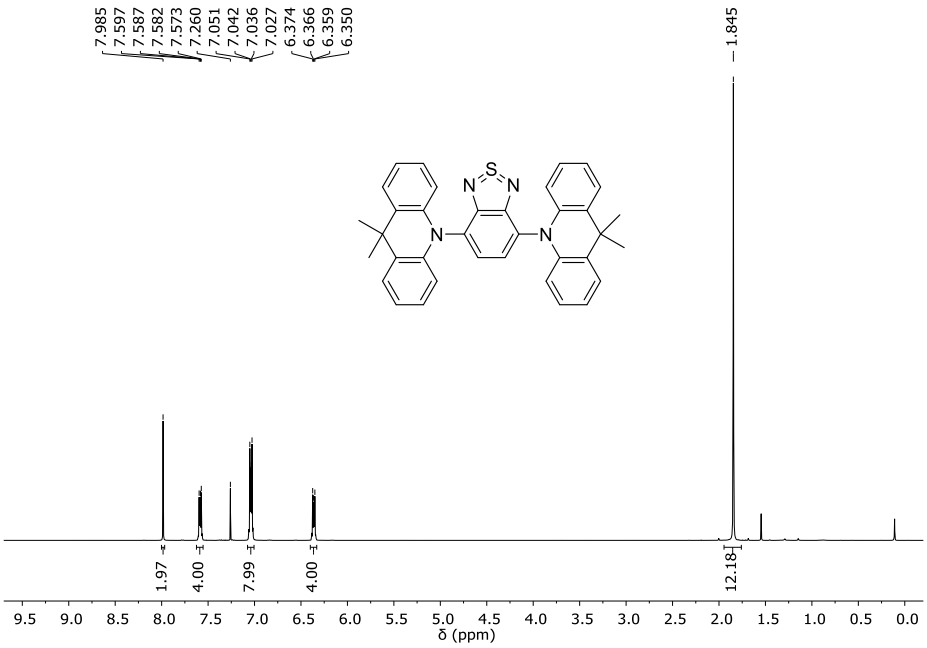

Figure S2.9: ^{1}H NMR spectrum of compound **4** in $CDCl_3$.

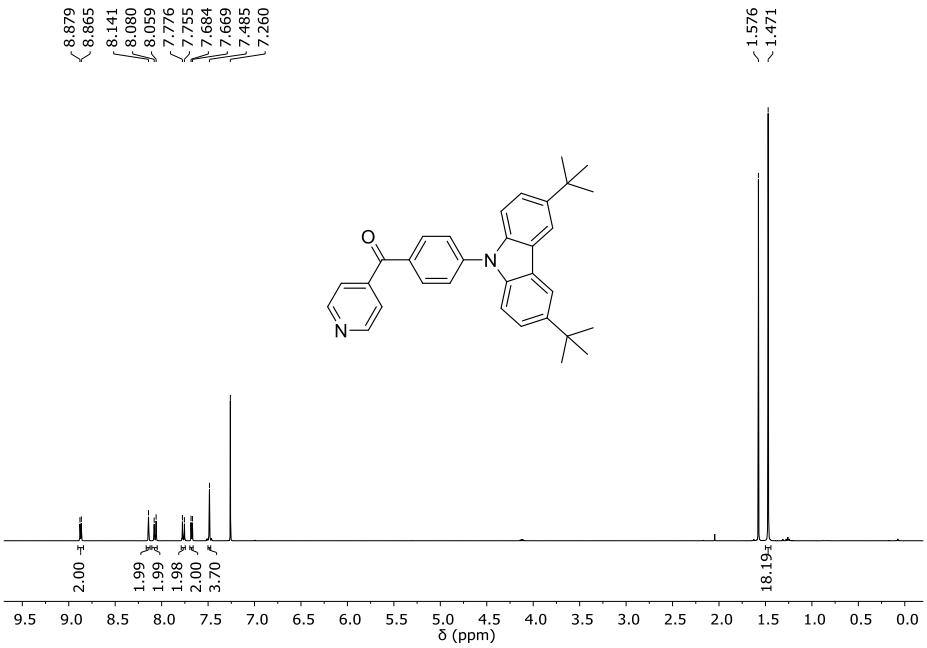

Figure S2.10: ^{1}H NMR spectrum of compound **5** in $CDCl_3$.

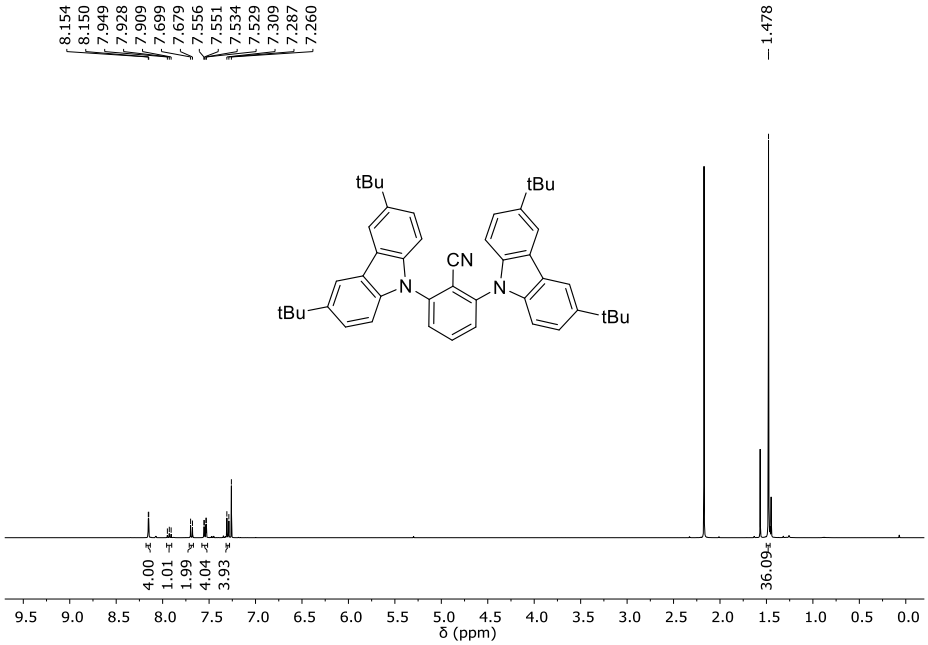

Figure S2.11: ^{1}H NMR spectrum of compound **6** in $CDCl_3$.

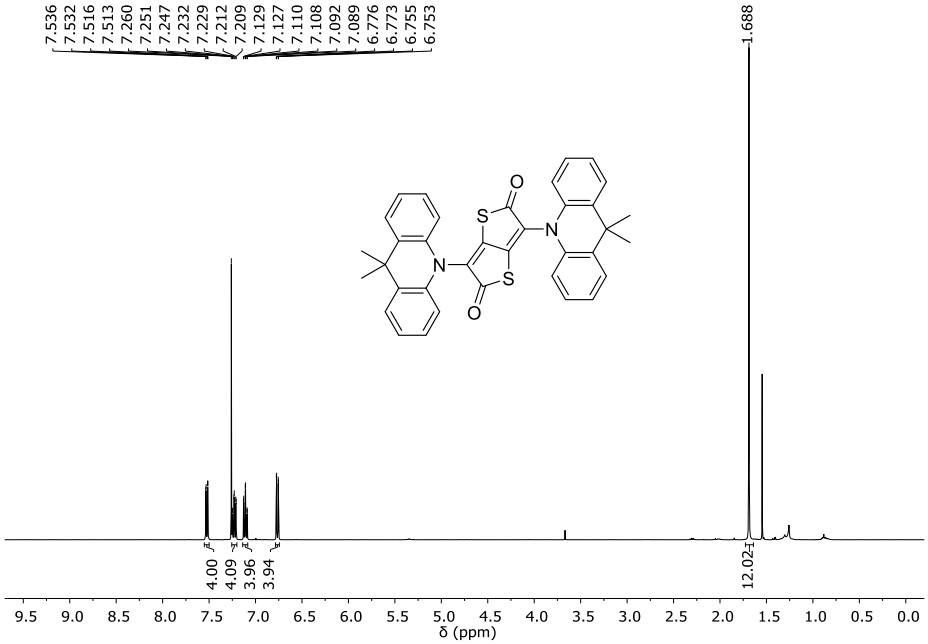

Figure S2.12: ^{1}H NMR spectrum of compound **7** in $CDCl_3$.

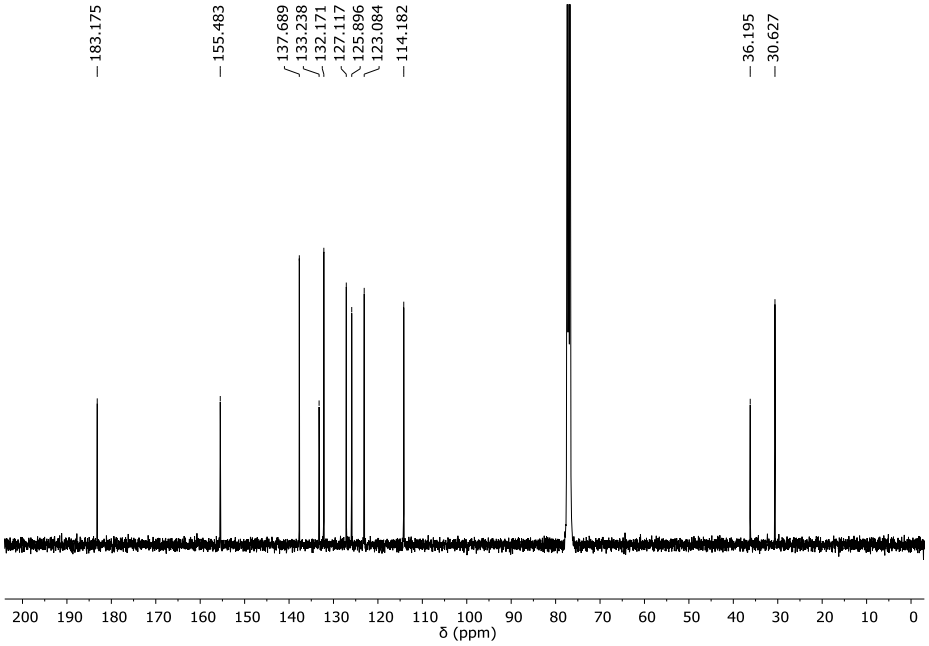

Figure S2.13: ^{13}C NMR spectrum of compound **7** in $CDCl_3$.

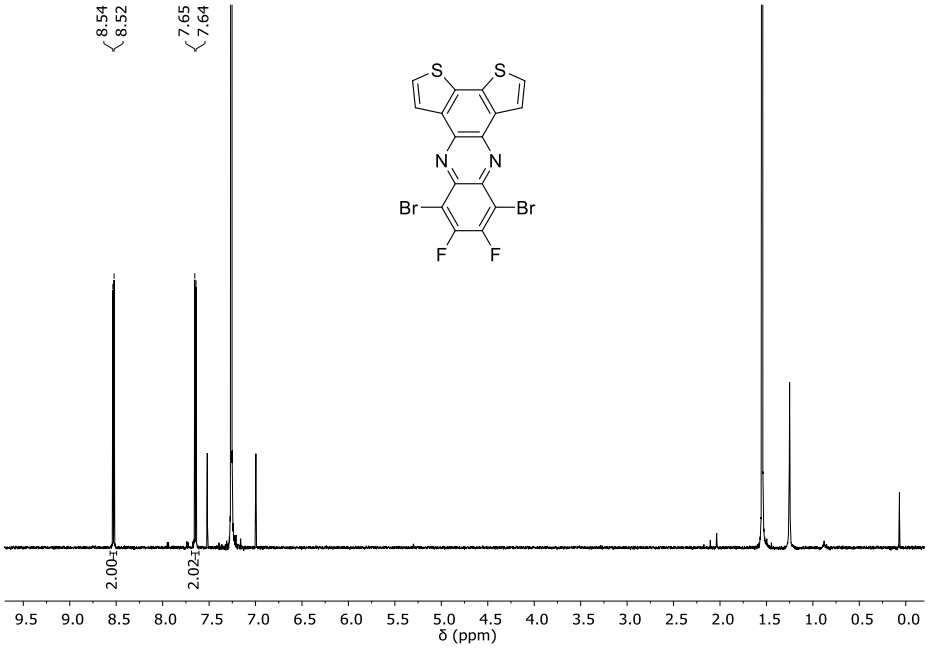

Figure S2.14: ^{1}H NMR spectrum of 8,11-dibromo-9,10-difluorodithieno[3,2-a:2',3'-c]phenazine (DTPz) in $CDCl_3$.

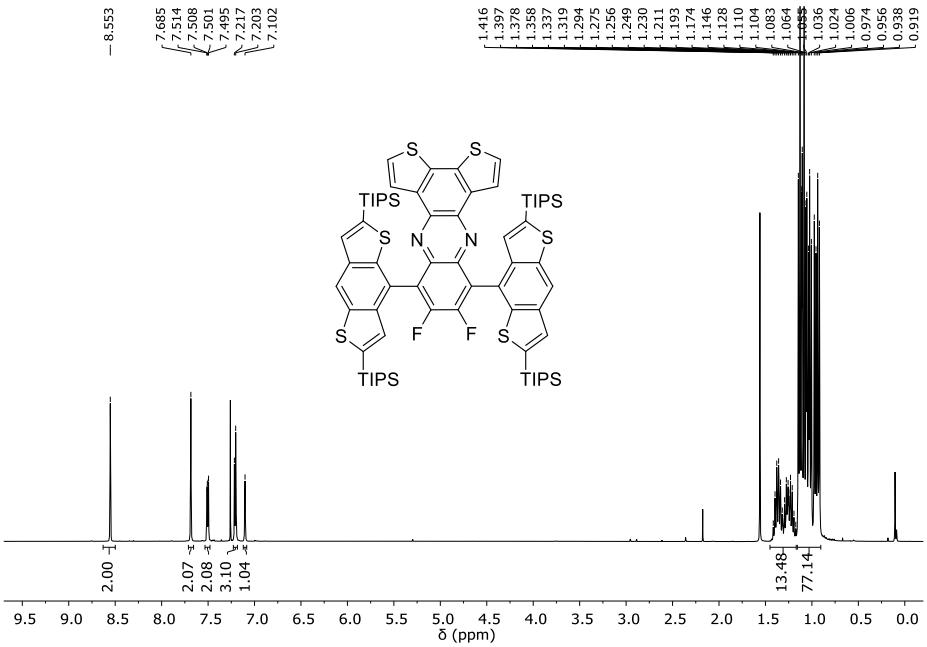

Figure S2.15: ^{1}H NMR spectrum of compound **8** in $CDCl_3$.

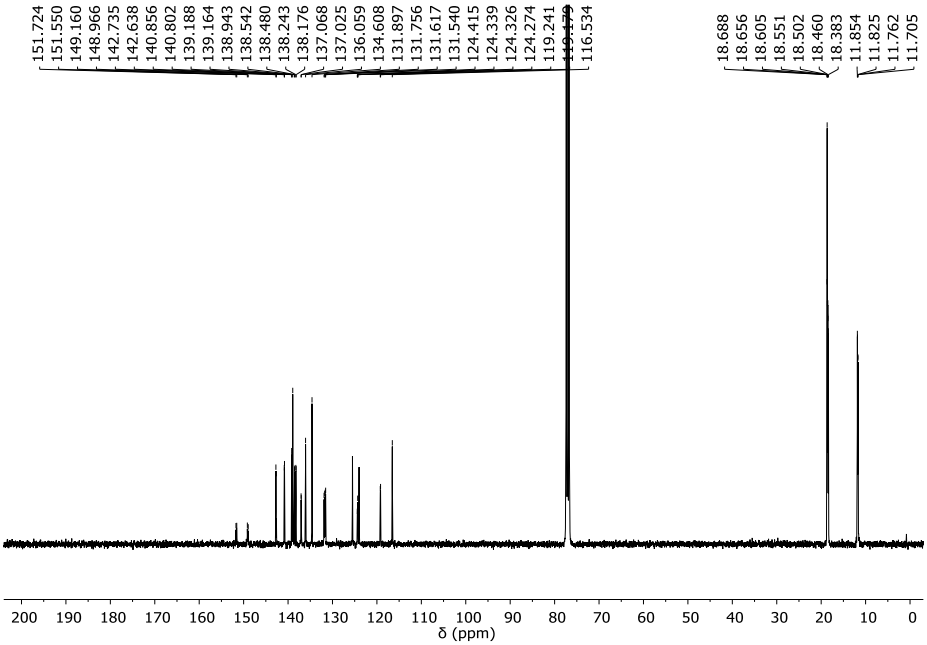

Figure S2.16: ^{13}C NMR spectrum of compound **8** in $CDCl_3$.

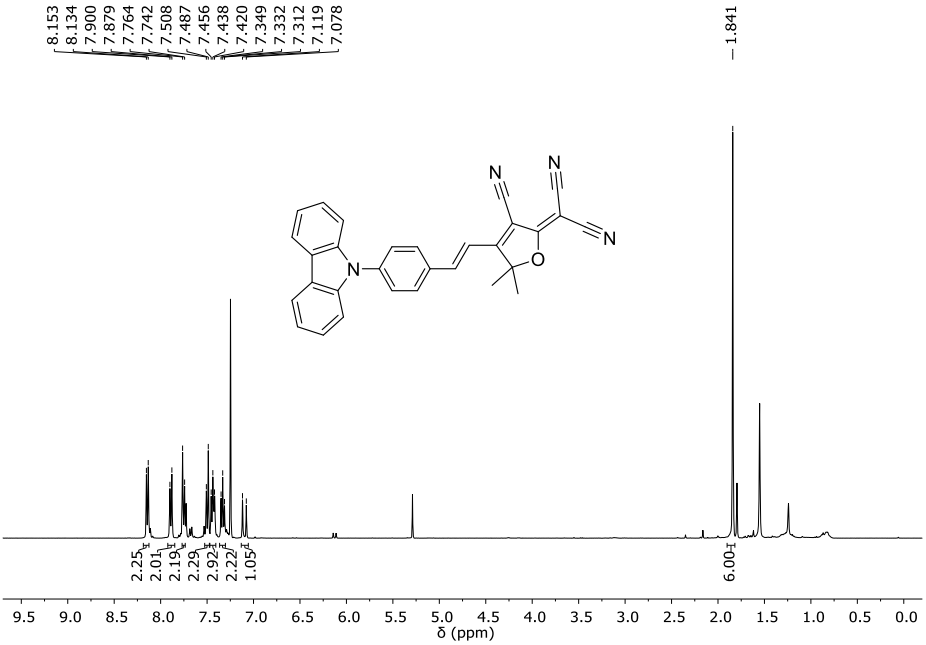

Figure S2.17: ^{1}H NMR spectrum of compound **9** in $CDCl_3$.

2.5.8. Supporting information references

1. K. Kawasumi, T. Wu, T. Zhu, H. S. Chae, T. Van Voorhis, M. A. Baldo and T. M. Swager, *J. Am. Chem. Soc.*, 2015, **137**, 11908-11911.
2. C. Y. Chan, L. S. Cui, J. U. Kim, H. Nakanotani and C. Adachi, *Adv. Funct. Mater.*, 2018, **28**, 1706023.
3. F. Ni, Z. Wu, Z. Zhu, T. Chen, K. Wu, C. Zhong, K. An, D. Wei, D. Ma and C. Yang, *J. Mater. Chem. C*, 2017, **5**, 1363-1368.
4. P. Rajamalli, N. Senthilkumar, P. Gandeepan, C. C. Ren-Wu, H. W. Lin and C. H. Cheng, *ACS Appl. Mater. Interfaces*, 2016, **8**, 27026-27034.
5. B. Zhao, G. Xie, H. Wang, C. Han and H. Xu, *Chemistry*, 2019, **25**, 1010-1017.
6. K. Kawabata, I. Osaka, M. Nakano, N. Takemura, T. Koganezawa and K. Takimiya, *Adv. Electron. Mater.*, 2015, **1**, 1500039.
7. M. Nakano, S. Shinamura, R. Sugimoto, I. Osaka, E. Miyazaki and K. Takimiya, *Org. Lett.*, 2012, **14**, 5448-5451.
8. H.-Y. Liu, P.-J. Wu, S.-Y. Kuo, C.-P. Chen, E.-H. Chang, C.-Y. Wu and Y.-H. Chan, *J. Am. Chem. Soc.*, 2015, **137**, 10420-10429.

Chapter 3

Benzo[1,2-*b*:4,5-*b*']dithiophene as a weak donor component for push-pull materials displaying thermally activated delayed fluorescence or room temperature phosphorescence

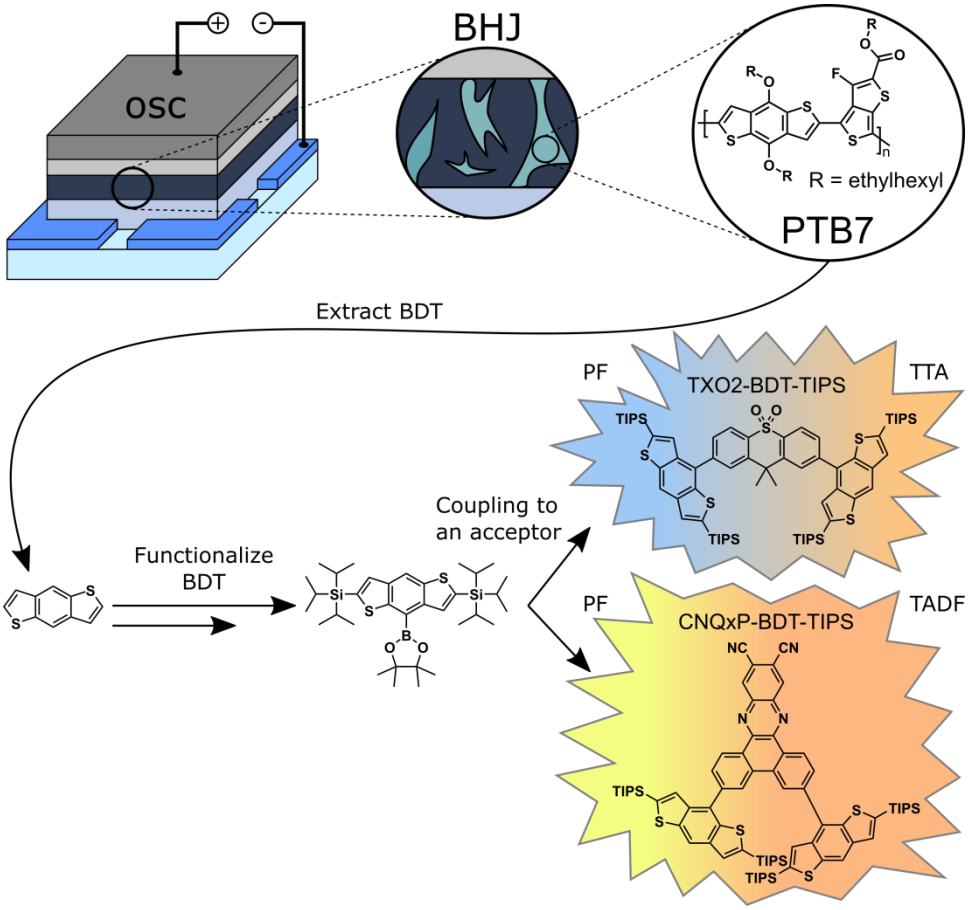

This chapter is based on a manuscript submitted to Dyes and Pigments:
T. Cardeynaels, S. Paredis, A. Danos, D. Vanderzande, A. P. Monkman, B. Champagne and W. Maes.

Contributions:
T. Cardeynaels: Synthesis and structural characterization of all compounds, all spectroscopic measurements and preparation of the manuscript.
S. Paredis: Spectroscopic measurements, discussion and revision of the manuscript.
A. Danos: Supervision of time-resolved spectroscopy, discussion and revision of the manuscript.
A. P. Monkman: Discussion of the results and revision of the manuscript.
D. Vanderzande, W. Maes and B. Champagne: Project management, discussion of the results and revision of the manuscript.

Abstract

In the search for high-performance donor-acceptor type organic compounds displaying thermally activated delayed fluorescence (TADF), triisopropylsilyl-protected benzo[1,2-*b*:4,5-*b*']dithiophene (BDT-TIPS) is presented as a novel donor component in combination with two known acceptors: dimethyl-9*H*-thioxanthenedioxide (TXO2) and dibenzo[*a*,*c*]phenazinedicarbonitrile (CNQxP). For a broader comparison, the same acceptors were also combined with the well-studied dimethyldihydroacridine (DMAC) donor. Optimized BDT-TIPS-containing structures show calculated dihedral angles of around 50° and well-separated highest occupied and lowest unoccupied molecular orbitals, although experimentally we observe rather large singlet-triplet energy gaps. By varying the acceptor moiety and the resulting ordering of excited states, room temperature phosphorescence (RTP) attributed to localized BDT-TIPS emission is observed in TXO2-BDT-TIPS, whereas CNQxP-BDT-TIPS affords a combination of TADF and triplet-triplet annihilation (TTA) delayed emission. In contrast, strong and pure TADF was observed for TXO2-DMAC as the donor unit, while CNQxP-DMAC showed a mixture of TADF and TTA at very long times. Overall, BDT-TIPS represents a new low-strength donor component for push-pull TADF emitters that is also able to induce RTP properties.

3.1. Introduction

While a near infinite number of D-A-D materials can be prepared, with their color and thermally activated delayed fluorescence (TADF) performance largely controlled by the choice of D and A, the pool of available donor units is relatively small. As indicated in Chapter 1, there are only about 7 different types of donor units or derivatives thereof which are being used in the design of most TADF emitters. Inspired by the field of organic photovoltaics (OPV), where it is widely used in push-pull type conjugated polymers,[1] benzo[1,2-*b*:4,5-*b*']dithiophene (BDT) was chosen here as a promising novel donor unit for TADF emitters. First used to construct polymers for OPV applications in 2008,[2] the BDT unit is favored for its rigid and planar nature, very high hole mobility and low-lying HOMO level. Another key aspect is that, via the conventional coupling on the BDT α-positions (Figure 3.1), highly planar, conjugated polymers can be constructed, leading to high charge-carrier mobility's, good inter-chain mobility's and red-shifted absorption necessary for low-band gap OPVs.[1] One of the most well-known polymers based on BDT is PTB7 (Figure 3.1), which was one of the few devices reaching a PCE of 7% at the time.[3-5] Because coupling via the α-positions leads to planar structures, this is not useful for TADF applications as the HOMO and LUMO would not be separated.

In 2012, Nakano *et al.*[6] reported on the direct borylation of α-silyl-protected BDT unit on the benzene core (Figure 3.1), making subsequent coupling to another

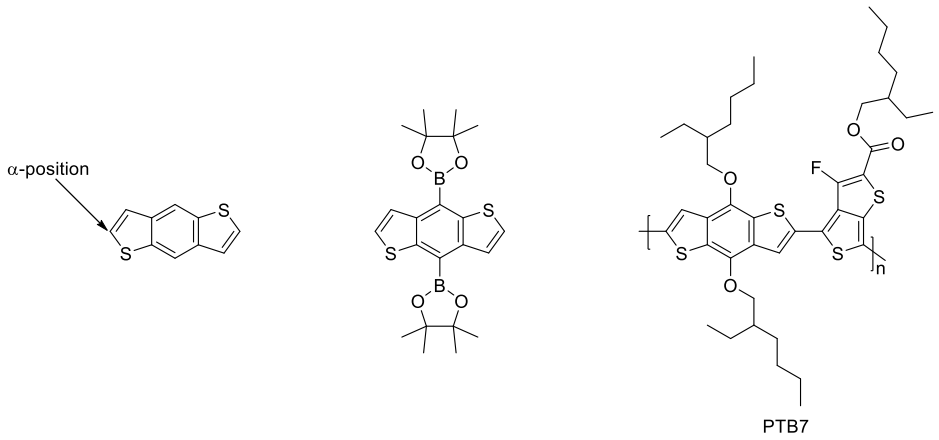

Figure 3.1: Chemical structures of benzo[1,2-*b*:4,5-*b*']dithiophene, 4,8-bis(4,4,5,5-tetramethyl-1,3,2-dioxaborolan-2-yl)benzo[1,2-*b*:4,5-*b*']dithiophene and PTB7.

halogen-functionalized aromatic molecule possible via Suzuki-Miyaura cross-coupling. Although their report was on the synthesis of di-substituted BDT molecules, tuning of the reaction conditions allows the synthesis of the monofunctionalised BDT molecule.[7] Coupling on the BDT benzene core could allow the synthesis of highly twisted D-A compounds when combined with a suitable acceptor molecule.

In this chapter, 2,6-bis(triisopropylsilyl)benzo[1,2-*b*:4,5-*b*']dithiophene (BDT-TIPS) was used to construct D-A-D compounds with two different acceptors, 9,9-dimethyl-9*H*-thioxanthene-10,10-dioxide (TXO2)[8-12] and dibenzo[*a*,*c*]phenazine-11,12-dicarbonitrile (CNQxP)[13]. For comparison, the 9,9-dimethyl-9,10-dihydroacridine (DMAC) analogues were also synthesized and investigated. Density functional theory (DFT) calculations showed large spatial separation between the HOMO and LUMO for the DMAC-based compounds and moderate separation for the BDT-TIPS-containing structures. Theoretical ΔE_{ST} values, as estimated from time-dependent DFT (TDDFT), are large for the BDT-TIPS compounds and very small for the DMAC-containing materials. Accordingly, BDT-TIPS was found to generate room temperature phosphorescence (RTP) or TADF emission depending on the choice of acceptor and resulting position of the relevant excited states.

While RTP is not common in organic molecules as discussed in Chapter 1, appropriate positioning of the singlet and triplet excited states can increase the rate of intersystem crossing (ISC) while a low-lying (localized) triplet state can trap the exciton. Because TADF emitters are designed to be rigid to overcome non-radiative transitions, this also benefits any trapped triplet excitons as they have the possibility of radiative transition from the excited triplet to the ground state if there is significant coupling between the two, leading to phosphorescence at room temperature. These RTP emitters typically show a relatively low triplet emission quantum yield making them inefficient for OLEDs, nonetheless their long-lived, and often red-shifted emission, can still be useful for other applications such as bio-imaging,[14-16] sensing applications[17, 18] and in glow-in-the-dark[19] or security inks[20].

3.2. Results and discussion

3.2.1. Material synthesis

The novel BDT-TIPS donor building block was synthesized as a boronic ester according to literature, as shown in Scheme 3.1.[7] Triisopropylsilyl (TIPS) protection is necessary to prevent boroester formation on the thienyl 2- and 3-positions. Coupling to different acceptors was achieved using Suzuki-Miyaura cross-coupling, while Buchwald-Hartwig cross-coupling was used for the DMAC compounds. Full details of all synthetic procedures are included in the supporting information (SI).

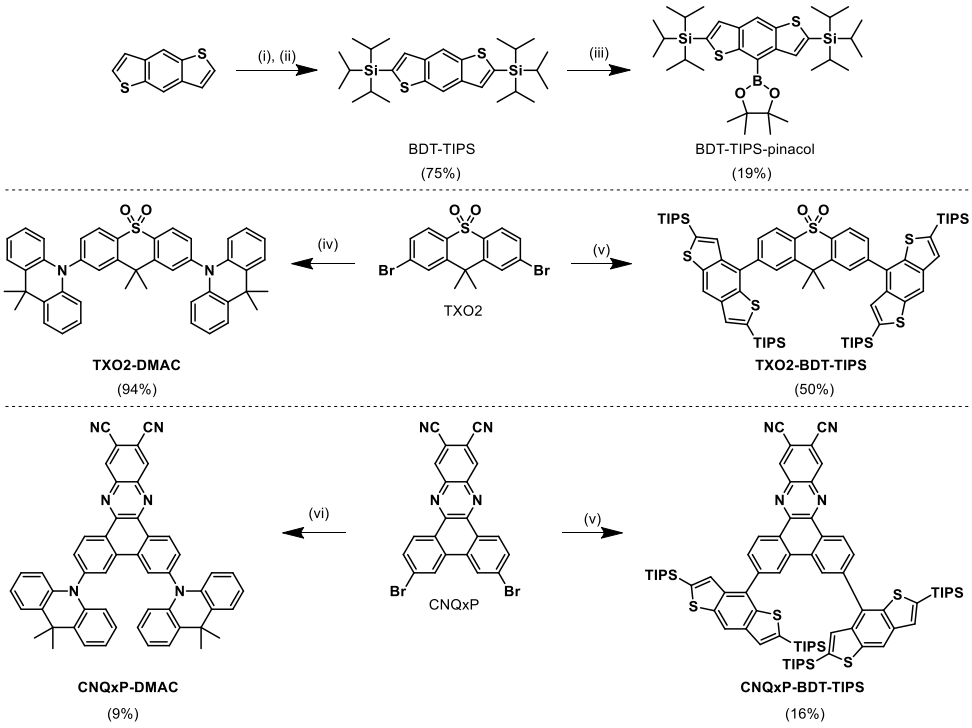

Scheme 3.1: Synthesis pathways for all studied compounds: (i) *n*-BuLi, THF, 0 °C, 1 h; (ii) TIPSCl, THF, 65 °C, 16 h; (iii) Bis(pinacolato)diboron, $[Ir(OMe)(COD)]_2$, 4,4'-di-*tert*-butyl-2,2'-bipyridine, cyclohexane, 80 °C, 24 h; (iv) 9,9-dimethyl-10*H*-acridine, $Pd_2(dba)_3$, HP*t*Bu_3BF_4, NaO*t*Bu, toluene, 107 °C, 21 h; (v) BDT-TIPS-pinacol, $Pd(PPh_3)_4$, K_2CO_3, toluene/H_2O (4/1), 80 °C, 24 h; (vi) 9,9-dimethyl-10*H*-acridine, $Pd(OAc)_2$, HP*t*Bu_3BF_4, NaO*t*Bu, toluene, 120 °C, 24 h.

3.2.2. Quantum-chemical calculations

Geometry optimizations were performed on the isolated BDT-TIPS donor (Figure S3.8) and the 4 different D-A-D emitters (Figure 3.2) using DFT (M06/6-311G(d)). The excited state properties were calculated by TDDFT using LC-BLYP with a modified range-separating parameter (ω=0.17 a_0^{-1}) as the exchange correlation (XC) functional.[7, 21] TDDFT calculations were performed under the Tamm-Dancoff approximation and using the polarizable continuum model (PCM) in cyclohexane to simulate a non-polar environment in the Gaussian16 package.[22] The CT character of the involved states was investigated by looking at the differences of ground and excited state electron densities (Figure S3.9 and S3.10). These were characterized by the distance over which charge is transferred, calculated according to the work of Le Bahers *et al.,*[23] and the related change in dipole moment. For the geometry optimizations, the TIPS groups were explicitly included to accurately judge their influence on the electronic and structural properties.

Although **TXO2-DMAC** has already been investigated before,[8-11, 24] it was included in the calculations to allow straightforward comparison between the DMAC and BDT-TIPS donor systems. The CNQxP acceptor is also known from literature and was previously used to construct D-A systems with phenyl-spaced DMAC and diphenylamine (DPA) units.[13] However, to the best of our knowledge, direct coupling between CNQxP and DMAC has not been reported before. A similar dibenzo[*f*,*h*]quinoxaline-2,3-dicarbonitrile entity was used to construct D-A-D systems containing DMAC (amongst other donors), but this acceptor has a lower electron deficiency, providing slightly blue-shifted emission.[25] In these two examples, TADF was observed experimentally.

Large dihedral angles of around 90° were observed for the two DMAC-containing compounds (Table 3.1), leading to well-separated HOMO and LUMO distributions (Figure 3.2). The two compounds with BDT-TIPS donor groups show considerably smaller dihedral angles of around 50°. This is not unexpected, since the central six-membered ring is flanked by two smaller five-membered rings, as opposed to the six-membered rings in DMAC, affording less steric control over the D-A dihedral angle.[26] The consequences of these smaller dihedral angles are also apparent looking at the HOMO and LUMO distributions (Figure 3.2), with the BDT-TIPS compounds showing increased overlap between

the HOMO and LUMO, in particular for TXO2, with the proximity of the two donor moieties in **CNQxP-BDT-TIPS** possibly leading to additional steric interactions. The smaller calculated dihedral angles for the BDT-TIPS compounds are consistent with larger oscillator strengths for the molecular S_0->S_1 transitions (having a largely dominant HOMO to LUMO character), along with their larger singlet-triplet energy gaps (Table 3.1).

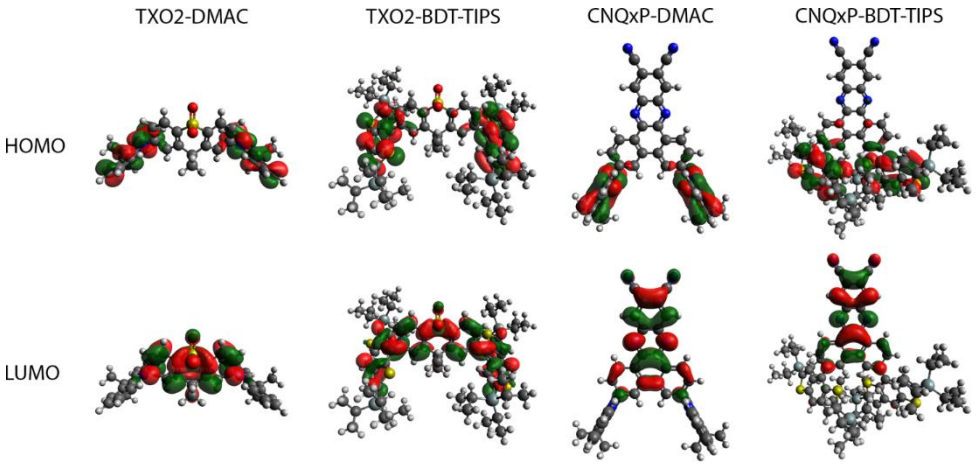

Figure 3.2: HOMO and LUMO topologies obtained using LC-BLYP(ω=0.17) for the optimized geometries of the different emitters investigated in this work. Isocontour values of 0.02 a.u. were used for all orbitals.

TDDFT calculations were then performed to investigate excited singlet and triplet energies and their respective energy differences (Table 3.1). The TXO2-based compounds have S_1 energies that are higher than those based on CNQxP, indicative of the lower acceptor strength of the TXO2 core. Similarly, the singlet energies of the compounds containing the BDT-TIPS donor are higher than for their DMAC counterparts, demonstrating the lower donor strength of the BDT-TIPS group. While all D-A-D compounds show small energy gaps between the first and second triplet energies ($\Delta E_{T_2-T_1}$), only the DMAC-containing compounds show a small calculated ΔE_{ST}. It is therefore anticipated that the BDT-TIPS donor will require highly sophisticated molecular design strategies to afford TADF behaviour, to overcome its intrinsically small D-A angles and the associated large orbital overlap. To account for vibration-induced symmetry-breaking effects, additional TDDFT calculations were performed with modified dihedral angles (±10°), revealing the weak intensity of the low-energy transitions of the

Table 3.1: TDDFT results for the first vertical singlet excitation energies and corresponding oscillator strengths, the first and second vertical triplet excitation energies and dihedral angles (obtained from DFT geometry optimization).

Compound	S_1 (eV)	f_{S_1}	S_2 (eV)	f_{S_2}	T_1(eV)	T_2 (eV)	$\Delta E_{T_2-T_1}$ (eV)	$\Delta E_{S_1-T_1}$ (eV)	D-A angle (°) [a]
TXO2-DMAC	3.26	0.00 (0.03)[b]	3.26	0.00 (0.01)[b]	3.24	3.25	0.01	0.02	90
TXO2-BDT-TIPS	3.57	0.60	3.62	0.12	2.64	2.65	0.01	0.93	54
CNQxP-DMAC	2.49	0.00 (0.01)[b]	2.50	0.00 (0.05)[b]	2.47	2.50	0.03	0.02	90
CNQxP-BDT-TIPS	2.92	0.64	2.99	0.08	2.47	2.49	0.02	0.45	48
BDT-TIPS	3.87	0.31	4.32	0.35	2.80	3.58	0.78	1.17	—

[a] Taken as the average of 4 possible torsion angles. [b] Oscillator strengths when the D-A dihedral angle is modified by ±10°.

Table 3.2: Nature of the various transitions, charge transfer distance (d_{CT}) and change in dipole moment ($\Delta\mu$, excited – ground state dipole) accompanying the S_0->S_x and S_0->T_x transitions in cyclohexane.

	S_1			S_2			T_1			T_2		
Compound	Nature	d_{CT} (Å)	$\Delta\mu$ (D)	Nature	d_{CT} (Å)	$\Delta\mu$ (D)	Nature	d_{CT} (Å)	$\Delta\mu$ (D)	Nature	d_{CT} (Å)	$\Delta\mu$ (D)
TXO2-DMAC	H->L	1.49	8.18	H-1->L	1.49	8.19	H->L	1.48	8.14	H-1->L	1.49	8.15
TXO2-BDT-TIPS	H->L	0.96	2.70	H-1->L	0.92	2.47	H->L	0.40	0.79	H-1->L	0.41	0.80
CNQxP-DMAC	H->L	4.18	24.64	H-1->L	4.08	24.18	H->L	4.04	21.54	H-1->L	4.17	24.76
CNQxP-BDT-TIPS	H->L	3.96	17.78	H-1->L	3.79	16.66	H->L	2.98	8.19	H-1->L	2.46	5.77

DMAC-based compounds, while the excitation energies and other excited state properties are only impacted in a negligible way (Figure S3.1). The CT nature of the first and second excited singlet and triplet states was also investigated (Table 3.2). **TXO2-DMAC** shows CT character in its first excited singlet and triplet states, as indicated in Figure S3.9. This property is associated with CT distance (d_{CT}) values of around 1.49 Å and relatively large change in dipole moment ($\Delta\mu$) upon excitation. This strong CT nature, combined with the small ΔE_{ST}, contributes significantly to the high EQEs (> 20%) obtained with this TADF emitter.[8-10, 27] **TXO2-BDT-TIPS**, on the other hand, shows more localized excitations for both the singlet and triplet excited states, as shown in Figure S3.8 and as indicated by the much smaller d_{CT} and $\Delta\mu$ values. This localized excitonic nature arises from the shared LUMO distribution on the BDT-TIPS and acceptor units, whereas for **TXO2-DMAC** the LUMO resides entirely on the TXO2 part. Despite having two triplet states in close proximity, the large ΔE_{ST} restricts the possibility for TADF to occur. Like **TXO2-DMAC**, **CNQxP-DMAC** also shows good HOMO-LUMO separation and a small ΔE_{ST}. The first singlet and triplet excited states also show strong CT character, with large values for d_{CT} and $\Delta\mu$. For **CNQxP-BDT-TIPS**, the situation is less straightforward. Whereas the two first singlet excited states show strong CT character, the first and second triplet excited states have mixed charge-transfer (CT) and localized excited (LE) state character (due to contributions of multiple one-particle transitions) as they show intermediate d_{CT} and $\Delta\mu$ values (Figure S3.10).

3.2.3. Photophysical characterization

The steady-state absorption and emission spectra of the BDT-TIPS containing D-A-D materials in 1wt% doped zeonex films show large differences in absorption and emission energy, due to the different electron-withdrawing strengths of the TXO2 and CNQxP acceptor units (Figure 3.3). **TXO2-DMAC**[8-11, 24, 27] has been studied in this host before, and data are presented here too to enable direct comparison to **TXO2-BDT-TIPS**. Both materials containing CNQxP have structured low energy absorption bands, corresponding to ππ* transitions of the CNQxP unit with some D-A CT character, and are slightly shifted with respect to each other due to the different electron-donating properties of the DMAC and BDT groups. The BDT-TIPS and DMAC donor units also have a large influence on

the D-A-D emission wavelengths, with the DMAC-based materials showing emission maxima red-shifted by 19 nm (0.12 eV) for TXO2 and 68 nm (0.22 eV) for CNQxP compared to the BDT-TIPS analogues. This is in line with the stronger donor character for the DMAC group, leading to a larger CT character of the emission and lower energy emission. These findings are in line with the results from the TDDFT calculations, as also evidenced by the simulated absorption spectra (Figure S3.1). The emission spectrum for **TXO2-BDT-TIPS** is quite narrow in comparison to that of **TXO2-DMAC**, suggesting a more localized nature of the emission. On the other hand, the emission spectra for both CNQxP-based compounds are broad, suggesting predominant CT character. The **CNQxP-BDT-TIPS** emission is unique in that it shows some structure and its onset is very close to the absorption edge, which could be due to dual emission of a higher energy ^{1}LE and lower ^{1}CT state. Indeed, separate emission bands

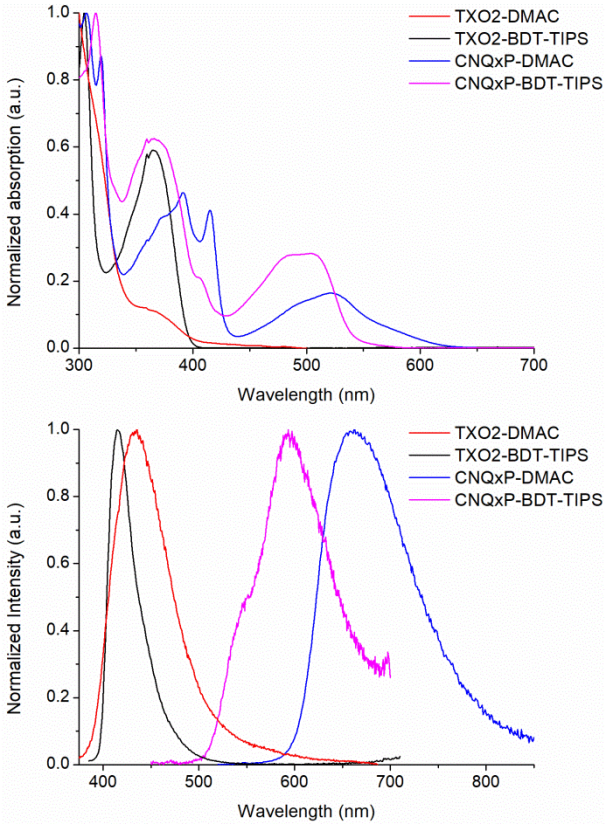

Figure 3.3: Steady-state absorption (top) and emission (bottom) spectra at room temperature in zeonex film.

corresponding to the shoulder and peak of the steady-state emission are observed in time-resolved measurements (Figure S3.3), supporting this assignment. Time-dependent emission spectra and decays were then obtained using a pulsed laser and iCCD camera to investigate the dynamic photophysics in these systems. From the contour plots of the normalized spectra and the total emission decays in zeonex (Figure 3.4a,c, and spectra in Figure S3.2), it is apparent that **TXO2-BDT-TIPS** has no delayed emission in the microseconds regime (the spectra in Figure 3.4a in this time region are consistent with normalized CCD baseline signal). High-energy LE emission consistent with the steady-state photoluminescence (PL) is observed at first, which relaxes over the first 50 ns to a red-shifted CT state before emission falls below the sensitivity limit of the instrument. A longer living and further red-shifted emission spanning into the millisecond domain is then observed. Comparing the millisecond emission spectra at room temperature and at 80 K (Figure 3.5 bottom), it is apparent that the room temperature and 80 K emission come from the same state in TXO2-BDT-TIPS and are therefore both attributed to phosphorescence. From the onset of the prompt fluorescence (PF) at room temperature and the phosphorescence at 80 K, the singlet and triplet energies and the corresponding singlet-triplet energy gap were calculated (Table 3.3). With an experimental ΔE_{ST} of 0.78 eV (vs. 0.93 eV calculated), TADF is excluded as a possible delayed fluorescence (DF) emission mechanism in **TXO2-BDT-TIPS**. The occurrence of RTP is attributed to the presence of the BDT-TIPS donor, as this emission mechanism was not observed for **TXO2-DMAC** (Figure 3.4b).

For **CNQxP-BDT-TIPS**, a combination of LE and CT emission seems to be present at early decay times (Figure S3.3), which implies a reduced electron transfer rate to form the CT state compared to the other materials. Like in **TXO2-BDT-TIPS**, this is probably due to the BDT group having moderate dihedral angles with respect to the acceptor unit and having a rather weak electron-donating strength (as judged by comparison of the PL colour to the DMAC compounds). As the "LE" emission dies out, the CT emission remains throughout the remainder of the decay, although at very long times (> 1 ms) the "LE" emission seemingly reappears. The same short-wavelength emission is present at early decay times at 80 K, but does not reappear near the end of the decay (Figure S3.3). Furthermore, the microsecond emission present at room

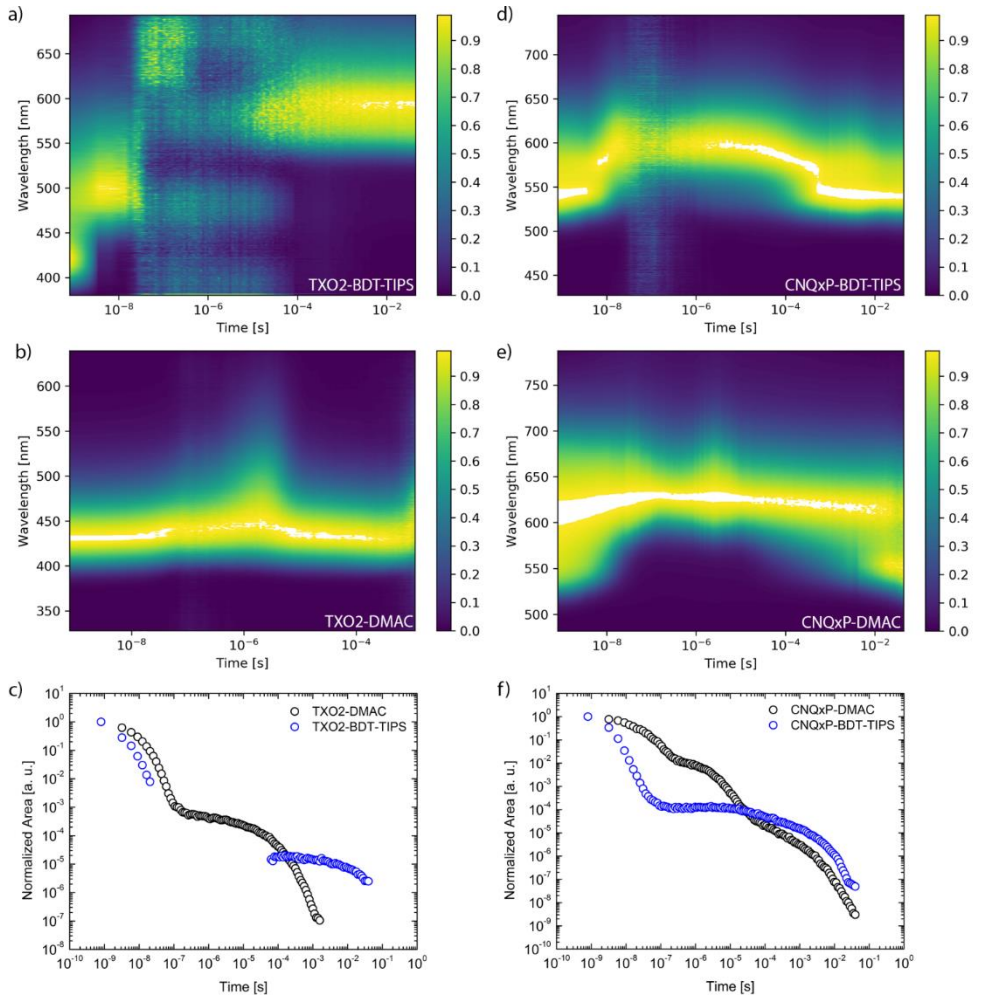

Figure 3.4: Contour plots for the normalized room temperature time-resolved emission spectra of **TXO2-BDT-TIPS** (a), **TXO2-DMAC** (b), **CNQxP-BDT-TIPS** (d) and **CNQxP-DMAC** (e) in zeonex, along with the emission intensity decays (c and f).

temperature is absent at 80 K. At long times in the decay at 80 K, a red-shifted emission is seen, which is attributed to the true phosphorescence of the system (Figure S3.3). The absence of the microsecond emission at 80 K demonstrates temperature dependency as expected for TADF emission. The singlet (2.35 eV) and triplet (2.17 eV) energies from the experimental data lead to a singlet-triplet gap of 0.18 eV, which is large but not insurmountable at room temperature (Table 3.3)[52] The red-shifted microsecond emission in zeonex at room temperature has an onset of around 2.30 eV, indicating that TADF is a

Table 3.3: Photophysical properties and kinetics for TXO2-DMAC, TXO2-BDT-TIPS, CNQxP-DMAC and CNQxP-BDT-TIPS in zeonex.

Compound	E_S (eV) [a]	E_T (eV) [b]	ΔE_{ST} (eV) [c]	τ_{Fp} (ns)[d]	τ_{Fd} (μs)[e]	k_{ISC} [f]	k_{rISC} [f]
TXO2-DMAC	3.20	3.02	0.18	12.71	67.89	$5.44x10^7$	$4.27x10^4$
TXO2-BDT-TIPS	3.14	2.36	0.78	4.51	$2.69x10^4$	—[g]	—[g]
CNQxP-DMAC	2.07	2.09	-0.02	52.66	4.67/ $1.80x10^3$	$1.04x10^7$	$5.17x10^5$
CNQxP-BDT-TIPS	2.35	2.17	0.18	2.12	$1.86x10^3$	—[g]	—[g]
BDT-TIPS	3.24	2.48	0.76	0.78	$4.40x10^4$	—[g]	—[g]

[a] Taken from the onset of the prompt fluorescence (PF) emission. [b] Taken from the onset of the phosphorescence emission at ms timescales at 80 K. [c] Calculated as E_s – E_T. [d] Lifetime of prompt fluorescence (F_p). [e] Lifetime of delayed fluorescence (F_d). [f] k_{ISC} and k_{rISC} rates were determined using kinetic fitting of the PF and DF emission according to literature.[45] [g] Due to the lack of microsecond emission and/or unambiguous identification of a pure TADF mechanism, kinetic fitting was not performed.

potential emission pathway. The blue-shifted millisecond emission in **CNQxP-BDT-TIPS** is instead suggested to arise from triplet-triplet annihilation (TTA) and subsequent emission from singlet LE states. The same LE states are also formed directly following photoexcitation, which is why they share the same spectra at very early and very late decay times. The signal arising from TTA is long lived but weak, and so it is only observable once the TADF emission has fully decayed, and is completed suppressed at low temperatures which restrict triplet migration through the film. This assignment is also verified by the TDDFT calculations. Due to the apparent symmetry in the system S_1 and S_2 are of HOMO and HOMO-1 to LUMO character, respectively, and consist of D->A CT transitions (Figure S3.10). Looking at the third excited singlet state (S_3), it represents the first singlet excited state with a localized character and has an energy only 0.12 eV (17 nm) higher than that of S_1 (Table S3.1, Figure S3.10). It is therefore possible that S_3 is the LE state that we observed in the experimental time-resolved decays at early and long times. Similarly, the first two excited triplet states (T_1, T_2) are D->A CT transitions whereas T_3 is localized on the acceptor and is 0.15 eV higher in energy than T_1 (Table S3.1, Figure S3.10). According to the spin-vibronic mechanism for TADF, these states have the potential to mix and decrease the effective ΔE_{ST}. While the theoretical ΔE_{S1T1} is rather large (0.45 eV), the experimental energy gap (0.18 eV) is not and

taking into account the precision of the TDDFT calculations, this mechanism is viable.

CNQxP-DMAC has consistent emission throughout the decay with an onset of about 2.15 eV (577 nm) in the microsecond regime. A short-wavelength contribution is present at very early decay times and reappears in the very long millisecond emission similar to that of **CNQxP-BDT-TIPS** (Figure 3.4e). At 80 K, the emission is slightly red-shifted and the short-wavelength contribution at the start of the decay is less intense and does not reappear at longer times (Figure S3.4). Even at 80 K, delayed emission is present at all times throughout the decay. As the onset of the spectra also remains the same, this is indicative of TADF emission with a very small ΔE_{ST}, as supported by the experimental determination of the singlet and triplet energies (Table 3.3). This is unusual as the TADF seemingly persists at 80 K whereas the low wavelength emission attributed is suppressed. We suggest that the very delayed high-energy emission is also generated by TTA and subsequent emission from LE states that are initially formed by photoexcitation as the position and localization of the S_3 state of **CNQxP-DMAC** is similar to that of **CNQxP-BDT-TIPS**. Additionally, the full decay of **CNQxP-DMAC** (Figure 3.4f) shows two regions of increased intensity at around 10^{-6} and 10^{-3} seconds, whereas Figure 3.4e shows delayed emission at a constant wavelength. While the first region can be attributed to TADF, the second region appears at earlier times with respect to the onset of TTA (> 10^{-3} s). This is unusual and may indicate the presence of two rISC pathways, showing TADF with largely varying k_{rISC} values.

To better understand the positioning of LE states in these materials, the BDT-TIPS donor itself was also embedded in a zeonex matrix and its time-dependent emission was recorded at room temperature and at 80 K (Figure 3.5, S3.5). As suggested by the calculations, the singlet and triplet emission are well separated with onsets at 3.24 and 2.48 eV, respectively (Table 3.3). It is remarkable how the BDT-TIPS group itself shows emission at several tens of milliseconds, even at room temperature. Comparing the spectra at room temperature and at 80 K shows that both the prompt and millisecond emission have the same onset at each temperature, and are thus coming from the same states in both cases. This is attributed to the presence of the sulphur atoms in the BDT core, which enhance SOC when compared to commonly used atoms such as carbon and

nitrogen. Having two of these sulphur atoms could boost the SOC enough to enhance ISC from the S_1 to the T_1 state and subsequently enable the strong RTP observed in the donor fragment.

For **TXO2-BDT-TIPS**, it is possible that the observed RTP is coming from localized emission corresponding to the BDT-TIPS unit (Figure 3.5). When looking at the the pure BDT-TIPS and **TXO2-BDT-TIPS** spectra at room temperature and at 80 K, the similarities in the peak shape and onset indicates that emission is coming from similar states in both materials. The difference in onset could be due to the acceptor properties of TXO2, slightly lowering the BDT triplet energy level in the D-A-D compound, or from the vibrational mode of the highest energy vibronic peak in the BDT-TIPS phosphorescence spectrum being suppressed in the D-A-D material. Furthermore, the ground–excited state electron density differences predict the T_1 and T_2 states to be localized on the BDT-TIPS group (Figure S3.9). **CNQxP-BDT-TIPS** behaves differently, as

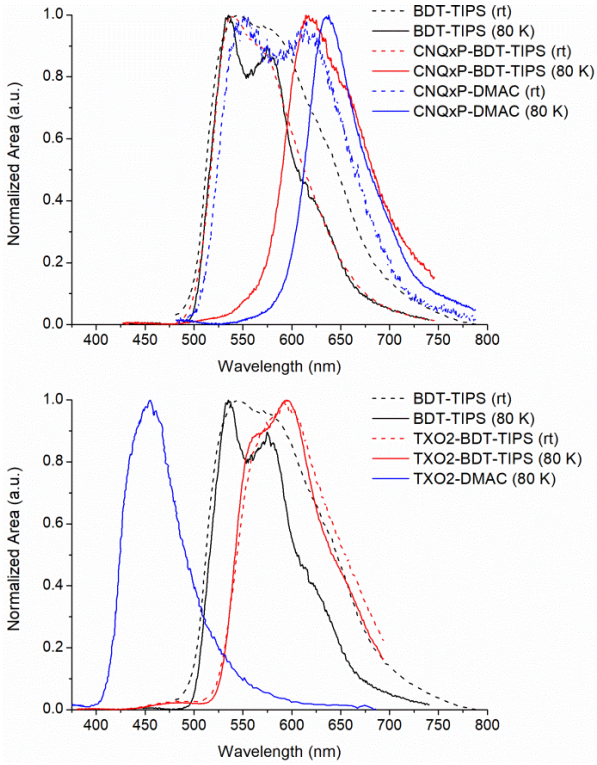

Figure 3.5: Emission spectra obtained at a 44.7 ms delay for BDT-TIPS, **CNQxP-BDT-TIPS** and **CNQxP-DMAC** (top), and for BDT-TIPS, **TXO2-BDT-TIPS** and **TXO2-DMAC** (bottom) at 80 K and at room temperature.

microsecond emission (attributed to TADF) is also observed. The large difference in the onset of the emission at several milliseconds at room temperature and at 80 K allows us to exclude RTP for this compound. One of the reasons for this is that the CT triplet of the D-A-D compound has a lower energy than the localized BDT-TIPS triplet state and coupling to the ground state from the CT triplet state is inefficient. Alternatively, rISC could be competing with the radiative relaxation from the T_1 state due to the smaller ΔE_{ST} with respect to **TXO2-BDT-TIPS** and the improved SOC. The ground–excited state electron density differences (Figure S3.10) show significant CT character for the lowest excited triplet state, supporting this hypothesis.

The short-wavelength emission at a few nanoseconds in the decays of **CNQxP-BDT-TIPS** (Figure 3.6) and **CNQxP-DMAC** (Figure S3.4) is attributed to the presence of a locally excited singlet state (^{1}LE) above the TADF-active CT singlet (*vide supra*). The sterically hindered conformation in which the donor units reside likely slows down electron transfer and hence the internal conversion of the photoexcited ^{1}LE state to the lower ^{1}CT state. This is especially true at 80 K, where nuclear motion is further restricted and the prompt emission exhibits dual character over a longer time span. To explain the reoccurring short-wavelength ^{1}LE emission at long lifetimes, we identify TTA as the most likely mechanism. Having a much longer lifetime than TADF, TTA typically occurs in the millisecond domain and requires two molecules to be in close proximity. In TTA, two triplet excitons are up-converted into one singlet exciton of higher energy, and even though the emitter is doped at only 1 wt% in zeonex, it is plausible that weak TTA is observed at very long times (once brighter and faster-decaying emission from TADF-active states is depleted). Because the energy of two triplet excitons is larger than the energy of the ^{1}LE state, this state can be populated. Loss of the red emission edge at several tens of milliseconds for **CNQxP-BDT-TIPS** suggests that as TADF emission dies out, the emission band becomes dominated by pure ^{1}LE emission with significant vibronic character. **CNQxP-DMAC** does not lose its red emission edge and is therefore a combination of both ^{1}LE and ^{1}CT emission even at very long lifetimes - resulting from TTA and very long-lived TADF, respectively. In **CNQxP-BDT-TIPS**, which also has a larger ΔE_{ST}, TTA seems to be more intense as it starts to appear at earlier decay times and becomes more prominent in the longer millisecond regime. The absence of LE

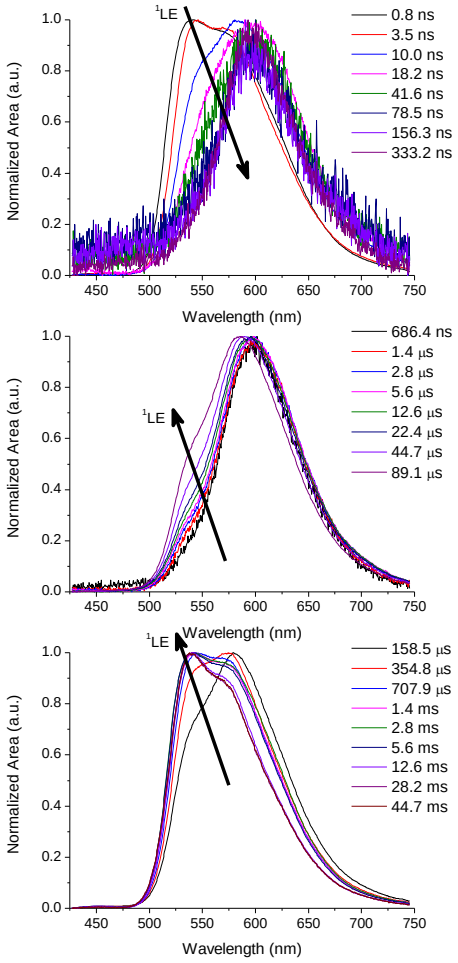

Figure 3.6: Time-resolved emission extracted from the room temperature decay of **CNQxP-BDT-TIPS** showing the slow transfer from ^{1}LE to ^{1}CT emission at short lifetimes and the reappearance of pure ^{1}LE emission at very long lifetimes.

emission in the millisecond domain for both compounds at 80 K is also consistent with either a TADF or TTA mechanism, as these processes are both inhibited at lower temperatures.

3.2.4. Laser power experiments

To verify a TADF mechanism in the microsecond domain in both CNQxP compounds, the dependence of emission intensity on excitation laser power was measured by attenuation of the excitation beam with reflective neutral density filters. Both compounds were probed with a delay time after the laser pulse of 4

μs and an integration time of 12 μs. Even at very low powers (0.2 μJ vs. 78.0 μJ at the start of the measurement), the slope of the log-log plot remains unity, suggesting TADF-like behaviour. In the case of TTA, we would expect this slope to increase at low excitation power (second order with the exciton density). Similar measurements at longer delay times reveal that the slopes become slightly larger (Figure S3.6b,d), which could indicate the presence of a TTA emission contribution at very long times. However as we observe a combination with TADF at these delay times, we still do not observe a gradient of 2 that is otherwise indicative of 'pure' TTA emission (Figure S3.7b,d).

3.3. Conclusions

In this work, we have introduced a triisopropyl-substituted benzo[1,2-*b*:4,5-*b*']dithiophene (BDT-TIPS) donor unit that is directly coupled via the central phenyl moiety, giving rise to two new donor-acceptor-donor emitters. In contrast with analogous 9,9-dimethyl-9,10-dihydroacridine (DMAC) containing compounds, **TXO2-BDT-TIPS** was found to show room temperature phosphorescence as a result of a low-lying localized triplet state on the BDT-TIPS group itself. The BDT-TIPS precursor was investigated and was found to also exhibit phosphorescence at room temperature, presumably due to the sulphur atoms that afford increased spin-orbit coupling and thereby enhance the radiative T_1->S_0 relaxation. The **CNQxP-DMAC** chromophore prepared in this work was found to show TADF, with a very small ΔE_{ST} value giving rise to delayed emission even at 80 K. Its BDT-TIPS counterpart also showed delayed emission attributed to TADF. Despite larger ΔE_{ST} (0.18 eV) than its DMAC counterpart, the BDT-TIPS promotes (r)ISC by increased spin-orbit coupling in the CNQxP compound, leading to long-lived orange TADF. At longer times, triplet-triplet annihilation (TTA) repopulating the ^{1}LE state gives rise to resurgent short-wavelength LE emission for both CNQxP compounds.

Although RTP and very long lived TADF/TTA emission are not desirable for OLED applications, the long-lived and red-shifted emission for **TXO2-BDT-TIPS** and **CNQxP-BDT-TIPS** may find future use in other applications such as imaging or sensing.[55-57] Furthermore, the BDT-TIPS donor investigated here represents a valuable addition to the library of available donor compounds for TADF, particularly suitable to generate deep-blue emission.

3.4. References

1. H. Yao, L. Ye, H. Zhang, S. Li, S. Zhang and J. Hou, *Chem. Rev.*, 2016, **116** (12), 7397-7457.
2. J. Hou, M.-H. Park, S. Zhang, Y. Yao, L.-M. Chen, J.-H. Li and Y. Yang, *Macromolecules*, 2008, **41** (16), 6012-6018.
3. Y. Liang, Z. Xu, J. Xia, S.-T. Tsai, Y. Wu, G. Li, C. Ray and L. Yu, *Adv. Mater.*, 2010, ***22*** (20), E135-E138.
4. C. Liu, K. Wang, X. Hu, Y. Yang, C.-H. Hsu, W. Zhang, S. Xiao, X. Gong and Y. Cao, *ACS Appl. Mater. Interfaces*, 2013, **5** (22), 12163-12167.
5. L. Lu and L. Yu, *Adv. Mater.*, 2014, **26** (26), 4413-4430.
6. M. Nakano, S. Shinamura, R. Sugimoto, I. Osaka, E. Miyazaki and K. Takimiya, *Org. Lett.*, 2012, **14** (21), 5448-5451.
7. T. Cardeynaels, S. Paredis, J. Deckers, S. Brebels, D. Vanderzande, W. Maes and B. Champagne, *Phys. Chem. Chem. Phys.*, 2020, **22** (28), 16387-16399.
8. P. L. Dos Santos, J. S. Ward, M. R. Bryce and A. P. Monkman, *J. Phys. Chem. Lett.*, 2016, **7** (17), 3341-6.
9. P. Stachelek, J. S. Ward, P. L. dos Santos, A. Danos, M. Colella, N. Haase, S. J. Raynes, A. S. Batsanov, M. R. Bryce and A. P. Monkman, *ACS Appl. Mater. Interfaces*, 2019, **11** (30), 27125-27133.
10. I. Lee and J. Y. Lee, *Org. Electron.*, 2016, **29**, 160-164.
11. N. Haase, A. Danos, C. Pflumm, A. Morherr, P. Stachelek, A. Mekic, W. Brütting and A. P. Monkman, *J. Phys. Chem. C*, 2018, **122** (51), 29173-29179.
12. P. L. Santos, J. S. Ward, P. Data, A. S. Batsanov, M. R. Bryce, F. B. Dias, and A. P. Monkman, *J. Mater. Chem. C*, 2016, **4** (17), 3815-3824.
13. R. Furue, K. Matsuo, Y. Ashikari, H. Ooka, N. Amanokura and T. Yasuda, *Adv. Opt. Mater.*, 2018, **6** (5).
14. S. M. A. Fateminia, Z. Mao, S. Xu, Z. Yang, Z. Chi and B. Liu, *Angew. Chem. Int. Ed.*, 2017, **56** (40), 12160-12164.
15. G. Zhang, G. M. Palmer, M. W. Dewhirst and C. L. Fraser, *Nat. Mater.*, 2009, **8** (9), 747-751.
16. F. Ni, Z. Zhu, X. Tong, M. Xie, Q. Zhao, C. Zhong, Y. Zou and C. Yang, *Chem. Sci.*, 2018, **9** (28), 6150-6155.
17. P. Lehner, C. Staudinger, S. M. Borisov and I. Klimant, *Nat. Commun.*, 2014, **5** (1), 4460.
18. D. Lee, O. Bolton, B. C. Kim, J. H. Youk, S. Takayama and J. Kim, *J. Am. Chem. Soc.*, 2013, **135** (16), 6325-6329.
19. K. Jinnai, R. Kabe and C. Adachi, *Adv. Mater.*, 2018, **30** (38), 1800365.
20. H. Li, S. Ye, J.-q. Guo, J.-t. Kong, J. Song, Z.-h. Kang and J.-l. Qu, *J. Mater. Chem. C*, 2019, **7** (34), 10605-10612.
21. T. J. Penfold, *J. Phys. Chem. C*, 2015, **119** (24), 13535-13544.
22. M. J. Frisch, G. W. Trucks, H. B. Schlegel, G. E. Scuseria, M. A. Robb, J. R. Cheeseman, G. Scalmani, V. Barone, G. A. Petersson, H. Nakatsuji, X. Li, M. Caricato, A. V. Marenich, J. Bloino, B. G. Janesko, R. Gomperts, B. Mennucci, H. P. Hratchian, J. V. Ortiz, A. F. Izmaylov, J. L. Sonnenberg, D. Williams-Young, F. Ding, F. Lipparini, F. Egidi, J. Goings, B. Peng, A. Petrone, T. Henderson, D. Ranasinghe, V. G. Zakrzewski, J. Gao, N. Rega, G. Zheng, W. Liang, M. Hada, M. Ehara, K. Toyota, R. Fukuda, J.

Hasegawa, M. Ishida, T. Nakajima, Y. Honda, O. Kitao, H. Nakai, T. Vreven, K. Throssell, J. A. Montgomery, Jr., J. E. Peralta, F. Ogliaro, M. J. Bearpark, J. J. Heyd, E. N. Brothers, K. N. Kudin, V. N. Staroverov, T. A. Keith, R. Kobayashi, J. Normand, K. Raghavachari, A. P. Rendell, J. C. Burant, S. S. Iyengar, J. Tomasi, M. Cossi, J. M. Millam, M. Klene, C. Adamo, R. Cammi, J. W. Ochterski, R. L. Martin, K. Morokuma, O. Farkas, J. B. Foresman, and D. J. Fox, Gaussian 16, Revision A.03, Gaussian, Inc.: Wallingford CT, 2016.

23. T. Le Bahers, C. Adamo and I. Ciofini, *J. Chem. Theory Comput.*, 2011, **7** (8), 2498-506.
24. J. S. Ward, A. Danos, P. Stachelek, M. A. Fox, A. S. Batsanov, A. P. Monkman and M. R. Bryce, *Mater. Chem. Front.*, 2020, DOI: 10.1039/D0QM00429D.
25. S. Wang, Z. Cheng, X. Song, X. Yan, K. Ye, Y. Liu, G. Yang and Y. Wang, *ACS Appl. Mater. Interfaces*, 2017, **9** (11), 9892-9901.
26. N. A. Kukhta, H. F. Higginbotham, T. Matulaitis, A. Danos, A. N. Bismillah, N. Haase, M. K. Etherington, D. S. Yufit, P. R. McGonigal, J. V. Gražulevičius and A. P. Monkman, *J. Mater. Chem. C*, 2019, **7** (30), 9184-9194.
27. E. Aksoy, A. Danos, C. Varlikli and A. P. Monkman, *Dyes Pigm.*, 2020, 108707.
28. C. I. C. Crucho, J. Avó, R. Nobuyasu, S. N. Pinto, F. Fernandes, J. C. Lima, M. N. Berberan-Santos and F. B. Dias, *Mater. Sci. Eng. C*, 2020, **109,** 110528.
29. X. Xiong, F. Song, J. Wang, Y. Zhang, Y. Xue, L. Sun, N. Jiang, P. Gao, L. Tian, X and Peng, *J. Am. Chem. Soc.*, 2014, **136** (27), 9590-7.
30. Y. Wu, L. Jiao, F. Song, M. Chen, D. Liu, W. Yang, Y. Sun, G. Hong, L. Liu and X. Peng, *Chem. Commun.*, 2019, **55** (96), 14522-14525.

3.5. Supporting information

3.5.1. Experimental details

3.5.1.1. Materials and methods

All reagents and chemicals were obtained from commercial sources and used without further purification. Benzo[1,2-*b*:4,5-*b*']dithiophene was acquired from TCI Europe. Dry solvents were obtained using an MBraun solvent purification system (MB SPS-800) equipped with alumina columns. Preparative (recycling) size exclusion chromatography (SEC) was performed on a JAI LC-9110 NEXT system equipped with JAIGEL 1H and 2H columns (eluent chloroform, flow rate 3.5 mL min^{-1}). Proton and carbon nuclear magnetic resonance (^{1}H and ^{13}C NMR) spectra were obtained on a Varian or Jeol spectrometer operating at 400 MHz for ^{1}H (100 MHz for ^{13}C). Chemical shifts (δ) are given in ppm relative to $CDCl_3$ (δ = 7.26 ppm for ^{1}H NMR, δ = 77.06 ppm for ^{13}C NMR). All NMR spectra were taken at room temperature, unless stated otherwise. Matrix-assisted laser desorption/ionization - time-of-flight (MALDI-ToF) mass spectra were recorded on a Bruker Daltonics Ultraflex II ToF/ToF. Approximately 1 µL of the matrix solution (16 mg mL^{-1} *trans*-2-[3-(4-*tert*-butylphenyl)-2-methyl-2-propenylidene]malononitrile (DTCB) in chloroform) was spotted onto an MTP Anchorchip 600/384 MALDI plate. The spot was allowed to dry and 1 µL of the analyte solution (0.5 mg mL^{-1} In chloroform) was spotted on top of the matrix. All solution-based absorption spectra were recorded on a Varian Cary 5000 UV-Vis-NIR spectrophotometer from Agilent Technologies. Steady-state emission spectra (in solution) were recorded on a Horiba-Jobin Yvon Fluorolog-3 spectrofluorometer equipped with a 450 W Xe lamp as the light source. All spectroscopic measurements were done in spectroscopic grade solvents. Films were prepared via drop-casting using a mixture of the emitter and host (zeonex) in toluene at 1 wt% of the emitter in zeonex. The initial solution concentrations were 100 mg mL^{-1} for zeonex. The films were drop-casted onto a quartz substrate at 65 °C to facilitate evaporation of the solvent. Absorption and emission spectra of the films were collected using a UV-3600 double beam spectrophotometer (Shimadzu) and a Fluoromax fluorimeter (Jobin Yvon), respectively. Time-resolved photoluminescence spectra and decays were recorded using a nanosecond gated spectrograph-coupled iCCD (Stanford) using

an Nd:YAG laser emitting at 355 nm (EKSPLA). Laser power experiments were conducted using an N_2 laser (Lasertechnik Berlin) emitting at 337 nm with the same nanosecond gated spectrograph-coupled iCCD (Stanford) camera, attenuating the excitation using reflective neutral density filters.

3.5.1.2. Synthesis procedures

9,9-Dimethyl-9,10-dihydroacridine (DMAC)[1], 2,7-dibromo-9,9-dimethyl-9*H*-thioxanthene-10,10-dioxide (TXO2)[2], 2,7-bis(9,9-dimethylacridin-10(9*H*)-yl)-9,9-dimethyl-9*H*-thioxanthene-10,10-dioxide (**TXO2-DMAC**)[3] and 3,6-dibromodibenzo[*a*,*c*]phenazine-11,12-dicarbonitrile (CNQxP)[4] were synthesized according to literature procedures.

2,6-bis(triisopropylsilyl)benzo[1,2-b:4,5-b']dithiophene (BDT-TIPS)[5]

To a solution of benzo[1,2-*b*:4,5-*b*']dithiophene (1.262 g, 6.63 mmol) in dry THF (10.0 mL), *n*-BuLi (2.5 M in hexane; 8.0 mL, 19.89 mmol) was added dropwise at 0 °C and the mixture was stirred for 1 h at room temperature. Afterwards, triisopropylsilyl chloride (4.2 mL, 19.6 mmol) was slowly added. After the mixture was heated to 65 °C for 16 h, it was poured out in a beaker containing water (100 mL) and hydrochloric acid (1 M, 100 mL). The resulting precipitate was collected by vacuum filtration and washed with water, methanol and *n*-hexane. The filtrate was then evaporated under reduced pressure and the remaining solid was triturated in *n*-hexane, followed by filtration and subsequent washing with *n*-hexane. BDT-TIPS was obtained as a white solid (2.49 g, 75%). ^{1}H NMR (400 MHz, $CDCl_3$): 8.29 (s, 2H), 7.50 (s, 2H), 1.48–1.37 (m, 6H), 1.15 (d, J = 7.4 Hz, 36H). ^{13}C NMR (100 MHz, $CDCl_3$): 140.62, 138.95, 138.31, 131.55, 115.63, 18.66, 11.85.

(4-(4,4,5,5-tetramethyl-1,3,2-dioxaborolan-2-yl)benzo[1,2-b:4,5-b'] dithiophene-2,6-diyl)bis(triisopropylsilane) (BDT-TIPS-pinacol)[6]

A mixture of BDT-TIPS (671.4 mg, 1.34 mmol), bis(pinacolato)diboron (571.0 mg, 2.25 mmol), $[Ir(OMe)(COD)]_2$ (53.0 mg, 0.08 mmol), and 4,4'-di-*tert*-butyl-2,2'-bipyridine (46.2 mg, 0.17 mmol) in dry cyclohexane was stirred in the dark at 80 °C for 16 h under nitrogen atmosphere. After cooling the reaction mixture down to room temperature, evaporation of the solvent under reduced pressure afforded a residue, which was purified by silica gel column chromatography

using CH_2Cl_2/petroleum ether (v/v= 20/80) as the eluent to yield BDT-TIPS-pinacol as a white solid (355.8 mg, 42%). The reaction also yielded unreacted BDT-TIPS (129.0 mg, 19%) as well as disubstituted BDT-TIPS-pinacol (127.3 mg, 13%) as the main side products. ^{1}H NMR (400 MHz, $CDCl_3$): 8.39 (s, 1H), 8.35 (s, 1H), 7.52 (s, 1H), 1.47 (s, 12H), 1.50–1.39 (m, 6H), 1.19 (d, *J* = 7.4 Hz, 36H). ^{13}C NMR (100 MHz, $CDCl_3$): 148.29, 143.97, 139.98, 138.68, 137.97, 137.73, 134.11, 130.77, 118.15, 115.95, 83.73, 24.77, 18.38, 18.37, 11.64, 11.55.

*2,7-bis(2,6-bis(triisopropylsilyl)benzo[1,2-b:4,5-b']dithiophen-4-yl)-9,9-dimethyl-9H-thioxanthene 10,10-dioxide (**TXO2-BDT-TIPS**)*

2,7-Dibromo-9,9-dimethyl-9*H*-thioxanthene-10,10-dioxide (TXO2: 99.7 mg, 239.6 µmol), BDT-TIPS-pinacol (333.2 mg, 529.8 µmol) and tetrakis(triphenylphosphine)palladium(0) (23.1 mg, 20.0 µmol) were added to a flame-dried Schlenk flask. The flask was evacuated and backfilled with nitrogen three times and pre-degassed anhydrous toluene (12 mL) and a K_2CO_3 solution (2 M, 4 mL) were added. The reaction mixture was heated at 80 °C and stirred for 24 h under a nitrogen atmosphere. The mixture was then poured into water and extracted with dichloromethane. The organic phase was dried over $MgSO_4$, filtered and the solvent was evaporated under reduced pressure. The product was purified by silica gel column chromatography using CH_2Cl_2/petroleum ether (v/v = 20/80) as the eluent. TXO2-BDT-TIPS was further purified using preparative (recycling) SEC and was obtained as a white solid (150.1 mg, 50%). ^{1}H NMR (400 MHz, $CDCl_3$, 50 °C): 8.52 (2x d, *J* = 8.1 Hz, 2H), 8.41 (2x s, 2H), 8.30 (2x d, *J* = 1.5 Hz, 2H), 8.03 (2x dd, *J* = 8.1, 1.5 Hz, 2H), 7.65 (2x s, 2H), 7.52 (2x s, 2H), 2.05 (2x s, 6H), 1.54–1.39 (m, 12H), 1.20 (2x d, J = 7.5 Hz, 72H). ^{13}C NMR (100 MHz, $CDCl_3$, 50 °C): 146.23, 144.69, 141.93, 140.81, 139.88, 139.39, 139.20, 137.00, 135.96, 132.13, 129.94, 128.76, 128.24, 127.71, 124.95, 115.95, 39.83, 31.20, 18.69, 11.91. MS (MALDI-ToF) Calcd. for $C_{71}H_{102}O_2S_5Si_4$ $[M]^+$: *m/z* 1258.56, found: 1258.48.

*3,6-bis(2,6-bis(triisopropylsilyl)benzo[1,2-b:4,5-b']dithiophen-4-yl)dibenzo[a,c]phenazine-11,12-dicarbonitrile (**CNQxP-BDT-TIPS**)*

CNQxP (99.8 mg, 204.4 µmol), BDT-TIPS-pinacol (283.5 mg, 452.0 µmol) and tetrakis(triphenylphosphine)palladium(0) (13.6 mg, 11.8 µmol) were added to a flame-dried Schlenk flask. The flask was evacuated and backfilled with nitrogen three times and pre-degassed toluene (12 mL) and a K_2CO_3 solution (2 M, 4 mL) were added. The reaction mixture was heated at 80 °C and stirred for 24 h under a nitrogen atmosphere. The mixture was then poured into water and extracted with dichloromethane. The organic phase was dried over $MgSO_4$, filtered and the solvent was evaporated under reduced pressure. The product was purified by silica gel column chromatography using CH_2Cl_2/petroleum ether (v/v = 20/80) as the eluent. CNQxP-BDT-TIPS was further purified using preparative (recycling) SEC and was obtained as an orange solid (43.0 mg, 16%). ^{1}H NMR (400 MHz, $CDCl_3$): 9.59 (d, *J* = 8.3 Hz, 2H), 8.98 (s, br., 2H), 8.88 (s, 2H), 8.34 (s, 2H), 8.33 (d, *J* = 8.3 Hz, 2H), 7.58 (s, 2H), 7.53 (s, 2H), 1.33 (h, *J* = 7.6 Hz, 6H), 1.18 (h, *J* = 7.4 Hz, 6H), 1.04 (d, *J* = 7.4 Hz, 36H), 0.87 (d, *J* = 7.4 Hz, 36H). ^{13}C NMR (100 MHz, $CDCl_3$): 146.15, 144.12, 142.20, 141.85, 140.70, 139.38, 139.34, 138.68, 137.46, 137.01, 133.47, 132.13, 129.95, 129.75, 128.54, 128.51, 128.09, 125.11, 115.88, 115.40, 113.49, 18.53, 18.33, 11.73, 11.61. MS (MALDI-ToF) Calcd. for $C_{78}H_{98}N_4S_4Si_4$ $[M]^+$: *m/z* 1330.58, found: 1330.59.

*3,6-bis(9,9-dimethylacridin-10(9H)-yl)dibenzo[a,c]phenazine-11,12-dicarbonitrile (**CNQxP-DMAC**)*

CNQxP (100.5 mg, 205.9 µmol), 9,9-dimethyl-9,10-dihydroacridine (96.1 mg, 459.2 µmol), palladium(II) acetate (12.6 mg, 56.1 µmol), tri-*tert*-butylphosphine tetrafluoroborate (16.8 mg, 57.9 µmol) and sodium *tert*-butoxide (47.3 mg, 492.2 µmol) were dissolved in dry toluene (16 mL) under argon atmosphere. The mixture was stirred at 120 °C for 24 h and then cooled down to room temperature. The mixture was then poured into water and extracted with CH_2Cl_2. The organic phase was dried over anhydrous $MgSO_4$, filtered and the solvent was removed under reduced pressure. The crude product was purified by column chromatography using CH_2Cl_2/petroleum ether (v/v = 20/80) as the eluent. CNQxP-DMAC was further purified using

preparative (recycling) SEC and was obtained as a red solid (13.4 mg, 9%). ^{1}H NMR (400 MHz, $CDCl_3$): 9.67 (d, *J* = 8.5 Hz, 2H), 8.90 (s, 2H), 8.45 (d, *J* = 1.9 Hz, 2H), 7.83 (dd, *J* = 8.5, 1.9 Hz, 2H), 7.61–7.40 (m, 4H), 7.12–6.72 (m, 8H), 6.42–6.14 (m, 4H), 1.72 (s, 12H). ^{13}C NMR (100 MHz, $CDCl_3$): 145.75, 145.49, 142.20, 140.43, 137.53, 135.31, 132.23, 130.55, 130.36, 128.61, 126.51, 126.17, 125.71, 121.25, 115.22, 114.19, 113.90, 36.11, 31.56. MS (MALDI-ToF) Calcd. for $C_{52}H_{36}N_6$ $[M]^+$: *m/z* 744.30, found: 744.31.

3.5.2. Additional TDDFT calculations

Table S3.1: TDDFT results for the vertical singlet excitation energies and corresponding oscillator strengths, the vertical triplet excitation energies, the nature of the various transitions, charge transfer distance (d_{CT}) and change in dipole moment ($\Delta\mu$, excited – ground state dipole) accompanying the S0->S_3 and S0->T_3 transitions in cyclohexane.

	S_3					T_3			
Compound	E (eV)	f	Nature	d_{CT} (Å)	$\Delta\mu$ (D)	E (eV)	Nature	d_{CT} (Å)	$\Delta\mu$ (D)
TXO2-DMAC	3.69	0.00[b]	H->L+1	1.37	6.98	3.43	H->L+1	0.59	1.53
TXO2-BDT-TIPS	3.94	0.02	H->L+2	1.86	4.19	3.46	H-3->L+1	1.59	2.75
CNQxP-DMAC	3.01	0.00[b]	H-10->L	0.56	1.84	2.61	H-10->L	1.20	4.08
CNQxP-BDT-TIPS	3.04	0.02	H-14->L	1.19	4.01	2.62	H-14->L	0.11	0.39

[b] The value for the oscillator strength does not change when modifying the D-A dihedral angle by ±10°.

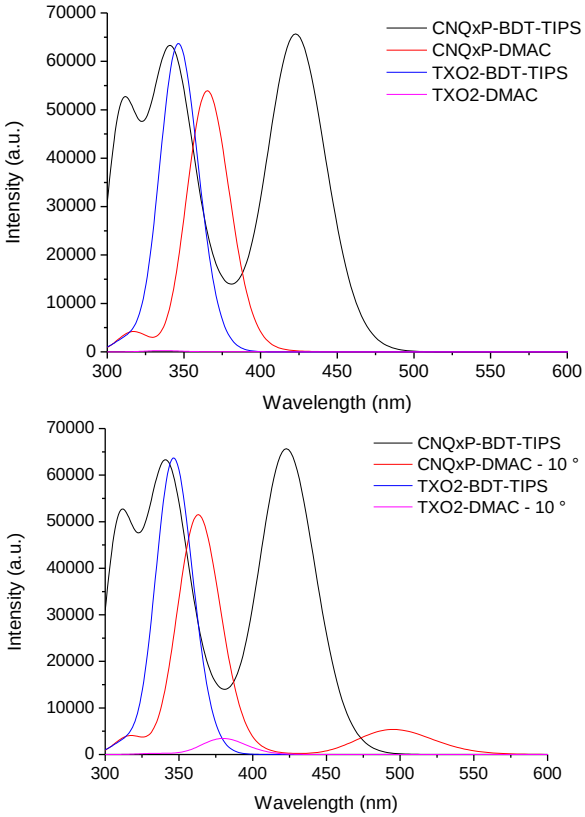

Figure S3.1: Simulated UV-VIS spectra from the TDDFT results for the optimized geometries (top) and molecules with a modified dihedral angle of ±10° for the DMAC-containing compounds (bottom).

3.5.3. Time-resolved emission spectra

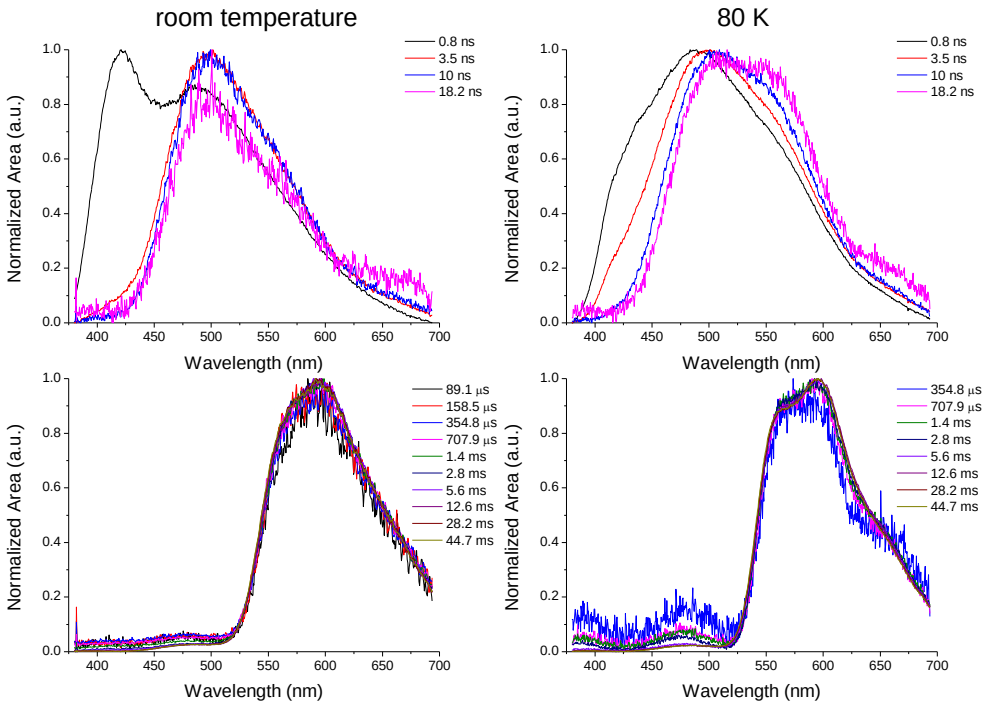

Figure S3.2: Time-resolved emission at various times in the photoluminescence decay for **TXO2-BDT-TIPS** in zeonex at room temperature (left) and at 80 K (right).

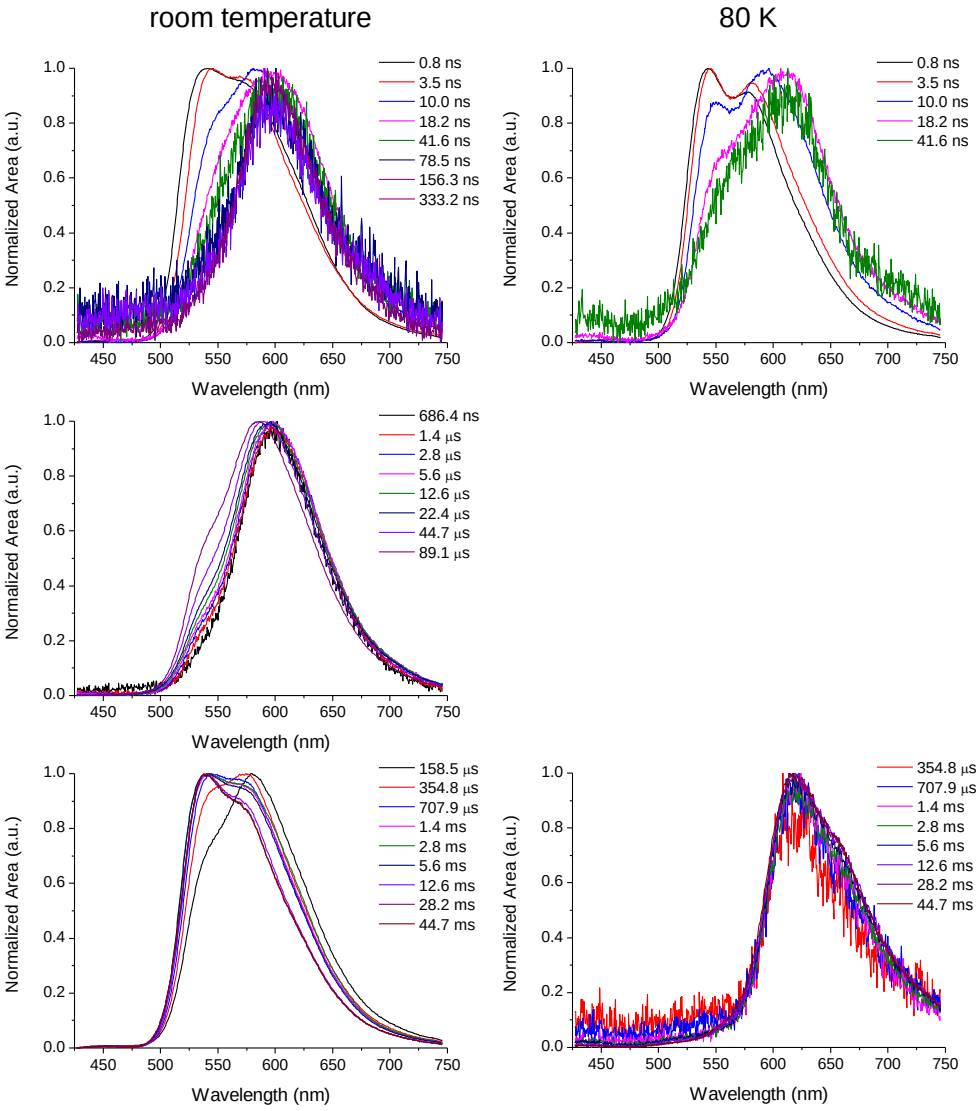

Figure S3.3: Time-resolved emission at various times in the photoluminescence decay for **CNQxP-BDT-TIPS** in zeonex at room temperature (left) and at 80 K (right).

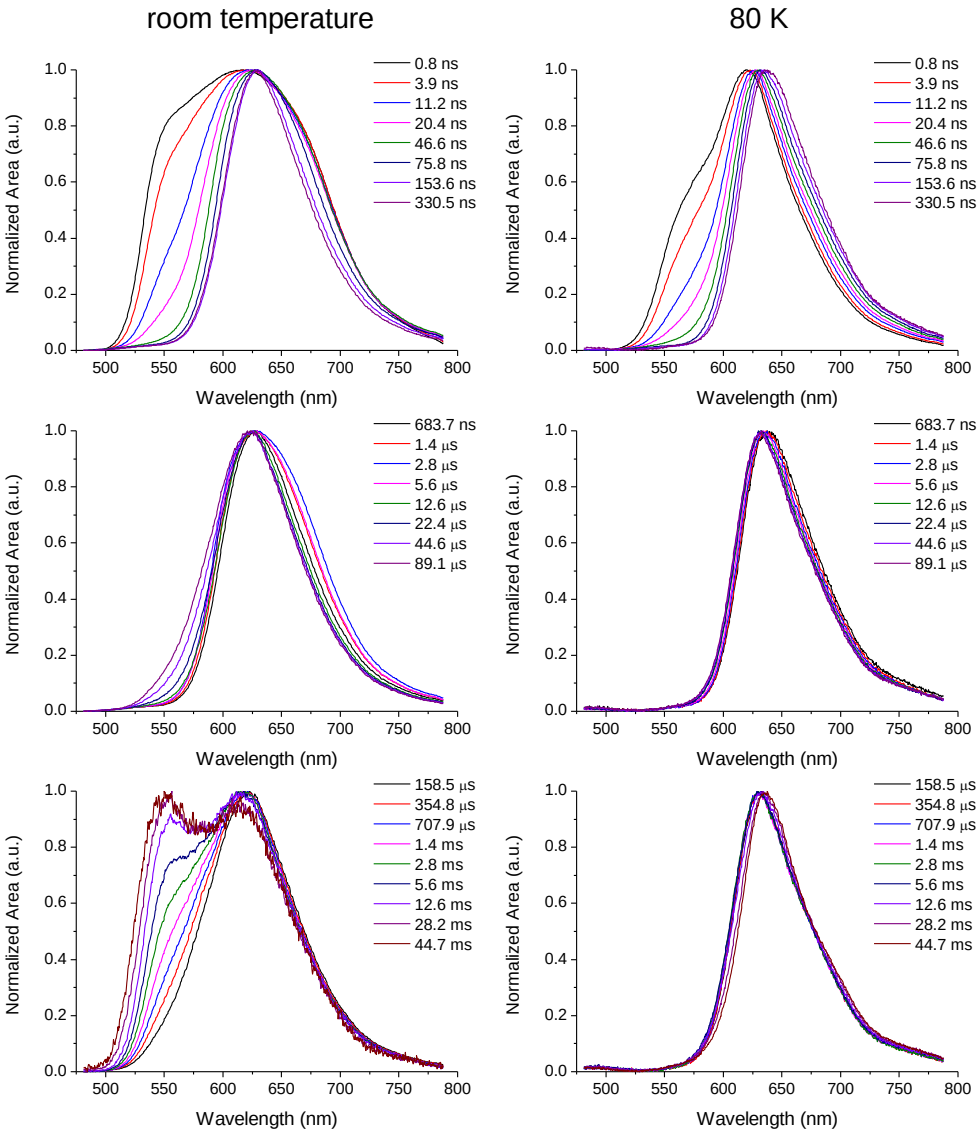

Figure S3.4: Time-resolved emission at various times in the photoluminescence decay for **CNQxP-DMAC** in zeonex at room temperature (left) and at 80 K (right).

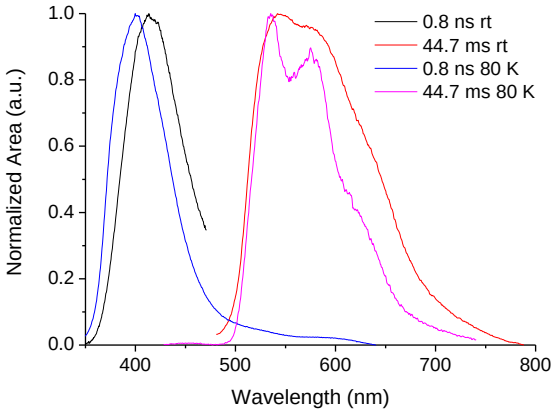

Figure S3.5: Prompt fluorescence and phosphorescence at room temperature (rt) and at 80 K for the BDT-TIPS precursor.

3.5.4. Laser power experiments

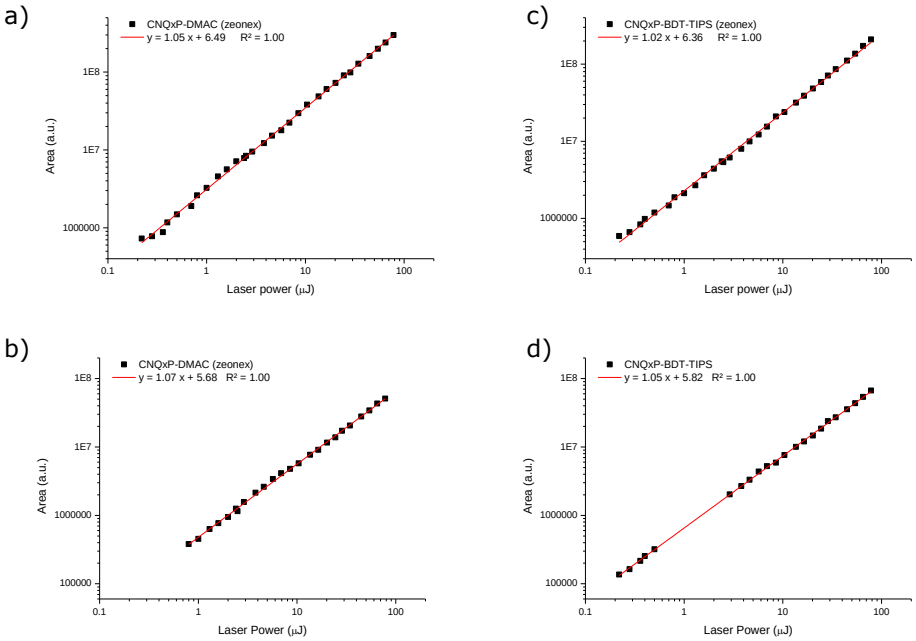

Figure S3.6: Laser power experiments using a N_2 laser: a) **CNQxP-DMAC**, time delay (TD) = 4 μs, integration time (IT) = 12 μs; b) **CNQxP-DMAC**, TD = 100 μs, IT = 10 ms; c) **CNQxP-BDT-TIPS**, TD = 4 μs, IT = 12 μs; d) **CNQxP-BDT-TIPS**, TD = 2 ms, IT = 3 ms.

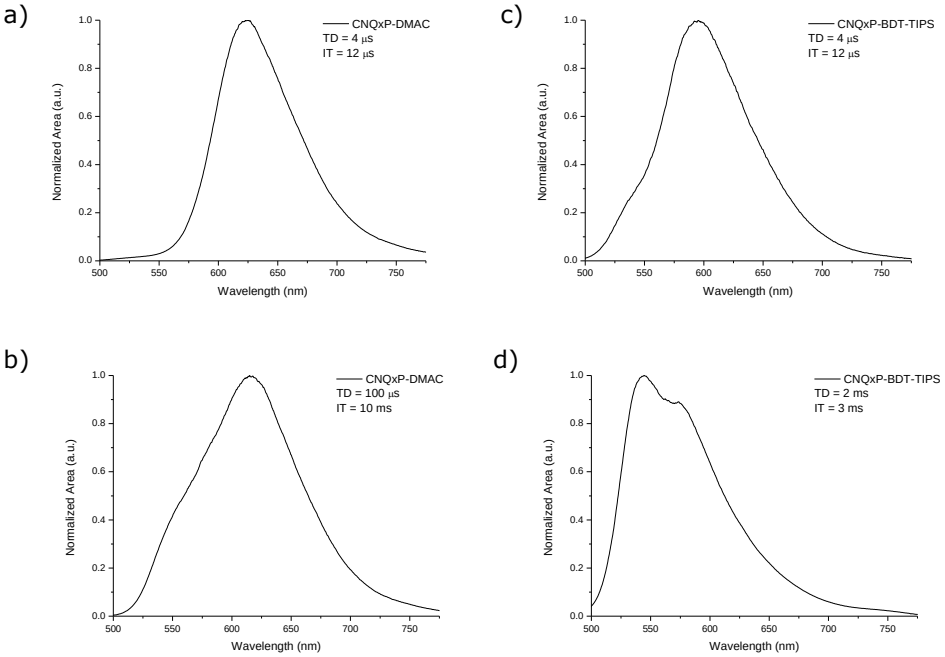

Figure S3.7: Time-resolved emission used for the determination of the laser power dependence of Figure S6 taken at a laser power of 78.2 μJ and at various time delays (TD) and integration times (IT).

3.5.5. Optimized geometry and orbital topologies for BDT-TIPS

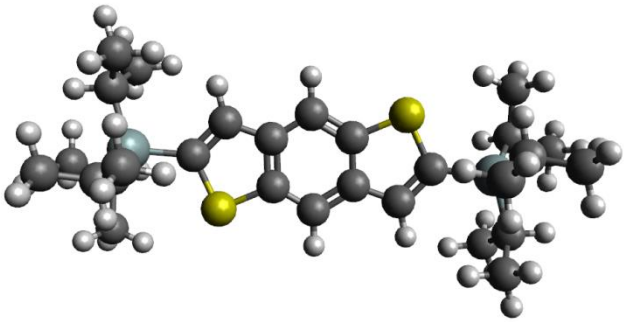

HOMO

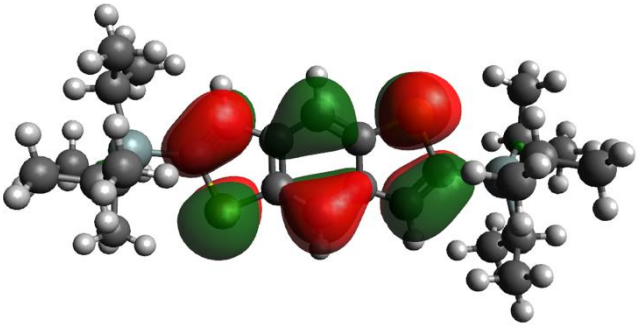

LUMO

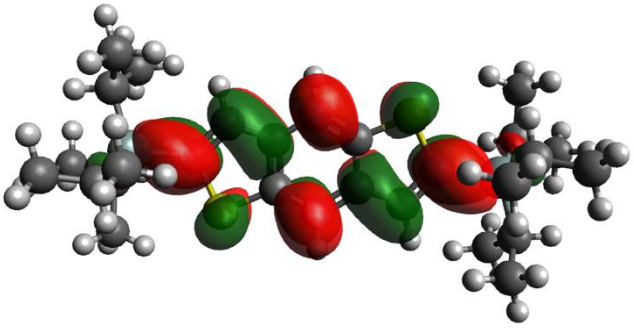

Figure S3.8: Optimized geometry and orbital topologies for the BDT-TIPS precursor.

3.5.6. Ground/excited state electron density differences

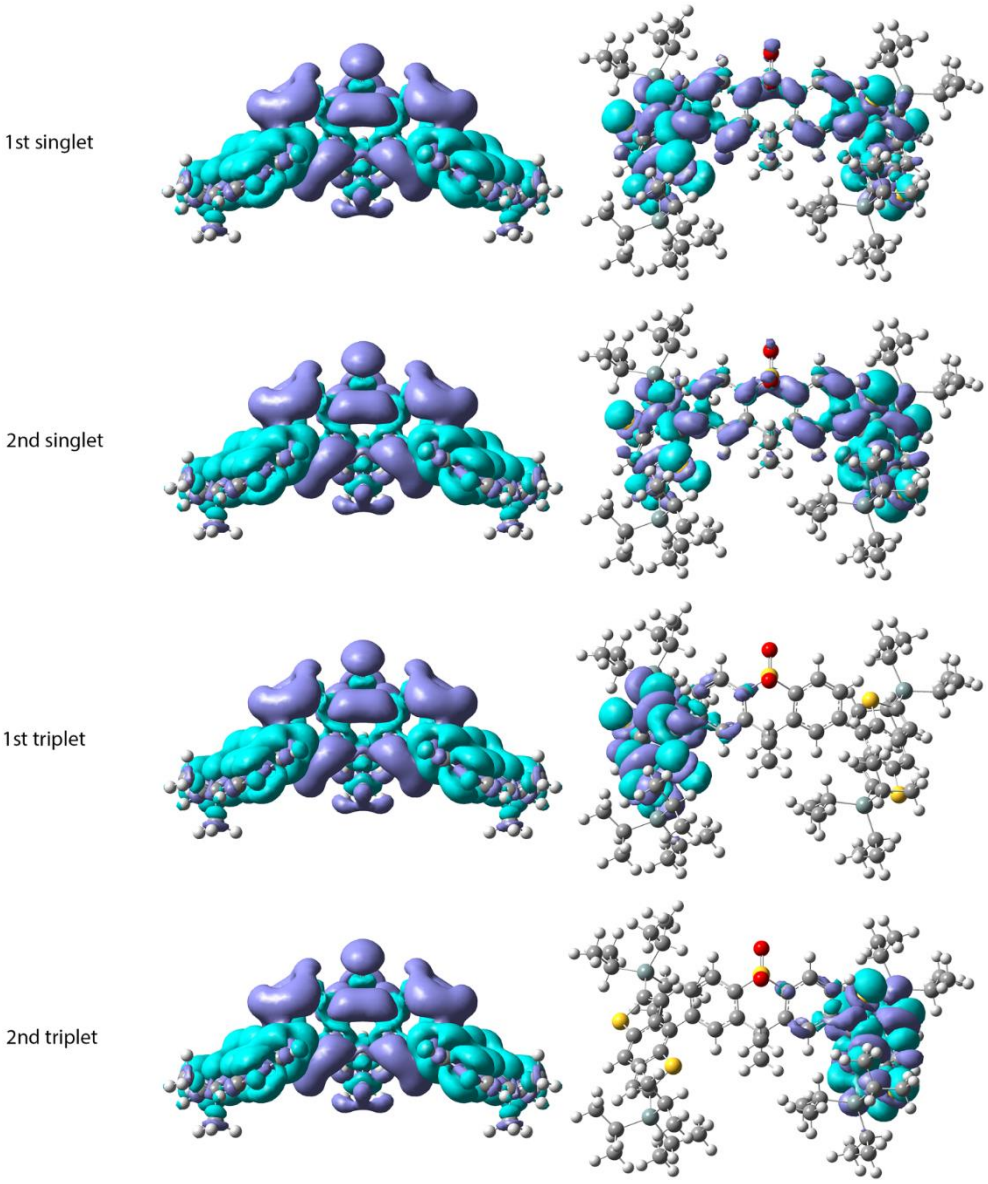

Figure S3.9: Ground/excited state electron density differences for **TXO2-DMAC** (left) and **TXO2-BDT-TIPS** (right). Isocontour values = 0.0004 a.u. for all densities. The cyan regions indicate a decrease in charge density whereas the purple regions indicate an increase in charge density.

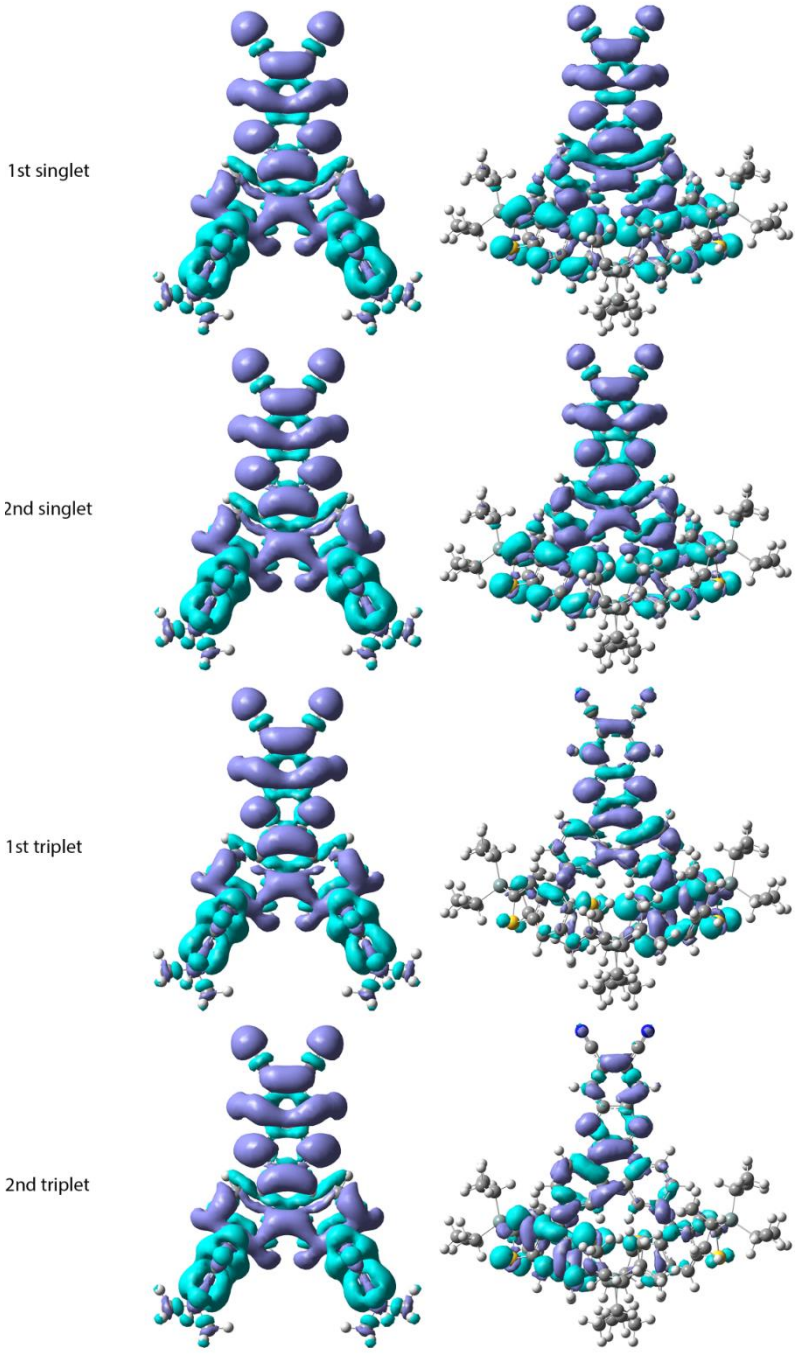

Figure S3.10: Ground/excited state electron density differences for **CNQxP-DMAC** (left) and **CNQxP-BDT-TIPS** (right). Isocontour values = 0.0004 a.u. for all densities. The cyan regions indicate a decrease in charge density whereas the purple regions indicate an increase in charge density.

3.5.7. NMR-spectra

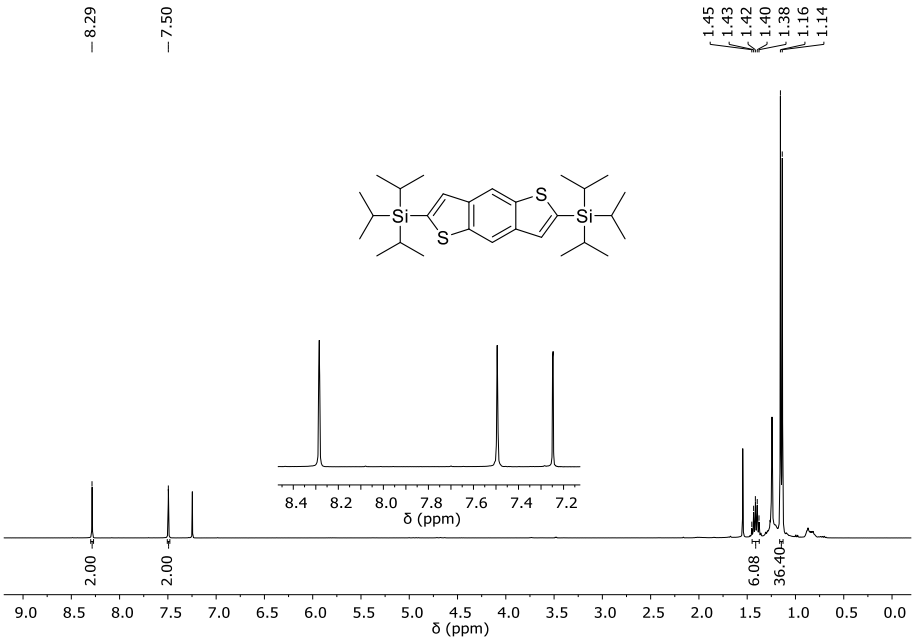

Figure S3.11: ^{1}H NMR spectrum of BDT-TIPS in $CDCl_3$.

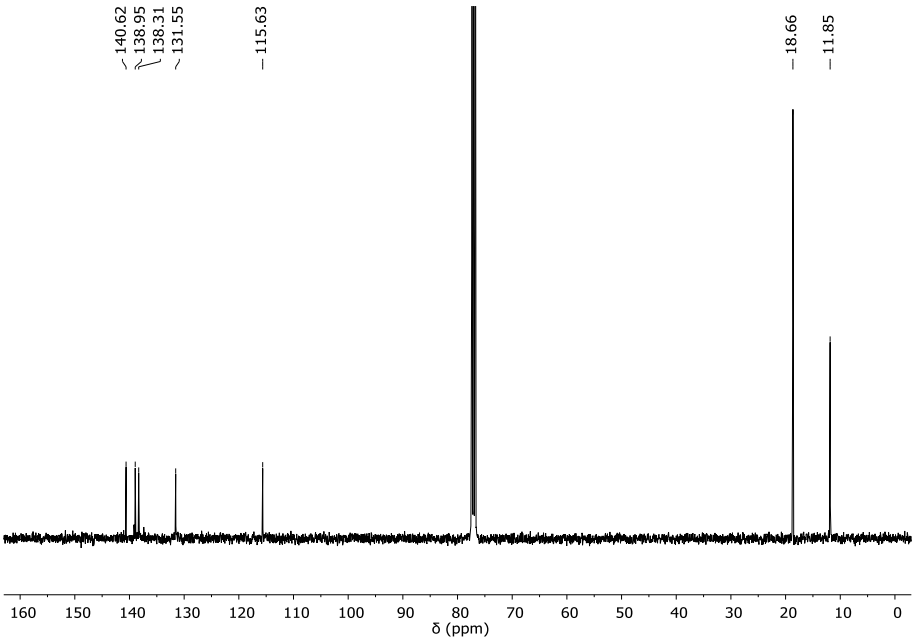

Figure S3.12: ^{13}C NMR spectrum of BDT-TIPS in $CDCl_3$.

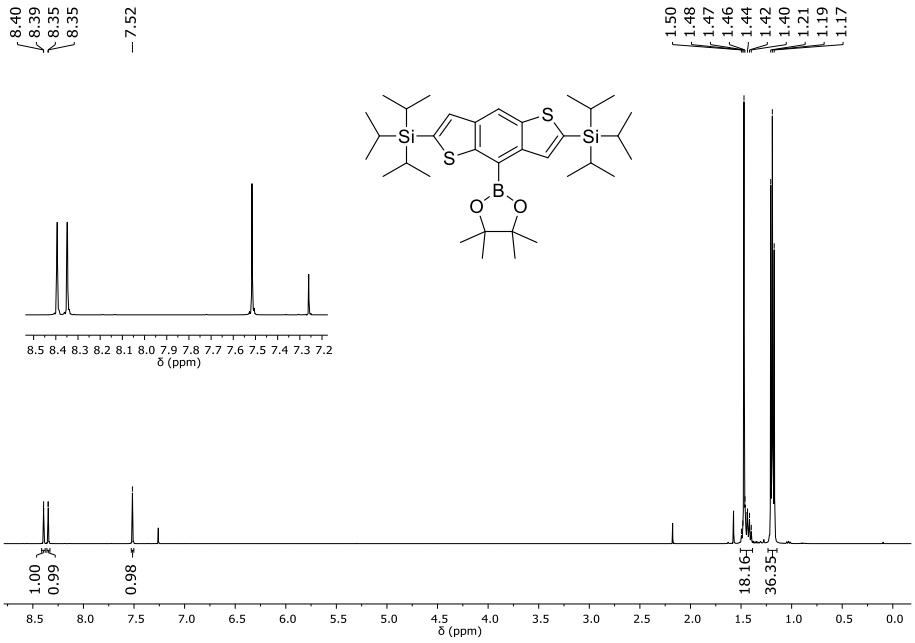

Figure S3.13: ^{1}H NMR spectrum of BDT-TIPS-pinacol in $CDCl_3$.

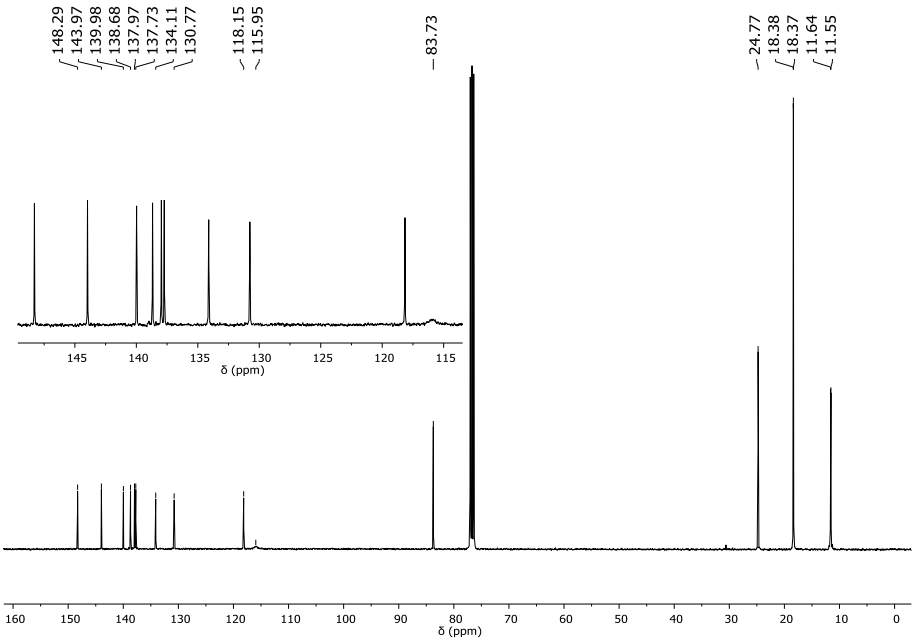

Figure S3.14: ^{13}C NMR spectrum of BDT-TIPS-pinacol in $CDCl_3$.

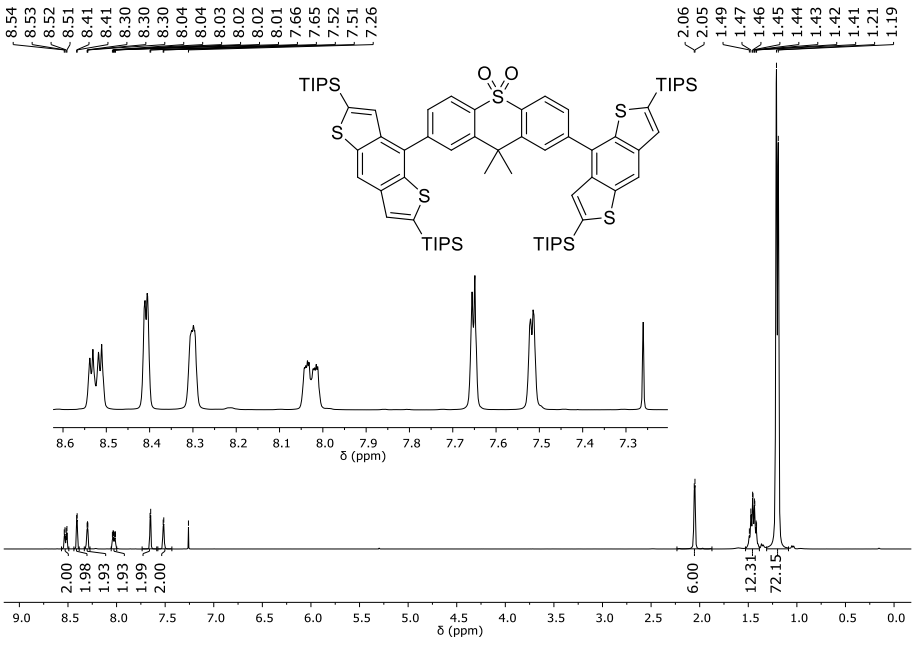

Figure S3.15: ^{1}H NMR spectrum of **TXO2-BDT-TIPS** in $CDCl_3$.

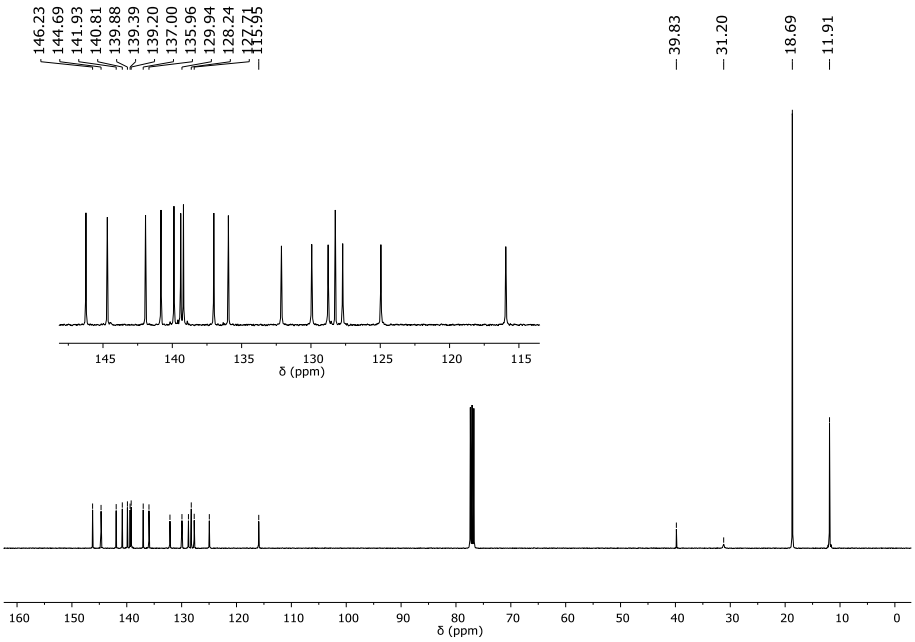

Figure S3.16: ^{13}C NMR spectrum of **TXO2-BDT-TIPS** in $CDCl_3$.

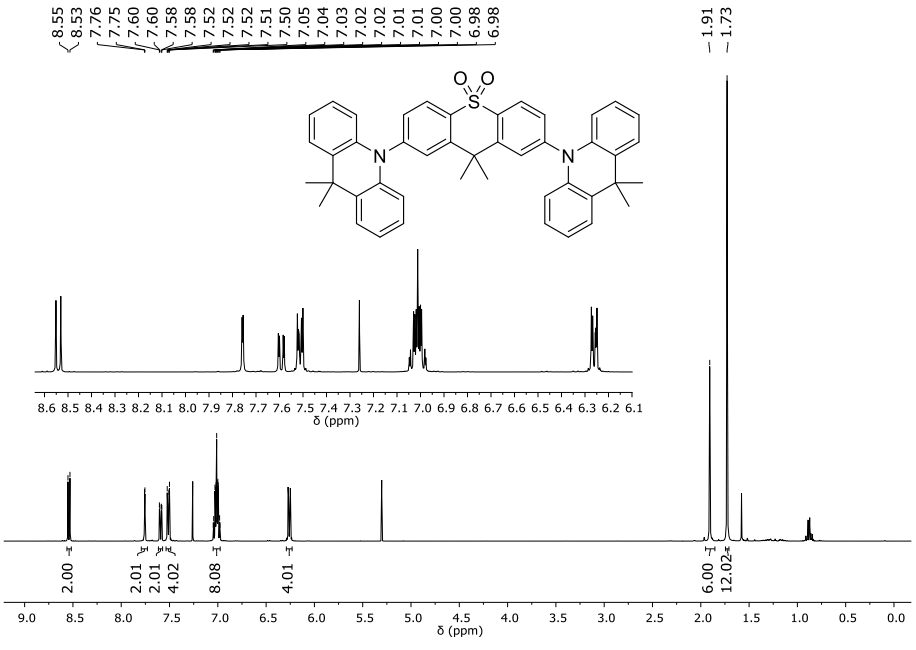

Figure S3.17: ^{1}H NMR spectrum of **TXO2-DMAC** in $CDCl_3$.

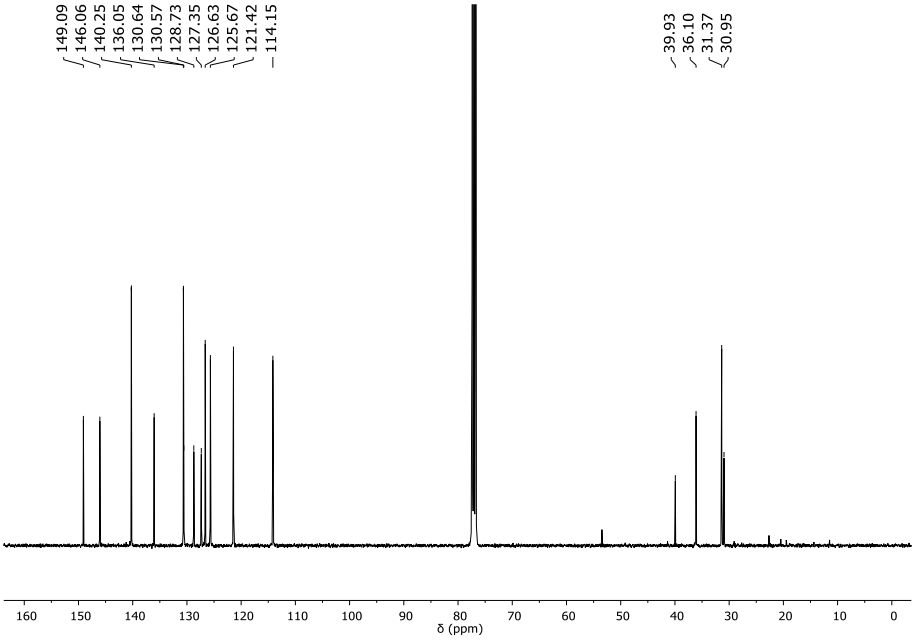

Figure S3.18: ^{13}C NMR spectrum of **TXO2-DMAC** in $CDCl_3$.

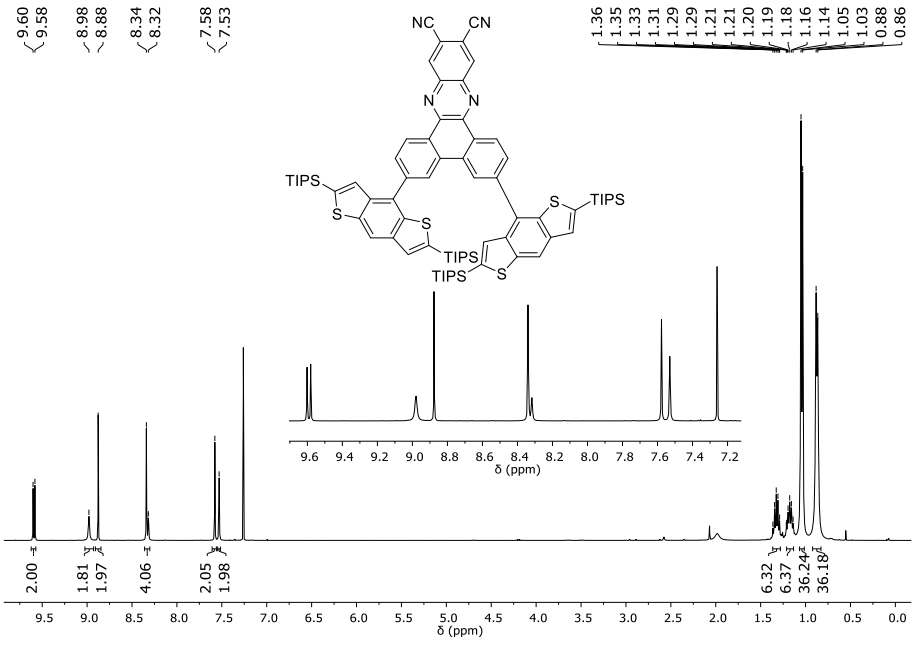

Figure S3.19: ^{1}H NMR spectrum of **CNQxP-BDT-TIPS** in $CDCl_3$.

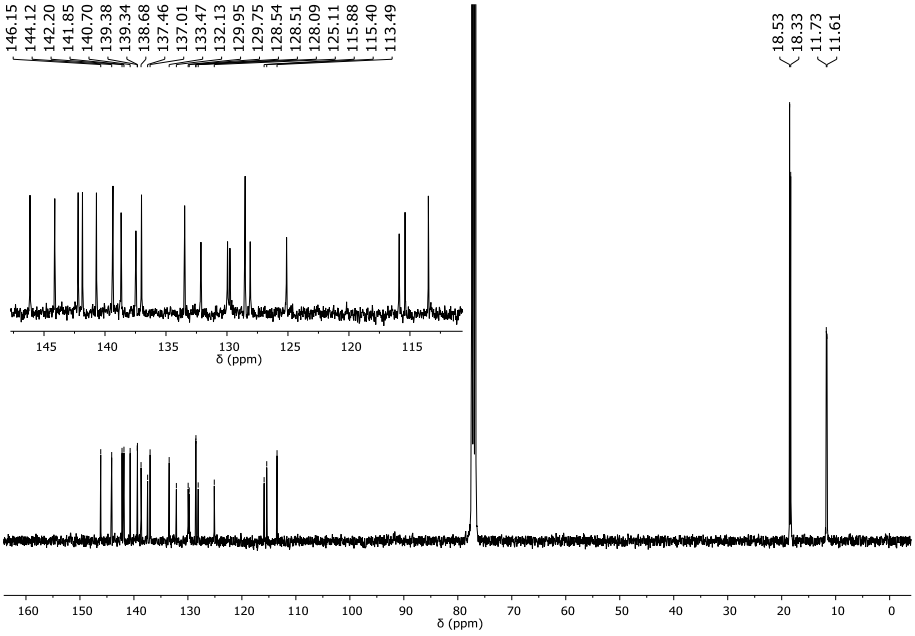

Figure S3.20: ^{13}C NMR spectrum of **CNQxP-BDT-TIPS** in $CDCl_3$.

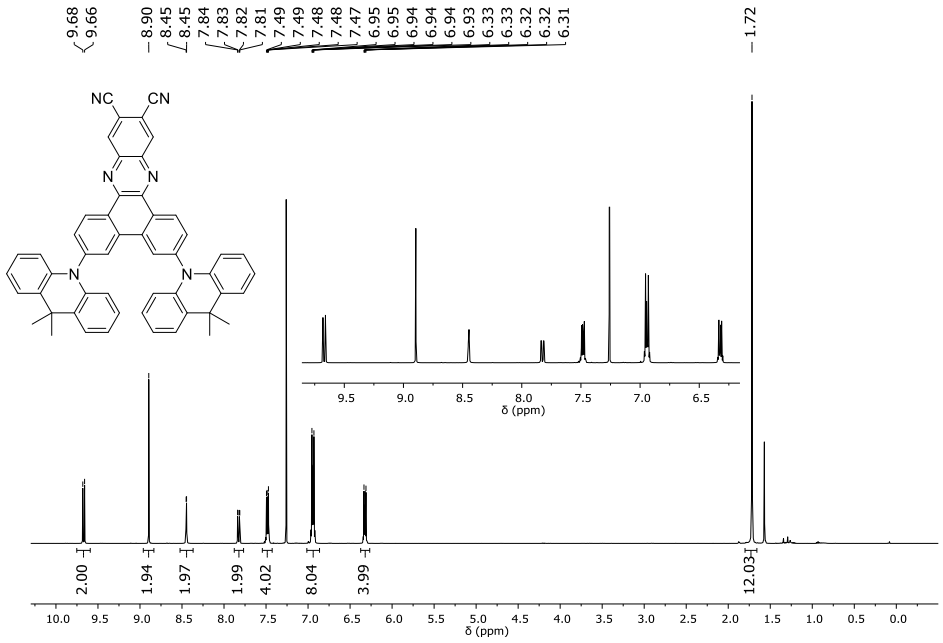

Figure S3.21: ^{1}H NMR spectrum of **CNQxP-DMAC** in $CDCl_3$.

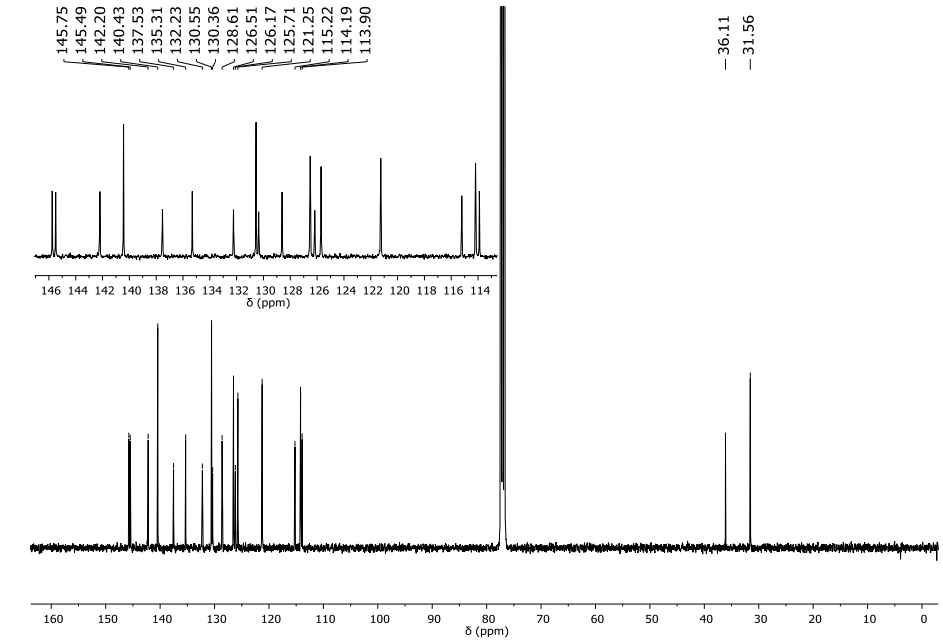

Figure S3.22: ^{13}C NMR spectrum of **CNQxP-DMAC** in $CDCl_3$.

3.5.8. Supporting information references

1. J. Deckers, T. Cardeynaels, H. Penxten, A. Ethirajan, M. Ameloot, M. Kruk, B. Champagne and W. Maes, *Chemistry*, 2020, DOI: 10.1002/chem.202002549.
2. P. L. Santos, J. S. Ward, P. Data, A. S. Batsanov, M. R. Bryce, F. B. Dias and A. P. Monkman, *J. Mater. Chem. C*, 2016, **4**, 3815-3824.
3. P. L. Dos Santos, J. S. Ward, M. R. Bryce and A. P. Monkman, *J. Phys. Chem. Lett.*, 2016, **7**, 3341-3346.
4. B. L. Watson, T. A. Moore, A. L. Moore and D. Gust, *Dyes Pigm.*, 2017, **136**, 893-897.
5. M. Nakano, S. Shinamura, R. Sugimoto, I. Osaka, E. Miyazaki and K. Takimiya, *Org. Lett.*, 2012, **14**, 5448-5451.
6. T. Cardeynaels, S. Paredis, J. Deckers, S. Brebels, D. Vanderzande, W. Maes and B. Champagne, *Phys. Chem. Chem. Phys.*, 2020, **22**, 16387-16399.

Chapter 4

Difluorodithieno[3,2-*a*:2',3'-*c*]phenazine as a strong acceptor for materials displaying thermally activated delayed fluorescence or room temperature phosphorescence

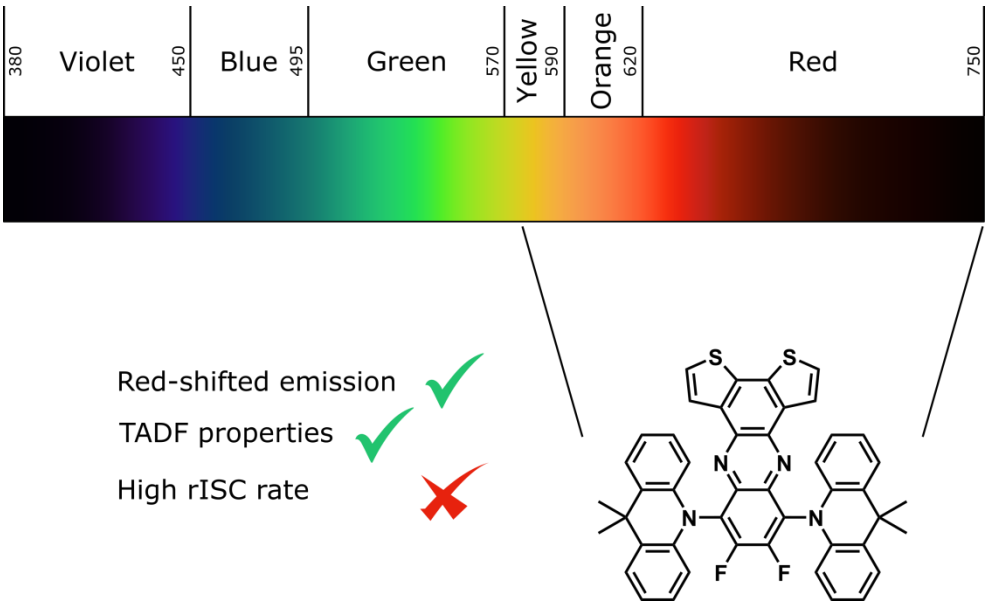

This chapter is based on a manuscript still to be submitted: T. Cardeynaels, S. Paredis, A. Danos, A. Harrison, S. Brebels, L. Lutsen, D. Vanderzande, A. P. Monkman, B. Champagne and W. Maes.

Contributions:
T. Cardeynaels: Synthesis and structural characterization of all compounds, time-resolved spectroscopic measurements, steady-state spectroscopic measurements and preparation of the manuscript.
S. Paredis: Discussion and revision of the manuscript.
A. Danos: Supervision of time-resolved spectroscopy, discussion and revision of the manuscript.
A. Harrison: Time-resolved spectroscopic measurements, discussion and revision of the manuscript.
S. Brebels: Synthesis of DTPz-BDT-TIPS.
A. P. Monkman: Discussion of the results and revision of the manuscript.
L. Lutsen, D. Vanderzande, W. Maes and B. Champagne: Project management, discussion of the results and revision of the manuscript.

Abstract

A novel strong electron-acceptor unit, 9,10-difluorodithieno[3,2-*a*:2',3'-*c*]phenazine (DTPz), is synthesized and applied in the design of two donor-acceptor type emitters. Using 9,9-dimethyl-9,10-dihydroacridine (DMAC) or triisopropyl-substituted benzo[1,2-*b*:4,5-*b'*]dithiophene (BDT-TIPS) as donor component, push-pull type chromophores exhibiting charge-transfer emission are obtained and found to afford long-lived delayed emission via either thermally activated delayed fluorescence (for DMAC) or room temperature phosphorescence (for BDT-TIPS).

4.1. Introduction

While research has mainly focused on the development of blue and green-emitting molecules showing thermally activated delayed fluorescence (TADF), red-emitting materials are equally useful for the development of all-TADF organic light-emitting diodes (OLEDs), as well as for bio-imaging applications.[1-3] Furthermore, research on red-emitting materials might lead to new insights for the development of near-infrared (NIR) emitting materials.[4] NIR-OLEDs can be useful in biomedical applications such as blood oximetry,[5, 6] photothermal and photodynamic therapeutic applications,[7-9] but are also used in security authentication technologies exploiting biometrics[10] and they could be integrated as transmitters in 'visible' light communication (VLC) networks.[11]

One of the main challenges in designing red-emitting materials is the energy gap law, as discussed in Chapter 1. As the energy levels of the singlet and triplet excited states come closer to that of the ground state, overlap between the vibrational levels of these states becomes more plausible and non-radiative transitions are enhanced. Furthermore, because red-emitting materials often consist of large conjugated systems or highly electron-deficient components, they typically have low-lying localized triplet states which act as exciton traps.

In recent years, the search for novel red-emitting TADF materials has focused heavily on the dibenzo[*a*,*c*]phenazine scaffold (Figure 4.1).[12-22] Even the CNQxP-based compounds from Chapter 3 are built from this phenazine acceptor.[20] Several functionalization strategies are employed to further red-shift the emission, such as incorporation of fluorine or cyano groups on various positions of the dibenzo[*a*,*c*]phenazine[13, 16-18] or extension to a dibenzo[*a*,*c*]dipyrido[3,2-*h*:2′,3′-*j*]phenazine scaffold.[12, 21] Multiple donor groups have been utilized, going from the very large triazatruxene[18] to the smaller 9,9-dimethyl-9,10-dihydro-

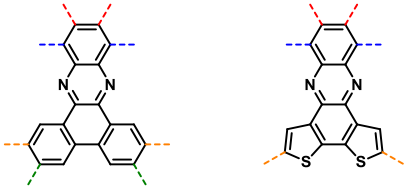

Figure 4.1: Molecular structures of dibenzo[*a*,*c*]phenazine (left) and dithieno[3,2-*a*:2',3'-*c*]phenazine (right), with the possible functionalization sites indicated by colored dashed bonds.

acridine (DMAC),[14, 16, 17, 19, 22] phenoxazine,[12, 19, 21] triphenylamine[13, 15, 17] and carbazole derivatives.[16] Having a similar structure, dithieno[3,2-*a*:2',3'-*c*]phenazine (DTPz, Figure 4.1) is a known acceptor unit in the field of organic photovoltaics, affording UV-VIS absorption maxima well over 600 nm when combined in a donor-acceptor copolymer.[23-25] In this chapter, we have further functionalized the DTPz unit with fluorine substituents on the 9 and 10 positions (indicated in red in Figure 4.1) to make it more electron-withdrawing and thus a stronger acceptor. To the 9,10-difluorodithieno[3,2-*a*:2',3'-*c*]phenazine, DMAC was coupled through a Buchwald-Hartwig type reaction. Additionally, the triisopropylsilyl-functionalized benzo[1,2-*b*:4,5-*b'*]dithiophene (BDT) unit, introduced in Chapter 3, was used as an alternative donor and coupled in a Suzuki cross-coupling reaction with DTPz. While the DTPz-BDT-TIPS molecule was already introduced in Chapter 2, we only investigated it from a theoretical perspective, having little information on its photophysical properties, which are investigated in the following sections.[20]

Quantum-chemical calculations show a small overlap between the HOMO and LUMO for both D-A combinations. Experimentally, TADF or RTP behavior is seen dependent on the donor unit and the resultant singlet and triplet energy levels. In the TADF material (DTPz-DMAC), the very long delayed fluorescence lifetime is attributed to a poor reverse intersystem crossing (rISC) rate, despite the small ΔE_{ST}.

4.2. Results and discussion

4.2.1. Material synthesis

DTPz, **DTPz-BDT-TIPS**[26] and DMAC[27] were prepared using previously reported methods. Coupling was done via Buchwald-Hartwig (DMAC) or Suzuki (BDT-TIPS) cross-coupling reactions (Scheme 4.1). Full synthetic details can be found in the supporting information.

4.2.2. Quantum-chemical calculations

The geometries of the DTPz acceptor and the two D-A-D chromophores were optimized using density functional theory (DFT) calculations with M06/6-311G(d). Time dependent DFT (TDDFT) calculations were performed to calculate

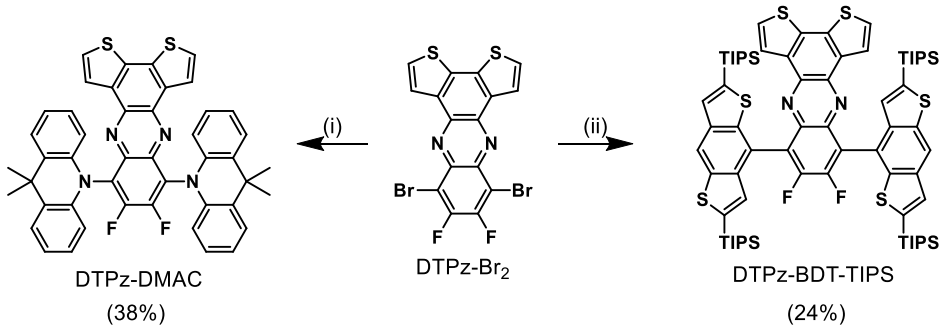

Scheme 4.1: Synthesis pathways towards **DTPz-DMAC** and **DTPz-BDT-TIPS**: (i) 9,9-dimethyl-9,10-dihydroacridine, $Pd(OAc)_2$, XPhos, NaO*t*Bu, toluene, 110 °C, 24 h; (ii) BDT-TIPS-pinacol, $Pd(PPh_3)_4$, K_2CO_3, DMF/H_2O 4/1, 130 °C, 24 h.

the singlet and triplet energies using a modified LC-BLYP (ω=0.17) XC functional with 6-311G(d) as the basis set under the Tamm-Dancoff approximation.[26] TDDFT calculations were performed using the polarizable continuum model (PCM) (cyclohexane) to simulate a non-polar environment. All calculations were performed using the Gaussian16 package.[28] The CT character of the involved states for the D-A-D compounds was calculated according to the work of Le Bahers *et al.*[29] Here, the difference between the ground and excited state densities is taken for a given transition, visualizing the regions of increased/decreased electron density upon transitioning from the ground to an excited state. These density differences allow to identify the donor and acceptor parts of the molecule in a (CT) transition and allow an estimate of the amount of charge-transfer character.

The optimized geometries (Figure 4.2) show large dihedral angles, around 85° for **DTPz-DMAC**, as often seen for DMAC-based compounds,[30] and around 59° for **DTPz-BDT-TIPS**. The smaller dihedral angles for the BDT-TIPS donor were also observed in previous work and are due to the decrease in steric hindrance for the five-membered fused rings.[20] The TIPS groups, although bulky, are not expected to hinder the vibrational modes of the BDT group as they are facing away from the acceptor unit. Furthermore, the acceptor acts as a spacer between the two BDT groups, and from the optimized geometries (Figure 4.2) it is apparent that the TIPS groups on two adjacent BDT units do not influence each other. The HOMO and LUMO orbitals are well separated (Figure 4.2), suggesting strong CT character, which is further confirmed by looking at the nature of the first singlet vertical excitation energies and the CT distances (d_{CT})

(Table 4.1). The increase in dipole moment ($\Delta\mu$) between the ground and excited state densities further supports this interpretation. For **DTPz-BDT-TIPS**, the first triplet excited state shows localized character as indicated by the much smaller d_{CT} and $\Delta\mu$ values. This is also visualized by considering the difference between the ground and excited state electron densities (Figure S4.7), where the densities are clearly localized on the DTPz unit. The HOMO-1 and HOMO-2 topologies are given in Figure S4.6 as they play a role in the other transitions under consideration here.

The TDDFT calculations predict singlet excitation energies of 2.20 eV (564 nm) for **DTPz-DMAC** and 2.73 eV (454 nm) for **DTPz-BDT-TIPS** (Table 4.2). **DTPz-DMAC** was found to have a theoretical ΔE_{ST} of 0.03 eV, whereas that of **DTPz-BDT-TIPS** is 0.43 eV. The acceptor DTPz was also included in the calculations,

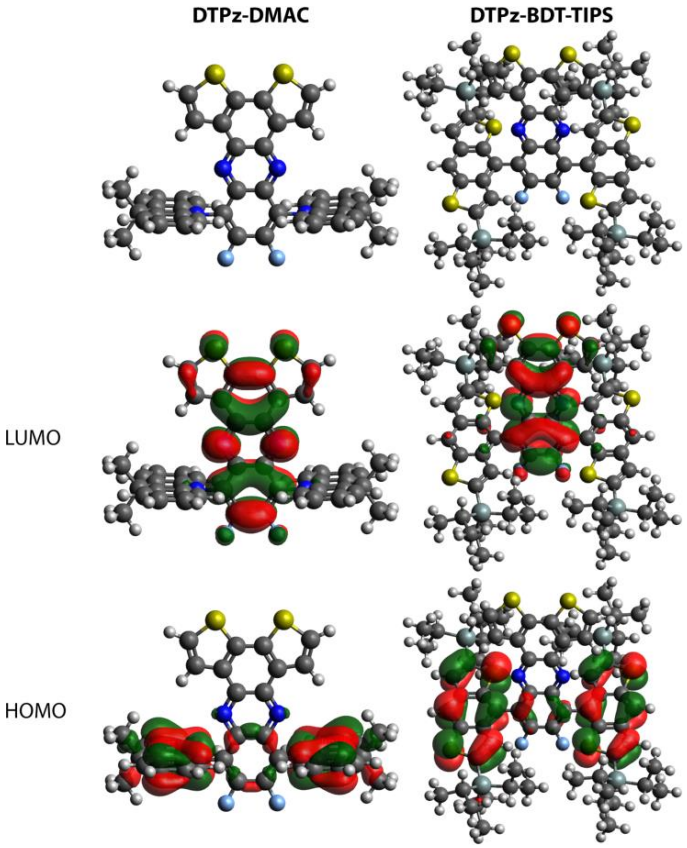

Figure 4.2: HOMO and LUMO topologies for **DTPz-DMAC** and **DTPz-BDT-TIPS** as obtained with LC-BLYP(ω=0.17)/6-311G(d).

Table 4.1: Nature of the various transitions (H = HOMO, L = LUMO), charge-transfer distance (d_{CT}) and change in dipole moment ($\Delta\mu$, excited – ground state dipole) accompanying the S_0->S_x and S_0->T_x transitions in cyclohexane.

	S_1			S_2			T_1			T_2		
Compound	Nature	d_{CT} (Å)	$\Delta\mu$ (D)	Nature	d_{CT} (Å)	$\Delta\mu$ (D)	Nature	d_{CT} (Å)	$\Delta\mu$ (D)	Nature	d_{CT} (Å)	$\Delta\mu$ (D)
DTPz-DMAC	H->L	1.53	8.37	H-1->L	1.54	8.58	H->L	1.51	8.00	H-1->L	1.54	8.56
DTPz-BDT-TIPS	H->L	2.06	10.82	H-1->L	2.01	10.67	H-2->L	0.29	0.64	H->L	1.46	5.14

Table 4.2: TDDFT results for the vertical first and second singlet excitation energies and corresponding oscillator strengths, and the first and second vertical triplet excitation energies.

Compound	S_1 (eV)	f_{S_1}	S_2 (eV)	f_{S_2}	T_1 (eV)	T_2 (eV)	$\Delta E_{T_2-T_1}$ (eV)	$\Delta E_{S_1-T_1}$ (eV)
DTPz-DMAC	2.20	0.00	2.23	0.00	2.17	2.22	0.05	0.03
DTPz-BDT-TIPS	2.73	0.05	2.83	0.02	2.30	2.55	0.25	0.43
DTPz	3.11	0.10	3.23	0.00	2.37	2.77	0.40	0.74

affording singlet and triplet excitation energies of 3.11 and 2.37 eV, respectively. From the analysis of the CT character of the excited states, we observed localization of the first excited triplet state of **DTPz-BDT-TIPS** on the acceptor (Figure S4.7). Therefore, we expected a similar excitation energy for this state as for the non-functionalised acceptor unit, which is confirmed by the calculations (Table 4.2). For **DTPz-DMAC**, the first triplet state is of CT character with electron density being transferred from the DMAC to the DTPz parts of the compound (Figure S4.7). UV-VIS absorption spectra were simulated (Figure S4.1) and are dominated by the LE bands which are higher in energy than the aforementioned CT states. Their profiles are in close agreement with the experimental spectra (Figure 4.3).

4.2.3. Photophysical characterization

From the steady-state emission spectra in zeonex film, a broad and non-structured emission is visible for both compounds (Figure 4.3). A distinct shift is observed between **DTPz-DMAC** and **DTPz-BDT-TIPS**, the onset of the former being red-shifted by nearly 77 nm (0.33 eV), indicating stronger CT character for the DMAC donor. The solvatochromism was investigated by measuring the steady-state emission in solvents of varying polarity, which is indicative of CT state emission for both materials (Figure S4.2). No solvatochromism was observed for the UV-VIS absorption spectra, indicating the LE character of these

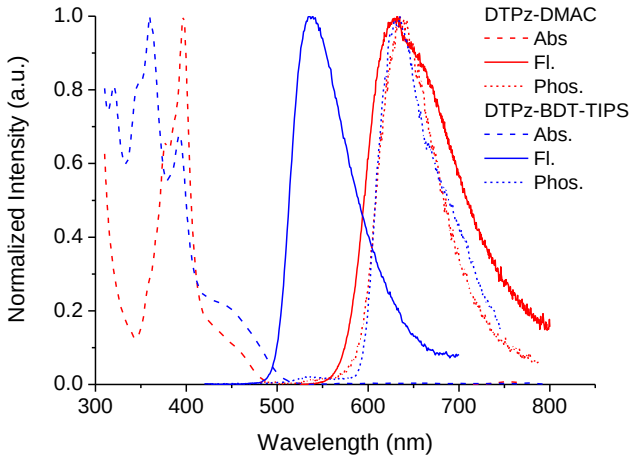

Figure 4.3: Steady-state absorption (dashed lines) and emission (full lines) spectra at room temperature and time-resolved emission at a 44.7 ms delay time at 80 K (dotted lines) in zeonex film for **DTPz-DMAC** (red) and **DTPz-BDT-TIPS** (blue).

bands. In Figure 4.4a,b the contour maps of the normalised time-resolved emission spectra of **DTPz-DMAC** in zeonex at room temperature and at 80 K are shown. After a fast decaying prompt emission, the intensity falls below the sensitivity limit of the camera. At several microseconds, the intensity reappears at exactly the same wavelength as the prompt emission and persists until around 12 milliseconds. In Figure 4.4c, the decay of the total emission intensity is plotted. At 80 K, the emission drops below the sensitivity of the iCCD after approximately 50 nanoseconds and it is not until several hundreds of microseconds that a new red-

Table 4.3: Photophysical properties for **DTPz-DMAC** and **DTPz-BDT-TIPS** in zeonex film.

Compound	E_S (eV)[a]	E_T (eV)[b]	ΔE_{ST} (eV)[c]	τ_{Fp} (ns)[d]	τ_{Fd} (µs)[e]	k_{ISC}[f]	k_{rISC}[f]
DTPz-DMAC	2.16	2.11	0.04	8.4	422.6	7.8×10^7	2.5×10^5
DTPz-BDT-TIPS	2.49	2.09	0.40	4.3	2.6×10^4	—[g]	—[g]

[a] Taken from the onset of the prompt fluorescence. [b] Taken from the onset of the phosphorescence at ms timescales at 80 K. [c] Calculated as $E_S - E_T$. [d] lifetime of prompt fluorescence (F_p) [e] lifetime of delayed fluorescence (F_d) [f] k_{ISC} and k_{rISC} were determined using kinetic fitting of prompt and delayed fluorescence according to literature. [31] [g] Cannot be determined due to the lack of TADF emission.

shifted emission band appears (attributed to phosphorescence and shown in Figure 4.3). Figure S4.3 shows individual spectra taken at various times showing a clear difference in onset between the room temperature and 80 K delayed emission. The lack of microsecond delayed emission at 80 K is consistent with a TADF mechanism being disrupted by the lack of available thermal energy at these temperatures, and phosphorescence emission instead dominating at longer times. Calculating ΔE_{ST} from the onsets of the fluorescence and phosphorescence emission (Table 4.3), a rather small gap of 0.04 eV is found, which is in good agreement with the quantum-chemical calculations. The long lifetime of the delayed emission at room temperature (422.6 µs) likely arises from slow rISC which is confirmed by kinetic fitting of the room temperature decay. **DTPz-BDT-TIPS** shows a very different behavior in zeonex films. Only short-lived prompt CT emission followed by a long-lived emission is observed (Figure 4.4d,f and Figure S4.4). The long micro- to millisecond emission can be attributed to phosphorescence rather than delayed fluorescence, as the spectra at room temperature and 80 K show the same structured peak shape and onset

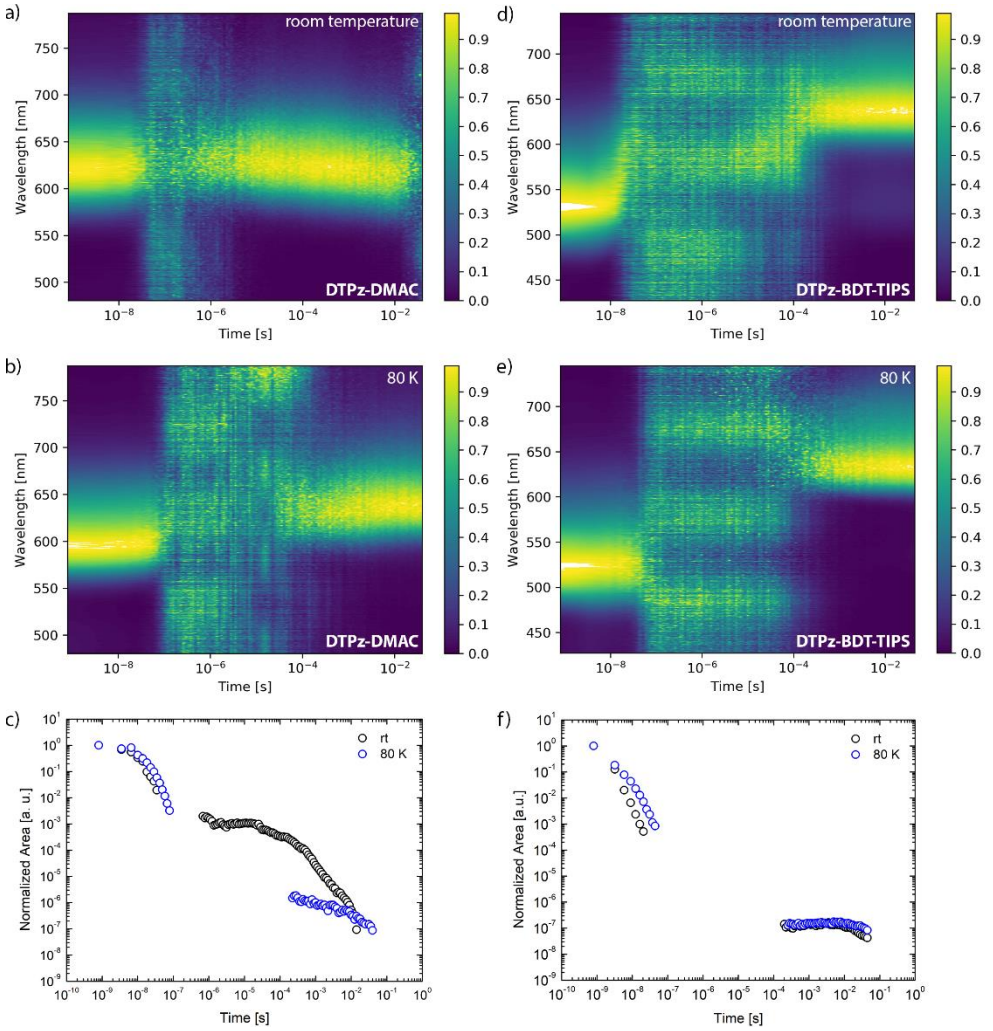

Figure 4.4: a) Normalized time-resolved emission spectra for **DTPz-DMAC** (a) and **DTPz-BDT-TIPS** (b) in zeonex at room temperature. Decay of the total emission for **DTPz-DMAC** (c) and **DTPz-BDT-TIPS** (d) at room temperature (rt) and at 80 K in zeonex.

(Figure 4.5 and Figure S4.3). Additionally, a small contribution likely arising from triplet-triplet annihilation (TTA) can be seen at around 525 nm in the room temperature delayed spectrum as the onset is similar to that of the prompt emission. The lack of TADF emission is not surprising given the much larger theoretical ΔE_{ST} for this material (0.43 eV). The experimental ΔE_{ST} calculated from the onset of the prompt fluorescence at room temperature and the phosphorescence at 80 K is 0.40 eV (Table 4.3) and is in excellent agreement with the calculations. Similar observations were also made for TXO2-BDT-TIPS in

previous work, where the lowest triplet excited state was found to be localized on BDT-TIPS and this donor unit showed RTP by itself.[20] However, the difference between the ground and excited state electron densities showed that the first excited triplet state is localized on the DTPz acceptor rather than on the BDT donor for **DTPz-BDT-TIPS** (Figure S4.7). Therefore, the phosphorescence likely originates from the acceptor core and not from the BDT-TIPS donor. The DTPz acceptor without bromine atoms was also subjected to time-resolved emission spectroscopy and was found to exhibit phosphorescence at room temperature (Figure 4.5). Given the presence of sulphur atoms in the DTPz core, it is plausible that the increased SOC accompanied with this is sufficient to allow radiative relaxation through the T_1->S_0 pathway.

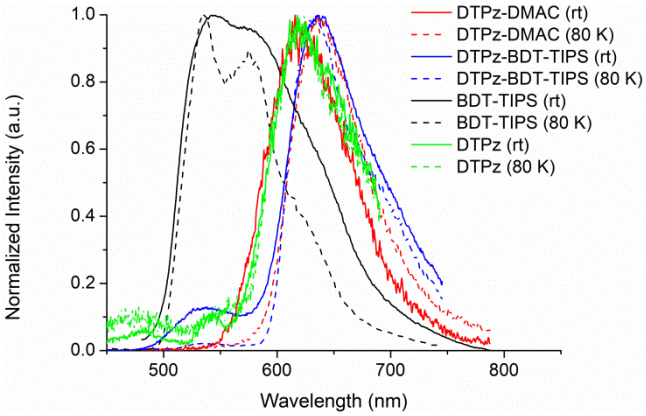

Figure 4.5: Overlap of the emission spectra at 44.7 ms for **DTPz-DMAC**, **DTPz-BDT-TIPS**, DTPz and BDT-TIPS at room temperature and at 80 K in zeonex.

The full decays as a function of normalized total emission versus time are shown in Figure 4.4c and 4.4d. For **DTPz-DMAC** in zeonex, a clear difference is seen between the decays at room temperature and 80 K. The relatively high intensity but very long-lived emission is indicative of a thermally activated process with a slow rate of rISC. **DTPz-BDT-TIPS** shows virtually no emission in the microsecond domain in zeonex films. At longer lifetimes, a small emission contribution is observed, illustrative of RTP behavior (as outlined above).

Finally, the dependence of the delayed fluorescence intensity with respect to the laser power was determined for both compounds in zeonex film. For **DTPz-DMAC**, the measurement was done at a 5 µs delay time and 750 µs integration time and shows a linear power law dependence with a slope of 1 (Figure S4.5),

indicating that we are not observing TTA but rather TADF in this time domain. **DTPz-BDT-TIPS** did not show any early microsecond emission. Therefore, we probed the late microseconds to milliseconds domain with a 630 µs delay time and 10 ms integration time to make sure the main delayed emission could be attributed RTP instead of TTA. However, from the time-resolved spectral measurements at room temperature and at 80 K we could already conclude that this emission band is most likely due to phosphorescence. The laser power measurement further solidified these observations (Figure S4.5).

4.3. Conclusions

We have synthesized two new D-A-D compounds based on the novel 9,10-difluorodithieno[3,2-*a*:2',3'-*c*]phenazine (DTPz) acceptor. This acceptor was coupled to the strong TADF donor 9,9-dimethyl-9,10-dihydroacridine (DMAC) and a weaker benzo[1,2-*b*:4,5-*b'*]dithiophene (BDT-TIPS). Photophysical analysis showed that both compounds exhibit long-lived delayed emission in a zeonex film. **DTPz-DMAC** was found to exhibit TADF properties. Despite a small singlet-triplet energy gap (0.05 eV), the rate of reverse intersystem crossing is rather small, leading to long-lived delayed fluorescence. **DTPz-BDT-TIPS** was found to show RTP from the acceptor unit at room temperature in a nonpolar zeonex matrix. Although the materials do not display ideal TADF properties for OLED applications, their long-lived and red-shifted emission clearly show that they can be used for other applications such as imaging, sensing or security inks.[1-3, 32] Combined with other appropriate donor groups and suitable hosts, DTPz may be valuable in the continuing pursuit of efficient deep-red TADF materials for OLEDs.

4.4. References

1. X. Xiong, F. Song, J. Wang, Y. Zhang, Y. Xue, L. Sun, N. Jiang, P. Gao, L. Tian and X. Peng, *J. Am. Chem. Soc.*, 2014, **136**, 9590-9597.
2. C. I. C. Crucho, J. Avó, R. Nobuyasu, S. N. Pinto, F. Fernandes, J. C. Lima, M. N. Berberan-Santos and F. B. Dias, *Mater. Sci. Eng. C*, 2020, **109**, 110528.
3. Y. Wu, L. Jiao, F. Song, M. Chen, D. Liu, W. Yang, Y. Sun, G. Hong, L. Liu and X. Peng, *Chem. Commun.*, 2019, **55**, 14522-14525.
4. A. Zampetti, A. Minotto and F. Cacialli, *Adv. Funct. Mater.*, 2019, **29**, 1807623.

5. C. M. Lochner, Y. Khan, A. Pierre and A. C. Arias, *Nat. Commun.*, 2014, **5**, 5745.
6. S. Park, K. Fukuda, M. Wang, C. Lee, T. Yokota, H. Jin, H. Jinno, H. Kimura, P. Zalar, N. Matsuhisa, S. Umezu, G. C. Bazan and T. Someya, *Adv. Mater.*, 2018, **30**, 1870252.
7. C. Shirata, J. Kaneko, Y. Inagaki, T. Kokudo, M. Sato, S. Kiritani, N. Akamatsu, J. Arita, Y. Sakamoto, K. Hasegawa and N. Kokudo, *Sci. Rep.*, 2017, **7**, 13958.
8. X. B. Han, H. X. Li, Y. Q. Jiang, H. Wang, X. S. Li, J. Y. Kou, Y. H. Zheng, Z. N. Liu, H. Li, J. Li, D. Dou, Y. Wang, Y. Tian and L. M. Yang, *Cell Death Dis.*, 2017, **8**, e2864-e2864.
9. L. Maggini, I. Cabrera, A. Ruiz-Carretero, E. A. Prasetyanto, E. Robinet and L. De Cola, *Nanoscale*, 2016, **8**, 7240-7247.
10. M. A. M. Abdullah, J. A. Chambers, W. L. Woo and S. S. Dlay, 2015.
11. P. A. Haigh, F. Bausi, Z. Ghassemlooy, I. Papakonstantinou, H. Le Minh, C. Fléchon and F. Cacialli, *Opt. Express*, 2014, **22**, 2830-2838.
12. J.-X. Chen, K. Wang, C.-J. Zheng, M. Zhang, Y.-Z. Shi, S.-L. Tao, H. Lin, W. Liu, W.-W. Tao, X.-M. Ou and X.-H. Zhang, *Adv. Sci.*, 2018, **5**, 1800436.
13. S. Wang, Y. Miao, X. Yan, K. Ye and Y. Wang, *J. Mater. Chem. C*, 2018, **6**, 6698-6704.
14. F.-M. Xie, H.-Z. Li, G.-L. Dai, Y.-Q. Li, T. Cheng, M. Xie, J.-X. Tang and X. Zhao, *ACS Appl. Mater. Interfaces*, 2019, **11**, 26144-26151.
15. K. Sun, Z. Cai, J. Jiang, W. Tian, W. Guo, J. Shao, W. Jiang and Y. Sun, *Dyes Pigm.*, 2020, **173**, 107957.
16. S. Kothavale, W. J. Chung and J. Y. Lee, *J. Mater. Chem. C*, 2020, **8**, 7059-7066.
17. R. Furue, K. Matsuo, Y. Ashikari, H. Ooka, N. Amanokura and T. Yasuda, *Adv. Opt. Mater.*, 2018, **6**, 1701147.
18. Y. Liu, Y. Chen, H. Li, S. Wang, X. Wu, H. Tong and L. Wang, *ACS Appl. Mater. Interfaces*, 2020, **12**, 30652-30658.
19. C. Zhou, W.-C. Chen, H. Liu, X. Cao, N. Li, Y. Zhang, C.-S. Lee and C. Yang, *J. Mater. Chem. C*, 2020, **8**, 9639-9645.
20. T. Cardeynaels, S. Paredis, A. Danos, D. Vanderzande, A. P. Monkman, B. Champagne and W. Maes, *Manuscript submitted*.
21. J.-X. Chen, W.-W. Tao, W.-C. Chen, Y.-F. Xiao, K. Wang, C. Cao, J. Yu, S. Li, F.-X. Geng, C. Adachi, C.-S. Lee and X.-H. Zhang, *Angew. Chem. Int. Ed.*, 2019, **58**, 14660-14665.
22. S. Kothavale, W. J. Chung and J. Y. Lee, *ACS Appl. Mater. Interfaces*, 2020, **12**, 18730-18738.
23. A. Efrem, K. Wang, P. N. Amaniampong, C. Yang, S. Gupta, H. Bohra, S. H. Mushrif and M. Wang, *Polym. Chem.*, 2016, **7**, 4862-4866.
24. J. Fan, Y. Zhang, C. Lang, M. Qiu, J. Song, R. Yang, F. Guo, Q. Yu, J. Wang and L. Zhao, *Polymer*, 2016, **82**, 228-237.
25. Y. Zhang, J. Zou, H.-L. Yip, K.-S. Chen, J. A. Davies, Y. Sun and A. K. Y. Jen, *Macromolecules*, 2011, **44**, 4752-4758.
26. T. Cardeynaels, S. Paredis, J. Deckers, S. Brebels, D. Vanderzande, W. Maes and B. Champagne, *Phys. Chem. Chem. Phys.*, 2020, **22**, 16387-16399.

27. J. Deckers, T. Cardeynaels, H. Penxten, A. Ethirajan, M. Ameloot, M. Kruk, B. Champagne and W. Maes, *Chemistry*, 2020, DOI: 10.1002/chem.202002549.
28. G. W. T. M. J. Frisch, H. B. Schlegel, G. E. Scuseria, M. A. Robb, J. R. Cheeseman, G. Scalmani, V. Barone, G. A. Petersson, H. Nakatsuji, X. Li, M. Caricato, A. V. Marenich, J. Bloino, B. G. Janesko, R. Gomperts, B. Mennucci, H. P. Hratchian, J. V. Ortiz, A. F. Izmaylov, J. L. Sonnenberg, D. Williams-Young, F. Ding, F. Lipparini, F. Egidi, J. Goings, B. Peng, A. Petrone, T. Henderson, D. Ranasinghe, V. G. Zakrzewski, J. Gao, N. Rega, G. Zheng, W. Liang, M. Hada, M. Ehara, K. Toyota, R. Fukuda, J. Hasegawa, M. Ishida, T. Nakajima, Y. Honda, O. Kitao, H. Nakai, T. Vreven, K. Throssell, J. A. Montgomery, Jr., J. E. Peralta, F. Ogliaro, M. J. Bearpark, J. J. Heyd, E. N. Brothers, K. N. Kudin, V. N. Staroverov, T. A. Keith, R. Kobayashi, J. Normand, K. Raghavachari, A. P. Rendell, J. C. Burant, S. S. Iyengar, J. Tomasi, M. Cossi, J. M. Millam, M. Klene, C. Adamo, R. Cammi, J. W. Ochterski, R. L. Martin, K. Morokuma, O. Farkas, J. B. Foresman, and D. J. Fox, *Journal*, 2016.
29. T. Le Bahers, C. Adamo and I. Ciofini, *J. Chem. Theory Comput.*, 2011, **7**, 2498-2506.
30. N. A. Kukhta, H. F. Higginbotham, T. Matulaitis, A. Danos, A. N. Bismillah, N. Haase, M. K. Etherington, D. S. Yufit, P. R. McGonigal, J. V. Gražulevičius and A. P. Monkman, *J. Mater. Chem. C*, 2019, **7**, 9184-9194.
31. N. Haase, A. Danos, C. Pflumm, A. Morherr, P. Stachelek, A. Mekic, W. Brütting and A. P. Monkman, *J. Phys. Chem. C*, 2018, **122**, 29173-29179.
32. Y. Lei, W. Dai, J. Guan, S. Guo, F. Ren, Y. Zhou, J. Shi, B. Tong, Z. Cai, J. Zheng and Y. Dong, *Angew. Chem. Int. Ed.*, 2020, DOI: 10.1002/anie.202003585.

4.5. Supporting information

4.5.1. Experimental details

4.5.1.1. Materials and methods

All reagents and chemicals were obtained from commercial sources and used without further purification. Dry solvents were obtained from an MBraun solvent purification system (MB SPS-800) equipped with alumina columns. Preparative (recycling) size exclusion chromatography (SEC) was performed on a JAI LC-9110 NEXT system equipped with JAIGEL 1H and 2H columns (eluent chloroform, flow rate 3.5 mL min^{-1}). Proton and carbon nuclear magnetic resonance (^{1}H and ^{13}C NMR) spectra were obtained on a Varian or Jeol spectrometer operating at 400 MHz for ^{1}H (100 MHz for ^{13}C). Chemical shifts (δ) are given in ppm relative to $CDCl_3$ (δ = 7.26 ppm for ^{1}H NMR, δ = 77.06 ppm for ^{13}C NMR). Matrix-assisted laser desorption/ionization - time-of-flight (MALDI-ToF) mass spectra were recorded on a Bruker Daltonics Ultraflex II ToF/ToF. 1 µL of the matrix solution (16 mg mL^{-1} *trans*-2-[3-(4-*tert*-butylphenyl)-2-methyl-2-propenylidene]malononitrile (DTCB) in chloroform) was spotted onto an MTP Anchorchip 600/384 MALDI plate. The spot was allowed to dry and approximately 1 µL of the analyte solution (0.5 mg mL^{-1} In chloroform) was spotted on top of the matrix. High-resolution electrospray ionization mass spectrometry (ESI-MS) was performed using an LTQ Orbitrap Velos Pro mass spectrometer equipped with an atmospheric pressure ionization source operating in the nebulizer assisted electrospray mode. All solution-based absorption spectra were recorded on a Varian Cary 5000 UV-Vis-NIR spectrophotometer from Agilent Technologies. Steady-state emission spectra in solution were recorded on a Horiba-Jobin Yvon Fluorolog-3 spectrofluorometer equipped with a 450 W Xe lamp as light source. All spectroscopic measurements were done in spectroscopic grade solvents. Zeonex films were prepared via drop-casting using a mixture of the emitter (1 wt%) and host (zeonex) in toluene. The initial solution concentrations were 1 mg mL^{-1} for the dopant and 100 mg mL^{-1} for zeonex. The films were drop-casted onto a quartz substrate at 65 °C to facilitate evaporation of the solvent. Absorption and emission spectra of the films were collected using a UV-3600 double beam spectrophotometer (Shimadzu) and a

Fluoromax fluorimeter (Jobin Yvon). Time-resolved photoluminescence spectra and decays were recorded using a nanosecond gated spectrograph-coupled iCCD (Stanford) using an Nd:YAG laser emitting at 355 nm (EKSPLA). Laser power experiments were conducted using an N_2 laser (Lasertechnik Berlin) emitting at 337 nm with the same nanosecond gated spectrograph-coupled iCCD (Stanford) camera, attenuating the excitation using reflective neutral density filters.

4.5.1.2. Material synthesis and characterization

8,11-Dibromo-9,10-difluorodithieno[3,2-*a*:2',3'-*c*]phenazine (DTPz-Br_2)[1], 9,9-dimethyl-9,10-dihydroacridine (DMAC)[2] and (4-(4,4,5,5-tetramethyl-1,3,2-dioxaborolan-2-yl)benzo[1,2-*b*:4,5-*b*']dithiophene-2,6-diyl)bis(triisopropylsilane) (BDT-TIPS-pinacol)[1] were synthesized according to literature procedures.

*8,11-bis(9,9-dimethylacridin-10(9H)-yl)-9,10-difluorodithieno[3,2-a:2',3'-c]phenazine (**DTPz-DMAC**)*

DTPz-Br_2 (199.9 mg, 411.2 µmol), 9,9-dimethyl-9,10-dihydroacridine (194.4 mg, 928.9 µmol), palladium(II) acetate (22.3 mg, 99.3 µmol), 2-Dicyclohexylphosphino-2',4',6'-triisopropylbiphenyl (XPhos, 80.6 mg, 169.0 µmol) and sodium *tert*-butoxide (101.6 mg, 1.1 mmol) were dissolved in dry toluene (12 mL) under argon atmosphere. The mixture was heated to reflux for 24 h while stirring and then cooled down to room temperature. The reaction mixture was poured into water and extracted with CH_2Cl_2. The organic phase was dried over anhydrous $MgSO_4$, filtered and the solvent was evaporated under reduced pressure. The crude product was purified by silica gel column chromatography using CH_2Cl_2/petroleum ether (v/v = 20/80) as the eluent. **DTPz-DMAC** was obtained as an orange solid (116.8 mg, 38%). ^{1}H NMR (400 MHz, $CDCl_3$): 7.76 (d, *J* = 5.3 Hz, 2H), 7.67-7.62 (m, 4H), 7.10 (d, *J* = 5.3 Hz, 2H), 7.07-7.03 (m, 8H), 6.42-6.39 (m, 4H), 2.00 (s, 6H), 1.98 (s, 6H). ^{13}C NMR (100 MHz, $CDCl_3$): 152.82 (dd, $^1J_{C\text{-}F}$ = 264.8 Hz, $^2J_{C\text{-}F}$ = 17.3 Hz), 140.07, 139.83, 137.65 (t, $^3J_{C\text{-}F}$ = 2.7 Hz), 136.77, 134.16, 131.13, 126.83, 125.39, 125.18 (d, $^2J_{C\text{-}F}$ = 17.3 Hz), 125.16, 124.60, 121.65, 113.49, 36.47, 32.81, 29.11. MS (MALDI-ToF) Calcd. for $C_{46}H_{32}F_2N_4S_2$ $[M]^+$: *m/z* 742.20, found: 742.17.

*8,11-bis(2,6-bis(triisopropylsilyl)benzo[1,2-b:4,5-b']dithiophen-4-yl)-9,10-difluorodithieno[3,2-a:2',3'-c]phenazine (**DTPz-BDT-TIPS**)*[1]

DTPz-Br_2 (90.2 mg, 186.5 µmol), BDT-TIPS-pinacol (245.0 mg, 389.6 µmol) and tetrakis(triphenylphosphine)palladium(0) (10.7 mg, 9.3 µmol) were added to a flame-dried Schlenk flask. The flask was evacuated and backfilled with nitrogen three times and pre-degassed DMF (16 mL) and a K_2CO_3 solution (2 M, 4 mL) were added. The reaction mixture was heated at 130 °C and stirred at this temperature for 24 h under a nitrogen atmosphere. The reaction mixture was poured into water and extracted with dichloromethane. The organic phase was dried over $MgSO_4$ and filtered. After evaporation of the solvent under reduced pressure, the product was purified by silica gel column chromatography using CH_2Cl_2/petroleum ether (v/v = 20/80) as the eluent. **DTPz-BDT-TIPS** was further purified using preparative (recycling) SEC and was obtained as a yellow solid (60.0 mg, 24%). ^{1}H NMR (400 MHz, $CDCl_3$): 8.57 (d, *J* = 2.0 Hz, 2H), 7.70 (d, *J* = 1.9 Hz, 2H), 7.47 (dd, *J* = 5.3, 1.7 Hz, 2H), 7.23 (s, 1H), 7.16 (dd, *J* = 5.3, 2.1 Hz, 2H), 7.12 (s, 1H), 1.45-1.18 (m, 12H), 1.17-0.90 (m, 72H). ^{13}C NMR (100 MHz, $CDCl_3$): 151.72, 151.55, 149.16, 148.97, 142.74, 142.64, 140.86, 140.80, 139.19, 139.16, 138.94, 138.54, 138.48, 138.24, 138.18, 137.07, 137.03, 136.06, 134.61, 131.90, 131.76, 131.62, 131.54, 124.41, 124.34, 124.33, 124.27, 119.24, 119.18, 116.53, 77.38, 18.69, 18.66, 18.60, 18.55, 18.50, 18.46, 18.38, 11.85, 11.82, 11.76, 11.71. MS (ESI+) Calcd. for $C_{72}H_{94}F_2N_2S_6Si_4$ [M]+: *m/z* 1328.479, found: 1328.475.

4.5.2. Simulated UV-VIS absorption spectrum

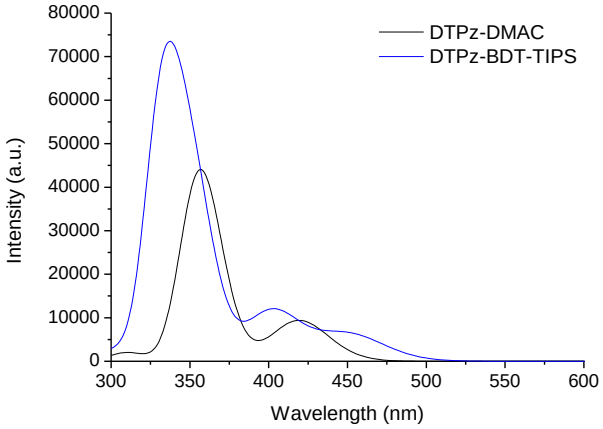

Figure S4.1: Simulated UV-VIS absorption spectra for **DTPz-DMAC** and **DTPz-BDT-TIPS** using LC-BLYP(ω=0.17)/6-311G(d) and the PCM (cyclohexane).

4.5.3. Steady-state absorption and emission spectra in solution

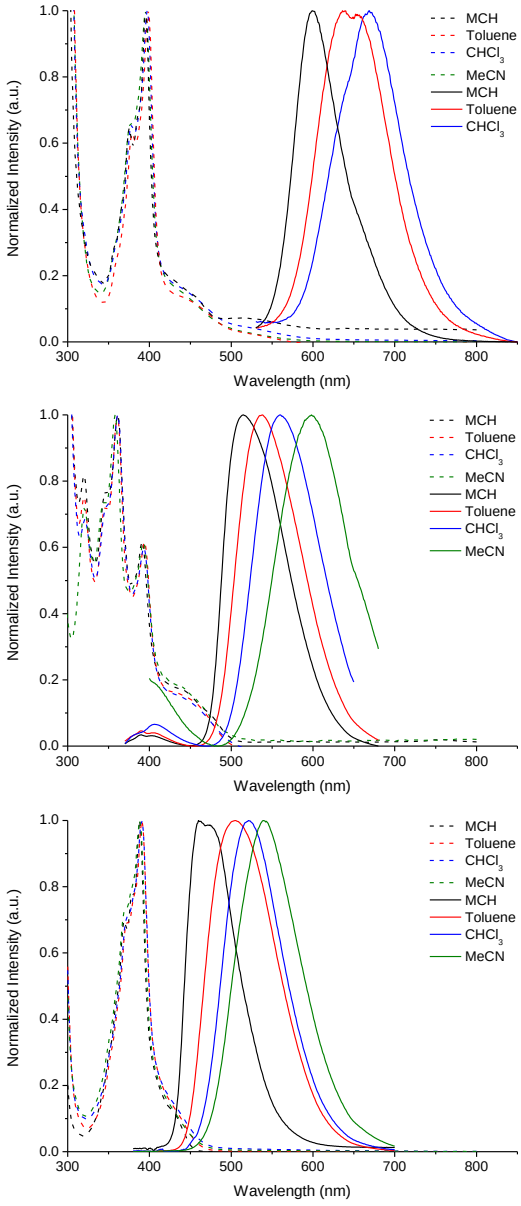

Figure S4.2: Steady-state absorption (dotted lines) and emission (full lines) spectra in methylcyclohexane (MCH), toluene, chloroform ($CHCl_3$) and acetonitrile (MeCN) for **DTPz-DMAC** (top), **DTPz-BDT-TIPS** (middle) and DTPz (bottom). For **DTPz-DMAC**, no emission was observed in MeCN. All spectra were recorded from non-degassed solutions.

4.5.4. Time-resolved emission spectra

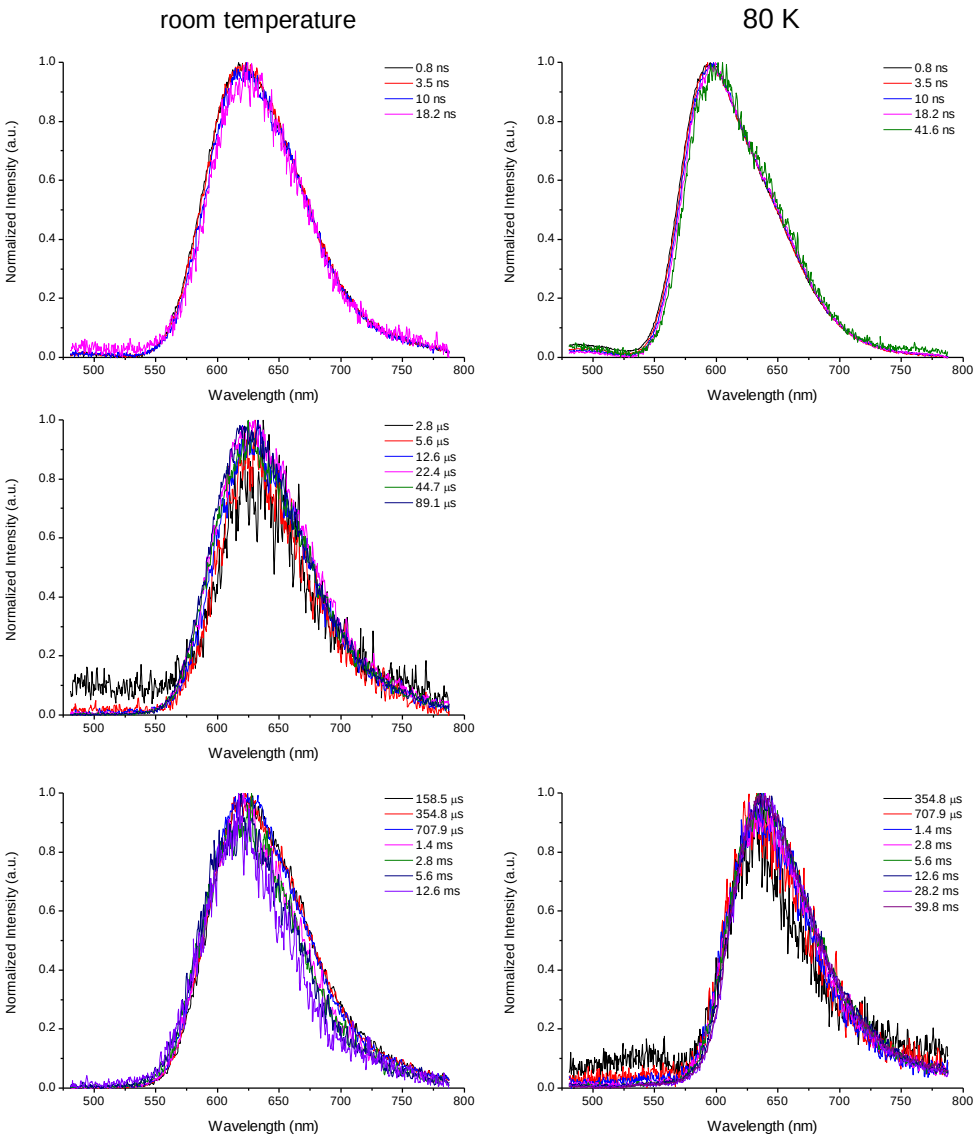

Figure S4.3: Time-resolved emission at various times in the photoluminescence decay for **DTPz-DMAC** in zeonex at room temperature (left) and at 80 K (right).

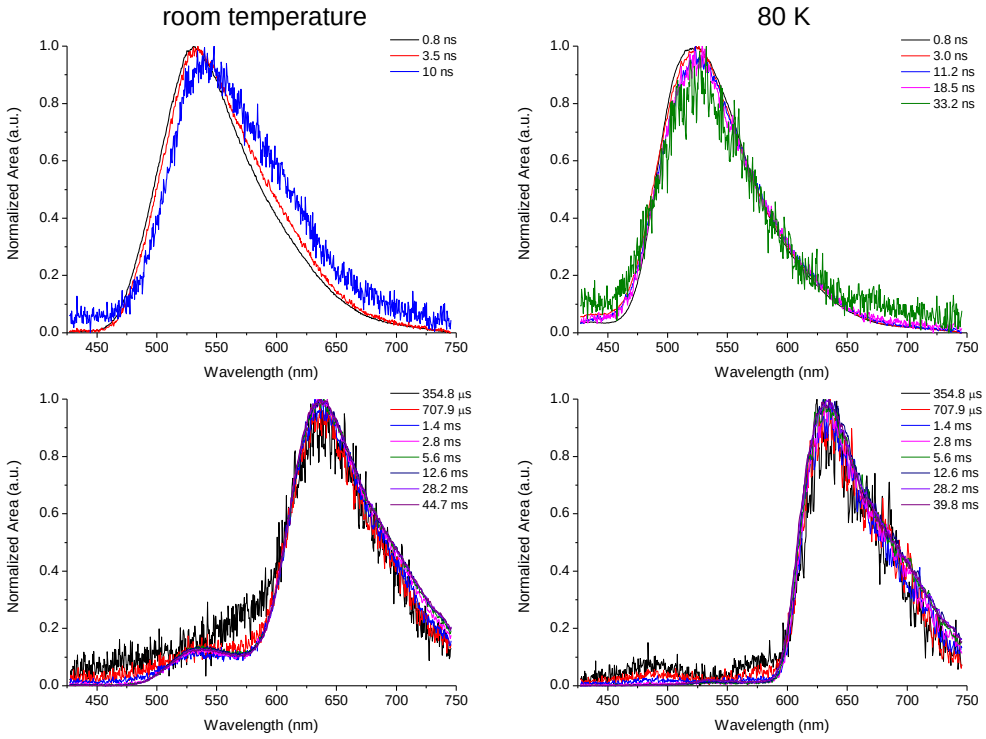

Figure S4.4: Time-resolved emission at various times in the photoluminescence decay for **DTPz-BDT-TIPS** in zeonex at room temperature (left) and at 80 K (right).

4.5.5. Laser power experiments

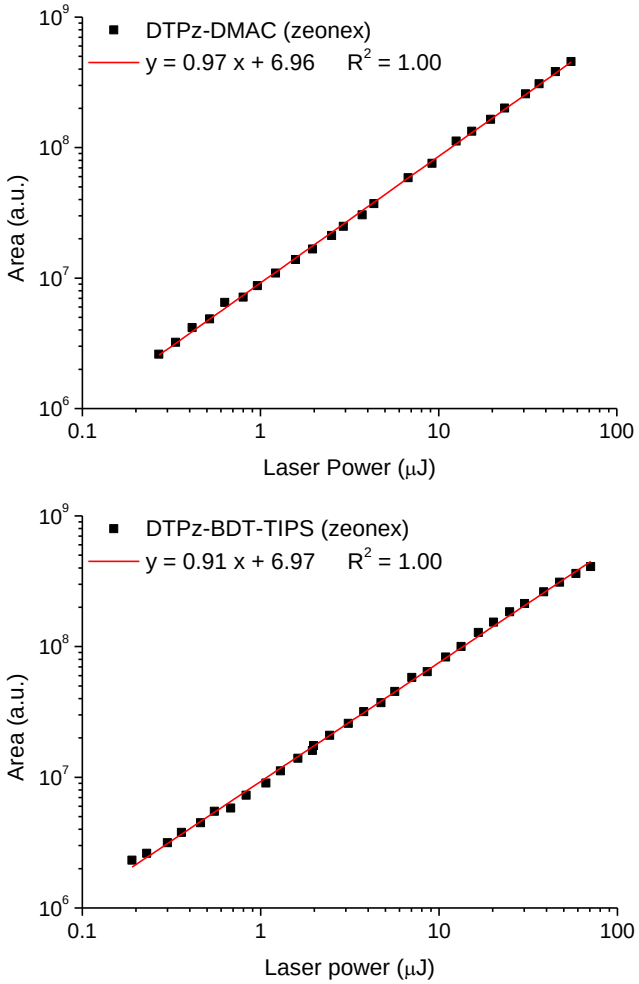

Figure S4.5: Laser power experiments using a N_2 laser: **DTPz-DMAC** was probed at a delay time of 5 µs for an integration time of 750 µs. **DTPz-BDT-TIPS** was probed at a delay time of 630 µs for an integration time of 10 ms.

4.5.6. Orbital topologies

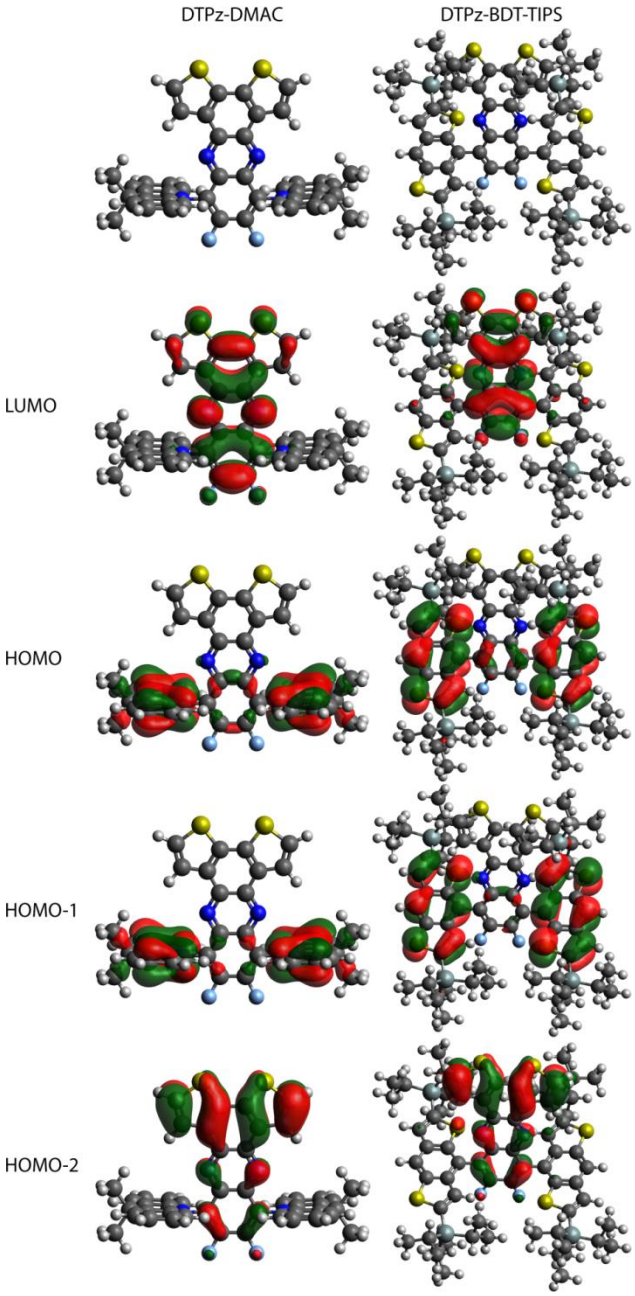

Figure S4.6: Orbital topologies for **DTPz-DMAC** (left) and **DTPz-BDT-TIPS** (right) obtained using DFT with LC-BLYP(ω=0.17)/6-311G(d). Isocontour values of 0.02 a.u. were used for all orbitals.

Table S4.1: Orbital energies for **DTPz-DMAC** and **DTPz-BDT-TIPS** as obtained using DFT with LC-BLYP(ω=0.17)/6-311G(d).

	HOMO-2 (eV)	HOMO-1 (eV)	HOMO (eV)	LUMO (eV)
DTPz-DMAC	-7.38	-6.62	-6.60	-1.56
DTPz-BDT-TIPS	-7.32	-6.89	-6.79	-1.42

4.5.7. Ground/excited state electron density differences

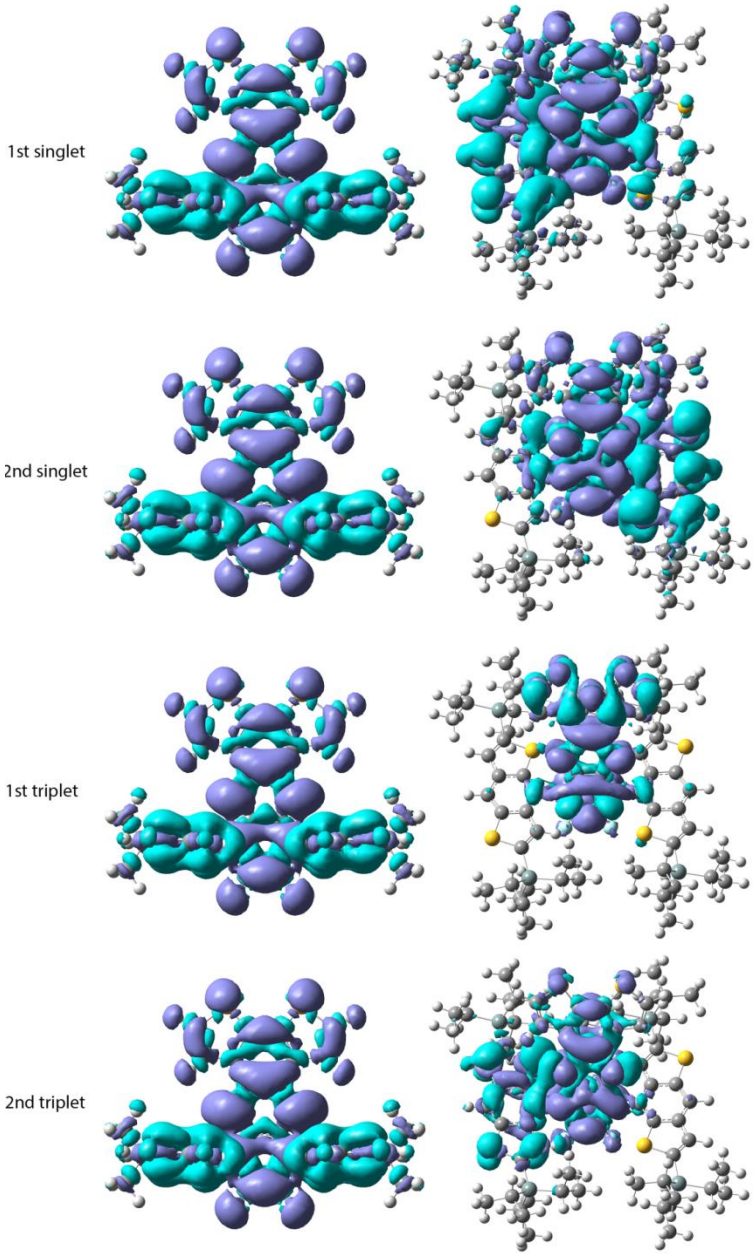

Figure S4.7: Ground/excited state electron density differences for **DTPz-DMAC** (left) and **DTPz-BDT-TIPS** (right). Isocontour values = 0.0004 for all densities. Cyan regions indicate a decrease in electron density upon excitation, while purple regions indicate an increase in electron density.

4.5.8. NMR spectra

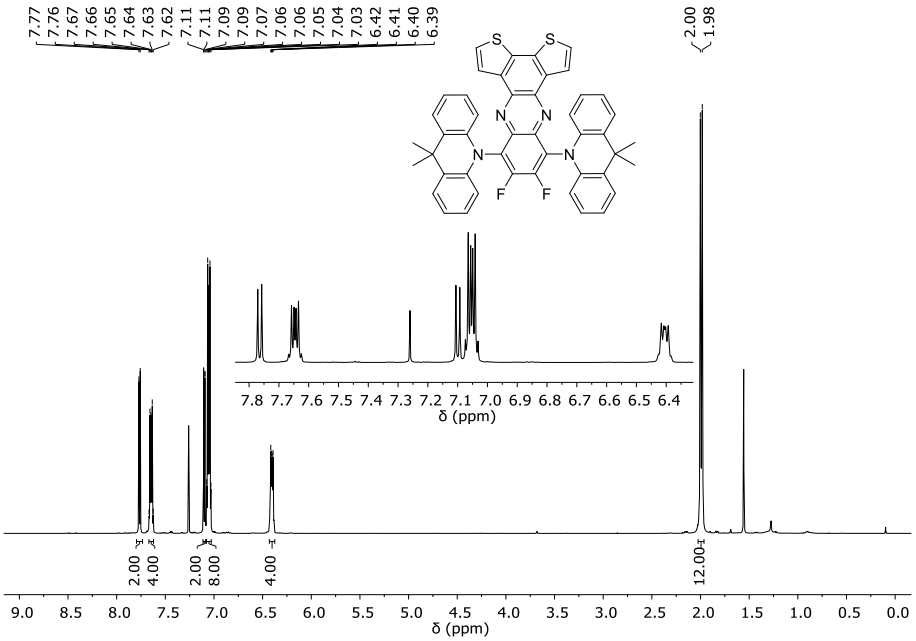

Figure S4.8: ^{1}H NMR spectrum of DTPz-DMAC in $CDCl_3$.

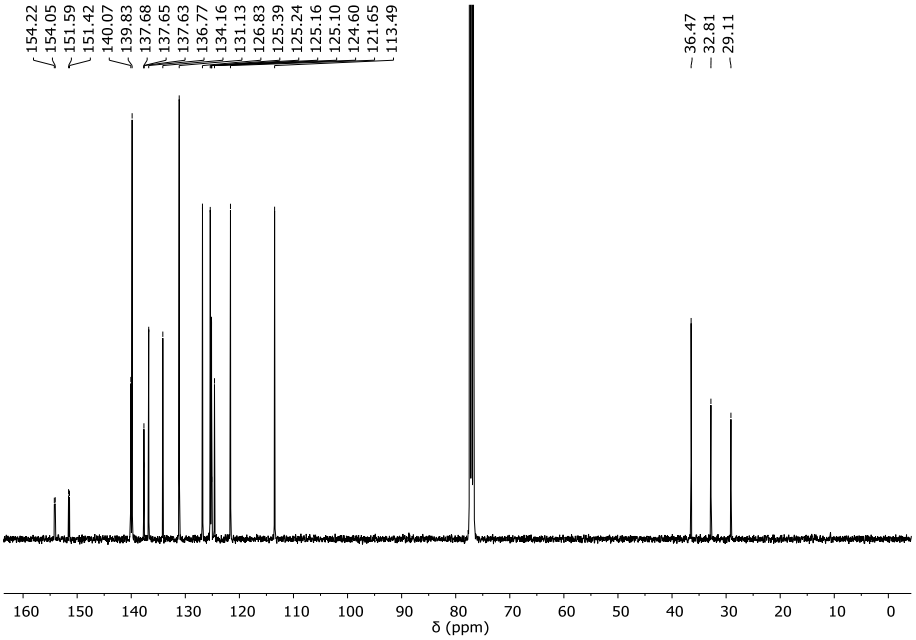

Figure S4.9: ^{13}C NMR spectrum of DTPz-DMAC in $CDCl_3$.

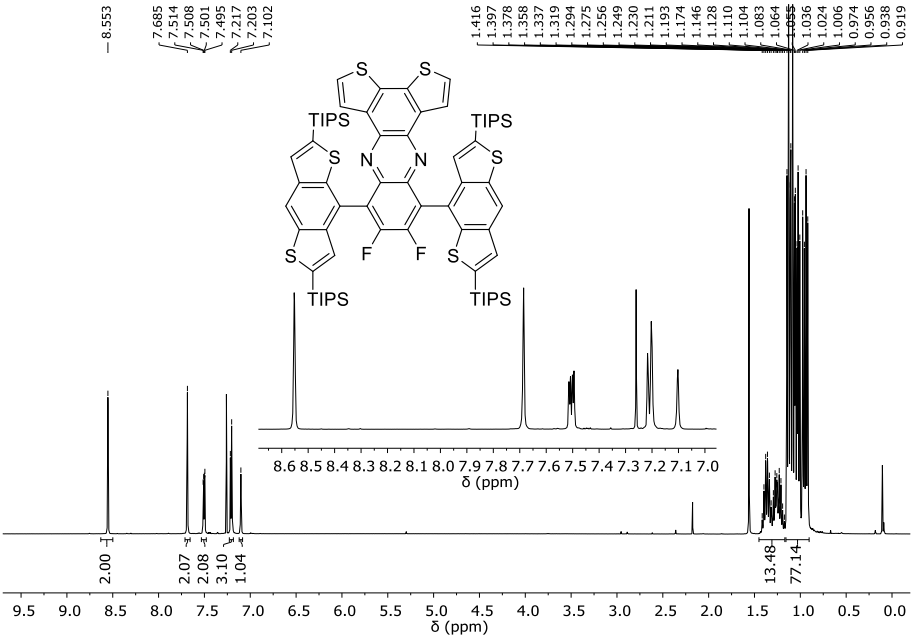

Figure S4.10: ^{1}H NMR spectrum of compound **DTPz-BDT-TIPS** in $CDCl_3$.

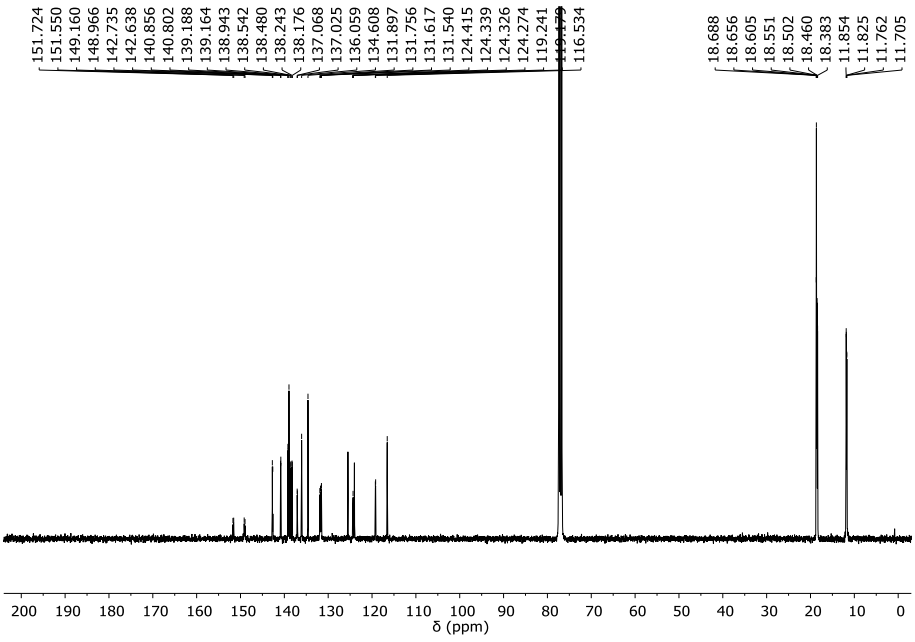

Figure S4.11: ^{13}C NMR spectrum of compound **DTPz-BDT-TIPS** in $CDCl_3$.

4.5.9. Supporting information references

1. T. Cardeynaels, S. Paredis, J. Deckers, S. Brebels, D. Vanderzande, W. Maes and B. Champagne, *Phys. Chem. Chem. Phys.*, 2020, **22**, 16387-16399.
2. J. Deckers, T. Cardeynaels, H. Penxten, A. Ethirajan, M. Ameloot, M. Kruk, B. Champagne and W. Maes, *Chemistry*, 2020, DOI: 10.1002/chem.202002549.

Chapter 5

Study of the aggregation behaviour of 4DTP-IPN – a novel red TADF emitter

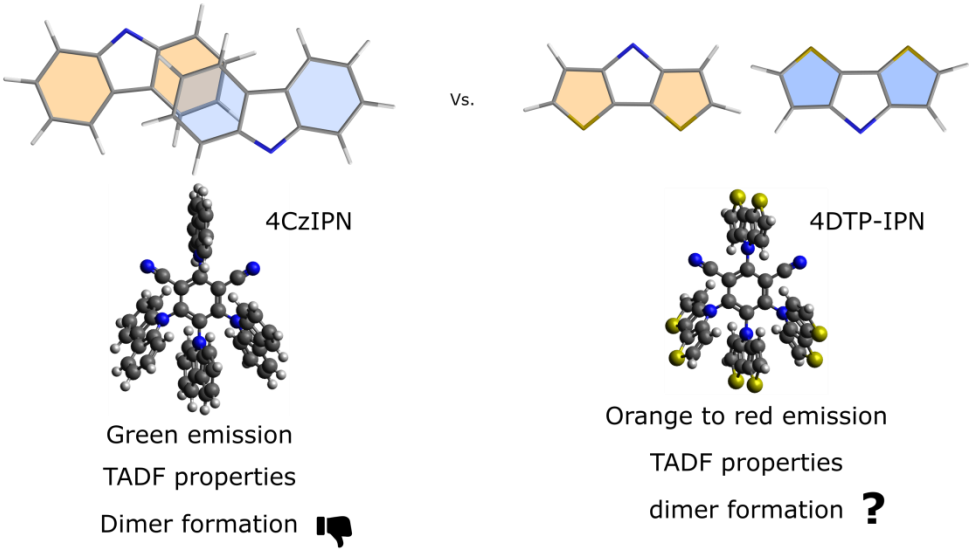

A manuscript based on this chapter is being prepared.

Contributions:
T. Cardeynaels: Synthesis of the DTP unit, quantum-chemical calculations, photophysical characterization and preparation of the manuscript.

S. Paredis: Synthesis of 4DTP-IPN, discussion of the results.

M. K. Etherington: Discussion of the results and revision of the manuscript.

D. Vanderzande, W. Maes and B. Champagne: Project management, discussion of the results and revision of the manuscript.

5.1 Introduction

First published in 2012 by Adachi *et al.*,[1] 2,4,5,6-tetra(9*H*-carbazol-9-yl)isophthalonitrile, better known as **4CzIPN** (Figure 5.1), is one of the most studied thermally activated delayed fluorescence (TADF) emitters to date, with over 450 search results (publications and patents) in Scifinder.[†] Adachi *et al.* investigated the electroluminescence properties of **4CzIPN** in an OLED device, achieving green emission and an external quantum efficiency (EQE) of 19.3±1.5%.[1] The steric hindrance created by the proximity of the 4 9*H*-carbazole (Cz) units and the two cyano groups induces a large twist between the donor (D) and acceptor (A) parts, separating the highest occupied and lowest unoccupied molecular orbitals (HOMO and LUMO, respectively). Furthermore, a very small experimental singlet-triplet energy difference (ΔE_{ST}) of 0.08 eV was found, indicative of fast rISC and efficient TADF properties.[1]

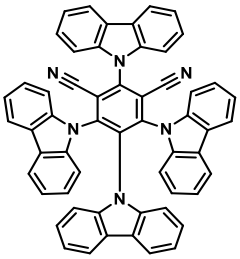

Figure 5.1: Molecular structure of **4CzIPN**.

Kim *et al.* showed that for **4CzIPN**, a significant batochromic shift in the CT state emission occurs with increasing concentration in a nonpolar host.[2] This behavior was attributed to the solid-state solvation effect (SSSE) in which the polarity of dopant **4CzIPN** molecules influences the other surrounding 4CzIPN molecules, just as solvent molecules would do in solution. However, this was refuted by Northey *et al.* as the SSSE was shown to be not as effective as the analogous phenomenon in liquid solvents due to the inability of the solid-state molecules to rearrange.[3] Etherington *et al.* investigated the photophysics of this materials in more detail, looking at potential dimer formation (Figure 5.2) that could lead to the shift of the CT emission.[4] Sublimation of pristine **4CzIPN** lead to the formation of several fractions, all consisting of crystal polymorphs but showing different emission properties. Photophysical characterization of **4CzIPN**

[†] Search conducted on 07/09/2020.

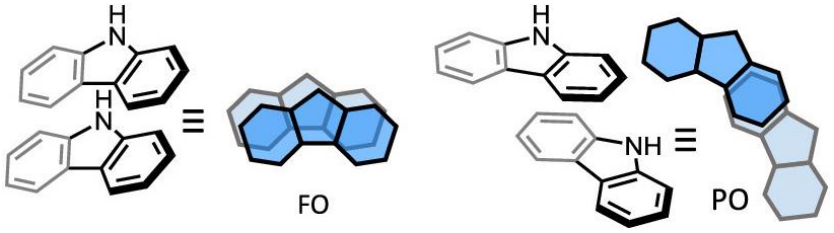

Figure 5.2: Schematic representation of the full (FO) or partial overlap (PO) between carbazole units. Reproduced from Ref. 4.

in different hosts and at different concentrations lead them to believe dimer formation in the solid state was responsible for the observed batochromic shift.[4] In this chapter, in an attempt to overcome these dimer emissions, 9*H*-carbazole was replaced by dithieno[3,2-*b*:2',3'-*d*]pyrrole (DTP). DTP is a widely used building block for the development of push-pull (small molecule and conjugated polymer) materials for organic solar cells (OSCs)[5-8] and has also been used for the design of fluorescent materials.[9] For OSC materials, DTP is attractive because of its planar and strong electron-donating nature and the tunability of the *N*-substituent. This helps in the construction of low bandgap copolymers with red-shifted absorption. While thiophene derivatives have been used for the development of fluorescent emitters, the photoluminescence quantum yield (PLQY) of such materials is generally rather low.[6, 9] Locking the flexible nature of 2,2'-bithiophene by ring fusion between the two thienyl units with an N-alkyl moiety leads to a significant increase in the PLQY as non-radiative decay pathways are restricted.[6, 9] Furthermore, the photochemical stability of the DTP unit renders DTP-based emitters one of the most successful thiophene-based fluorescent materials.[9-11]

While coupling of DTP via the α-positions would lead to largely planar molecules, coupling via the N-atom yields sterically hindered and twisted architectures. Using isophthalonitrile (IPN) as the acceptor to construct 2,4,5,6-tetrakis(4*H*-dithieno[3,2-*b*:2',3'-*d*]pyrrol-4-yl)isophthalonitrile (**4DTP-IPN**), a very similar structure to that of **4CzIPN** can be obtained. In this chapter, the synthesis and photophysical characterization of **4DTP-IPN** are reported and a preliminary investigation into the presence or absence of dimer formation for this compound is performed.

5.2 Results and discussion

5.2.1 Synthesis

For the synthesis of DTP, several methods have been reported.[12, 13] Förtsch *et al.* compared several synthetic pathways and developed a single-step synthesis using triphenylsilylamine as the ring-closing reagent.[12] The intermediate triphenylsilyl-protected DTP is not found and instead the reaction proceeds directly to the unprotected DTP in high yields of around 72%. However, after several attempts, no product could be obtained under these conditions and even changing the catalytic system to $Pd_2(dba)_3$ - $(t\text{Bu})_3\text{PH}(BF_4)$ did not lead to the formation of the desired product. Instead, a two-step procedure was used, involving the synthesis of a carbamate protected DTP and subsequent deprotection (Scheme 5.1). This synthesis protocol was also reported by Förtsch *et al.*, but gives a lower overall yield due to the ring-closure and deprotection steps with yields of around 46 and 81%, respectively.[13] Despite having a lower overall yield, the two-step synthesis affords better control over the reaction conditions and allows the intermediate to be isolated and purified before the final deprotection step. The final nucleophilic substitution reaction between DTP and tetrafluoroisophthalonitrile was performed according to the synthesis procedure for the analogous **4CzIPN**.[1] The detailed synthetic procedure can be found in the supporting information.

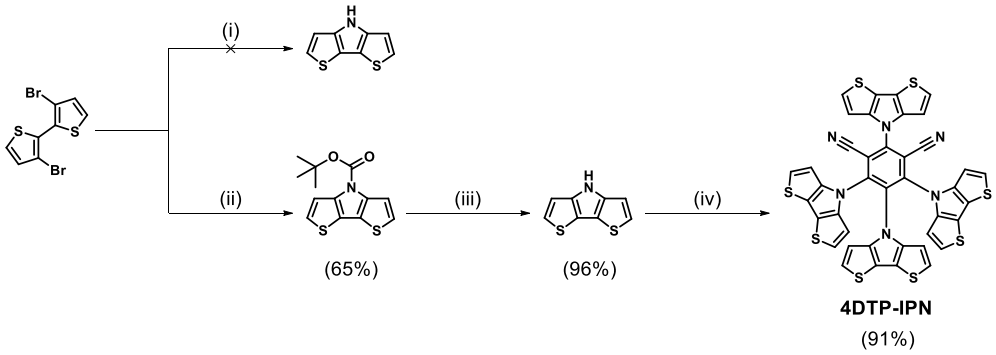

Scheme 5.1: Synthesis pathways for 4DTP-IPN: (i) $Pd_2(dba)_3$, $(t\text{Bu})_3\text{P}$, triphenylsilylamine, NaO*t*Bu, toluene, 80 °C, 16 h; (ii) CuI, *tert*-butyl carbamate, *N*,*N*'-dimethylethylenediamine, K_2CO_3, toluene, 110 °C, 24 h; (iii) K_2CO_3, methanol, room temperature, 5 h; (iv) tetrafluoroisophthalonitrile, NaH, THF, 50 °C, 16 h.

5.2.2 Quantum-chemical calculations

Density functional theory (DFT) calculations were performed to optimize the geometry of **4DTP-IPN** and **4CzIPN**[‡] (M06/6-311G(d)).[14] All frequencies were found to be real, indicating that the optimized geometries correspond to minima on the potential energy surfaces. Time-dependent DFT (TDDFT) calculations using a modified LC-BLYP[15] range-separated exchange-correlation functional with the Pople 6-311G(d) basis set under the Tamm-Dancoff approximation[16] were performed. The range-separating parameter ω was set to 0.17 bohr^{-1} for LC-BLYP, in accordance with the findings of previous works.[17, 18] Furthermore, the TDDFT calculations were performed using the polarizable continuum model (PCM) with cyclohexane to simulate a non-polar environment. All calculations were performed in the Gaussian16 package.[19] Following the work of Le Bahers *et al.*[20], the charge-transfer (CT) character of the singlet and triplet transitions under consideration was investigated by looking at the difference between the ground and excited state electron densities.

The calculated geometries of **4CzIPN** and **4DTP-IPN** (Figure 5.3) are similar because of the steric repulsion among the donor units, resulting in similar D-A dihedral angles (Table 5.1). The main difference between the two compounds can be found in the HOMO distribution. For **4DTP-IPN**, the HOMO is located solely on the neighboring three DTP units and any HOMO-LUMO overlap comes from the LUMO extending onto the DTP units. On the other hand, **4CzIPN** shows mutual overlap between the HOMO and LUMO on both the donor and acceptor parts. This difference in frontier orbital overlap is reflected in the oscillator strengths of the first and second excited singlet states (Table 5.1), which are significantly smaller for **4DTP-IPN**. The overlap also influences ΔE_{ST}, which is smaller for **4DTP-IPN** as well.

Table 5.1: TDDFT results for the first vertical singlet excitation energies and corresponding oscillator strengths, the first and second vertical triplet excitation energies and dihedral angles (obtained from DFT geometry optimization).

Compound	ΔE_{S_1} (eV)	f_{S_1}	ΔE_{S_2} (eV)	f_{S_2}	ΔE_{T_1} (eV)	ΔE_{T_2} (eV)	$\Delta E_{T_2-T_1}$ (eV)	$\Delta E_{S_1-T_1}$ (eV)	D-A angle (°)[a]
4DTP-IPN	2.63	0.001	2.76	0.009	2.57	2.63	0.06	0.06	57
4CzIPN	2.84	0.095	3.11	0.156	2.68	2.82	0.14	0.16	62

[a] Taken as the average of 8 possible torsion angles.

[‡] Although 4CzIPN has been investigated using quantum-chemical calculations (M06-2X/6-31G(d)) in the past,[1] they have been repeated using our methodology for consistency and facile comparison of the properties.

The TDDFT calculations show that the first excited singlet state of **4DTP-IPN** is slightly lower in energy, illustrative of the stronger electron-donating strength of the DTP with respect to the carbazole unit (Table 5.1). This also implies that **4DTP-IPN** will lean more closely toward the red end of the spectrum, whereas **4CzIPN** is a green emitter. Both compounds have a relatively small theoretical ΔE_{ST}, with **4DTP-IPN** having the smaller of the two. The calculated triplet-triplet gaps have about the same size as the singlet-triplet gaps for both compounds, indicating that S_1 and T_2 are close in energy. According to the spin-vibronic mechanism of TADF, this is beneficial for the rISC as the two triplet states become coupled.[21, 22]

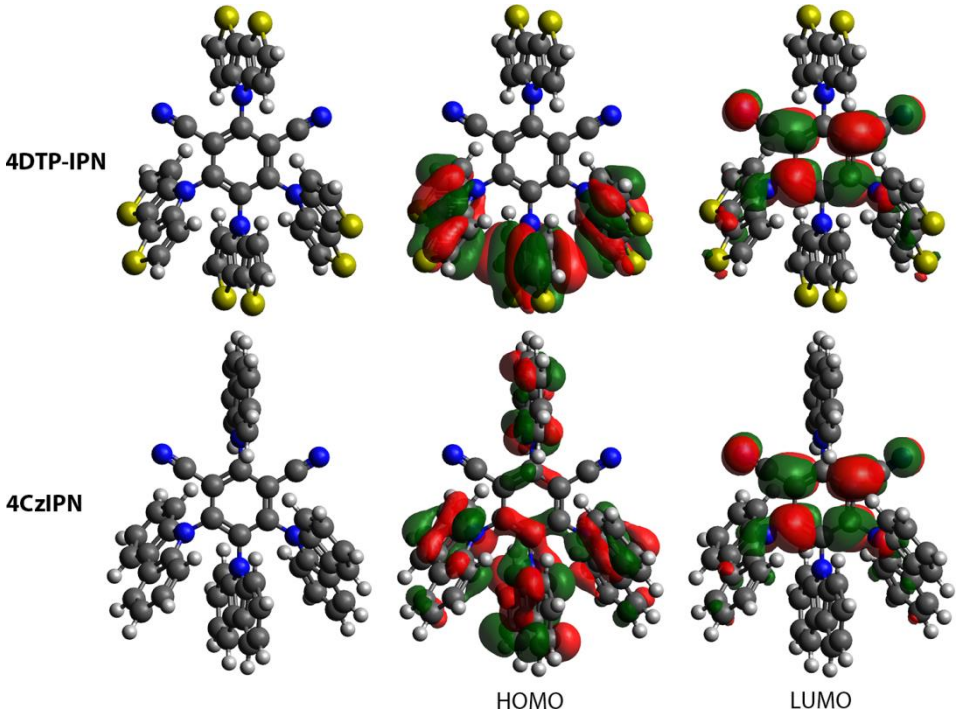

Figure 5.3: Optimized geometries and HOMO and LUMO for **4DTP-IPN** and **4CzIPN**. Isosurface values of 0.02 a.u. were used for all orbitals.

Looking at the differences between the ground and excited state electron densities (Figure 5.4), both compounds show predominant CT character, as indicated by the localized nature of the diminishing (cyan) and increasing (purple) charge density regions on the donor and acceptor units, respectively. This is quantified as the amount of charge that is transferred (q_{CT}) during the

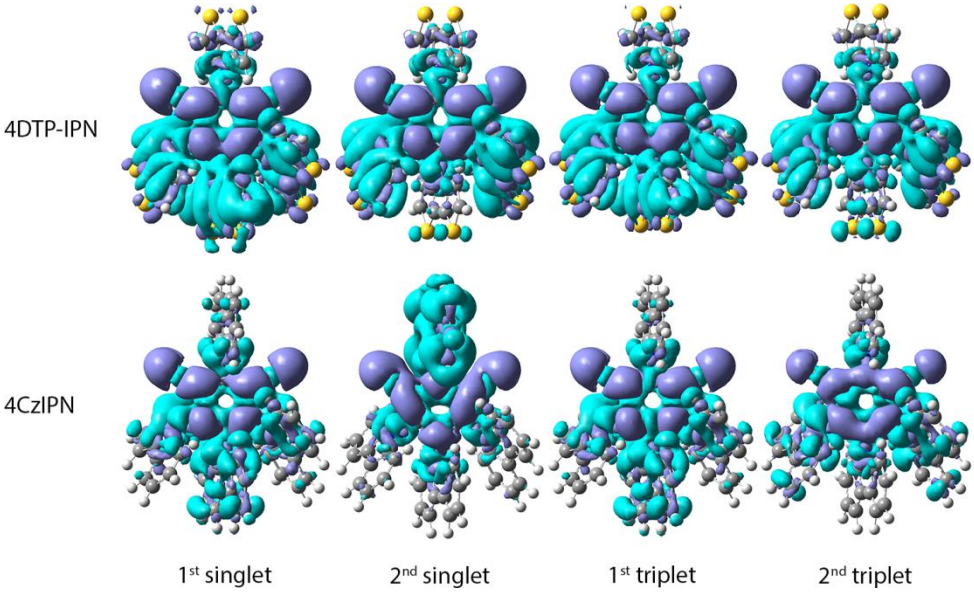

Figure 5.4: Ground-excited state electron density differences for the first and second excited singlet and triplet states. Isosurface values of 0.0004 a.u. were used for all densities. The cyan regions indicate a decrease in charge density, whereas the purple regions indicate an increase in charge density.

transition in Table 5.2. 4DTP-IPN shows full CT character (q_{CT} = 1.0) for its first and second singlet excited states and also for the first triplet excited state. The second triplet excited state shows slightly less CT character. Overall, **4CzIPN** shows less CT character, indicated by the reduced q_{CT} values (Table 5.2). This is likely due to the better overlap between the frontier orbitals, as illustrated in Figure 5.3 and Figure S5.3.

Table 5.2: Nature of the various transitions (H = HOMO, L = LUMO) and amount of charge transfer (q_{CT}) accompanying the S_0->S_x and S_0->T_x transitions in cyclohexane.

	S1		S2		T1		T2	
Compound	Nature	q_{CT}	Nature	q_{CT}	Nature	q_{CT}	Nature	q_{CT}
4DTP-IPN	H->L	1.00	H-1->L	1.00	H->L	1.00	H-1->L	0.84
4CzIPN	H->L	0.84	H->L+1	0.97	H->L	0.83	H-4->L	0.65

5.2.3 Photophysical characterization

The steady-state absorption and emission spectra for **4DTP-IPN** and **4CzIPN** in a solid host are shown in Figure 5.5. While the UV-VIS absorption spectra are very similar, the emission shows a clear red-shift for **4DTP-IPN**, confirming the aforementioned stronger electron-donating character of the DTP unit. Solution

measurements for **4DTP-IPN** (Figure 5.5) show the solvatochromic behavior of the emission, indicating CT character, whereas the absorption is virtually independent of the solvent. Additionally, the emission spectra in toluene and chloroform show a shoulder on the red side of the emission peak, which could be indicative of aggregation in solution. Simulation of the UV-VIS absorption spectra (Figure S5.2) revealed the influence of higher energy localized singlet states for the absorption spectra of both.

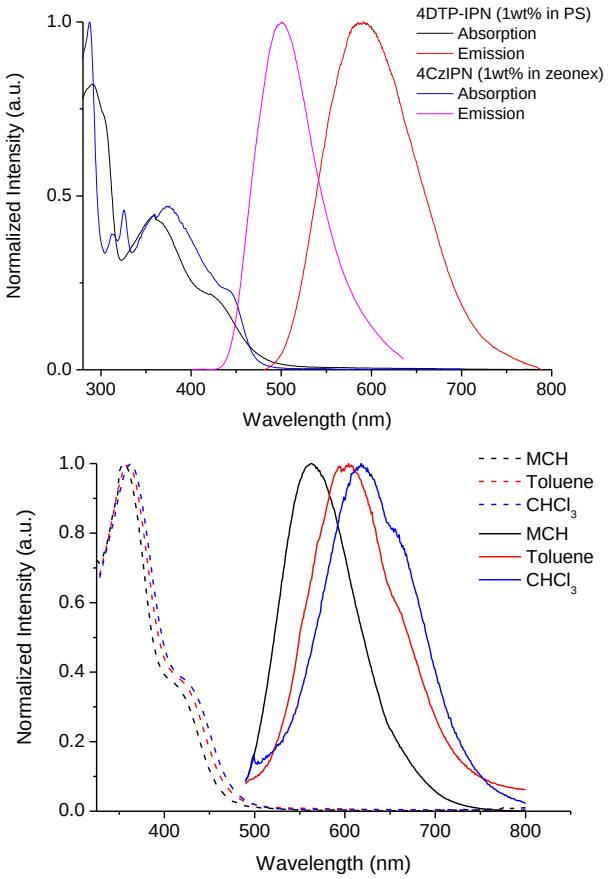

Figure 5.5: Steady-state absorption and prompt (0.8 ns) time-resolved emission spectra in polystyrene for **4DTP-IPN** and in zeonex for **4CzIPN** (top) and steady-state absorption and emission spectra for **4DTP-IPN** in methylcyclohexane (MCH), toluene and chloroform ($CHCl_3$) (bottom).

Time-resolved emission experiments were then conducted to obtain the room temperature and 80 K emission decays for **4DTP-IPN** in a variety of host materials. Zeonex and polystyrene were chosen as two polymeric hosts in which

the emitter was doped at 0.1 and 1 wt% with respect to the polymer (Figure S5.9). Bis[2-(diphenylphosphino)phenyl]ether oxide (DPEPO) and 1,3-bis(triphenylsilyl)benzene (UGH-3) (Figure S5.9) were used as small molecule hosts at a 10 wt% dopant concentration to mimic their doping concentration in potential light-emitting devices.

Polymeric hosts are typically more flexible in nature and are found to give similar photophysical results as solution measurements for solvents of a similar polarity. This is because the polymer chains are not ordered and steric hindrance between the polymer chains can give rise to voids in which solvent can get trapped. For these reasons, the emitter doped in zeonex often behaves similar to being dissolved in methylcyclohexane.[23] Polystyrene is less often reported in literature, but is expected to behave similarly to toluene. However, because these polymers are not conjugated, they are unable to transport charge carriers and cannot be used in optoelectronic devices. For this purpose, small molecule semiconducting materials with a large HOMO-LUMO offset such as DPEPO and UGH-3 are often used. In contrast to polymers, small molecule host materials can be co-evaporated with the active materials to create more homogeneous device layers with a higher control over layer thickness and morphology. The packing in these small molecule host layers is tighter and can influence the dihedral angles, and thus indirectly influence the optical properties of the emitter material. Furthermore, the polarizability and dielectric constant of the small molecule host materials can also influence the optical properties of the TADF emitter.[23-25] Despite their inherent inability to conduct charge carriers, polymeric host materials are still useful to probe the photophysical properties of TADF emitters. The samples can easily be prepared via drop-casting and due to the high polymer viscosity, thicker films can be made.

In Figure 5.6, the time-resolved emission spectra extracted from the full emission decays at room temperature (left) and at 80 K (right) for **4DTP-IPN** doped at 1 wt% in zeonex are shown. Following the excitation (λ_{exc} = 355 nm), emission with an onset of around 513 nm (2.42 eV; Table 5.3) is observed at room temperature until several microseconds, when it starts to blue-shift slightly over time. In Figure 5.6c, the intensity has become very weak, nearing the detection limit of the iCCD camera, and seemingly stabilizes. At 80 K (Figure 5.6d-f), the emission at 0.8 ns is very similar to that at room temperature at 0.8

ns, indicating that the same emissive excited state is involved. However, the emission then red-shifts slightly over the course of several hundred nanoseconds until it stabilizes again in the microseconds regime. Contrary to the room temperature spectra, the emission persists into the milliseconds regime and slightly blue-shifts again as time increases. With typical lifetimes of several up to tens of nanoseconds for prompt fluorescence, the long-lived emission at room temperature is likely caused by ISC followed by a triplet upconversion mechanism such as TADF. The blue-shift in the microsecond regime for **4DTP-IPN** at room temperature (Figure 5.6b) could be due to the non-homogeneous distribution of the dihedral angles of the various **4DTP-IPN** molecules in the polymer host.[23] Molecules with a less ideal conformation, i.e. smaller dihedral angles, will have a larger ΔE_{ST} because the overlap between the HOMO and LUMO increases. This imposes a smaller rISC rate because the energy gap that needs to be overcome is now larger and the resulting emission emerges at a later time. The changing dihedral angles also destabilize the position of the ^{1}CT state, causing the emission to blue-shift.

For triplet upconversion mechanisms such as TADF or triplet-triplet annihilation (TTA), one would expect them to be absent at 80 K due to their temperature dependency. This is apparently not the case as the delayed emission is present throughout the decay at 80 K, although a decrease in emission intensity is apparent by the decreased signal to noise ratio at 156.3 and 333.2 ns (Figure 5.6d). With an experimental ΔE_{ST} of 0.04 eV (0.06 eV theoretically), obtained from the onsets of the prompt fluorescence at room temperature and the time-resolved millisecond emission at 80 K, it is possible to have delayed emission even at 80 K, as is sometimes also seen for other compounds.[23] Therefore, we attribute the initial red-shift at 80 K (Figure 5.6d) to prompt CT emission followed by TADF emission from the lowest vibrational energy level of the ^{1}CT state. Upon excitation by the laser, higher vibrational levels are reached as the excitation energy is larger than the energy of the ^{1}CT state. However, due to the decreased thermal energy at 80 K, rISC is likely to occur to the lowest vibrational energy level of the ^{1}CT state because this requires the least amount of energy. This is visible as the blue edge of the emission red-shifts, whereas the red-edge of the emission remains relatively constant throughout this initial period in the decay (Figure 5.6d). In the microseconds regime, the emission at

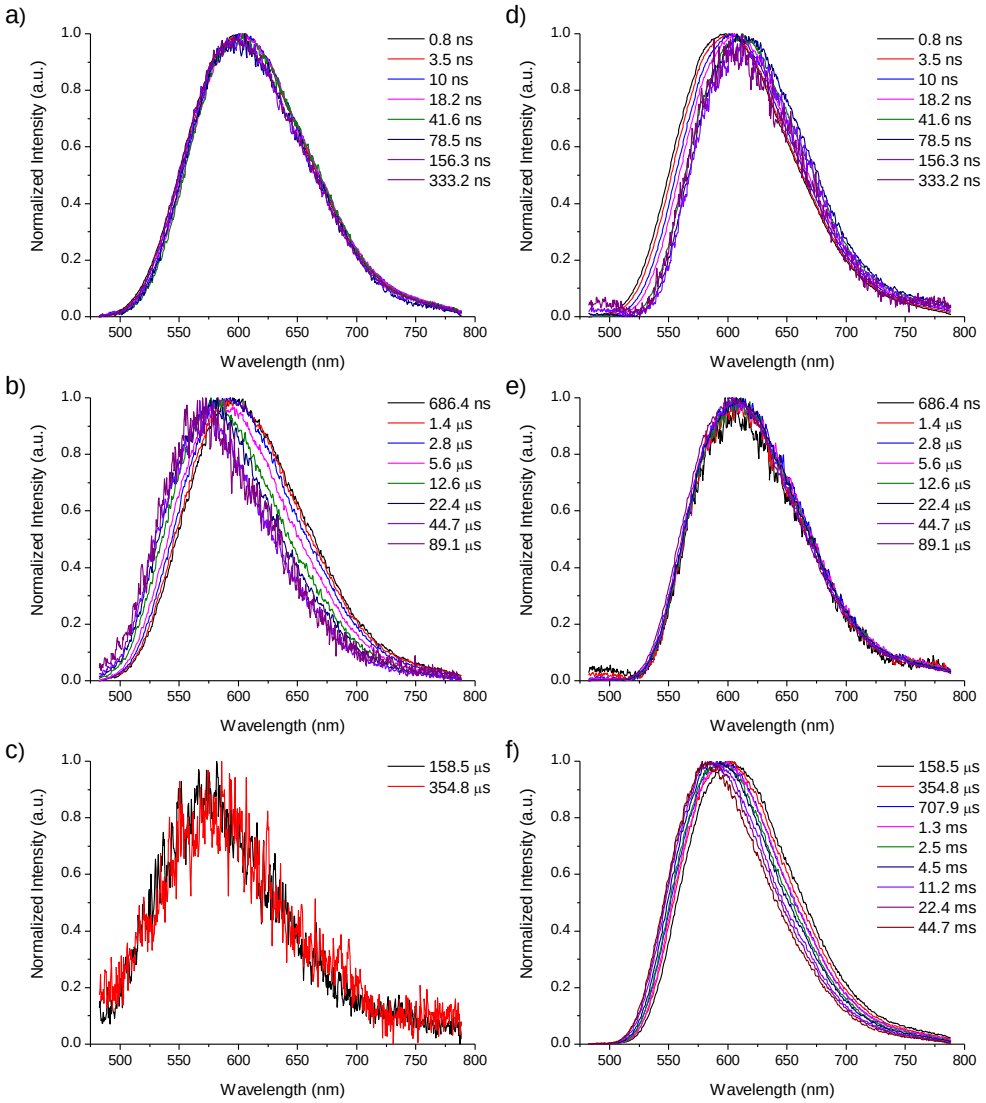

Figure 5.6: Emission spectra extracted from the time-resolved emission decay of **4DTP-IPN** in a 1 wt% doped zeonex film at room temperature (left) and 80 K (right).

80 K remains constant because of the reduced thermal energy and hence smaller rISC values (Figure 5.6e). In the milliseconds regime, the emission blue-shifts (Figure 5.6f) and, similar to what we observed at room temperature in the microseconds regime, we attribute this behavior to the non-homogeneous distribution of the dihedral angles in the host. These effects are again delayed in time because the experiment is taking place at 80 K. The small ΔE_{ST} makes it

Table 5.3: Photophysical properties for **4DTP-IPN** and **4Cz-IPN** doped at 1 wt% in zeonex.

Compound	ΔE_S (eV)[a]	ΔE_T (eV)[b]	ΔE_{ST} (eV)[c]	τ_{Fp} (ns)[d]	τ_{Fd} (μs)[e]	k_{ISC}[f]	k_{rISC}[f]
4DTP-IPN	2.42	2.38	0.04	30.33	8.30	1.82×10^7	3.90×10^5
4CzIPN	2.79	2.69	0.10	19.68	12.25	1.33×10^7	1.37×10^5

[a] Taken from the onset of the prompt fluorescence (PF) emission. [b] Taken from the onset of the phosphorescence emission at millisecond times at 80 K. [c] Calculated as $E_S - E_T$. [d] Lifetime of prompt fluorescence (F_p). [e] Lifetime of delayed fluorescence (F_d). [f] k_{ISC} and k_{rISC} rates were determined using kinetic fitting of the PF and DF emission according to literature.[26]

difficult to distinguish between the TADF and phosphorescence pathways, and depending on the rISC and phosphorescence rates, a combination of the two mechanisms may be observed. The observed behaviour of **4DTP-IPN** seems to be independent of the concentration (0.1 vs 1 wt% doped in zeonex), but also independent of the used host material as it behaves the same in polystyrene, DPEPO and UGH. The time-resolved emission spectra of **4DTP-IPN** in these host materials can be found in the supporting information (Figures S5.4-S5.8). The full emission decays for **4DTP-IPN** at room temperature in the various host materials are plotted in Figure 5.7. It is apparent that the decays all show the same shape, indicating the similar behaviour in the various host materials. In the small molecule hosts, the decays are a little bit shorter, which is due to the fact that the films are less thick and the emission intensity drops below the sensitivity of the iCCD camera at earlier time scales.

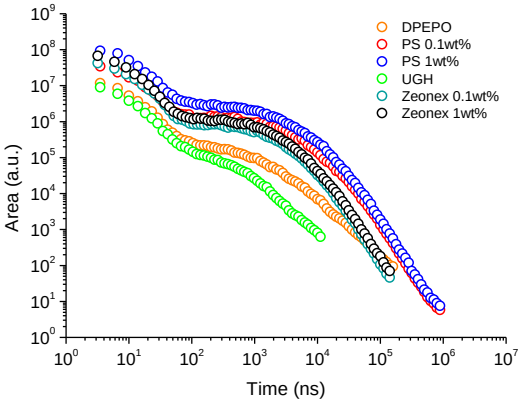

Figure 5.7: Time-resolved emission decays for **4DTP-IPN** in various host materials.

5.2.4 Laser power experiments

Measuring the emission intensity at various laser powers can help to distinguish between TADF and TTA as the delayed emission mechanism since TADF scales with the laser power as a power 1, whereas TTA scales as a power 2.[27] This is especially valid at very low laser powers where the triplet generation is not saturated by the laser power. As can be seen in Figure 5.8, the area of the emission spectrum versus the laser power yields a linear correlation with a slope of 1.01 and an R^2 value of 1, indicative of a TADF mechanism.

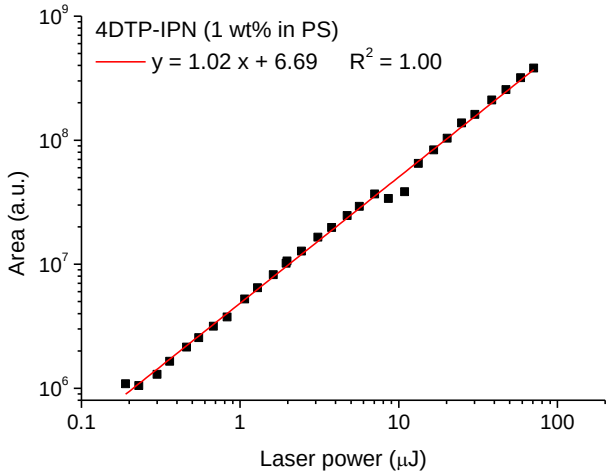

Figure 5.8: Area under the emission curve versus the laser power for a 1 wt% polystyrene film of **4DTP-IPN**.

5.2.5 Dimer formation

In the original report by Etherington *et al.*,[4] dimer formation was observed for 4CzIPN when comparing different fractions obtained using sublimation as a material purification tool. Although all fractions corresponded to **4CzIPN**, their photophysical properties were clearly different, indicating the presence of different species of **4CzIPN**, including monomeric and dimeric species. Increasing the dopant concentration of **4CzIPN** in zeonex from 0.3 to 1 wt% revealed a red-shift in the emission over the course of several tens of nanoseconds, followed by a blue-shift when the TADF emission appeared (Figure 5.9a,b). The 10wt% films are dominated by dimer emission, but have contributions of monomeric species at very early times (Figure 5.9c).

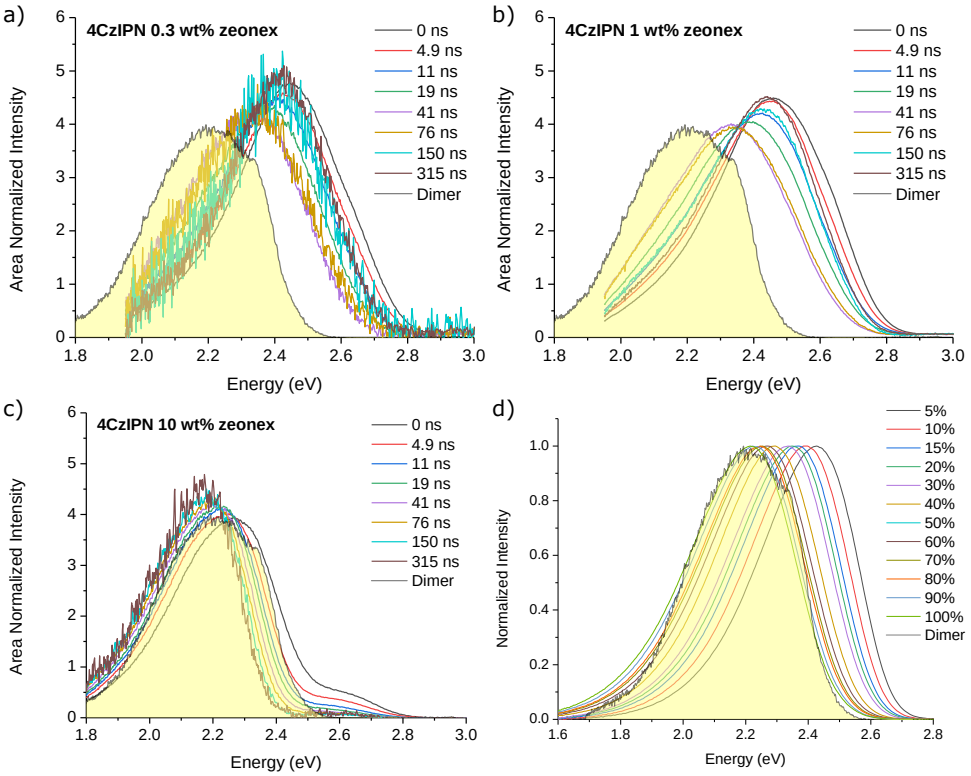

Figure 5.9: Nanosecond emission of **4CzIPN** doped at various concentrations in zeonex (a-c) and electroluminescence of a device based on **4CzIPN** doped in mCBP at various concentrations. The filled yellow peak overlaid in each panel is the dimer emission observed after a 11 ns delay time from a 10 wt% zeonex film of **4CzIPN** at RT using 532 nm excitation. Used with permission of Etherington *et al.*

Furthermore, dimer formation was also seen in the small molecule host 3,3′-di(9*H*-carbazol-9-yl)-1,1′-biphenyl (mCBP, Figure S5.9). Devices with varying doping concentrations of 4CzIPN in mCBP revealed a gradual shift of the emission with increasing 4CzIPN concentration towards that of the neat film (100%) or pure dimer emission (Figure 5.9d). When looking at **4DTP-IPN**, these variations in the nanoseconds regime are not seen in any of the host materials (Figure 5.6, Figure S5.4-S5.8). In fact, the emission remains the same throughout this entire region, only showing a blue-shift in the microseconds regime. This blue-shift was attributed to the presence of a heterogeneous mixture of dihedral angles within the various 4DTP-IPN compounds. However, they could also indicate similar dimer properties as ascribed to 4CzIPN. Although the blue-shift for 4CzIPN (1wt% in zeonex) at early times was of much larger

energy (±0.1 eV), especially when looking at 80 K (±0.3 eV), it could be that the prompt emission of 4DTP-IPN is dominated by dimer emission, whereas the microseconds emission (RT) and milliseconds emission (80K) show increasing contribution from the monomeric species. This would also be in line with the decreased solubility of 4DTP-IPN with respect to 4CzIPN and the observed aggregation shoulder in the solution based emission measurements. However, as these blue and red shifts in the time-resolved spectra can be attributed to many factors or even a combinations of factors, it is challenging to resolve the underlying mechanisms based on the available data and additional measurements, for example using different concentrations are needed to fully elucidate their cause.

5.3 Conclusions

We have shown the synthesis and photophysical characterization of **4DTP-IPN**, using the 4*H*-dithieno[3,2-*b*:2',3'-*d*]pyrrole (DTP) moiety as a novel donor unit to construct emissive D-A type compounds. Time-resolved emission spectroscopy showed the presence of TADF, as observed by the long-lived fluorescence emission and small theoretical (0.06 eV) and experimental (0.04 eV) ΔE_{ST} values. **4DTP-IPN** afforded a red-shifted emission in comparison to the 9*H*-carbazole analogue (**4CzIPN**), which has been investigated extensively in literature prior to this study. A recent report by Etherington *et al.* showed a high tendency for **4CzIPN** to form dimers in doped films at concentrations of 10 wt% or higher.[4] The presented experiments with **4DTP-IPN** illustrated that, at the minimum, there is a different tendency towards dimer formation. The current results are inconclusive to determine whether dimer formation is decreased or effectively enhanced by incorporation of the DTP unit.

Nevertheless, these results show that **4DTP-IPN** has the potential of achieving higher color purity than **4CzIPN**, whereas the red-shifted nature suggests high-efficiency red-emitting OLEDs might be produced when incorporated into a suitable host. Further studies of the concentration-dependent behavior in doped films, sublimation, and PLQY of **4DTP-IPN**, as well as incorporation in OLED devices, is planned.

5.4 References

1. H. Uoyama, K. Goushi, K. Shizu, H. Nomura and C. Adachi, *Nature*, 2012, **492**, 234-238.
2. H. S. Kim, S.-R. Park and M. C. Suh, *J. Phys. Chem. C*, 2017, **121**, 13986-13997.
3. T. Northey, J. Stacey and T. J. Penfold, *J. Mater. Chem. C*, 2017, **5**, 11001-11009.
4. M. K. Etherington, N. A. Kukhta, H. F. Higginbotham, A. Danos, A. N. Bismillah, D. R. Graves, P. R. McGonigal, N. Haase, A. Morherr, A. S. Batsanov, C. Pflumm, V. Bhalla, M. R. Bryce and A. P. Monkman, *J. Phys. Chem. C*, 2019, **123**, 11109-11117.
5. Y. Geng, A. Tang, K. Tajima, Q. Zeng and E. Zhou, *J. Mater. Chem. A*, 2019, **7**, 64-96.
6. G. Turkoglu, M. E. Cinar and T. Ozturk, *Top. Curr. Chem.*, 2017, **375**, 84.
7. S. C. Rasmussen and S. J. Evenson, *Prog. Polym. Sci.*, 2013, **38**, 1773-1804.
8. W. Vanormelingen, J. Kesters, P. Verstappen, J. Drijkoningen, J. Kudrjasova, S. Koudjina, V. Liégeois, B. Champagne, J. Manca, L. Lutsen, D. Vanderzande and W. Maes, *J. Mater. Chem. A*, 2014, **2**, 7535-7545.
9. S. C. Rasmussen, S. J. Evenson and C. B. McCausland, *Chem. Commun.*, 2015, **51**, 4528-4543.
10. H. Mo, K. R. Radke, K. Ogawa, C. L. Heth, B. T. Erpelding and S. C. Rasmussen, *Phys. Chem. Chem. Phys.*, 2010, **12**, 14585-14595.
11. K. R. Radke, K. Ogawa and S. C. Rasmussen, *Org. Lett.*, 2005, **7**, 5253-5256.
12. S. Förtsch, A. Vogt and P. Bäuerle, *J. Phys. Org. Chem.*, 2017, **30**, e3743.
13. S. Förtsch and P. Bäuerle, *Polym. Chem.*, 2017, **8**, 3586-3595.
14. Y. Zhao and D. G. Truhlar, *Theor. Chem. Acc.*, 2008, **120**, 215-241.
15. Y. Tawada, T. Tsuneda, S. Yanagisawa, T. Yanai and K. Hirao, *J. Chem. Phys.*, 2004, **120**, 8425-8433.
16. S. Hirata and M. Head-Gordon, *Chem. Phys. Lett.*, 1999, **314**, 291-299.
17. T. Cardeynaels, S. Paredis, J. Deckers, S. Brebels, D. Vanderzande, W. Maes and B. Champagne, *Phys. Chem. Chem. Phys.*, 2020, **22**, 16387-16399.
18. T. J. Penfold, *J. Phys. Chem. C*, 2015, **119**, 13535-13544.
19. G. W. Trucks, M. J. Frisch, H. B. Schlegel, G. E. Scuseria, M. A. Robb, J. R. Cheeseman, G. Scalmani, V. Barone, G. A. Petersson, H. Nakatsuji, X. Li, M. Caricato, A. V. Marenich, J. Bloino, B. G. Janesko, R. Gomperts, B. Mennucci, H. P. Hratchian, J. V. Ortiz, A. F. Izmaylov, J. L. Sonnenberg, D. Williams-Young, F. Ding, F. Lipparini, F. Egidi, J. Goings, B. Peng, A. Petrone, T. Henderson, D. Ranasinghe, V. G. Zakrzewski, J. Gao, N. Rega, G. Zheng, W. Liang, M. Hada, M. Ehara, K. Toyota, R. Fukuda, J. Hasegawa, M. Ishida, T. Nakajima, Y. Honda, O. Kitao, H. Nakai, T. Vreven, K. Throssell, J. A. Montgomery, Jr., J. E. Peralta, F. Ogliaro, M. J. Bearpark, J. J. Heyd, E. N. Brothers, K. N. Kudin, V. N. Staroverov, T. A. Keith, R. Kobayashi, J. Normand, K. Raghavachari, A. P. Rendell, J. C.

Burant, S. S. Iyengar, J. Tomasi, M. Cossi, J. M. Millam, M. Klene, C. Adamo, R. Cammi, J. W. Ochterski, R. L. Martin, K. Morokuma, O. Farkas, J. B. Foresman, and D. J. Fox, Gaussian, Inc., Wallingford CT, 2016.
20. T. Le Bahers, C. Adamo and I. Ciofini, *J. Chem. Theory Comput.*, 2011, **7**, 2498-2506.
21. M. K. Etherington, J. Gibson, H. F. Higginbotham, T. J. Penfold and A. P. Monkman, *Nat. Commun.*, 2016, **7**, 13680.
22. J. Gibson, A. P. Monkman and T. J. Penfold, *ChemPhysChem*, 2016, **17**, 2956-2961.
23. K. Stavrou, L. G. Franca and A. P. Monkman, *ACS Appl. Electron. Mater.*, 2020, DOI: 10.1021/acsaelm.0c00514.
24. P. L. Dos Santos, J. S. Ward, M. R. Bryce and A. P. Monkman, *J. Phys. Chem. Lett.*, 2016, **7**, 3341-3346.
25. M. Etherington, *Front. Chem.*, 2020, DOI: 10.3389/fchem.2020.00716.
26. N. Haase, A. Danos, C. Pflumm, A. Morherr, P. Stachelek, A. Mekic, W. Brütting and A. P. Monkman, *J. Phys. Chem. C*, 2018, **122**, 29173-29179.
27. F. B. Dias, T. J. Penfold and A. P. Monkman, *Methods Appl. Fluoresc.*, 2017, **5**, 012001.

5.5 Supporting information

5.5.1 Experimental details

5.5.1.1 Materials and methods

All reagents and chemicals were obtained from commercial sources and used without further purification. Dry solvents were obtained using an MBraun solvent purification system (MB SPS-800) equipped with alumina columns. Preparative (recycling) size exclusion chromatography (SEC) was performed on a JAI LC-9110 NEXT system equipped with JAIGEL 1H and 2H columns (eluent chloroform, flow rate 3.5 mL min^{-1}). Proton and carbon nuclear magnetic resonance (^{1}H and ^{13}C NMR) spectra were obtained on a Varian or Jeol spectrometer operating at 400 MHz for ^{1}H (100 MHz for ^{13}C). Chemical shifts (δ) are given in ppm relative to $CDCl_3$ (δ = 7.26 ppm for ^{1}H NMR, δ = 77.06 ppm for ^{13}C NMR). All NMR spectra were taken at room temperature. Matrix-assisted laser desorption/ionization - time-of-flight (MALDI-ToF) mass spectra were recorded on a Bruker Daltonics Ultraflex II ToF/ToF. Approximately 1 µL of the matrix solution (16 mg mL^{-1} *trans*-2-[3-(4-*tert*-butylphenyl)-2-methyl-2-propenylidene]malononitrile (DTCB) in chloroform) was spotted onto an MTP Anchorchip 600/384 MALDI plate. The spot was allowed to dry and 1 µL of the analyte solution (0.5 mg mL^{-1} In chloroform) was spotted on top of the matrix. All solution-based absorption spectra were recorded on a Varian Cary 5000 UV-Vis-NIR spectrophotometer from Agilent Technologies. Steady-state emission spectra (in solution) were recorded on a Horiba-Jobin Yvon Fluorolog-3 spectrofluorometer equipped with a 450 W Xe lamp as the light source. All spectroscopic measurements were done in spectroscopic grade solvents. Films were prepared via drop-casting using a mixture of the emitter and host in toluene at the designated concentrations. The films were drop-casted onto a quartz substrate at 65 °C to facilitate evaporation of the solvent. Absorption and emission spectra of the films were collected using a UV-3600 double beam spectrophotometer (Shimadzu) and a Fluoromax fluorimeter (Jobin Yvon), respectively. Time-resolved photoluminescence spectra and decays were recorded using a nanosecond gated spectrograph-coupled iCCD (Stanford) using an Nd:YAG laser emitting at 355 nm (EKSPLA). Laser power experiments were conducted using an N_2 laser (Lasertechnik Berlin) emitting at 337 nm with the

same nanosecond gated spectrograph-coupled iCCD (Stanford) camera, attenuating the excitation using reflective neutral density filters.

5.5.1.2 Synthesis procedures

4*H*-Dithieno[3,2-*b*:2',3'-*d*]pyrrole (DTP) was synthesized according to literature.[1]

*2,4,5,6-tetrakis(4H-dithieno[3,2-b:2',3'-d]pyrrol-4-yl)isophthalonitrile (**4DTP-IPN**)*

NaH (60% in oil; 105.1 mg, 2.63 mmol) was added slowly to a stirred solution of DTP (455.7 mg, 2.54 mmol) in dry THF under nitrogen atmosphere at room temperature. After 10 min, tetrafluoroterephthalonitrile (101.6 mg, 0.51 mmol) was added and the reaction mixture was stirred for 16 h at 50 °C in an oil bath. Thereafter, the excess of NaH was quenched with water (0.5 mL). The resulting solid was filtered off, washed with water and EtOH, and dried under vacuum. 4DTP-IPN was obtained as a yellow solid (388.0 mg, 91%). ^{1}H NMR (400 MHz, $CDCl_3$): 7.43 (d, *J* = 5.4 Hz, 2H), 7.28 (d, *J* = 5.4 Hz, 2H), 6.98 (d, *J* = 5.4 Hz, 4H), 6.69 (d, *J* = 5.4 Hz, 2H), 6.62 (d, *J* = 5.4 Hz, 4H), 6.04 (d, *J* = 5.4 Hz, 2H). ^{13}C NMR (100 MHz, $CDCl_3$): 144.92, 143.99, 143.39, 142.50, 141.77, 130.29, 125.27, 124.51, 123.77, 120.21, 119.88, 118.75, 111.97, 111.79, 110.93, 109.24.

5.5.2 Additional calculations

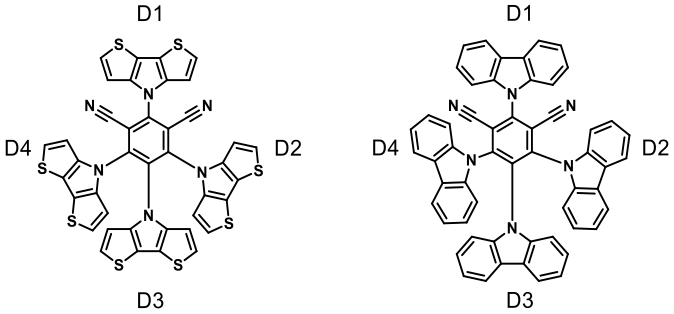

Figure S5.1: Chemical structures of **4DTP-IPN** and **4CzIPN** indicating the donor units D1-D4 for the determination of the dihedral angles in Table S5.1.

Table S5.1: Dihedral angles for the individual donor units of **4DTP-IPN** and **4CzIPN** as indicated in Figure S5.1.

	D1 (°)	**D2 (°)**	**D3 (°)**	**D4 (°)**
4DTP-IPN[a,b]	56.1	58.3	58.5	56.3
4CzIPN[a,b]	72.0	57.8	61.1	57.8

[a] Taken as the average of 2 possible torsion angles. [b] For 4DTP-IPN and 4CzIPN, D1 and D3 have 2 similar dihedral angles whereas D2 and D4 have two largely differing angles.

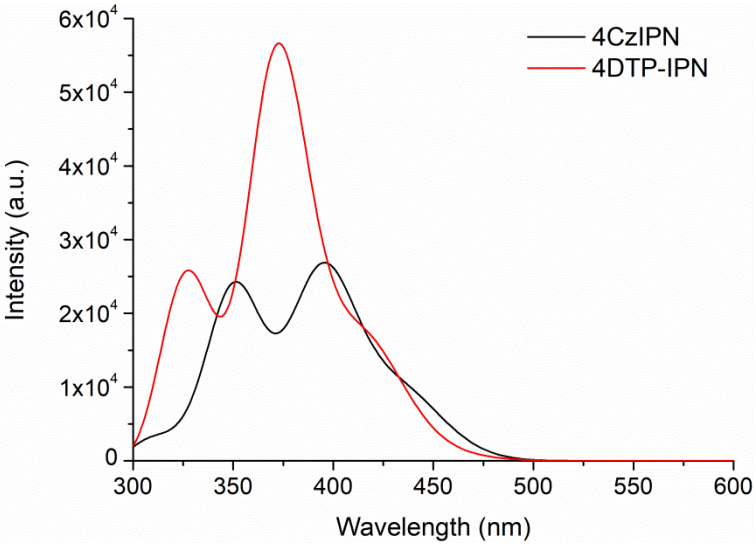

Figure S5.2: Simulated UV-VIS spectra from the TDDFT results for the optimized geometries of **4DTP-IPN** and **4CzIPN**.

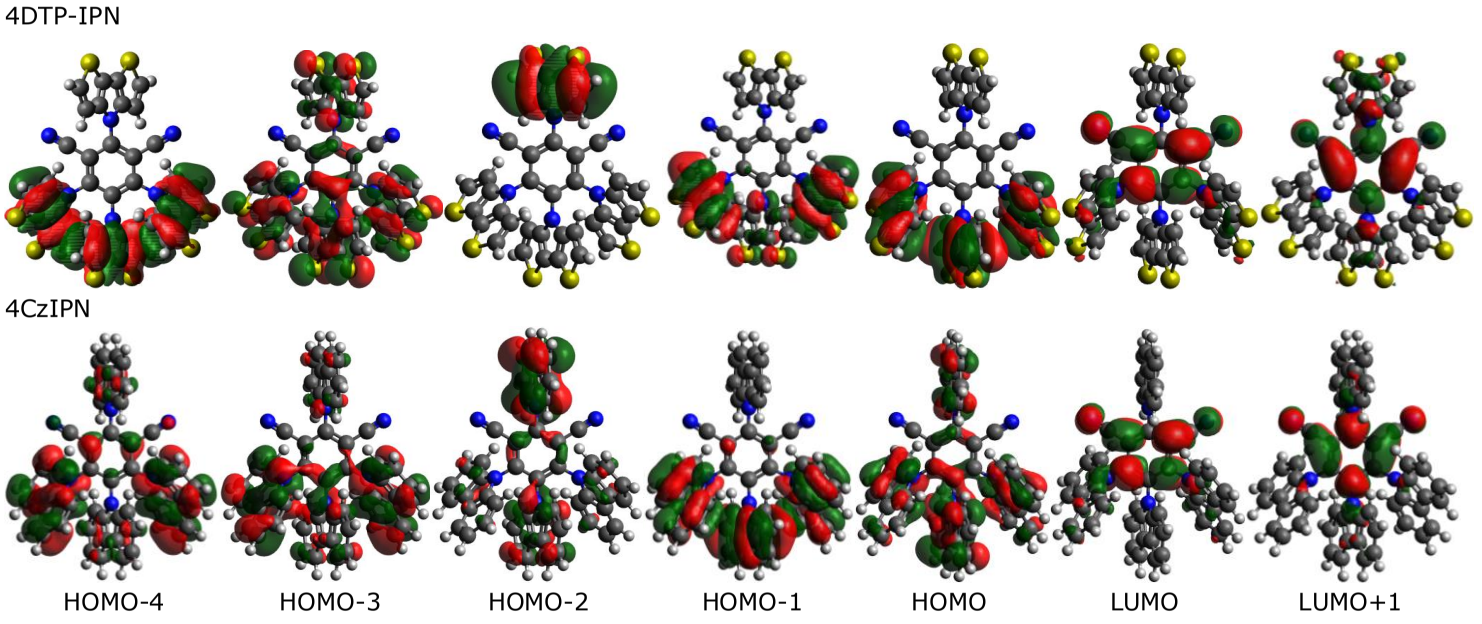

Figure S5.3: Orbital topologies for **4DTP-IPN** and **4CzIPN**. Orbitals obtained using LC-BLYP(ω=0.17 bohr 1)/6-311G(d) and the PCM (cyclohexane). Isosurface values of 0.02 a.u. were used for all orbitals.

Table S5.2: Orbital energies for the orbitals shown in Figure S3 for **4DTP-IPN** and **4CzIPN**. Orbitals obtained using LC-BLYP(ω=0.17 $bohr^{-1}$)/6-311G(d) and the PCM (cyclohexane).

	HOMO-4 (eV)	HOMO-3 (eV)	HOMO-2 (eV)	HOMO-1 (eV)	HOMO (eV)	LUMO (eV)	LUMO+1 (eV)
4DTP-IPN	-7.30	-7.27	-7.08	-7.06	-6.84	-1.45	-1.07
4CzIPN	-7.51	-7.45	-7.38	-7.34	-7.15	-1.36	-1.03

5.5.3 Time-resolved emission spectra

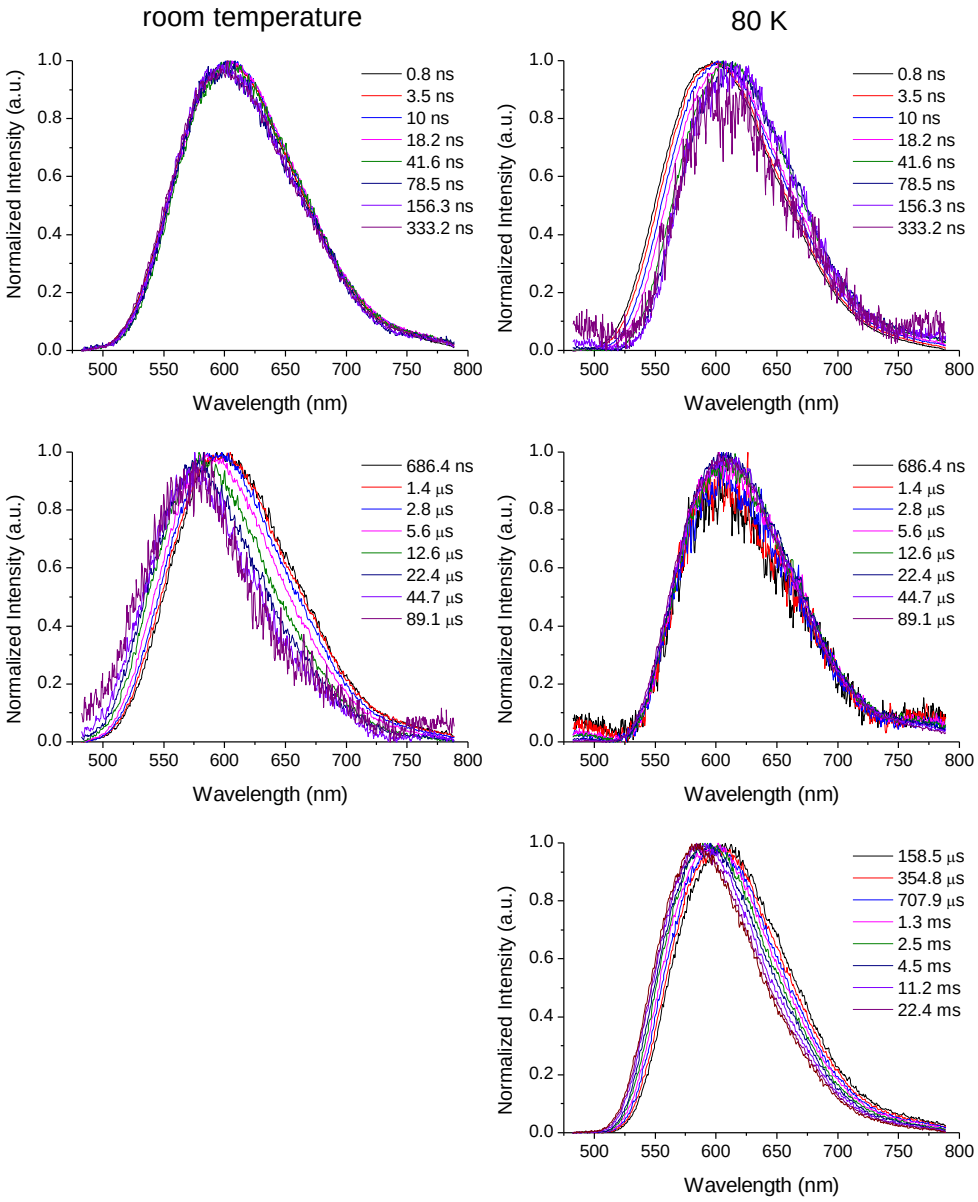

Figure S5.4: Emission spectra extracted from the time-resolved emission decay of **4DTP-IPN** in a 0.1 wt% doped zeonex film at room temperature (left) and 80 K (right).

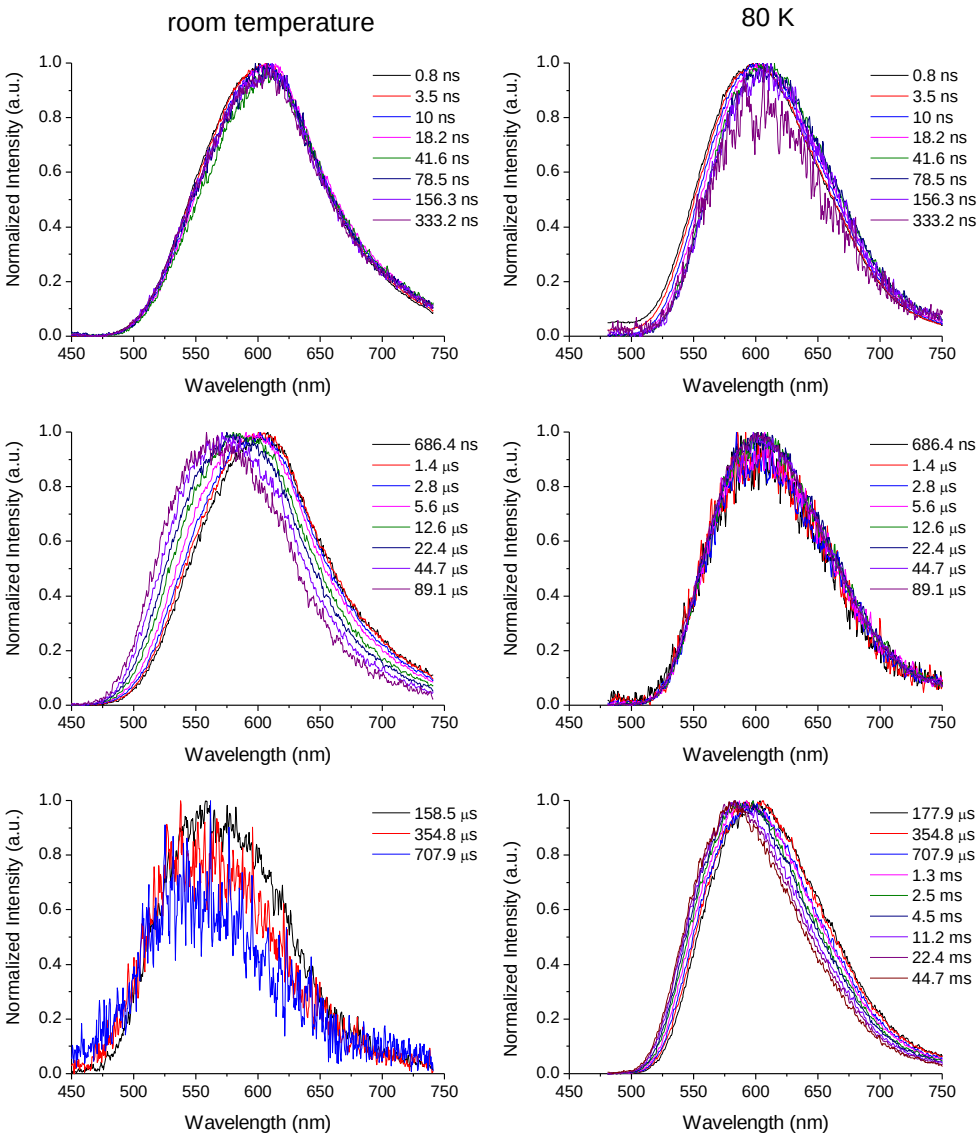

Figure S5.5: Emission spectra extracted from the time-resolved emission decay of **4DTP-IPN** in a 0.1 wt% doped polystyrene (PS) film at room temperature (left) and 80 K (right).

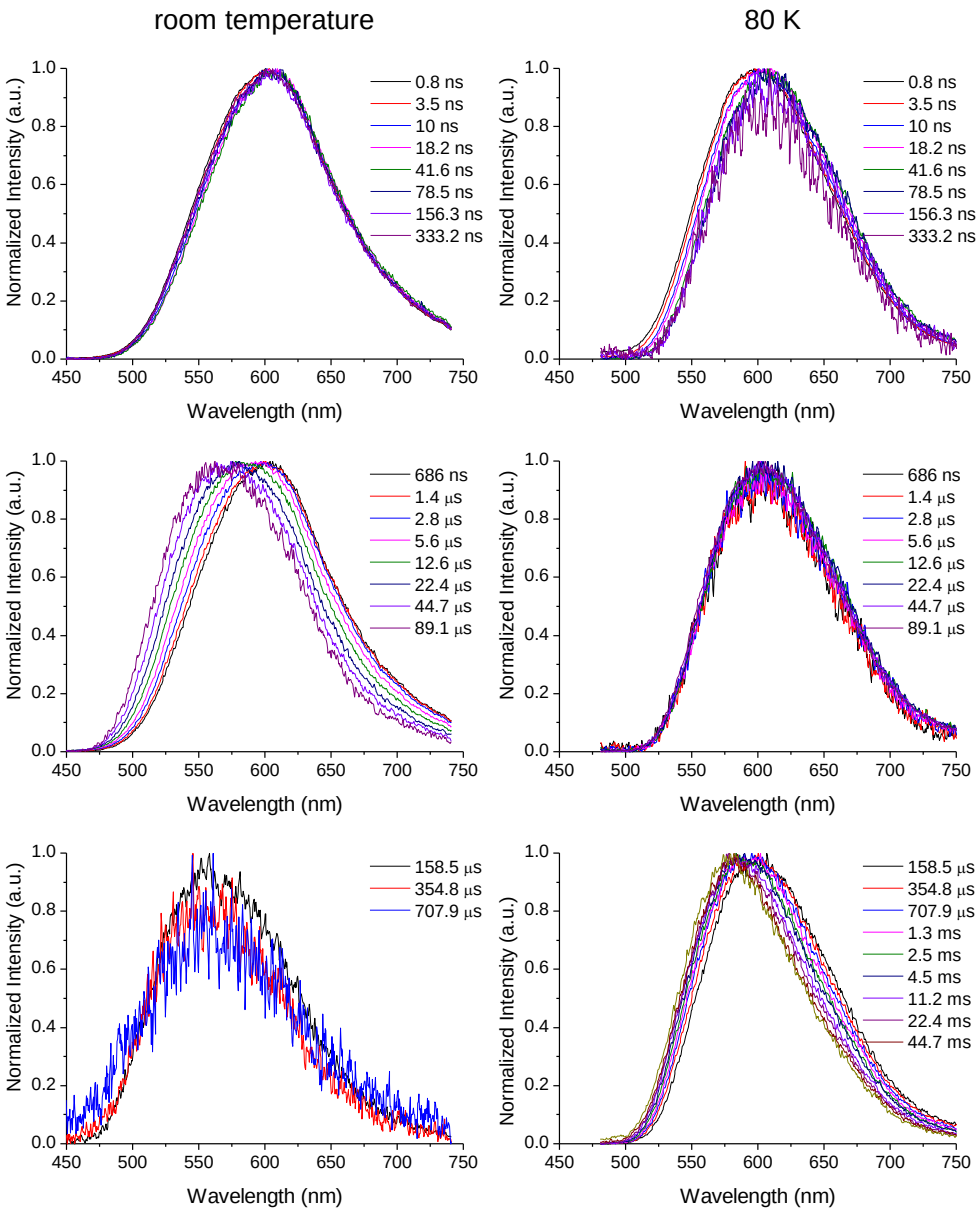

Figure S5.6: Emission spectra extracted from the time-resolved emission decay of **4DTP-IPN** in a 1 wt% doped polystyrene (PS) film at room temperature (left) and 80 K (right).

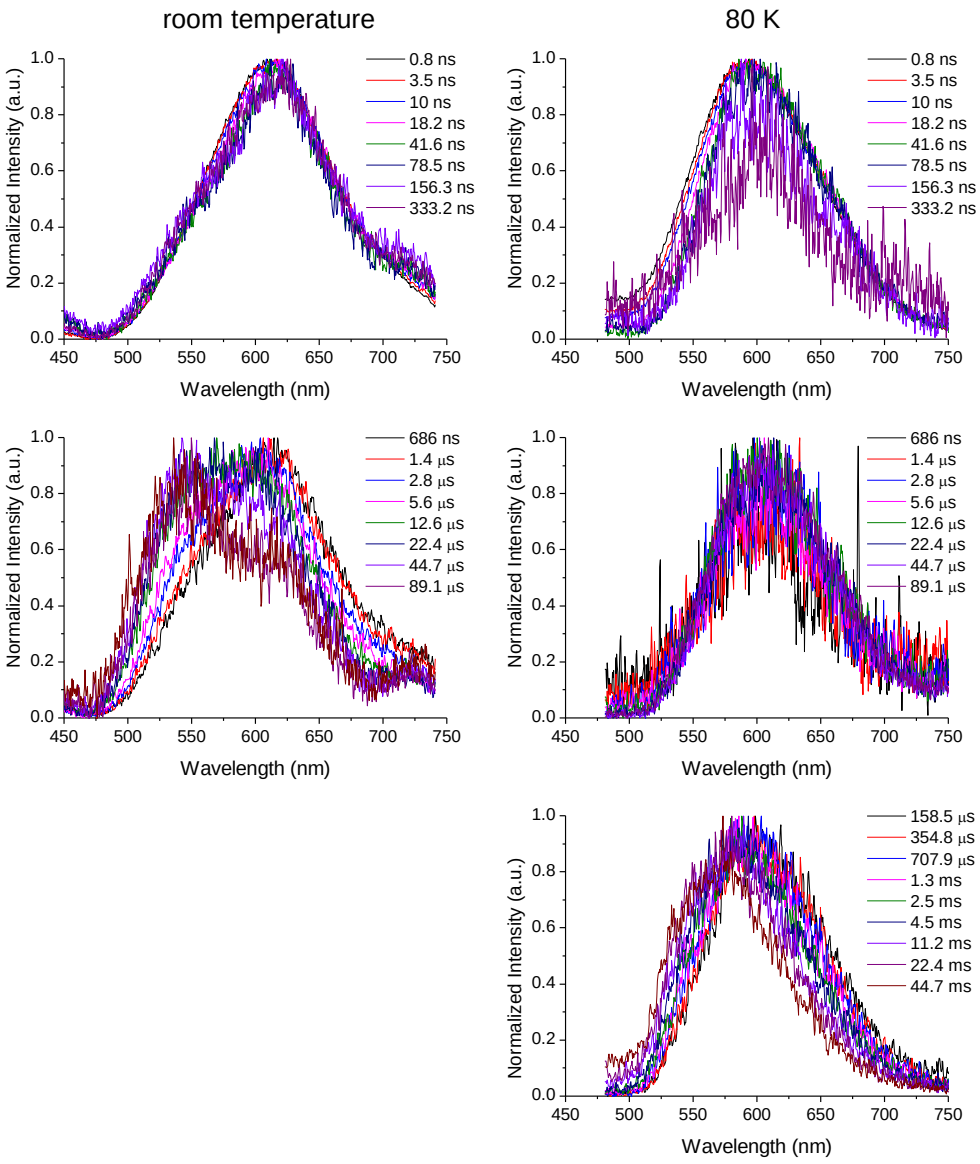

Figure S5.7: Emission spectra extracted from the time-resolved emission decay of **4DTP-IPN** in a 10 wt% doped DPEPO film at room temperature (left) and 80 K (right).

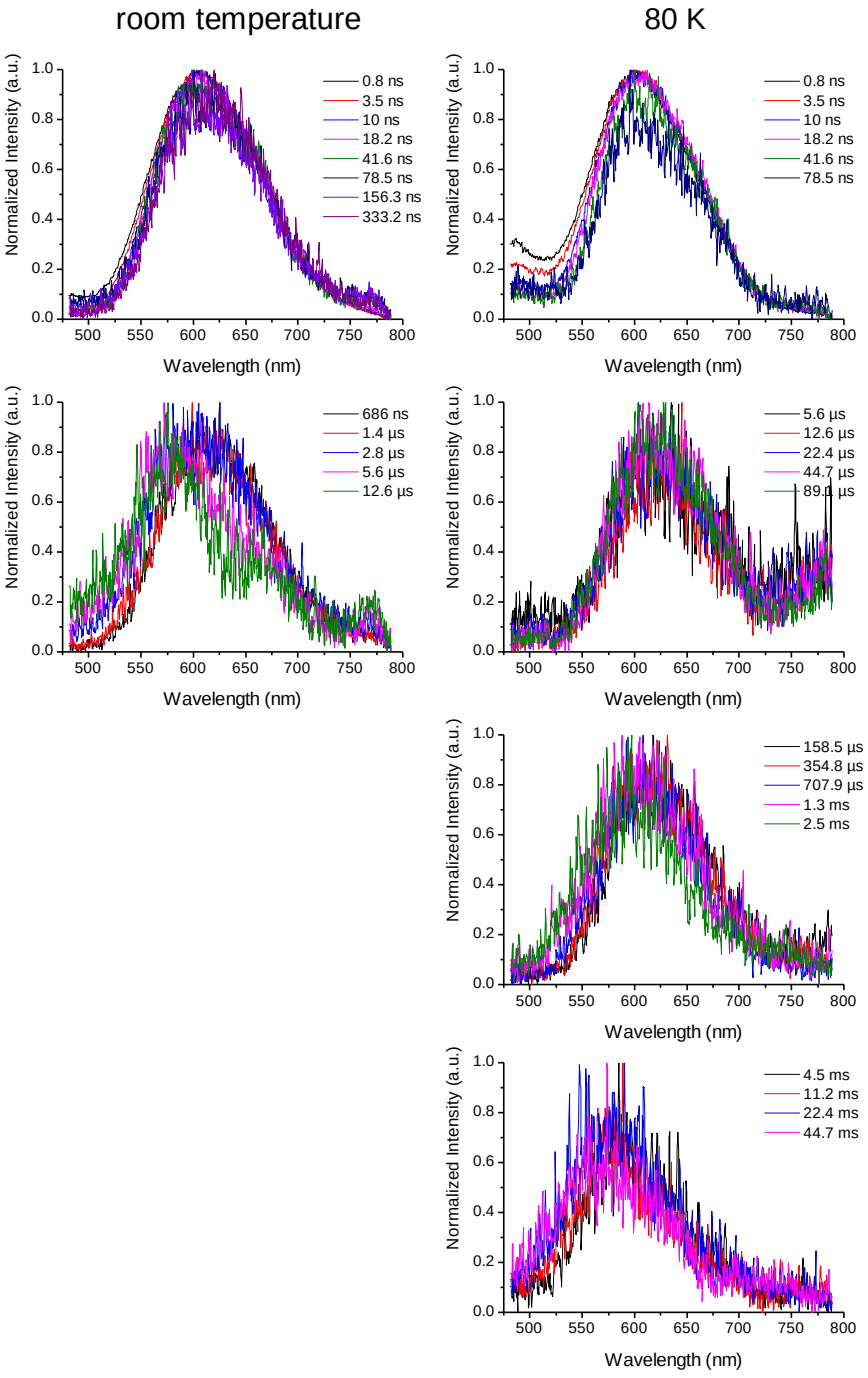

Figure S5.8: Emission spectra extracted from the time-resolved emission decay of **4DTP-IPN** in a 10 wt% doped UGH film at room temperature (left) and 80 K (right).

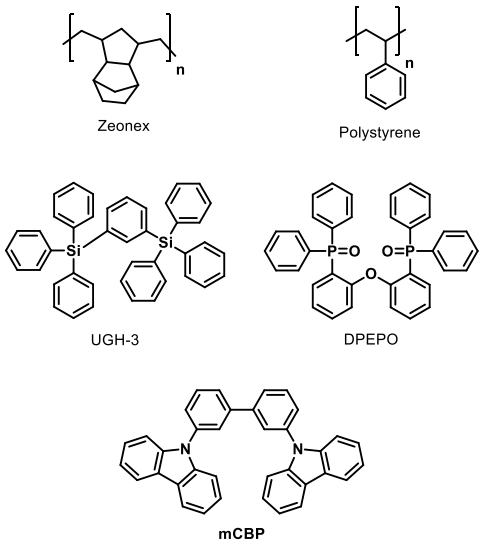

Figure S5.9: Molecular structures of zeonex, polystyrene, UGH-3, DPEPO and mCBP.

5.5.4 NMR spectra

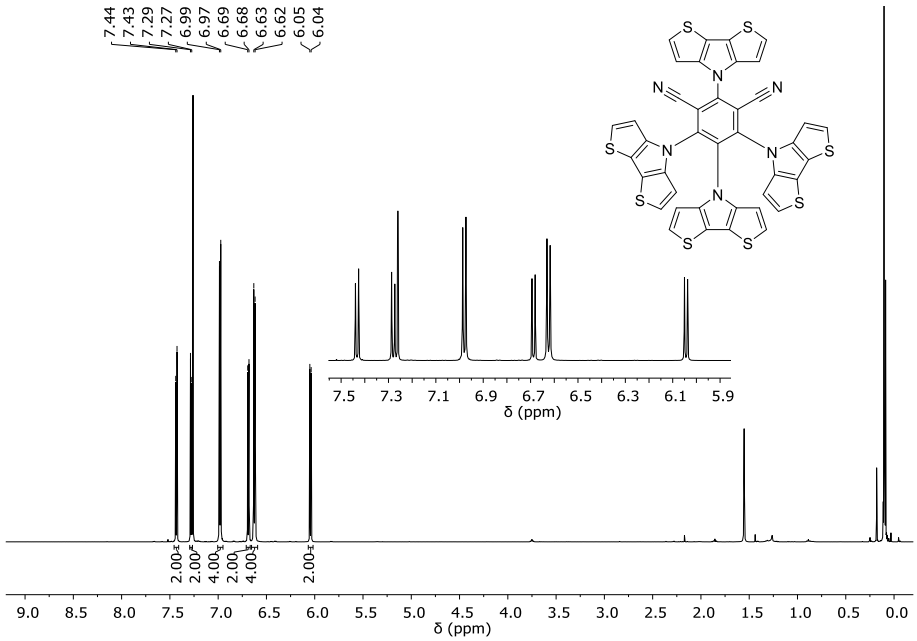

Figure S5.10: ^{1}H NMR spectrum of **4DTP-IPN** in $CDCl_3$.

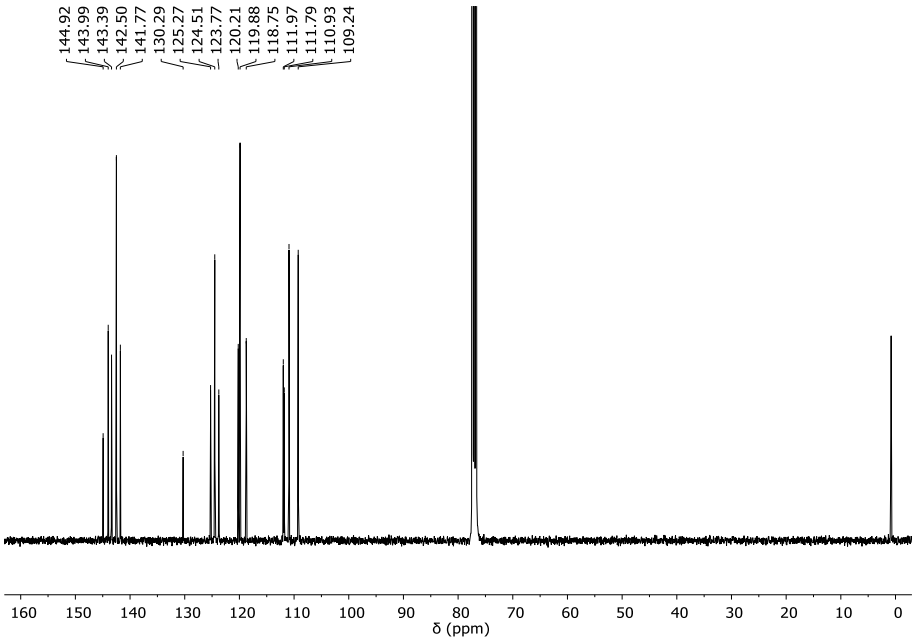

Figure S5.11: ^{13}C NMR spectrum of **4DTP-IPN** in $CDCl_3$.

5.5.5 Coordinates of optimized geometries

4DTP-IPN

C	0.31593	-1.16290	-0.34644
C	-0.39206	0.00001	0.00001
C	0.31587	1.16295	0.34647
C	1.72037	1.15729	0.35022
C	2.42811	0.00008	0.00005
C	1.72044	-1.15717	-0.35015
C	2.42087	-2.30016	-0.83224
N	2.98234	-3.22664	-1.22812
C	2.42074	2.30033	0.83231
N	2.98216	3.22683	1.22818
N	3.82283	0.00011	0.00007
C	4.65547	0.86799	-0.71020
C	5.97854	0.55013	-0.44710
C	5.97855	-0.55000	0.44708
C	4.65549	-0.86780	0.71028
S	7.04345	-1.55311	1.36308
C	5.68424	-2.36992	2.07876
C	4.47853	-1.90591	1.65198
C	4.47849	1.90611	-1.65188
C	5.68419	2.37008	-2.07874
S	7.04342	1.55321	-1.36317
N	-1.79101	-0.00003	0.00001
C	-2.62127	0.83282	-0.74735
C	-3.94559	0.53241	-0.46697
C	-3.94557	-0.53259	0.46695
C	-2.62123	-0.83293	0.74734
S	-5.00829	-1.47731	1.44674
C	-3.64602	-2.24790	2.21059
C	-2.44116	-1.80937	1.75390
C	-2.44124	1.80928	-1.75389
C	-3.64612	2.24774	-2.21061
S	-5.00836	1.47706	-1.44678
N	-0.36070	-2.32671	-0.72574
C	-1.44216	-2.40782	-1.60674
C	-2.10005	-3.61347	-1.42369
C	-1.40988	-4.31869	-0.40536
C	-0.35737	-3.51956	0.00918
S	-1.52697	-5.73358	0.57543
C	-0.15958	-5.21556	1.51816
C	0.36603	-4.02662	1.11148
C	-1.97227	-1.60176	-2.63872
C	-3.05235	-2.20495	-3.20428
S	-3.42306	-3.76338	-2.52088
N	-0.36084	2.32673	0.72575
C	-1.44231	2.40779	1.60674
C	-2.10025	3.61342	1.42367
C	-1.41010	4.31866	0.40535

C	-0.35755	3.51958	-0.00918
S	-1.52724	5.73354	-0.57545
C	-0.15982	5.21557	-1.51817
C	0.36584	4.02666	-1.11148
C	-1.97240	1.60172	2.63872
C	-3.05251	2.20485	3.20426
S	-3.42328	3.76327	2.52085
H	5.87149	-3.17585	2.77655
H	3.52806	-2.29856	1.99753
H	3.52801	2.29882	-1.99736
H	5.87143	3.17601	-2.77654
H	-3.82969	-3.01794	2.94912
H	-1.49112	-2.19239	2.11463
H	-1.49122	2.19236	-2.11461
H	-3.82982	3.01777	-2.94914
H	0.20694	-5.86465	2.30313
H	1.23521	-3.56828	1.57176
H	-1.59754	-0.63206	-2.94879
H	-3.67839	-1.82436	-4.00126
H	0.20667	5.86467	-2.30314
H	1.23504	3.56835	-1.57175
H	-1.59763	0.63203	2.94879
H	-3.67854	1.82425	4.00123

4CzIPN

C	-0.24202	1.13518	-0.44212
C	0.46683	-0.00024	0.00010
C	-0.23916	-1.13728	0.44270
C	-1.64361	-1.11836	0.46242
C	-2.34619	-0.00338	0.00118
C	-1.64641	1.11307	-0.46087
C	-2.37676	2.19184	-1.03961
N	-2.97965	3.05166	-1.51582
C	-5.90338	0.46485	0.54901
C	-5.90304	-0.47108	-0.54934
C	-4.55928	-0.74006	-0.86211
N	-3.74595	-0.00476	0.00190
C	-4.55981	0.73206	0.86409
C	-6.90768	-1.08485	-1.29043
C	-6.55670	-1.94222	-2.31880
C	-5.21480	-2.18641	-2.61909
C	-4.19509	-1.58728	-1.89712
C	4.02837	0.56248	0.45421
C	4.02932	-0.55493	-0.45633
C	2.68748	-0.86971	-0.72657
N	1.86641	0.00134	-0.00032
C	2.68600	0.87426	0.72534
C	2.33492	1.86190	1.63312
C	3.35734	2.58076	2.23103

C	4.69723	2.30730	1.94747
C	5.03914	1.29162	1.07122
C	5.04130	-1.28181	-1.07406
C	4.70106	-2.29821	-1.95012
C	3.36159	-2.57465	-2.23278
C	2.33798	-1.85810	-1.63414
C	2.15965	3.55166	-1.65821
C	1.45672	4.31266	-0.65463
C	0.39245	3.51853	-0.19845
N	0.42275	2.28632	-0.88024
C	1.49685	2.32114	-1.78377
C	1.88749	1.37096	-2.71276
C	3.01079	1.64230	-3.47678
C	3.70732	2.84437	-3.33738
C	3.27809	3.81031	-2.44323
C	1.67373	5.56266	-0.08621
C	0.83526	5.99631	0.92627
C	-0.21433	5.19147	1.37122
C	-0.45114	3.94291	0.81693
C	-2.37104	-2.19908	1.04119
N	-2.97142	-3.06074	1.51727
C	2.16849	-3.54809	1.65834
C	1.46702	-4.31088	0.65509
C	0.40085	-3.51923	0.19900
N	0.42858	-2.28682	0.88050
C	1.50295	-2.31903	1.78378
C	1.89167	-1.36775	2.71245
C	3.01574	-1.63640	3.47629
C	3.71493	-2.83693	3.33701
C	3.28769	-3.80403	2.44317
C	1.68660	-5.56055	0.08692
C	0.84878	-5.99631	-0.92517
C	-0.20270	-5.19390	-1.37005
C	-0.44208	-3.94572	-0.81603
C	-4.19630	1.57917	1.89945
C	-5.21646	2.17987	2.61947
C	-6.55817	1.93727	2.31698
C	-6.90849	1.08006	1.28827
H	-7.95446	-0.88930	-1.06581
H	-7.33213	-2.42928	-2.90455
H	-4.96343	-2.85788	-3.43656
H	-3.15026	-1.76576	-2.14494
H	1.29700	2.07755	1.87467
H	3.10486	3.37375	2.93137
H	5.47694	2.89133	2.43017
H	6.08363	1.06225	0.86859
H	6.08541	-1.05011	-0.87212
H	5.48174	-2.88048	-2.43336
H	3.11040	-3.36817	-2.93298
H	1.30038	-2.07603	-1.87498

H	1.34210	0.43979	-2.84123
H	3.35268	0.90014	-4.19479
H	4.58649	3.02732	-3.95013
H	3.80632	4.75755	-2.35336
H	2.49941	6.18398	-0.42782
H	0.99087	6.97259	1.37837
H	-0.86796	5.55099	2.16219
H	-1.27777	3.33261	1.17308
H	1.34422	-0.43779	2.84085
H	3.35611	-0.89331	4.19407
H	4.59465	-3.01777	3.94961
H	3.81804	-4.75010	2.35340
H	2.51374	-6.17997	0.42846
H	1.00640	-6.97238	-1.37706
H	-0.85576	-5.55507	-2.16074
H	-1.27012	-3.33729	-1.17210
H	-3.15165	1.75629	2.14905
H	-4.96562	2.85127	3.43716
H	-7.33396	2.42550	2.90128
H	-7.95514	0.88584	1.06188

5.5.6 Supporting information references

1. S. Förtsch and P. Bäuerle, *Polym. Chem.*, 2017, **8**, 3586-3595.

Chapter 6

Elucidation of the influence of structural and electronic parameters on the experimental properties of small molecule and polymer materials

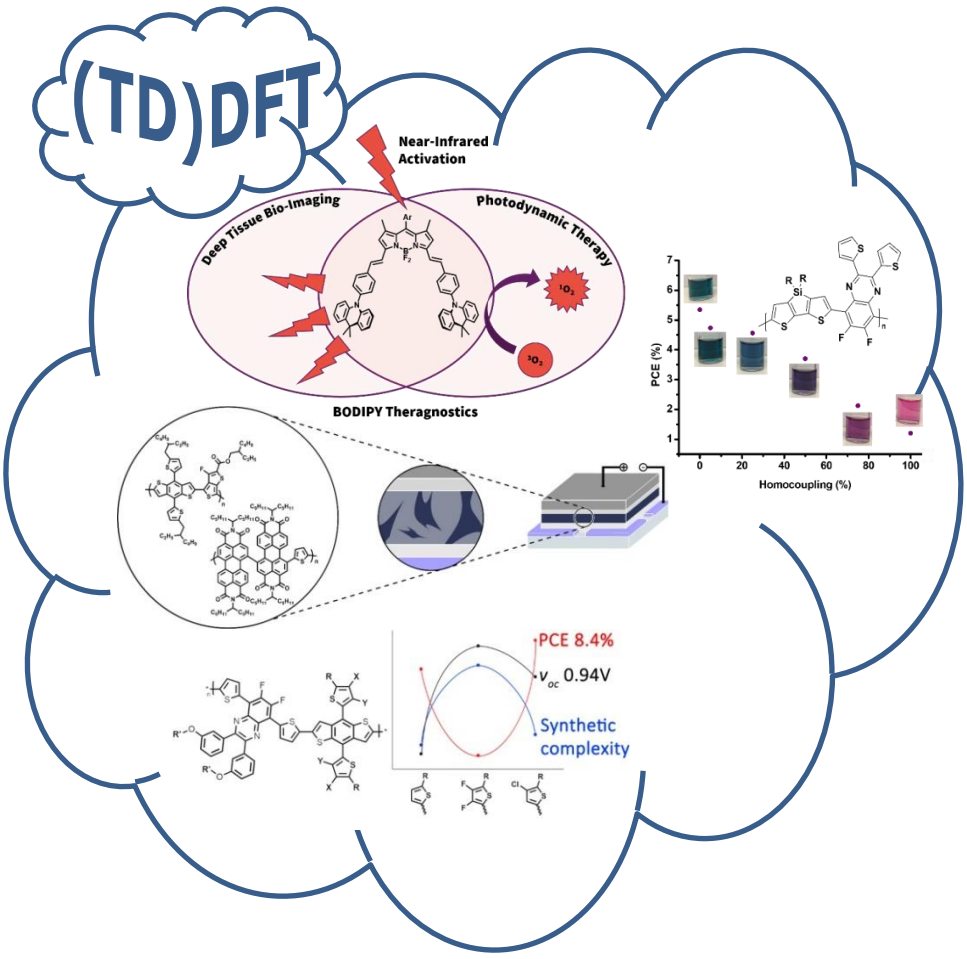

This chapter is based on the following publications:

J. Deckers, T. Cardeynaels, H. Penxten, A. Ethirajan, M. Ameloot, M. Kruk, B. Champagne and W. Maes, *Chem. Eur. J.*, 2020, DOI: 10.1002/chem.202002549.

Contribution:
Design of the novel BODIPY compounds, all quantum-chemical calculations, writing the discussion on the quantum-chemical calculations and revision of the manuscript.

G. Pirotte, J. Kesters, T. Cardeynaels, P. Verstappen, J. D'Haen, L. Lutsen, B. Champagne, D. Vanderzande and W. Maes, *Macromolecular Rapid Communications*, 2018, 39, 1800086.

R. Lenaerts, T. Cardeynaels, I. Sudakov, J. Kesters, P. Verstappen, J. Manca, B. Champagne, L. Lutsen, D. Vanderzande, K. Vandewal, E. Goovaerts and W. Maes, *Solar Energy Materials and Solar Cells*, 2019, 196, 178-184.

R. Lenaerts, D. Devisscher, G. Pirotte, S. Gielen, S. Mertens, T. Cardeynaels, B. Champagne, L. Lutsen, D. Vanderzande, P. Adriaensens, P. Verstappen, K. Vandewal and W. Maes, *Dyes and Pigments*, 2020, 181, 108577.

Contribution:
All quantum-chemical calculations, writing the discussion on the quantum-chemical calculations and revision of the manuscript.

6.1 General introduction

While in the previous chapters, the importance of density functional theory (DFT) and time-dependent DFT (TDDFT) for thermally activated delayed fluorescence (TADF) has been illustrated, its uses are much more widespread. In photodynamic therapy (PDT), a therapeutic agent (i.e. a photosensitizer) absorbs light to form an exciton and, via intersystem crossing (ISC), is able to convert this exciton to the triplet state, after which the energy is transferred to an oxygen molecule which is excited from its triplet ground state to the highly reactive singlet excited state.[1-3] Similar to TADF, the excited state properties (excitation energy, ISC, etc.) of the applied photosensitizer play a crucial role in the efficient application of the technology. In section 6.2, a report by Deckers *et al.*[4] on the design, experimental and quantum-chemical analysis of novel BODIPY-based photodynamic therapy agents is highlighted, in which the quantum-chemical calculations played a major role in resolving the underlying mechanism for efficient ISC in these materials.

Next to the excited-state properties, analysis of the geometrical parameters of conjugated polymer materials can help to explain experimental properties such as the HOMO and LUMO energies as obtained via cyclic voltammetry (CV). The first example deals with homocoupling, which occurs when two donor (D) or acceptor (A) units are coupled to each other (D-D or A-A) instead of forming D-A linkages during the polymerization reaction (section 6.3).[5] Homocoupling is often detrimental for the device performance as large structural changes occur in the polymer backbone, leading to changes in the mixing between the donor and acceptor materials in a bulk heterojunction (BHJ) blend, reduced charge transport along the polymer backbone, the formation of charge traps and the potential mismatching between the frontier orbital energy levels of the donor polymer and its surrounding layers.[6-9] Using quantum-chemical calculations, we were able to explain the increase in HOMO energy and the observed reduction in OPV device efficiency for a series of polymers with increasing homocoupling content. In a third study (section 6.4), the bis(perylene diimide) acceptor unit was polymerized with various thiophene-based donor units to construct electron donor polymers for organic solar cells.[10] To understand the experimental CV and UV-VIS absorption data, DFT calculations were performed on the optimized

geometries of the resulting polymers and their implications on the experimental data. Finally, halogenation of the donor or acceptor polymers applied in BHJ organic solar cells is used to fine-tune various properties, such as the UV-VIS absorption profile, the frontier orbital energy levels, mixing enthalpy and charge carrier mobility. Investigation of the effects of halogenation on a series of donor and acceptor polymers for BHJ solar cells via DFT and TDDFT calculations helped to solidify the experimental findings (section 6.4).[11]

In the following sections, the quantum-chemical calculations performed in the aforementioned examples will be discussed in more detail. A complete overview of the work performed can be found in the respective publications.[4, 5, 10, 11]

6.2 Functionalized BODIPYs for photodynamic therapy

Boron dipyrromethene (BODIPY) dyes represent a particular class within the broad array of potential photosensitizers. Their highly fluorescent nature opens the door for theragnostic applications, combining imaging and therapy using a single, easily synthesized chromophore.[12-15] However, near-infrared (NIR) absorption is strongly desired for photodynamic therapy to enhance tissue penetration.[16] Furthermore, singlet oxygen should preferentially be generated without the incorporation of heavy atoms, as these often require additional synthetic efforts and/or afford dark cytotoxicity.[14, 15, 17, 18] Solutions for both problems are known, but have never been successfully combined in one simple BODIPY material. Here, we present a series of compact BODIPY-acridine dyads, active in the phototherapeutic window and showing balanced brightness and phototoxic power. Although the donor-acceptor design was envisioned to introduce a charge transfer state to assist in intersystem crossing, quantum-chemical calculations refute this. Further photophysical investigations suggest the presence of exciplex states and their involvement in singlet oxygen formation.

6.2.1 Design of BODIPY dyes

The design of the photosensitizers (PSs) started from the highly fluorescent 1,3,5,7-tetramethyl-BODIPYs, with varying *meso*-functionalities such as a hydrogen atom (**7a**), mesityl (**7b**) or 1,5-dichlorophenyl (**7c**) group (Scheme 6.1). The *meso*-positions are easily modifiable during the BODIPY synthesis and typically do not influence the photophysical properties of the resulting compounds to a large extent. Groups with a large steric hindrance such as mesityl or 1,5-dichlorophenyl can reduce non-radiative losses, leading to an improvement in the photoluminescence quantum yield (PLQY). The methyl groups on the BODIPY core are acidic enough to enable Knoevenagel-type condensations to extend the *π*-conjugated system and shift the absorption and emission toward the red end of the spectrum.[19, 20] We chose a strongly electron donating acridine group, generating a push-pull type structure (Scheme 6.1) to further increase the bathochromic shift. The idea behind the donor-acceptor dyad design was, similar to the spin-vibronic mechanism for TADF,[21-23] to

increase the mixing between triplet states in order to improve ISC between the first singlet excited and an upper triplet excited state.[24] The first triplet excited state for BODIPY dyes is typically very low in energy with respect to the first singlet excited state (see below, Table 6.2). Two different spacer units (phenyl and thienyl) were chosen to functionalize the acridine group with and to enable the Knoevenagel-type condensation with the BODIPY core.

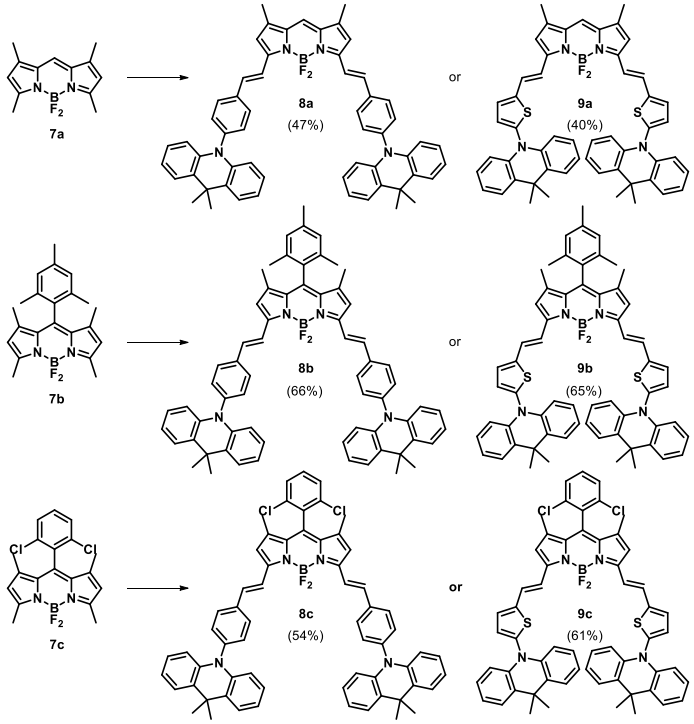

Scheme 6.1: Molecular structures of the various BODIPY compounds used in this work.

Density functional theory (DFT) calculations were then performed to optimize the geometries of all 6 BODIPY compounds. For this purpose, the M06

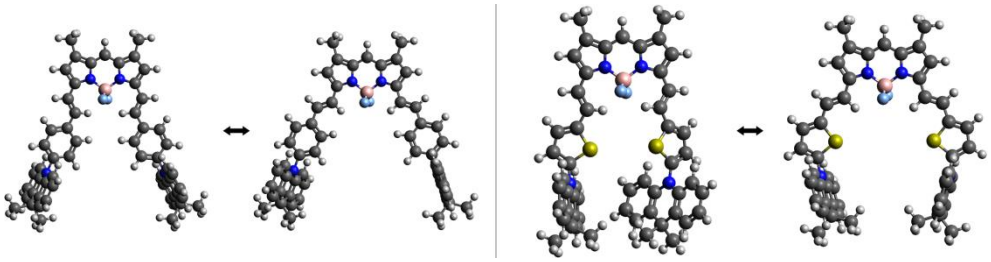

Figure 6.1: Different possible conformers for **8a** and **9a**. Geometries were optimized using M06/6-311G(d).

exchange-correlation functional was used in combination with the 6-311G(d) basis set. Two types of conformers were thought to be possible for both the phenyl (**8a-c**) and thienyl-spaced (**9a-c**) BODIPYs (Figure 6.1). They differ in the orientation of the double bond with respect to the BODIPY core and result in a larger or smaller distance between the acridines, which is especially visible for **9a**. In Figure 6.1, the right hand side conformer for both **8a** and **9a** has the lowest energy and was hence chosen for all the calculations in this work. The optimized geometries show a large dihedral angle (> 80°) between the acridine donor and the phenyl or thienyl spacer for BODIPYs **8b,c** and **9b,c**. The *meso*-groups are nearly perpendicular to the BODIPY core and are therefore not expected to influence the BODIPY properties to a large extent. The BODIPY core and styryl/thienylvinyl spacer are coplanar, extending the conjugation and

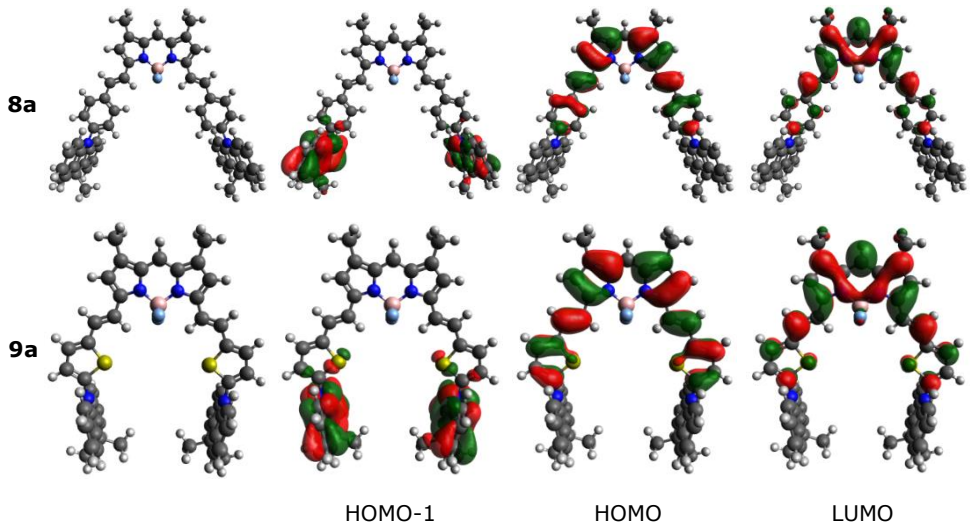

Figure 6.2: Optimized geometries and frontier orbitals for BODIPYs **8a** and **9a** in chloroform as obtained using DFT calculations with M06-2X/6-311G(d) and the PCM. Isosurface values of 0.02 a.u. were used for all orbitals.

leading to the desired red-shifted absorption and emission. From the geometry optimization, the frontier orbital topologies are obtained, showing localization of the HOMO and LUMO on the styryl/thienylvinyl-BODIPY, whereas the HOMO-1 is localized on the acridines for all BODIPYs (Figure 6.2). The orbitals shown in Figure 6.2 were obtained using M06-2X to have a more consistent picture with the time-dependent DFT (TDDFT) calculations. This is because the HOMO and

HOMO-1/HOMO-2 being close in energy and a reversal occurs when calculating the orbital energies with M06 instead of M06-2X.

6.2.2 Photophysics

BODIPYs **8a-c** and **9a-c** were subjected to a detailed photophysical characterization (performed by J. Deckers) to examine their intended use as theragnostic agents. Initial characterization was performed in chloroform, but was later extended to toluene and dimethyl sulfoxide (DMSO). UV-VIS absorption and fluorescence measurements (Figure 6.3) were performed to estimate whether the photosensitizers could act in the phototherapeutic window (i.e. the wavelengths where scattering is small, the absorption in human tissue

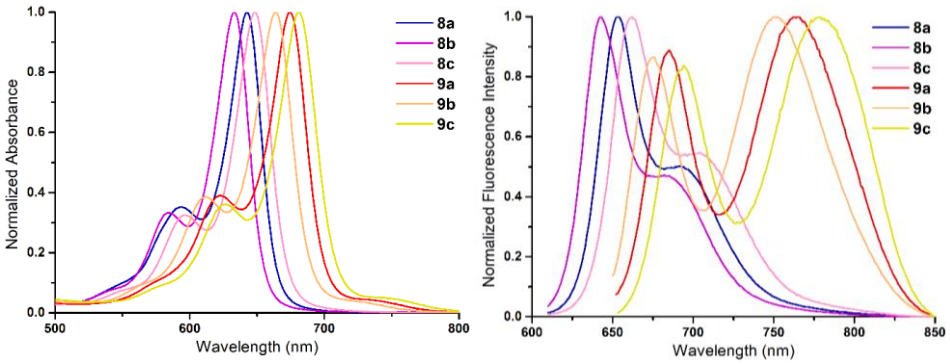

Figure 6.3: Normalized absorption spectra for BODIPYs **8a-c** and **9a-c** (left) and their corresponding normalized fluorescence emission spectra (right) in chloroform solution.

Table 6.1: Spectroscopic data for BODIPY dyads **8a-c** and **9a-c** as obtained in chloroform solution.[a]

BODIPY	λ_{abs} (nm)[b]	λ_{em} (nm)[c]	ε ($M^{-1}cm^{-1}$)[d]	Φ_f[e]	Φ_Δ[f]
8a	643	654	122,300	0.47 ±0.02	0.29 ±0.04
8b	633	645	119,900	0.63 ±0.03	0.23 ±0.02
8c	648	664	100,100	0.38 ±0.02	0.31 ±0.07
9a	674	689, 764	107,300	0.069 ±0.002	0.03 ±0.01
9b	664	678, 751	98,200	0.091 ±0.002	0.05 ±0.03
9c	681	697, 782	98,400	0.052 ±0.002	0.06 ±0.04

[a] All values are averages from three independent measurements. [b] Absorption maximum. [c] Fluorescence emission maximum/maxima. [d] Molar attenuation coefficient. [e] Fluorescence quantum yield determined *vs* nile blue (Φ_f = 0.27, λ_{exc} = 605 nm) (for **8a-c**) or *vs* aluminum phthalocyanine chloride (Φ_f = 0.41, λ_{exc} = 645 nm) (for **9a-c**) in spectrograde ethanol as a reference. Standard deviations are reported. [f] Singlet oxygen quantum yield determined *vs* methylene blue (Φ_Δ = 0.52, λ_{exc} = 639 nm) in spectroscopic grade ethanol as a reference by monitoring the absorbance of 1,3-DPBF at 414 nm. Standard deviations are reported.

is minimized and the irradiation has the largest penetration depth; 600 – 800 nm). Furthermore, the singlet oxygen quantum yields (Φ_Δ) were collected by monitoring the absorbance of 1,3-diphenylisobenzofuran (1,3-DPBF) as singlet oxygen scavenger during excitation at 639 nm (Table 6.1).[25, 26] Additionally, all systems were found to be photostable for more than three hours under 639 nm illumination. The fluorescence quantum yields (Φ_f) are moderate, but still significant (47, 63, and 38% for **8a**, **8b**, and **8c**, respectively). Both the absorption and emission profiles resemble the typical narrow BODIPY shape with a smaller shoulder. Furthermore, the BODIPY dyads with a phenyl spacer between the BODIPY and acridine subunits were able to generate $^1O_2$. Relative Φ_Δ measurements resulted in good values ranging from 23% for the *meso*-mesityl variant **8b** to 31% for the *meso*-2,6-dichlorophenyl variant **8c**. We can exclude that the $^1O_2$ generation capability originates from the orthogonality between the *meso*-group and the BODIPY core, since *meso*-unsubstituted BODIPY **8a** also affords a significant Φ_Δ value of 29%. Moreover, the high molar attenuation coefficients (above 100,000) indicate their excellent light harvesting abilities. The absorption profiles of BODIPYs **9a-c** resemble these of their styryl counterparts, but are red-shifted to a greater extent, as expected due to the more electron donating character of the thienyl linkers. Remarkably, the thienyl spacer results in a very different fluorescence emission profile. The first emission maxima are found between 680 and 700 nm, while a second, more intense and broad emission band with maxima ranging from 750 up to 780 nm appears. Although high molar attenuation coefficients are obtained for these systems, Φ_f and Φ_Δ values are very low.

To understand where these absorption and emission peaks are coming from, and to verify whether we are dealing with charge-transfer (CT) emission or not, TDDFT calculations using M06-2X as the exchange-correlation functional and 6-311G(d) as the basis set were performed. The vertical excitation energies were calculated in various environments (toluene, chloroform and DMSO) using the polarizable continuum model (Table 6.2). The singlet excitation energies for BODIPYs **8a-c** show that **8b** has the highest first excitation energy, followed by **8a** and **8c**. This is expected given the electron donating nature of the mesityl group, whereas the 2,6-dichlorophenyl group is slightly electron withdrawing. BODIPYs **9a-c** have lower excitation energies, in correspondence to the

bathochromically shifted absorption and emission spectra. Furthermore, these compounds follow the same trend concerning variations of the *meso*-groups. In all cases, the energy differences between the different solvents are minimal. These observations correspond nicely to the trends that were also found experimentally (Figure 6.3). The oscillator strength of the $S_0 \rightarrow S_1$ transition is large (> 0.9) for all compounds, hinting to a large extinction coefficient for this transition. The second singlet energy level is much higher in energy (> 0.7 eV) in all cases, with the corresponding oscillator strength being negligible, except for dyad **9a** in DMSO and **9c** in all three solvents, where it is still very small. There are two triplet states of interest in these BODIPY compounds. The lowest triplet state has an excitation energy of around 1.00 eV for all molecules. This means there is still enough energy to overcome the excitation barrier for $^3O_2$, which is around 0.98 eV (1270 nm). The second triplet state is around 2.49 eV for BODIPYs **8a-c** and around 2.24 eV for BODIPYs **9a-c**. Based on the calculations, and keeping the possible error on the obtained triplet excitation energies in mind, the lowest triplet state in **9a** and **9c** might be too low in energy for efficient $^1O_2$ formation, as observed experimentally. The dominant nature of the one-particle transitions for the first singlet states is of HOMO→LUMO (localized) character. For the second singlet excited state, the character varies between HOMO-1→LUMO (**8a**, **8b** in chloroform, **9a**, **9b**, and **9c** in DMSO) and HOMO-2→LUMO (**8b** in toluene and DMSO, **8c** and **9c** toluene and chloroform), depending on the compound and the solvent in which it was calculated. However, the nature remains the same, since both HOMO-1 and HOMO-2 are localized on the acridine moiety, leading to a CT-type excitation. For the first and second triplet excited states, the dominant nature is of HOMO→LUMO and HOMO-3→LUMO character, respectively.

The CT character of the various transitions was investigated and the distance over which charge is transferred (denoted as d_{CT}) and the change in dipole moment upon excitation ($\Delta\mu$) were calculated (Table 6.3). The CT distance was calculated according to the work by Le Bahers *et al.*[27] From the d_{CT} values (< 1.0 Å), it is clear that the $S_0 \rightarrow S_1$, $S_0 \rightarrow T_1$, and $S_0 \rightarrow T_2$ transitions are of local character. On the other hand, the $S_0 \rightarrow S_2$ transition is of CT character (d_{CT} >> 1.0 Å). The change in dipole moment ($\Delta\mu$) follows the same trend: a large increase in dipole moment is observed for $S_0 \rightarrow S_2$, whereas the other transitions

Table 6.2: Calculated vertical singlet (S_1 and S_2) and triplet (T_1 and T_2) excitation energies and their corresponding oscillator strengths for BODIPYs **8a-c** and **9a-c**.

BODIPY	Solvent[a]	S_1				S_2			T_1		T_2	
		ΔE (eV)[b]	λ (nm)[b]	Osc. Str.[c]	Nature[d,e]	ΔE (eV)[b]	Osc. Str.[c]	Nature[d,f]	ΔE (eV)[b]	Nature[d,g]	ΔE (eV)[b]	Nature[d,h]
8a	Toluene	2.17	572	1.25	H→L	2.96	0.00	H-1→L	1.05	H→L	2.51	H-3→L
	Chloroform	2.18	569	1.24	H→L	3.00	0.00	H-1→L	1.06	H→L	2.51	H-3→L
	DMSO	2.19	567	1.23	H→L	3.04	0.00	H-1→L	1.07	H→L	2.51	H-3→L
8b	Toluene	2.21	560	1.16	H→L	3.03	0.00	H-2→L	1.16	H→L	2.50	H-3→L
	Chloroform	2.22	558	1.15	H→L	3.05	0.00	H-1→L	1.16	H→L	2.49	H-3→L
	DMSO	2.23	557	1.14	H→L	3.08	0.00	H-2→L	1.17	H→L	2.50	H-3→L
8c	Toluene	2.16	573	1.19	H→L	2.93	0.00	H-2→L	1.06	H→L	2.49	H-3→L
	Chloroform	2.17	571	1.18	H→L	2.95	0.00	H-2→L	1.06	H→L	2.49	H-3→L
	DMSO	2.18	569	1.17	H→L	2.96	0.00	H-2→L	1.07	H→L	2.489	H-3→L
9a	Toluene	2.07	598	1.08	H→L	3.02	0.00	H-1→L	0.99	H→L	2.26	H-3→L
	Chloroform	2.08	596	1.06	H→L	3.05	0.00	H-1→L	1.00	H→L	2.25	H-3→L
	DMSO	2.10	591	0.90	H→L	3.06	0.01	H-1→L	1.03	H→L	2.27	H-3→L
9b	Toluene	2.12	585	1.00	H→L	3.08	0.00	H-1→L	1.10	H→L	2.25	H-3→L
	Chloroform	2.13	583	0.99	H→L	3.09	0.00	H-1→L	1.10	H→L	2.25	H-3→L
	DMSO	2.13	583	0.94	H→L	3.10	0.00	H-1→L	1.10	H→L	2.24	H-3→L
9c	Toluene	2.07	599	1.06	H→L	3.11	0.01	H-2→L	1.00	H→L	2.24	H-3→L
	Chloroform	2.08	597	1.05	H→L	3.12	0.01	H-2→L	1.00	H→L	2.24	H-3→L
	DMSO	2.08	596	1.03	H→L	3.13	0.01	H-1→L	1.00	H→L	2.23	H-3→L

[a] Solvents are listed from top to bottom according to increasing polarity *$E_T(30)$*. [b] Vertical excitation energy. [c] Oscillator strength. [d] H = HOMO, L = LUMO. [e] All transitions consist of more than 95% H→L character. [f] All transitions consist of more than 70% H-1→L or H-2→L character. [g] All transitions consist of more than 90% H→L character. [h] All transitions consist of around 50% H-3→L character.

show a slight decrease in dipole moment upon excitation. The TDDFT calculations correspond well with the observed localized absorption and emission spectra, in which very little solvatochromism is observed (Figure 6.4). However, from Table 6.2, the CT emission attributed to the high-wavelength emission band in dyads **9a-c** in all solvents could not be confirmed at the theoretical level. There is indeed an energy level with CT character, but it is much higher in energy than the first singlet excited state, and not slightly lower as would be expected from the photophysical data. Furthermore, the oscillator strengths are negligible for this transition in all cases. Therefore, another process is expected to be involved in these BODIPY systems.

Table 6.3: Charge-transfer distance (d_{CT}) and change in dipole moment ($\Delta\mu$, excited state dipole - ground state dipole) accompanying the S_0->S_n and S_0->T_n transitions in chloroform.

BODIPY	$S_0 \rightarrow S_1$		$S_0 \rightarrow S_2$		$S_0 \rightarrow T_1$		$S_0 \rightarrow T_2$	
	d_{CT} (Å)	$\Delta\mu$ (D)	d_{CT} (Å)	$\Delta\mu$ (D)	d_{CT} (Å)	$\Delta\mu$ (D)	d_{CT} (Å)	$\Delta\mu$ (D)
8a	0.57	-1.1	4.86	17.8	0.48	-1.2	0.47	-0.7
8b	0.67	-1.4	5.00	18.1	0.65	-1.8	0.38	-0.6
8c	0.79	-1.6	5.13	17.8	0.71	-2.0	0.62	-1.0
9a	0.82	-1.7	4.53	18.1	0.52	-1.5	0.64	-1.2
9b	0.94	-2.0	4.79	19.3	0.71	-2.1	0.62	-1.1
9c	0.99	-2.1	4.93	20.8	0.71	-2.2	0.74	-1.4

Solvatochromic experiments were conducted in toluene and DMSO in addition to chloroform to distinguish the localized and CT emission bands. The absorption bands remained similar in all solvents for all BODIPYs. While the low-wavelength emission remains unaltered in the various solvents, the observed high-

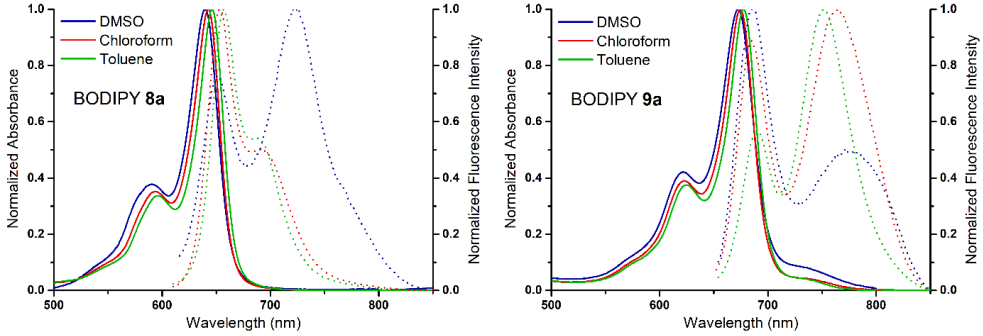

Figure 6.4: Normalized absorption spectra (solid lines) for BODIPYs **8a** and **9a** and their corresponding normalized fluorescence emission spectra (dashed lines) in toluene, chloroform, and DMSO. The same trends were generally observed for the other BODIPY dyads.

wavelength emission for BODIPYs **9a-c** (Figure 6.4) red-shifts with solvent polarity from toluene to DMSO, suggesting CT character for this emission. In addition, this high-wavelength emission band also appears for BODIPYs **8a-c** in DMSO. This solvent-dependent behavior seems indicative of CT emission and the proximity of the CT and LE bands for BODIPYs **8a-c** points toward a narrow energetic spacing between these states. These findings are in contrast with the aforementioned TDDFT calculations for the singlet excitation energies. As the mutual ratio between the intensities of the LE and CT emission bands seemed to change between measurements and solvents, exciplex formation was coined as a possible explanation for the observed photophysics. BODIPYs **8a** and **9a** were investigated in chloroform (Figure 6.5) and DMSO at various concentrations to verify whether the emission bands were indeed concentration dependent.

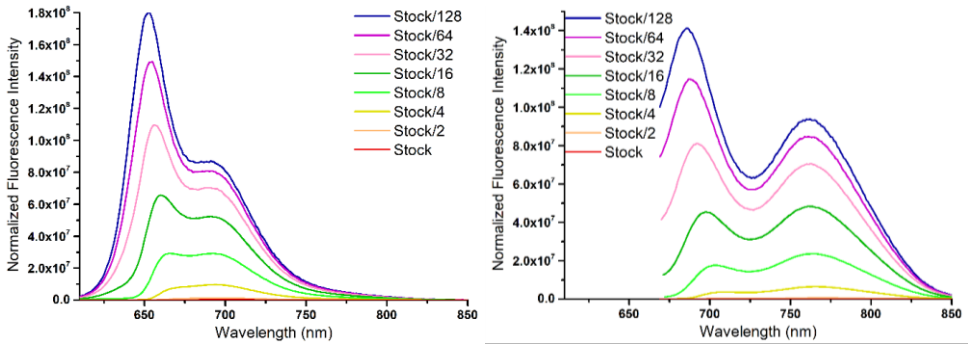

Figure 6.5: Fluorescence emission spectra, normalized to concentration, for a dilution series of **8a** (left) and **9a** (right) in chloroform (λ_{exc} = 605 nm, slit width = 2 nm for **8a**; λ_{exc} = 645 nm, slit width = 5 nm for **9a**). The stock solution contained ca. 1 mg BODIPY dissolved in 5 mL chloroform.

As shown in Figure 6.5, the emission intensity decreases with concentration, as expected, but more importantly, a clear shift between the relative intensities of the LE and CT bands occurs for **8a** (±650 and ±700 nm, respectively) and **9a** (±680 and ±755 nm, respectively), which is indicative for exciplex formation. The **9a-c** series seems more affected by the concentration as the exciplex or CT emission band is seen in all solvents. Similar results were found for both compounds in DMSO and can be found in the original work.[4]

As direct ISC from singlet to triplet is unlikely, exciplex formation could be a key element in the ISC abilities. Exciplex states can live relatively long as there is no

ground state counterpart, and they have a strong polar nature, as seen for CT states.[28] Hence, exciplexes can serve the same purpose as CT states, assisting in triplet formation. In the BODIPY-acridine dyads described in this work, ISC from a ^{1}Exciplex state to a ^{3}Exciplex state is expected to provide ISC, immediately followed by a fast internal conversion to the lowest ^{3}LE state. Exciplexes have also been used in OLED devices, where the spatial separation between the donor and acceptor molecules of the exciplex (i.e. one molecule transfers an exciton to the second molecule) provides a small energy splitting between the ^{1}Exciplex and ^{3}Exciplex states, respectively.[29, 30] Additionally, similar ISC to an exciplex triplet state from an excited state complex has already been observed for some BODIPY dyes, although the examples are scarce.[28, 31, 32] Finally, the crucial influence of the acridine moiety was proven by synthesizing BODIPY dyes that lack this functionality. For this purpose, the BODIPY dyads

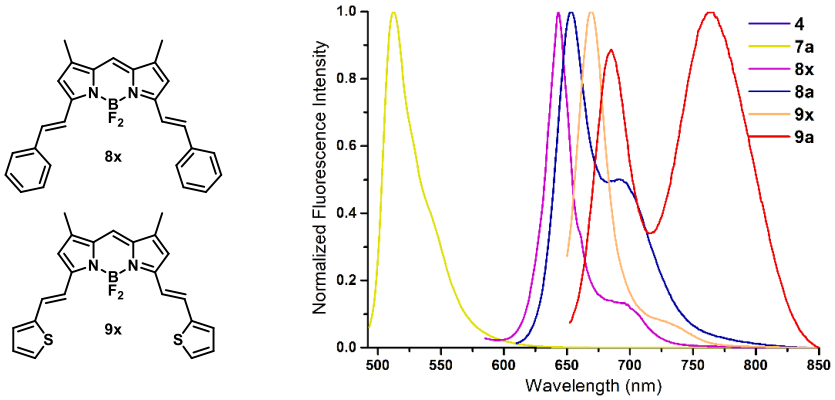

Figure 6.6: Chemical structures of BODIPYs **8x** and **9x** (left) and normalized fluorescence emission spectra (right) of **4**, **7a**, **8x**, **9x**, **8a**, and **9a** in chloroform solution.

without *meso*-group were chosen and the new acridine-free BODIPYs are dubbed **8x** and **9x** (Figure 6.6). The acridine unit by itself (**4**) was also measured. The emission spectra (Figure 6.6) reveal BODIPY-like emission for **8x** and **9x**, lacking the observed CT or exciplex emission bands which were especially visible for BODIPY **9a**. Measurement of the fluorescence and singlet oxygen quantum yields revealed very high Φ_f values with no tendency for singlet oxygen formation (Table 6.4). We therefore concluded that the acridine moieties play a key role in the exciplex formation and that the exciplexes are responsible for efficient ISC leading to balanced Φ_f and Φ_Δ.

Table 6.4: Spectroscopic data for **4**, **7a**, **8x**, and **9x** as obtained in chloroform solution.

Compound	λ_{abs} (nm)[a]	λ_{em} (nm)[b]	Φ_f[c]	Φ_Δ[d]
4	285	457	0.01	-[e]
7a	509	513	0.96	-[e]
8x	634, 346	644	0.79	0.01
9x	661, 371	671	0.50	0.02

[a] Absorption maximum. [b] Fluorescence emission maximum/maxima. [c] Fluorescence quantum yield determined *vs* 1,4-bis(5-phenyl-2-oxazolyl)benzene (λ_{exc} = 300 nm, Φ_f = 0.97 in cyclohexane; for **4**), rhodamine 6G (λ_{exc} = 488 nm, Φ_f = 0.94 in ethanol; for **7a**), cresyl violet (λ_{exc} = 580 nm, Φ_f = 0.56 in ethanol; for **8x**), or nile blue (λ_{exc} = 605 nm, Φ_f = 0.27 in ethanol; for **9x**) as a reference. [d] Singlet oxygen quantum yield determined *vs* methylene blue (Φ_Δ = 0.52, λ_{exc} = 639 nm) in spectroscopic grade ethanol as a reference by monitoring the absorbance of 1,3-DPBF at 414 nm. [e] Not determined.

6.2.3 Conclusions

We successfully designed novel BODIPY photosensitizers which are active in the phototherapeutic window with balanced fluorescence and singlet oxygen generation quantum yields. Extension of the conjugated BODIPY core lead to red-shifted absorption and emission while the introduction of the acridine moiety was key to the singlet oxygen generation. While the quantum-chemical calculations were not able to provide direct proof for the exciplex mechanism, the lack of viable CT states motivated us to further investigate the optical properties of the BODIPYs dyes. Concentration dependent emission, as seen for BODIPYs **8a** and **9a**, was attributed to exciplex emission. Exciplexes are known to exhibit efficient ISC and are likely the reason why our photosensitizers performed as well as they did. The acridine unit plays a crucial role in this behavior as BODIPY compounds without the acridine (**8x** and **9x**) did not show exciplex emission, were unable to generate singlet oxygen and instead showed high fluorescence quantum yields. Further investigation of the exciplex mechanism for these BODIPY compounds is planned.

Additionally, these BODIPY photosensitizers cannot be tested in cells without embedding as they are not water-soluble and will therefore be used in nanoparticles for cell studies in the future.

6.3 *The effects of homocoupling on the optoelectronic properties of low bandgap polymers for organic photovoltaic applications*

Push-pull type conjugated polymers applied in organic electronics do not always contain a perfect alternation of donor and acceptor building blocks. Mis-couplings can occur, which have a noticeable effect on the device performance.[6-9] In this work, the influence of homocoupling on the optoelectronic properties and photovoltaic performance of PDTSQx$_{ff}$ polymers is investigated, with a specific focus on the quinoxaline acceptor moieties. A homocoupled biquinoxaline segment was intentionally inserted in specific ratios during the polymerization. These homocoupled units caused a gradually blue-shifted absorption, while the HOMO energy levels decreased only significantly upon the presence of 75 to 100% of homocouplings. DFT calculations showed that the homocoupled acceptor unit generates a twist in the polymer backbone, which leads to a decreased conjugation length and a reduced aggregation tendency. The virtually defect-free PDTSQx$_{ff}$ afforded a solar cell efficiency of 5.4%, which only decreased strongly upon incorporating a homocoupling degree over 50%.

6.3.1 Results and discussion

A series of PDTSQx$_{ff}$ (i.e. poly(dithienosilole-difluoroquinoxaline) copolymers (Figure 6.7) with an increasing amount of acceptor-acceptor homocoupling (**P1** = 0%, **P2** = 5%, **P3** = 25%, **P4** = 50%, **P5** = 75%, **P6** = 100%) was synthesized by G. Pirotte and submitted to a variety of characterization techniques such as size-exclusion chromatography (SEC; to estimate the molar masses), cyclic voltammetry (CV; to estimate the HOMO and LUMO energy

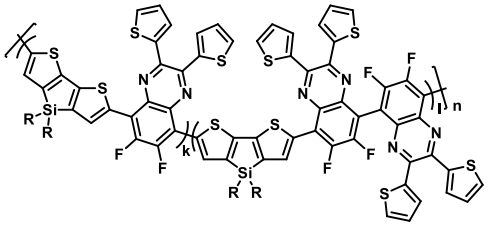

R = 2-ethylhexyl
k = 1, 0.95, 0.75, 0.5, 0.25, 0
l = 1-k

Figure 6.7: Molecular structures of the PDTSQx$_{ff}$ polymers synthesized by G. Pirotte.

levels) and UV-VIS absorption spectroscopy (to verify the absorption profile).

The obtained CV values (Table 6.5) show that the LUMO energy level of the pristine PDTSQx$_{ff}$ polymer is barely affected by the presence of homocoupling. The HOMO levels also remain constant up to 50% homocoupling and significant differences were only detected for the 75% and pure homocoupled polymers (**P5** and **P6**). Because of the constant LUMO and decreasing HOMO, the bandgap increases with increasing homocoupling content. UV-VIS absorption spectroscopy in solution and thin film (Figure 6.8) showed that a small percentage of homocoupling (5%) does not significantly change the absorption profile of the polymer, while the presence of larger amounts clearly causes a blue-shift of the absorption maximum (Table 6.5) and alters the color of the polymer in solution. The blue-shift is most pronounced when comparing 0-25, 25-50 and 50-75% of homocoupling, whereas increasing the homocoupling content from 75 to 100% only changes the width of the absorption band. Very similar observations were made for the solid state spectra. In the solid state spectra, the blue-shift is likely enhanced due to a decrease in aggregation upon increasing the homocoupling percentage, with the virtually defect-free polymer having a clear red-shifted shoulder in the absorption spectrum, similar to the behaviour of (semi-crystalline) polythiophenes. A diminishing presence of this shoulder across the polymer series indicates that homocoupling significantly decreases the tendency to aggregate, even at low concentrations (5%).

Table 6.5: Overview of the characterization data for PDTSQx$_{ff}$ polymers **P1**-**P6** with different homocoupling content.

Parameter	**P1**	**P2**	**P3**	**P4**	**P5**	**P6**
$(Qx_{ff})_2$ [%][a]	0	5	25	50	75	100
M_n [kDa][b]	30.1	25.2	27.6	24.5	25.6	30.2
Đ[c]	1.29	1.12	1.31	1.49	1.25	1.28
λ_{max} [nm][d,e]	649 [630]	647	617	587 [608]	570	568 [577]
$E_{(HOMO)}$ [eV][e,f]	-5.49 [-5.21]	-5.51	-5.48	-5.51 [-5.29]	-5.62	-5.71 [-5.41]
$E_{(LUMO)}$ [eV][e,f]	-3.40 [-2.63]	-3.42	-3.40	-3.40 [-2.64]	-3.42	-3.43 [-2.63]
ΔE_{EC} [eV][e,g]	2.09 [2.58]	2.09	2.08	2.11 [2.65]	2.20	2.28 [2.78]
ΔE_{opt} [eV][h]	1.65	1.68	1.66	1.68	1.89	1.95

[a] Percentage of homocoupling. [b] Number average molecular weight obtained via SEC. [c] Dispersity taken as M_w/M_n. [d] Determined from the UV-VIS absorption spectra of the polymer solutions in chloroform. [e] Values in brackets are obtained using (TD)DFT calculations. [f] Determined by CV measurements from the onset of oxidation/reduction. [g] Electrochemical gaps determined as LUMO-HOMO. [h] Optical gaps estimated from the wavelength at the intersection of the tangent line drawn at the low energy side of the absorption spectrum with the x-axis.

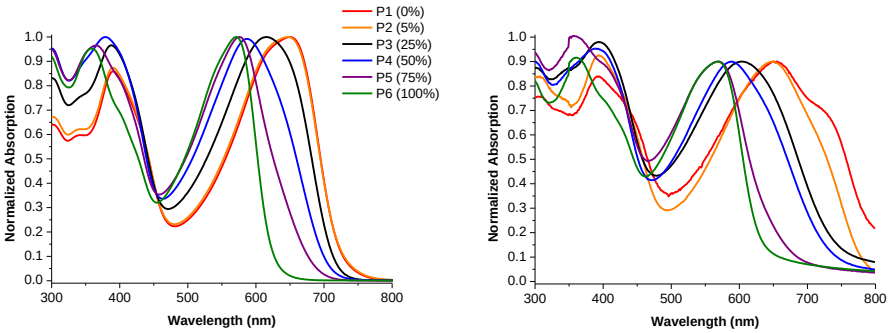

Figure 6.8: Normalized UV-VIS absorption spectra of polymers **P1**-**P6** in chloroform solution (left) and in thin film (right).

To further unravel the influence of homocoupling on the backbone conjugation, DFT calculations were performed using the M06 exchange-correlation functional[33] and the 6-311G(d) basis set. First, the ground state geometries were optimized for the individual donor and acceptor moieties, the donor-acceptor combinations (DA) and acceptor-acceptor (AA) homocoupled moieties (Figure 6.9). The alkyl chains were replaced with methyl groups to facilitate the calculations without changing the electronic properties of the oligomers. Several conformations for the donor and acceptor units have been considered and the calculations were performed using the most stable conformers (Table 6.6). D-A-D-A-D oligomers were constructed to mimic their polymeric counterparts with 0 (**P1**), 50% (**P4**) (one A-A linkage) and 100% (**P6**) (two A-A linkages) homocoupling (Figure 6.10). From the geometry optimizations for both the AA homocoupled units and the oligomers containing 50% and 100% homocoupling (Figure 6.10), a large dihedral angle between the adjacent acceptor units of around 57° was observed. The insertion of a homocoupled acceptor unit therefore causes a deviation from planarity, which will significantly lower the ability of the polymer chains to aggregate upon film formation. Within the same polymer chain, this deviation results in a decrease of orbital overlap and therefore in a decrease in conjugation. This is also apparent from the obtained orbital topologies (Figure 6.11), in which it is clear that upon increasing the level of homocoupling, the HOMO is more localized on the dithienosilole (DTS) units instead of the entire backbone, whereas the LUMO remains largely unchanged. This is reflected in the calculated HOMO and LUMO energies (Table 6.5). Time-

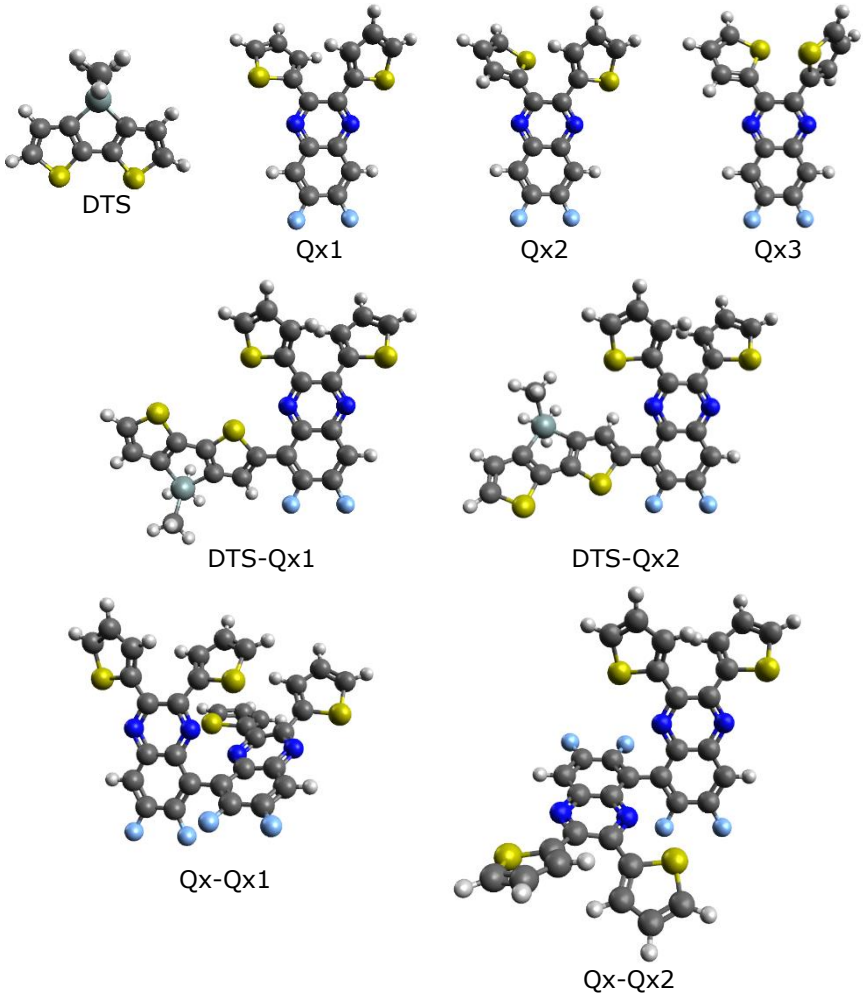

Figure 6.9: Optimized geometries and conformational study on the donor and acceptor units and D-A and A-A combinations. Calculations were performed using M06/6-311G(d).

dependent density functional theory (TD-DFT) calculations using the M06 exchange-correlation functional[33] and the 6-311G(d) basis set, and taking into account the environment (chloroform) effects using the polarizable continuum model, were performed to simulate the absorption spectra of the polymers containing 0, 50 and 100% homocoupling (Figure 6.12). These simulated spectra show a blue-shift with increasing homocoupling percentage, in line with the experimental observations. The calculations also confirm a stabilization of the HOMO level, while the LUMO remains constant.

Table 6.6: Energies, populations and HOMO/LUMO energies for the donor, acceptor and D-A and A-A combinations in Figure 6.9.

Name	Energy (Hartree)	ΔE (kJ/mol)	Pop. (%)	ε_{HOMO} (eV)	ε_{LUMO} (eV)	$\Delta\varepsilon$ (eV)
DTS	-1472.71334	—	—	-5.84	-1.31	4.53
Qx1	-1719.64836	—	94.72	-6.37	-2.35	4.02
Qx2	-1719.64554	7.41	5.04	-6.41	-2.34	4.07
Qx3	-1719.64264	15.00	0.24	-6.50	-2.35	4.15
DTS-Qx1	-3191.18229	—	65.34	-5.66	-2.42	3.24
DTS-Qx2	-3191.18129	2.63	34.66[a]	-5.72	-2.40	3.32
Qx-Qx1	-3438.12002	—	99.36	-6.32	-2.42	3.90
Qx-Qx2	-3438.11526	12.52	0.64	-6.30	-2.43	3.87

[a] After consideration of the HOMO/LUMO topologies and first excited state, this conformer was deemed to not show a significant influence on the electronic properties of the oligomers and was therefore not taken into account.

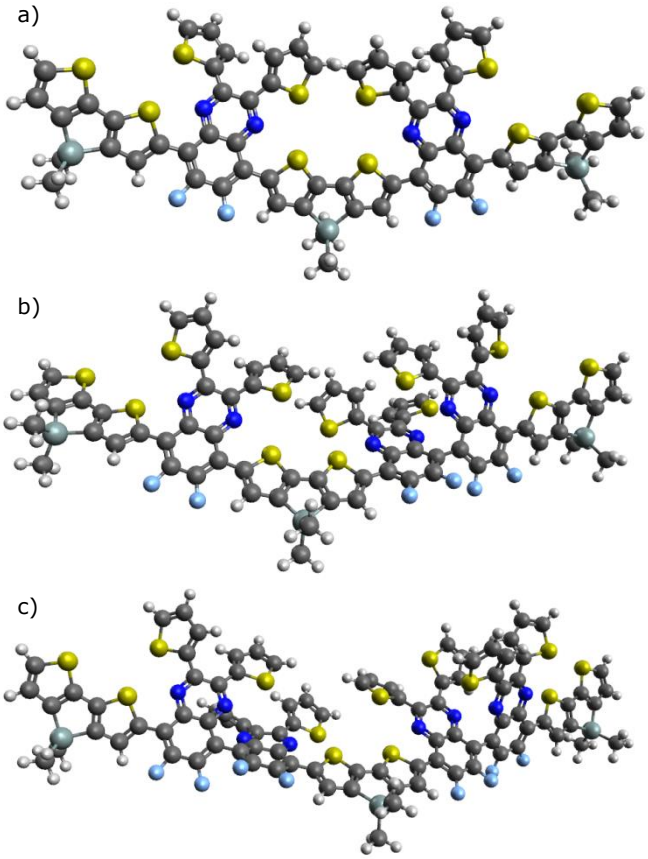

Figure 6.10: Optimized geometries of oligomers containing a) **P1**: 0%, b) **P4**: 50% and c) **P6**: 100% of homocoupling. Calculations were performed using M06, 6-311G(d).

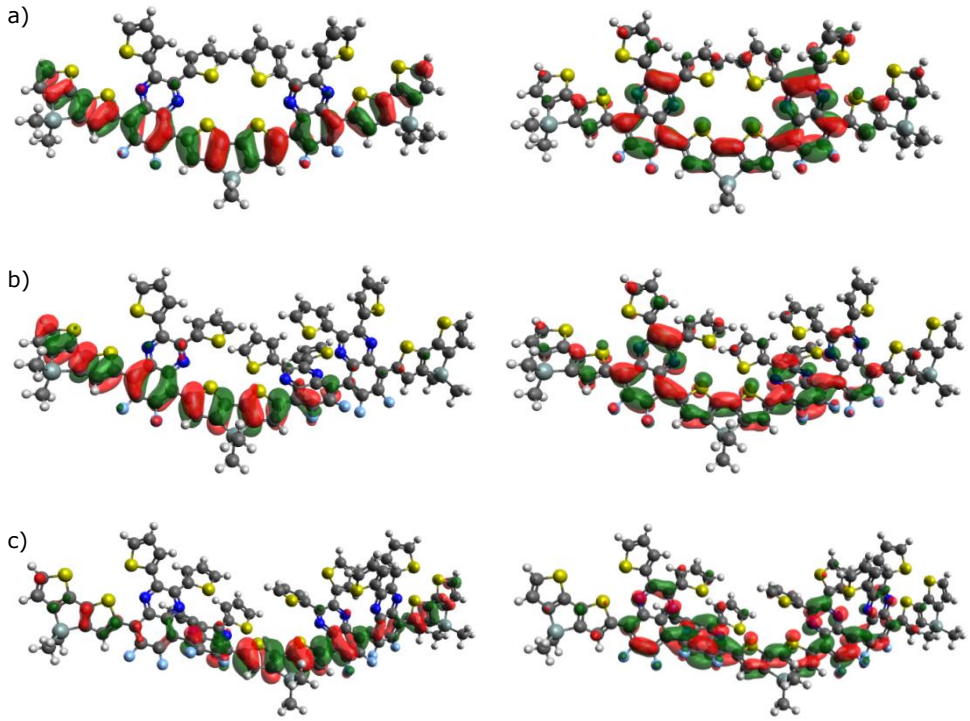

Figure 6.11: HOMO (left) and LUMO (right) topologies for the oligomers containing a) **P1**: 0%, b) **P4**: 50% and c) **P6**: 100% homocoupling. Calculations were performed using M06, 6-311G(d).

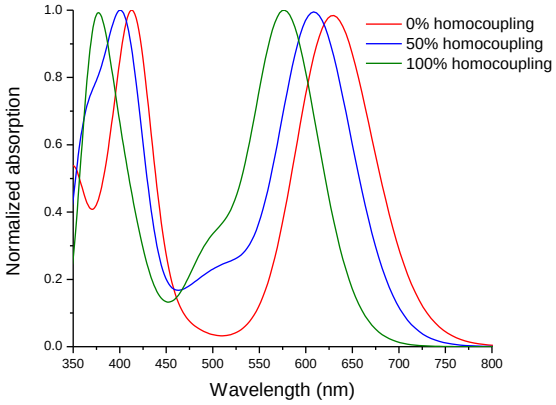

Figure 6.12: Simulated UV-VIS spectra for the different oligomers. Calculations were performed using TDDFT with M06, 6-311G(d), IEFPCM with chloroform as a solvent and taking into account the first 30 excited states. A full-width at half maximum of 0.3 eV was chosen for the Gaussian around each excitation energy.

6.3.2 Conclusions

Using DFT calculations, we were able to understand the structural changes that A-A homocoupling imposes on a PDTSQx$_{ff}$ polymer chain by varying the amount of homocoupling. This was done by creating oligomers of alternating D-A or D-A-A units followed by geometry optimization and calculation of the excited states using time-dependent DFT. From simple parameters like dihedral angles and HOMO and LUMO topologies, we were able to explain the observed experimental properties. Twisting of the polymer backbone leads to localization of the HOMO on the polymer donor unit (DTS) and is the cause for the observed increase in HOMO energy and the blue-shift in UV-VIS absorption as a result of the decrease in conjugation length. This also influences the charge-carrier transport, which is found to diminish upon increasing the percentage of homocoupling. As a result, solar cell efficiency goes down with an increasing amount of homocoupling.
These large systems showcase the potential of DFT and TDDFT calculations for geometry optimization and excited state property calculations.

6.4 Understanding the optoelectronic properties of bis(perylene diimide) acceptor polymers for organic photovoltaic applications

Fullerene-free organic photovoltaics have recently reached impressive power conversion efficiencies above 18% for single junctions, increasing their competitiveness with respect to alternative thin-film technologies.[34] In most record devices, electron-donating conjugated polymers are combined with novel generation small molecule acceptors.[35-38] All-polymer organic solar cells, on the other hand, still lag behind in efficiency, although they have specific advantages in terms of ink formulation and long-term operational stability.[38-41] Another point of attention is the synthetic complexity of the active layer materials, notably on the side of the new acceptor molecules. Therefore, the present study focuses on the implementation of the stable and cost-effective perylene diimide structure as the key component of high-performance electron-accepting polymers. The synthesis, structural and optoelectronic characterization of four push-pull type copolymers containing the electron-deficient bis(perylene diimide) (bis-PDI) unit are reported, as well as the photovoltaic analysis of these acceptor materials in combination with a well-known donor polymer (PTB7-Th). The acceptor polymers differ in the electron-rich part of the alternating push-pull structure and their solar cell power conversion efficiencies range from 3.2 to 4.7%. The maximum efficiency - the best performance achieved with a bis-PDI polymer so far - is obtained for the structurally most simple polymer, containing merely thiophene as the electron-rich building block. Controlled degradation under blue light in air is monitored by the bleaching of the relevant UV-Vis absorption bands, demonstrating high stability for the bis-PDI-thiophene containing polymers as compared to some prototype small molecule acceptors (FBR and ITIC).

6.4.1 Results and discussion

Four acceptor polymers for bulk heterjunction solar cells based on bis(perylene diimide) (bisPDI) were synthesized by R. Lenaerts, with varying electron-donating groups such as thiophene (**PTbPDI**), dithiophene (**PTTbPDI**), terthiophene (**PTTTbPDI**) and benzodithiophene (**PBDTbPDI**) (Figure 6.13).

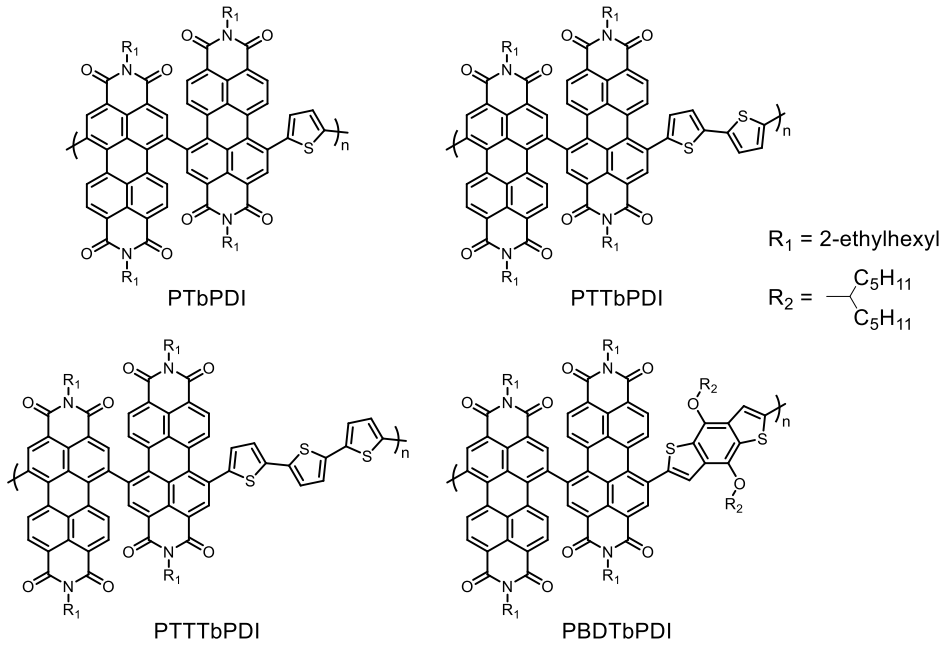

Figure 6.13: Chemical structures of the bisPDI acceptor polymers.

Similar to the previous section, these polymers were characterized using SEC, CV and UV-VIS absorption spectroscopy. SEC analysis demonstrated number-average molar masses (M_n's) of 19, 23, 37 and 30 kg mol^{-1} for **PTbPDI**, **PTTbPDI**, **PTTTbPDI** and **PBDTbPDI**, respectively, all with a dispersity ($Đ$) of 2.0 or lower (Table 6.7). All four polymers have similar low-lying lowest unoccupied molecular orbital (LUMO) levels around -4.2 eV, as estimated from cyclic voltammetry (CV) experiments, while the highest occupied molecular orbital (HOMO) levels and HOMO-LUMO gaps (E_g^{EC}) differ depending on the electron-rich monomer used (Table 6.7). **PTbPDI** has the largest E_g^{EC} of the four polymers (1.81 eV), followed by **PBDTbPDI** (1.80 eV), **PTTbPDI** (1.73 eV) and **PTTTbPDI** (1.45 eV). The UV-Vis absorption spectra in solution (Figure 6.14) show a gradual red-shift of the absorption onset, starting in solution from 674 nm for **PTbPDI** to 742 nm for **PTTbPDI**, 761 nm for **PBDTbPDI** and 800 nm for **PTTTbPDI**.

From the CV measurements, a substantial increase in HOMO energy appears when moving from **PTTbPDI** to **PTTTbPDI**. To shed more light on this, density functional theory (DFT) calculations were carried out with the M06 exchange-correlation functional[33] and the 6-311G(d) basis set. For each of the acceptor

Table 6.7: Molar mass (distribution), optical and electrochemical properties of the acceptor polymers.

	M_n (kg mol^{-1})[a]	$Đ$[b]	λ_{max} (nm)[c]	HOMO[d,e] (eV)	LUMO[d,e] (eV)	E_g^{EC} [f] (eV)	E_g^{OP} [g] (eV)
PTbPDI	19	2.0	551	-6.03 [-6.36]	-4.22 [-3.81]	1.81 [2.55]	1.84
PTTbPDI	23	2.0	494, 337	-5.96 [-6.17]	-4.23 [-3.76]	1.73 [2.41]	1.67
PTTTbPDI	37	1.4	512, 400	-5.68 [-5.90]	-4.23 [-3.73]	1.45 [2.17]	1.55
PBDTbPDI	30	1.9	545, 377	-6.05 [-5.99]	-4.25 [-3.75]	1.80 [2.24]	1.63

[a] Number average molecular weight obtained via SEC. [b] Dispersity taken as M_w/M_n. [c] Determined from the UV-VIS absorption spectra of the polymer solutions in chloroform. [d] Determined by CV from the onset of oxidation/reduction. [e] Calculated values (DFT) between brackets. [f] Electrochemical gaps determined as LUMO-HOMO. [g] Optical gaps estimated from the wavelength at the intersection of the tangent line drawn at the low energy side of the absorption spectrum with the x-axis.

polymers, two conformations of the same model oligomer were optimized to find the most stable form (Figure 6.15, Table 6.8). These conformers differ in the orientation of the two bis-PDI units with respect to each other. From the most stable conformers, it is clear that the HOMO energy increases linearly when going from **PTbPDI** to **PTTbPDI** and finally **PTTTbPDI** (Table 6.7). When looking at the HOMO distribution in Figure 6.16, this becomes clear as the HOMO becomes less delocalized over the entire backbone and more localized on the donor unit. The energy of the LUMO, which is mostly localized on the bis-PDI

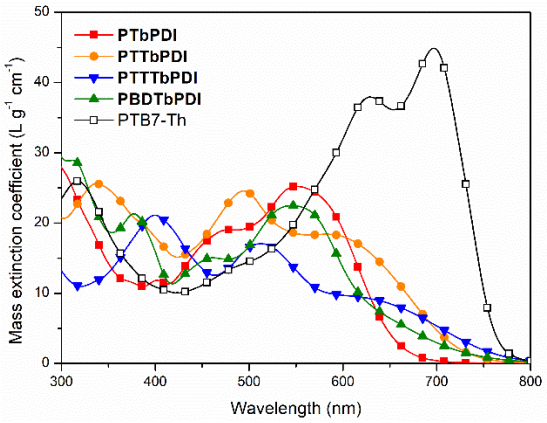

Figure 6.14: UV-Vis absorption spectra of the different polymers in chloroform solution.

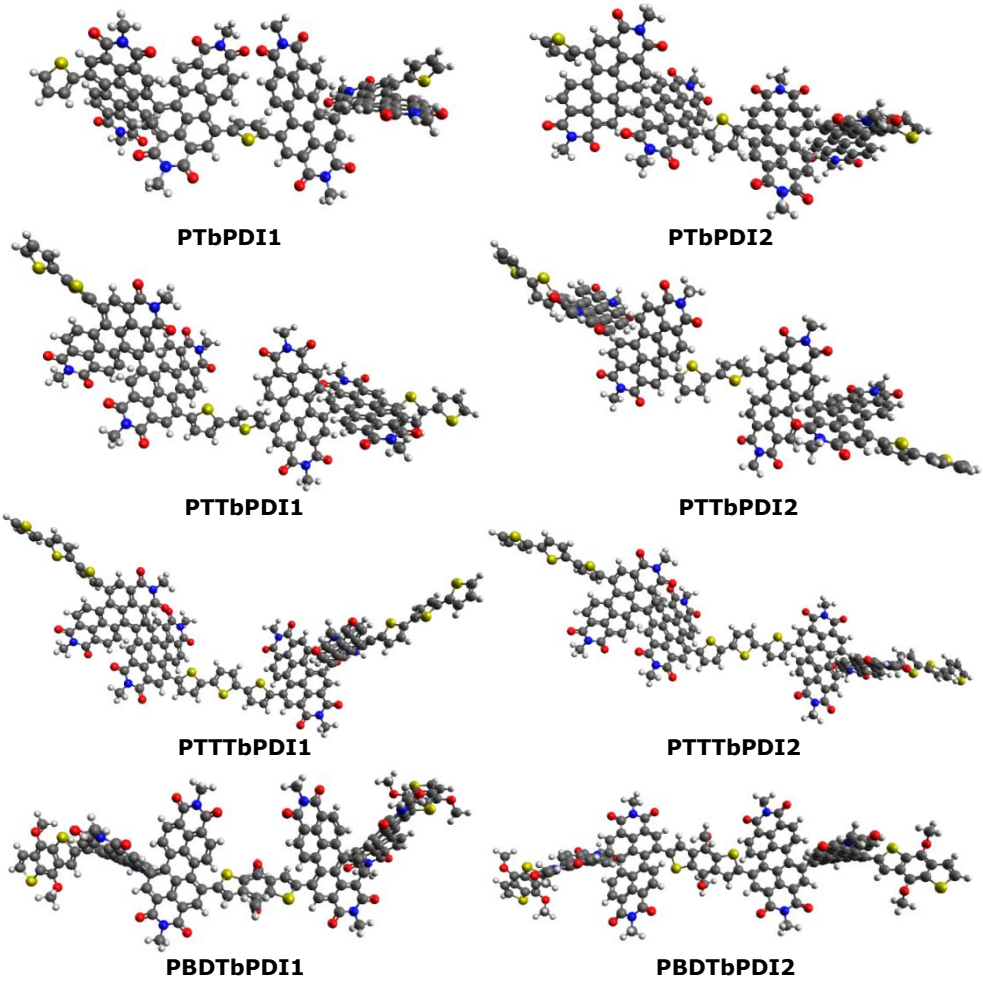

Figure 6.15: Optimized geometries of the D-A-D-A-D oligomers mimicking **PTbPDI**, **PTTbPDI**, **PTTTbPDI** and **PBDTbPDI.**

Table 6.8: Energies and HOMO/LUMO energies for the oligomers depicted in Figure 6.14.

Name	Energy (Hartree)	ΔE [kJ mol^{-1}]	ε_{HOMO} [eV]	ε_{LUMO} [eV]	$\Delta\varepsilon$ [eV]
PTbPDI1	-7287.9427	4.54	-6.39	-3.81	2.58
PTbPDI2	-7287.9444	—	-6.36	-3.81	2.55
PTTbPDI1	-8943.1053	0.35	-6.17	-3.75	2.42
PTTbPDI2	-8943.1055	—	-6.17	-3.76	2.41
PTTTbPDI1	-10598.2690	-1.28	-5.90	-3.73	2.17
PTTTbPDI2	-10598.2685	—	-5.90	-3.74	2.16
PBDTbPDI1	-9858.6004	2.23	-5.98	-3.75	2.23
PBDTbPDI2	-9858.6013	—	-5.99	-3.75	2.24

units (Figure 6.16), remains almost constant throughout the entire series, as also concluded from the CV experiments. The calculated values for the HOMO-LUMO gap follow a linear trend, which is in line with the CV and UV-VIS data. The seemingly large jump in the CV data from **PTTbPDI** to **PTTTbPDI** is also observed in the calculations (Table 6.8), but less in the UV-VIS data. From the optimized geometries, it is clear that a large twist is present between the two PDI subunits, as well as between the PDI and the donor segments. This twisting of the polymer backbone hinders the stacking behavior of the acceptor polymers, allowing better mixing with the donor polymer.[42]

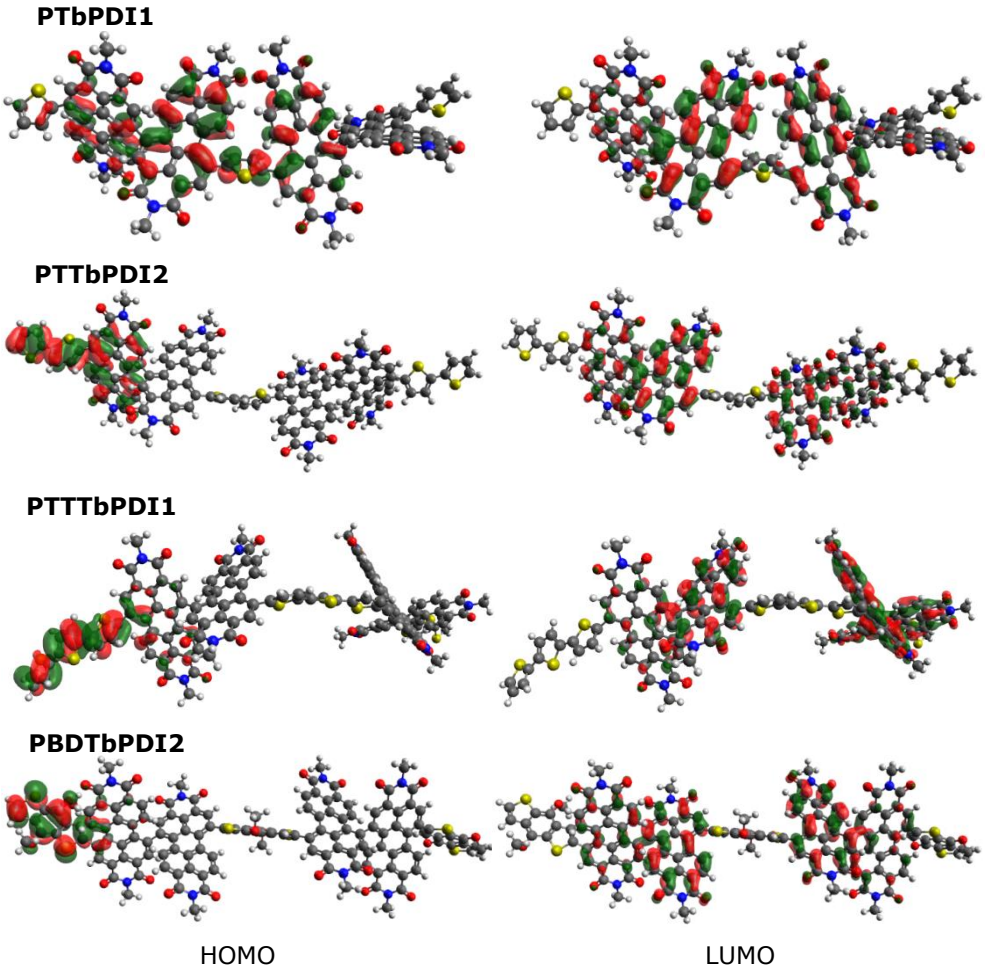

Figure 6.16: HOMO (left) and LUMO (right) distributions for the most stable conformers of **PTbPDI**, **PTTbPDI**, **PTTTbPDI** and **PBDTbPDI**.

6.4.2 Conclusions

The bis-PDI unit was chosen because its twisted nature reduces phase separation between the donor and bisPDI acceptor polymer in all-polymer bulk heterojunction solar cells. Unfortunately, it also breaks conjugation along the polymer backbone, reducing charge carrier transport. A conformational analysis was required to ensure conformers with the lowest possible energy to allow comparison with experimental results. Using density functional calculations (DFT), we were again able to deduce structure-property relationships. Good qualitative agreements between experimental and theoretical results were found. The bis-PDI polymers were especially "tricky" as the largest one (**PBDTbPDI**) consists of 250 atoms, making these oligomers the largest compounds that I have performed DFT calculations on.

6.5 The effects of halogenation on PBDTT-TQxT based non-fullerene polymer solar cells

The rapid advancement in the development of non-fullerene acceptors has led to single-junction polymer solar cells with efficiencies over 18%.[34] Even with these novel acceptor materials, the choice of the donor polymer remains important. Tuning of the donor and acceptor compatibility in terms of absorption, frontier orbital energy levels, mixing enthalpy and charge carrier mobility is routinely performed by side chain variation.[43] Fluorination presents an additional powerful approach to optimize these parameters.[44-50] Although significantly less studied, chlorination can give rise to similar effects, while donor-acceptor phase separation due to fluorophobic interactions is less of an issue.[51-54] Moreover, from a material synthesis point of view, the introduction of chlorine groups is in many cases much more straightforward. In this work, we present a series of push-pull type benzo[1,2-*b*:4,5-*b*']dithiophene-*alt*-quinoxaline donor polymers and compare the behavior of the non-halogenated, fluorinated and chlorinated derivatives in polymer solar cells when combined with small molecule and polymer type non-fullerene acceptors. The solar cell efficiencies vary from 2.4 to 8.4%, elucidating the large impact of these small structural variations. Best results are achieved for the chlorinated donor polymer, affording a high open-circuit voltage, balanced charge carrier mobilities and favorable donor-acceptor interactions. Combined with the easier synthesis of chlorinated materials, this indicates that more emphasis should be put on chlorination as a valuable approach to tune the properties of organic semiconductors for solar cell blends (and other optoelectronic applications).

6.5.1 Results and discussion

Three different donor copolymers based on thiophene-substituted benzodithiophene (BDTT) combined with a difluorinated quinoxaline (Qx) were synthesized (Figure 6.17). The impact of halogenation was investigated by functionalizing the BDT monomer with either non-halogenated, difluorinated or monochlorinated thienyl moieties. One single chlorine atom was introduced (as opposed to two fluorine atoms) to prevent severe twisting of the thienyl side chains. Additionally, chlorination of the established acceptor polymer

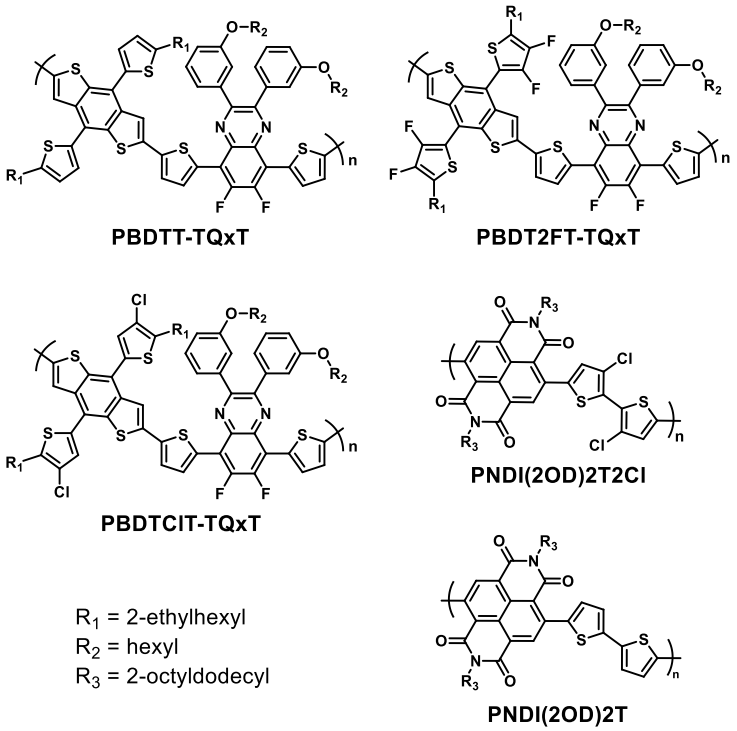

Figure 6.17: Chemical structures of the donor polymers **PBDTT-TQxT**, **PBDT2FT-TQxT** and **PBDTClT-TQxT**, and the acceptors **PNDI(2OD)2T** and **PNDI(2OD)2T2Cl**.

PNDI(2OD)2T[38] was performed to see whether halogenation of the acceptor polymer can have the same beneficial effects as chlorination of the donor polymer.

The polymer donor materials have similar absorption patterns with a main band due to intramolecular charge transfer peaking around 600 nm and smaller bands which can be attributed to π-π transitions of the individual building blocks (Figure 6.18). The absorption spectra of the halogenated polymers are slightly blue-shifted compared to the reference polymer **PBDTT-TQxT**. The optical gaps are within the range of 1.71 to 1.79 eV (Table 6.9). Based on cyclic voltammetry (CV) measurements, the HOMO energy level for both the fluorinated and the chlorinated donor polymer are found to be around −5.55 eV, whereas the HOMO of **PBDTT-TQxT** is slightly higher (−5.46 eV). The LUMO energy levels remain virtually the same (−3.35 eV) (Table 6.9), as expected since the quinoxaline monomer remains unaffected. The lower HOMO levels for the halogenated donor polymers are in line with the blue-shifted absorption spectra. Chlorination of the

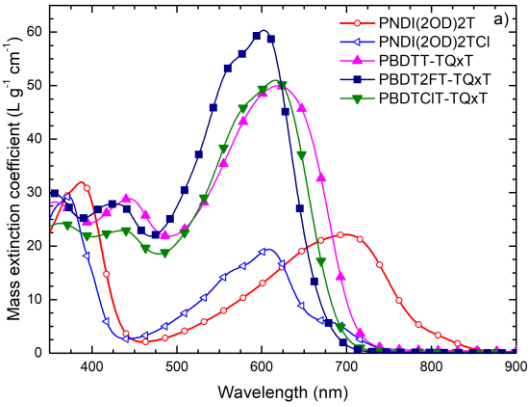

Figure 6.18: UV-Vis-NIR absorption spectra of the different donor and acceptor polymers in chloroform.

the polymer acceptor **PNDI(2OD)2T**, yielding **PNDI(2OD)2T2Cl**, has a more significant impact on the absorption spectrum. The absorption spectrum of the latter is strongly blue-shifted compared to that of the former, with an optical gap in film of 1.70 eV, compared to 1.52 eV, for the pristine polymer (Table 6.9, Figure 6.18). The absorption maximum of **PNDI(2OD)2T2Cl** is blue-shifted to ~600 nm (vs ~700 nm for **PNDI(2OD)2T** and 684 nm for the fluorinated analogue[55, 56]), likely due to a combination of electronic and steric factors.

To achieve additional insights on the above optical and electrochemical results and to get an idea of the geometry of the BDTT-TQxT and NDI-2T copolymer structures, density functional theory (DFT) calculations were carried out with the M06 exchange-correlation functional[33] and the 6-311G(d) basis set. The geometries of D-A-D-A-D (D = donor, A = acceptor) type oligomers for NDI-2T and D-A-D-A oligomers for BDTT-TQxT were optimized (Figure 6.19). Different conformations (with respect to the orientation of the D and A subunits) were investigated and the most stable conformers were further analyzed. For the NDI-2T oligomers, the influence of the relatively large chlorine atoms on the dihedral angle between the two thiophene units is obvious. The torsion angle between the central thiophene units enlarges from 24.4° for **PNDI(2OD)2T** to 46.0° for **PNDI(2OD)2T2Cl**. This is in line with the blue-shifted absorption for **PNDI(2OD)2T2Cl** as the larger twist disrupts conjugation along the polymer backbone. The HOMO is also slightly less delocalized along the oligomer backbone (Figure 6.20). For the PBDT-TQxT series, the influence of the halogen

Table 6.9: Molar mass (distribution), optical and electrochemical data for the donor and acceptor polymers.

	M_n (10^4 g mol^{-1})[a]	$Đ$[b]	HOMO (eV)[c,d]	LUMO (eV)[c,d]	λ_{max} (nm)[d,e]	E_g^{OP} (eV)[f]
PBDTT-TQxT	4.5	2.0	-5.46	-3.35	623	1.71
			[-5.34]	[-2.69]	[500]	
PBDT2FT-TQxT	5.0	2.1	-5.58	-3.37	604	1.79
			[-5.43]	[-2.80]	[507]	
PBDTClT-TQxT	7.1	1.8	-5.53	-3.35	617	1.78
			[-5.45]	[-2.81]	[506]	
PNDI(2OD)2T	4.2	2.4	-6.02	-3.99	698	1.52
			[-5.92]	[-3.49]	[548]	
PNDI(2OD)2T2Cl	5.7	2.0	-6.30	-4.13	609	1.70
			[-6.40]	[-3.70]	[484]	

[a] Number average molecular weight obtained via SEC. [b] Dispersity taken as M_w/M_n. [c] Determined by CV from the onset of oxidation/reduction. [d] Calculated values (DFT/TDDFT) between brackets. [e] Determined from UV-VIS absorption spectra of the polymer solutions in chloroform. [f] Optical gaps estimated from the wavelength at the intersection of the tangent line drawn at the low energy side of the absorption spectrum with the x-axis.

atoms is smaller because they are found in the BDT side chains, as opposed to being in the backbone for the acceptor polymers. No apparent changes in the HOMO nor LUMO topologies can be observed as the thiophene units in the BDT side chains appear to be electronically decoupled from the BDT unit itself. However, due to the electron-deficient nature of these atoms, it is viable that they decrease the donor strength of the BDT units. The calculated HOMO-LUMO energy levels are in good (qualitative) agreement with the trends observed experimentally (Table 6.9). Additionally, time-dependent DFT (TDDFT) calculations using a modified LC-BLYP (ω = 0.2) exchange-correlation functional[57] and 6-311G(d) as the basis set were performed to simulate the UV-VIS absorption spectra in cyclohexane using the polarizable continuum model (PCM) (Figure 6.21). While the blue-shift for **PNDI(2OD)2T2Cl** with respect to **PNDI(2OD)2T** is reflected correctly, this is not the case for the halogenated PBDTT polymers, although the effects are small, even in the experimental data. As discussed before, the chlorine atoms in the PNDI polymers cause a large twist in the polymer backbone, breaking the conjugation. This effect plays a much larger role than the halogenation does for the PBDTT-based polymers, where the structural changes take place in the BDT side chain, showing a large dihedral angle with the BDT, even without halogenation.

PBDTT-TQxT

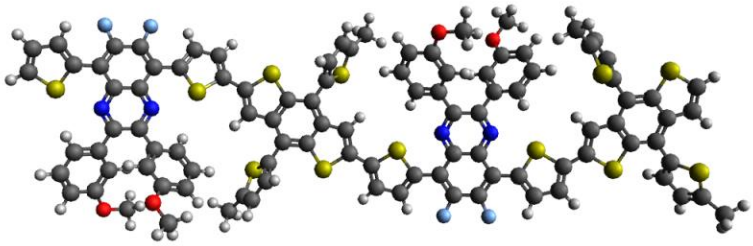

PBDT2FT-TQxT

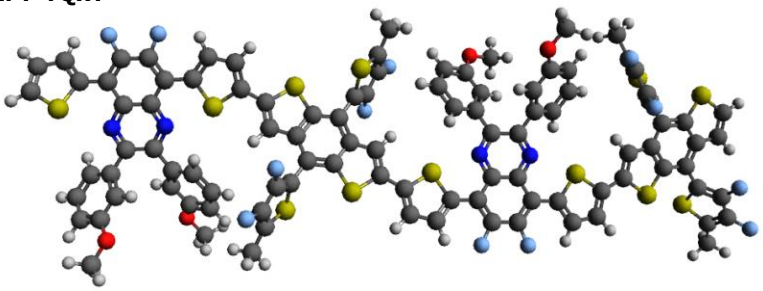

PBDTClT-TQxT

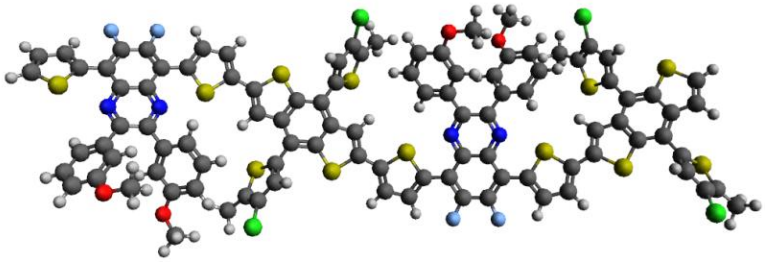

PNDI(2OD)2T

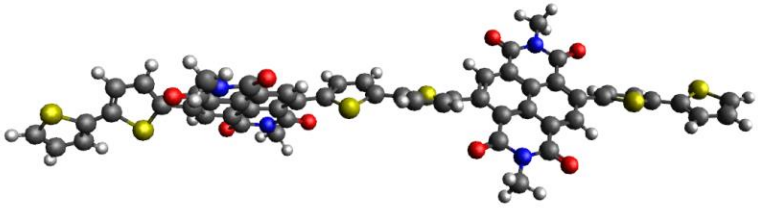

PNDI(2OD)2T2Cl

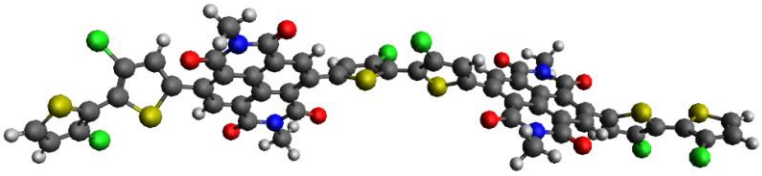

Figure 6.19: Optimized geometries for **PBDTT-TQxT**, **PBDT2FT-TQxT**, **PBDTClT-TQxT**, **PNDI(2OD)2T** and **PNDI(2OD)2T2Cl**.

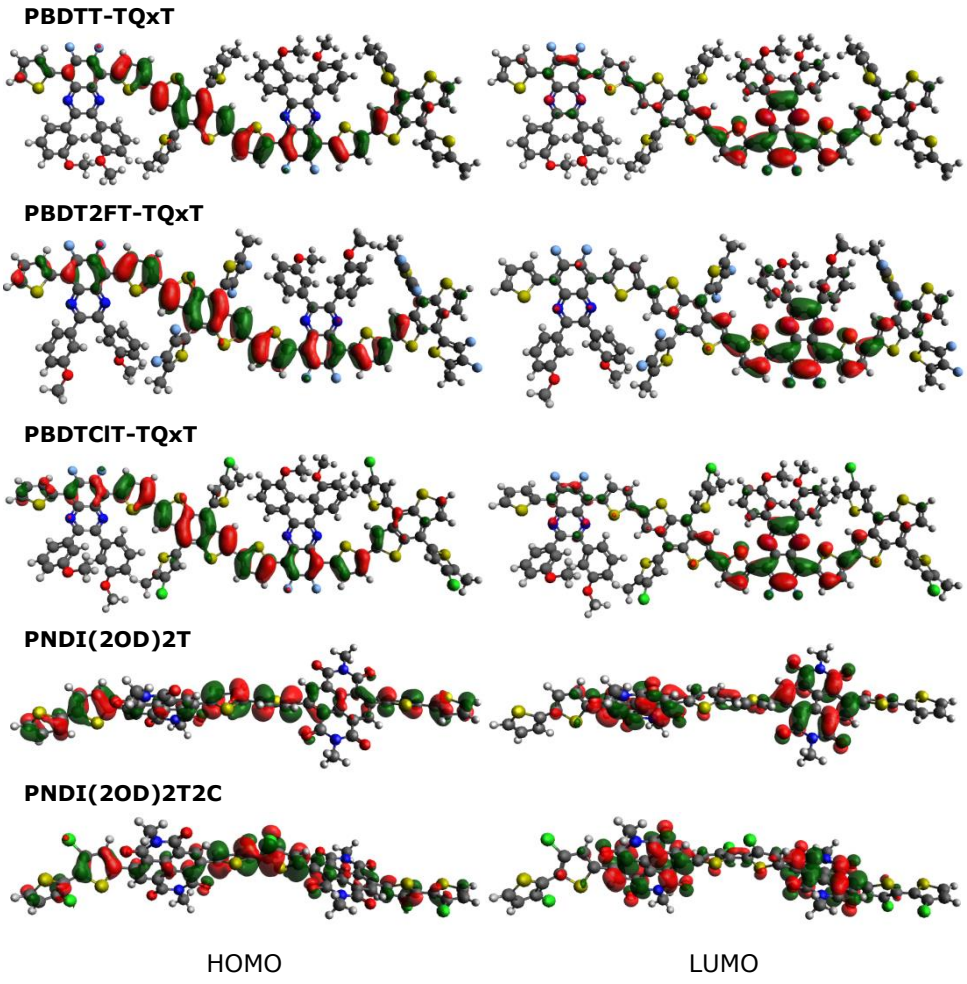

Figure 6.20: HOMO/LUMO topologies for **PBDTT-TQxT**, **PBDT2FT-TQxT**, **PBDTClT-TQxT**, **PNDI(2OD)2T** and **PNDI(2OD)2T2Cl**. (isocontour values of 0.02 a.u. for all orbitals).

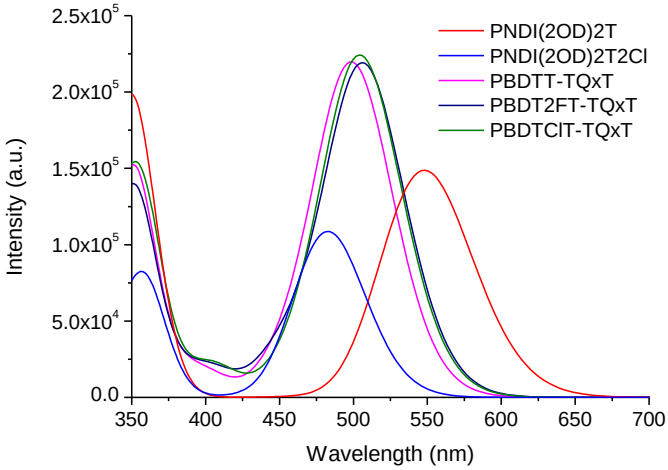

Figure 6.21: Simulated UV-VIS absorption spectra for the polymers considered in this section. Cyclohexane was chosen as the solvent in the PCM. A full-width at half maximum of 0.3 eV was chosen for the Gaussian around each excitation energy.

6.5.2 Conclusions

While halogenation of either the donor or acceptor polymer in a bulk heterojunction organic solar cell might afflord higher device efficiencies, the positioning of the halogenation sites is crucial. As shown for the PNDI-based polymers, halogenation of the backbone thiophene units leads to a large increase in the dihedral angle between the various units, disrupting the conjugation along the backbone and leading to an increase of the HOMO energy. Halogenation of the thiophene side chain on the BDT donor unit has a negligible influence on the calculated properties of the PBDTT-based polymers. Experimentally, a small blue-shift is observed in the UV-VIS spectra upon moving from the non-halogenated to chlorinated and finally fluorinated thiophene side chain, which could be due to the varying electron-withdrawing strength of the halogen substituents. The calculated HOMO and LUMO energies are in qualitative agreement with the experimental values derived from CV measurements.

6.6 References

1. C.-N. Ko, G. Li, C.-H. Leung and D.-L. Ma, *Coord. Chem. Rev.*, 2019, **381**, 79-103.
2. B. del Rosal, B. Jia and D. Jaque, *Adv. Funct. Mater.*, 2018, **28**, 1803733.
3. X. Li, S. Kolemen, J. Yoon and E. U. Akkaya, *Adv. Funct. Mater.*, 2017, **27**, 1604053.
4. J. Deckers, T. Cardeynaels, H. Penxten, A. Ethirajan, M. Ameloot, M. Kruk, B. Champagne and W. Maes, *Chemistry*, 2020, DOI: 10.1002/chem.202002549.
5. G. Pirotte, J. Kesters, T. Cardeynaels, P. Verstappen, J. D'Haen, L. Lutsen, B. Champagne, D. Vanderzande and W. Maes, *Macromol. Rapid Commun.*, 2018, **39**, 1800086.
6. K. H. Hendriks, W. Li, G. H. L. Heintges, G. W. P. van Pruissen, M. M. Wienk and R. A. J. Janssen, *J. Am. Chem. Soc.*, 2014, **136**, 11128-11133.
7. F. Lombeck, H. Komber, D. Fazzi, D. Nava, J. Kuhlmann, D. Stegerer, K. Strassel, J. Brandt, A. D. de Zerio Mendaza, C. Müller, W. Thiel, M. Caironi, R. Friend and M. Sommer, *Adv. Energy Mater.*, 2016, **6**, 1601232.
8. L. Lu, T. Zheng, T. Xu, D. Zhao and L. Yu, *Chem. Mater.*, 2015, **27**, 537-543.
9. T. Vangerven, P. Verstappen, J. Drijkoningen, W. Dierckx, S. Himmelberger, A. Salleo, D. Vanderzande, W. Maes and J. V. Manca, *Chem. Mater.*, 2015, **27**, 3726-3732.
10. R. Lenaerts, T. Cardeynaels, I. Sudakov, J. Kesters, P. Verstappen, J. Manca, B. Champagne, L. Lutsen, D. Vanderzande, K. Vandewal, E. Goovaerts and W. Maes, *Sol. Energy Mater. Sol. Cells*, 2019, **196**, 178-184.
11. R. Lenaerts, D. Devisscher, G. Pirotte, S. Gielen, S. Mertens, T. Cardeynaels, B. Champagne, L. Lutsen, D. Vanderzande, P. Adriaensens, P. Verstappen, K. Vandewal and W. Maes, *Dyes Pigm.*, 2020, **181**, 108577.
12. C. S. Kue, S. Y. Ng, S. H. Voon, A. Kamkaew, L. Y. Chung, L. V. Kiew and H. B. Lee, *Photochem. Photobiol. Sci.*, 2018, **17**, 1691-1708.
13. A. Kamkaew, S. H. Lim, H. B. Lee, L. V. Kiew, L. Y. Chung and K. Burgess, *Chem. Soc. Rev.*, 2013, **42**, 77-88.
14. A. Turksoy, D. Yildiz and E. U. Akkaya, *Coord. Chem. Rev.*, 2019, **379**, 47-64.
15. S. G. Awuah and Y. You, *RSC Adv.*, 2012, **2**, 11169-11183.
16. K. Deng, C. Li, S. Huang, B. Xing, D. Jin, Q. Zeng, Z. Hou and J. Lin, *Small*, 2017, **13**, 1702299.
17. R. K. Pandey, *J. Porphyr. Phthalocyanines*, 2000, **04**, 368-373.
18. J. Zhao, K. Xu, W. Yang, Z. Wang and F. Zhong, *Chem. Soc. Rev.*, 2015, **44**, 8904-8939.
19. O. Buyukcakir, O. A. Bozdemir, S. Kolemen, S. Erbas and E. U. Akkaya, *Org. Lett.*, 2009, **11**, 4644-4647.
20. K. Rurack, M. Kollmannsberger and J. Daub, *Angew. Chem. Int. Ed.*, 2001, **40**, 385-387.

21. J. Gibson, A. P. Monkman and T. J. Penfold, *ChemPhysChem*, 2016, **17**, 2956-2961.
22. T. J. Penfold, F. B. Dias and A. P. Monkman, *Chem. Commun.*, 2018, **54**, 3926-3935.
23. T. J. Penfold, E. Gindensperger, C. Daniel and C. M. Marian, *Chem. Rev.*, 2018, **118**, 6975-7025.
24. Y. Hou, X. Zhang, K. Chen, D. Liu, Z. Wang, Q. Liu, J. Zhao and A. Barbon, *J. Mater. Chem. C*, 2019, **7**, 12048-12074.
25. F. Wilkinson, W. P. Helman and A. B. Ross, *J. Phys. Chem. Ref. Data*, 1993, **22**, 113-262.
26. R. W. Redmond and J. N. Gamlin, *Photochem. Photobiol.*, 1999, **70**, 391-475.
27. T. Le Bahers, C. Adamo and I. Ciofini, *J. Chem. Theory Comput.*, 2011, **7**, 2498-2506.
28. A. Nano, R. Ziessel, P. Stachelek, M. A. H. Alamiry and A. Harriman, *ChemPhysChem*, 2014, **15**, 177-186.
29. C. Adachi, *Jpn. J. Appl. Phys.*, 2014, **53**, 060101.
30. M. Chapran, P. Pander, M. Vasylieva, G. Wiosna-Salyga, J. Ulanski, F. B. Dias and P. Data, *ACS Appl. Mater. Interfaces*, 2019, **11**, 13460-13471.
31. A. C. Benniston, G. Copley, H. Lemmetyinen and N. V. Tkachenko, *ChemPhysChem*, 2010, **11**, 1685-1692.
32. N. Mataga, H. Chosrowjan and S. Taniguchi, *J. Photochem. Photobiol. C: Photochem. Rev.*, 2005, **6**, 37-79.
33. Y. Zhao and D. G. Truhlar, *Theor. Chem. Acc.*, 2008, **120**, 215-241.
34. Q. Liu, Y. Jiang, K. Jin, J. Qin, J. Xu, W. Li, J. Xiong, J. Liu, Z. Xiao, K. Sun, S. Yang, X. Zhang and L. Ding, *Sci. Bull.*, 2020, **65**, 272-275.
35. S. Li, L. Ye, W. Zhao, H. Yan, B. Yang, D. Liu, W. Li, H. Ade and J. Hou, *J. Am. Chem. Soc.*, 2018, **140**, 7159-7167.
36. W. Zhao, S. Li, H. Yao, S. Zhang, Y. Zhang, B. Yang and J. Hou, *J. Am. Chem. Soc.*, 2017, **139**, 7148-7151.
37. J. Hou, O. Inganäs, R. H. Friend and F. Gao, *Nat. Mater.*, 2018, **17**, 119-128.
38. C. Yan, S. Barlow, Z. Wang, H. Yan, A. K. Y. Jen, S. R. Marder and X. Zhan, *Nat. Rev. Mater.*, 2018, **3**, 18003.
39. B. Fan, L. Ying, P. Zhu, F. Pan, F. Liu, J. Chen, F. Huang and Y. Cao, *Adv. Mater.*, 2017, **29**, 1703906.
40. Z. Li, L. Ying, P. Zhu, W. Zhong, N. Li, F. Liu, F. Huang and Y. Cao, *Energy Environ. Sci.*, 2019, **12**, 157-163.
41. Z. Li, X. Xu, W. Zhang, X. Meng, Z. Genene, W. Ma, W. Mammo, A. Yartsev, M. R. Andersson, R. A. J. Janssen and E. Wang, *Energy Environ. Sci.*, 2017, **10**, 2212-2221.
42. F. Fernández-Lázaro, N. Zink-Lorre and Á. Sastre-Santos, *J. Mater. Chem. A*, 2016, **4**, 9336-9346.
43. S. Holliday, Y. Li and C. K. Luscombe, *Prog. Polym. Sci.*, 2017, **70**, 34-51.
44. S. Xu, L. Feng, J. Yuan, Z.-G. Zhang, Y. Li, H. Peng and Y. Zou, *ACS Appl. Mater. Interfaces*, 2017, **9**, 18816-18825.
45. S. Xu, X. Wang, L. Feng, Z. He, H. Peng, V. Cimrová, J. Yuan, Z.-G. Zhang, Y. Li and Y. Zou, *J. Mater. Chem. A*, 2018, **6**, 3074-3083.
46. D. Liu, W. Zhao, S. Zhang, L. Ye, Z. Zheng, Y. Cui, Y. Chen and J. Hou, *Macromolecules*, 2015, **48**, 5172-5178.

47. H.-C. Chen, Y.-H. Chen, C.-C. Liu, Y.-C. Chien, S.-W. Chou and P.-T. Chou, *Chem. Mater.*, 2012, **24**, 4766-4772.
48. H. Meng, Y. Li, B. Pang, Y. Li, Y. Xiang, L. Guo, X. Li, C. Zhan and J. Huang, *ACS Appl. Mater. Interfaces*, 2020, **12**, 2733-2742.
49. C.-K. Wang, B.-H. Jiang, J.-H. Lu, M.-T. Cheng, R.-J. Jeng, Y.-W. Lu, C.-P. Chen and K.-T. Wong, *ChemSusChem*, 2020, **13**, 903-913.
50. Y. Cui, H. Yao, J. Zhang, T. Zhang, Y. Wang, L. Hong, K. Xian, B. Xu, S. Zhang, J. Peng, Z. Wei, F. Gao and J. Hou, *Nat. Commun.*, 2019, **10**, 2515.
51. S. J. Jeon, Y. W. Han and D. K. Moon, *Solar RRL*, 2019, **3**, 1900094.
52. H. Zhang, H. Yao, J. Hou, J. Zhu, J. Zhang, W. Li, R. Yu, B. Gao, S. Zhang and J. Hou, *Adv. Mater.*, 2018, **30**, 1800613.
53. S. Zhang, Y. Qin, J. Zhu and J. Hou, *Adv. Mater.*, 2018, **30**, 1800868.
54. Z. Liu, Y. Gao, J. Dong, M. Yang, M. Liu, Y. Zhang, J. Wen, H. Ma, X. Gao, W. Chen and M. Shao, *J. Phys. Chem. Lett.*, 2018, **9**, 6955-6962.
55. X. Xu, Z. Li, J. Wang, B. Lin, W. Ma, Y. Xia, M. R. Andersson, R. A. J. Janssen and E. Wang, *Nano Energy*, 2018, **45**, 368-379.
56. J. W. Jung, J. W. Jo, C.-C. Chueh, F. Liu, W. H. Jo, T. P. Russell and A. K. Y. Jen, *Adv. Mater.*, 2015, **27**, 3310-3317.
57. T. Cardeynaels, S. Paredis, J. Deckers, S. Brebels, D. Vanderzande, W. Maes and B. Champagne, *Phys. Chem. Chem. Phys.*, 2020, **22**, 16387-16399.

Chapter 7

Summary, conclusions and outlook

7.1 Summary

Organic light-emitting diodes (OLEDs) are nowadays part of our everyday life, since they can be found in display applications such as modern television or smartphone screens and in solid-state lighting. OLEDs have become the most successful branch of organic electronics owing to their ability to compete with other technologies such as inorganic LEDs, which is related to their ability to achieve high efficiencies (i.e. the light output versus the power input), high color purity and color tunability. Especially for display applications, their contrast and color gamut are unparalleled.

OLED technology has come a long way since Pope et al. discovered electroluminescence in an anthracene crystal.[1] Several classes of compounds have been used, moving from fluorescent molecules (1st generation OLEDs) to heavy-metal containing organometallic complexes (2nd generation OLEDs) and, ultimately, the use of emitters displaying thermally activated delayed fluorescence (TADF, 3rd generation OLEDs). The 1st generation fluorescent emitters suffered from rather low device efficiencies as the triplet state acts as a loss pathway for 75% of the excitons formed in a charge recombination process. Heavy-metal organometallic complexes allowed to overcome this issue by using the triplet state as the main radiative pathway. This emission, known as phosphorescence, enabled up to 100% exciton conversion as the heavy-metal complexes possess significant spin-orbit coupling (SOC) for the remaining 25% singlet excitons to cross over to the triplet state via intersystem crossing (ISC). These phosphorescent emitters make up most of the current commercial OLEDs.

However, the use of heavy-metal atoms, which are scarce and expensive, is discouraged by the ongoing search for a more sustainable and eco-friendly society. Here, TADF emitters might provide an answer. By tuning of the molecular structure of donor-acceptor type compounds, the singlet and triplet excited state energy levels can be brought close enough for reverse intersystem crossing (rISC) to occur. The remaining energy barrier can be overcome by thermal energy and the main emission pathway is fluorescence. Due to the thermally activated rISC, the secondary emission is delayed with a lifetime in between that of the prompt fluorescence and phosphorescence for organic compounds.

Nowadays, the main focus of OLED research, is on the emissive material, as many advances have already been made for the other parts of the OLED device stack and these are generally applicable to all generations. Most attention has been given to blue emitters as these are the most difficult material to obtain due to stability issues. Investigations on red emitters have lagged behind. However, an increasing interest for the red and near-infrared (NIR) range of the electromagnetic spectrum is apparent in recent literature.

In this PhD thesis, the main goal was to expand on the known pool of donor and acceptor moieties that can be used to construct D-A and D-A-D type emissive materials for 3rd generation OLEDs. To achieve this, different fields of organic electronics, most notably the field of organic photovoltaics (OPV), served as an inspiration for new building blocks that have not been applied before in the field of OLEDs. The use of quantum chemistry methods such as density functional theory (DFT) allowed me to rationally design new emitters based on the findings from the calculations.

The second chapter therefore dealt with the quest to find the optimal exchange-correlation functional (XCF), a crucial part of the DFT calculations as it determines the accuracy of the obtained properties to a large extent. A series of 10 prototypical donor-acceptor compounds were subjected to thorough investigation with DFT and time-dependent DFT (TDDFT) and their excited state properties such as the excitation energies and oscillator strengths were calculated using 19 different XCFs with various levels of complexity. These values were benchmarked against a high level wavefunction method called resolution-of-the-identity second order approximation coupled-cluster (riCC2).

While some XCFs performed well for the singlet-triplet energy splitting, the individual singlet and triplet energies were highly over- or underestimated, rendering these functionals untrustworthy. Finally, we opted for range-separated XCFs, which include a given percentage of exact Hartree-Fock (HF) exchange that increases with the interelectronic distance. Proper tuning of the range-separating parameter (ω) leads to a correct balance between a small amount of HF exchange at small distances and a large amount of HF exchange at large distances and gave the best results. The most notable functionals were LC-BLYP and LC-ωPBE with a value for ω of 0.17 $bohr^{-1}$. Additionally, a so-called global hybrid XCF M06-2X, with a fixed percentage of HF exchange of 54% at all distances, gave comparable results. Application of the Tamm-Dancoff approximation (often used to overcome triplet instabilities) was found to improve the error on the triplet excitation energies with respect to those obtained using riCC2, and resulted in even smaller errors for the singlet-triplet energy splittings.

With the best-performing XCF, I engaged in the design of novel TADF emitters. Benzo[1,2-*b*:4,5-*b*']dithiophene (BDT) is a well-known donor unit in organic photovoltaics as it possesses a high electron-donating strength, high planarity and often affords a high charge carrier mobility. Unfortunately, conventional coupling via the α-positions would lead to planar D-A molecules, not-likely to show TADF properties. As such, a synthetic pathway to couple the donor and acceptor units via the benzene core of the BDT had to be developed. In chapter 3, the BDT unit was coupled to 2 different acceptors: 9,9-dimethyl-9*H*-thioxanthene-10,10-dioxide (TXO2) and dibenzo[*a*,*c*]phenazine-11,12-dicarbonitrile (CNQxP). Moreover, to compare their properties, two 9,9-dimethyl-9,10-dihydroacridine (DMAC) analogues were designed, which previously showed TADF behavior. Although the TDDFT calculations predicted a rather large gap for the novel BDT compounds, the large HOMO/LUMO separation seemed promising and the compounds were synthesized in order to investigate their photophysical properties. Photophysical characterization in zeonex films showed prompt and delayed emission for all 4 compounds. However, their nature differed. The DMAC-containing compounds showed TADF, whereas the BDT-based compounds showed room temperature phosphorescence (RTP) when TXO2 was chosen as the acceptor and TADF when CNQxP was

chosen as the acceptor. The RTP behavior of **TXO2-BDT-TIPS** is unusual and was attributed to the presence of multiple sulfur atoms in the BDT unit. Therefore, we investigated the BDT-TIPS donor unit by itself and found similar RTP behavior in zeonex film. **CNQxP-BDT-TIPS** and **CNQxP-DMAC** showed long-lived TADF with some triplet-triplet annihilation (TTA) at very long emission times. The main difference between **TXO2-BDT-TIPS** and **CNQxP-BDT-TIPS** is the acceptor strength. While the localized triplet state of the BDT-TIPS group, responsible for the phosphorescent behavior, is below the CT states for **TXO2-BDT-TIPS**, this is not the case for **CNQxP-BDT-TIPS**. The smaller experimental singlet-triplet energy splitting also resulted in the possibility of rISC to occur for **CNQxP-BDT-TIPS**, whereas this is not possible for **TXO2-BDT-TIPS**.

In Chapter 4, the difluorodithieno[3,2-*a*:2',3'-*c*]phenazine (DTPz) scaffold, again known from the OPV field, was used as an acceptor unit to construct (TADF) emissive materials. DTPz possesses a significant electron-accepting strength allowing the development of red-emitting materials. Two donor materials, BDT-TIPs (introduced in chapter 3) and DMAC, were coupled to the DTPz acceptor, resulting in D-A type compounds with CT emission. The calculated singlet-triplet energy splitting was small for **DTPz-DMAC** (0.03 eV), whereas for **DTPz-BDT-TIPS** (0.43 eV) it was of the same order as for **CNQxP-BDT-TIPS** (chapter 3). Time-resolved emission decays in zeonex film revealed a different behavior for the DMAC and BDT-TIPS containing compounds. While **DTPz-DMAC** showed TADF behavior with long-lived emission and a peak maximum around 630 nm, **DTPz-BDT-TIPS** showed RTP behavior with an onset similar to the phosphorescence of **DTPz-DMAC**. This suggests emission from the DTPz core instead of the BDT-TIPS unit, as found in chapter 3. Subsequent analysis of DTPz in zeonex showed that DTPz by itself indeed shows similar RTP behavior.

One of the most well-known TADF emitter materials, is **4CzIPN**, originally reported by Adachi and coworkers.[2] It was further studied by Etherington *et al.*[3] and was found to show extensive dimer formation in doped OLED films. Dimer emission is undesired in OLED devices as it compromises the color purity. The dimers are formed by interactions between the carbazole units of the **4CzIPN** molecules. To overcome these interactions, 4*H*-dithieno[3,2-*b*:2',3'-*d*]pyrrole (DTP) was chosen as the donor unit to replace 9*H*-carbazole in chapter 5. DTP is

a well-known donor unit in the field of OPV, where it is typically coupled via the α-positions and the central nitrogen atom is alkylated for improved solubility of the resulting polymers. Synthesis via a carbamate intermediate allows the free-base DTP to be obtained after which it can be used in nucleophilic aromatic substitution or Buchwald-Hartwig type reactions. The former was applied in this thesis to construct **4DTP-IPN**, using similar reaction conditions as for the synthesis of **4CzIPN**. **4DTP-IPN** showed red-shifted emission with respect to that of **4CzIPN** and exhibited TADF properties in a variety of films. Due to the very small theoretical and experimental singlet-triplet splittings, it was difficult to distinguish between its delayed emission and phosphorescence, even at 80 K. While its aggregation behavior is certainly different to that of **4CzIPN**, the photophysics of **4DTP-IPN** at various concentrations in solution and thin film give rise to contradicting observations and further experiments are needed to solidify whether it is less likely or rather more likely to form dimers.

In the final chapter (Chapter 6), four additional publications were discussed in which quantum-chemical calculations were applied to gain insights into the experimental properties of small molecule or polymeric compounds. The first publication dealt with the design of boron dipyrromethene (BODIPY) photosensitizers, developed to efficiently form singlet oxygen for photodynamic therapy. (TD)DFT calculations lead to insights in the photophysics of the BODIPY dyes and indirectly pointed toward the presence of exciplex emission, which was confirmed experimentally. The incorporation of a DMAC unit was found to be crucial for the singlet oxygen generation and the exciplex formation and the latter is expected to be responsible for the efficient ISC. The remaining publications all dealt with structure-property relationships in which oligomeric species were used to mimic the behavior of polymer chains. By looking at their optimized geometries, we were able to explain the interplay between the electronic properties and molecular orbital delocalizations in series of similar polymers.

7.2 Conclusions and outlook

In this thesis, the strengths, weaknesses and possibilities of quantum-chemical calculations, specifically using density functional theory, have been discussed. It has presented an enormous advantage for the design of novel TADF materials as

screening of large numbers of potentially interesting compounds is possible in a limited timeframe. Furthermore, the same principles used to study TADF emitters can readily be expanded to other fields employing organic chromophores, as was illustrated for the BODIPY photosensitizers in Chapter 6. By simplifying polymer structures to more accessible oligomers, DFT calculations have also helped to establish structure-property relationships. While the calculation of other properties such as spin-orbit coupling (SOC) is accessible by (TD)DFT, their use in TADF has not been demonstrated to a large extent. Additionally, SOC alone is not always sufficient to explain the observed TADF properties, as discussed in the introduction of this thesis when exploring the spin-vibronic mechanism of TADF. Such spin-vibronic calculations are more time-consuming and more difficult to perform on a screening basis.

The results from Chapter 2 show that a good estimate for the first singlet and triplet excitation energies can be obtained given the correct choice of the exchange-correlation functional (XCF). Despite several publications stressing the use of modified range-separated XCFs, the majority of literature relies on the use of regular hybrid XCFs (such as B3LYP) or non-optimal range-separated XCFs (such as CAM-B3LYP). In this thesis, we have shown the ability to correctly predict the behavior of a variety of real, TADF-targeted D-A compounds and we strongly encourage others to do the same.

In Chapters 3, 4 and 5, the successful development of novel emitters using building blocks from the field of organic photovoltaics was shown. Although not all compounds showed TADF, their properties are interesting from a fundamental point of view. With a focus on red-emitting materials, **CNQxP-BDT-TIPS**, **DTPz-DMAC** and **4DTP-IPN** all show orange to red emission. The implementation of BDT-TIPS as a new donor unit and DTPz as a new acceptor unit lead to a mixture of TADF and room temperature phosphorescence (RTP), depending on the donor/acceptor used. This was attributed to the presence of sulfur atoms, affording a larger amount of SOC than the usual carbon and nitrogen atoms. However, **TXO2-DMAC**, also containing a sulfur atom, does not show the same RTP behavior. It is therefore interesting to further investigate the effects that sulfur atoms can have on the emissive properties of TADF emitters, as well as the effects on ISC in other fields such as photodynamic therapy.

Although several TADF emitters were synthesized and their photophysics was investigated via time-resolved fluorescence, the delayed emission was rather long-lived. This is indicative that, although our approach was successful, there is still room for progress. Additionally, it also shows that simply designing a molecule on paper, and having promising calculated ground and excited state properties, is not a guarantee for success. This is one of the reasons why the TADF community is still continuously looking for new emitter materials. What we have not been able to verify in this work are the electroluminescence properties when incorporating our newly designed emitters in OLED devices. Here, thermal deposition of the doped films can lead to slight alterations in the emitter photophysics as different host materials from the herein employed zeonex host are being used. The most important device characteristic ultimately is the external quantum efficiency (EQE). Even though a high photoluminescence quantum yield (PLQY) and a high rate of rISC are prerequisites for efficient TADF, there is no guarantee that an emitter will show a high EQE when incorporated into an OLED device and as such this largely remains a trial and error approach. With the large number of TADF emitters known in literature, the next steps toward the development of highly efficient and commercially viable TADF OLEDs will be optimization of the device physics and stability. While device stability is still an issue, new types of emitting materials might be able to overcome this. Furthermore, knowledge of the degradation pathways for these devices could lead to new insights to design more stable architectures. Another major factor limiting device performance is the light outcoupling efficiency of OLED devices. Here, roughly 75% of all the photons emitted in the active layer are lost through the formation of surface plasmon polarons on the metal-electrode interface or total internal reflection owing to the refractive index mismatch between the various layers in the OLED stack.[4] This is mainly related to the random orientation of the transition dipoles of all the emitter molecules in the active layer, leading to light emission in all directions. Fixed orientation of the transition dipole, preferably parallel to the layer orientation, could significantly improve light outcoupling efficiencies and this is likely influential in some of the best performing OLED devices reported in literature.

Alternatively, development of TADF emitters for other applications such as time-resolved bio-imaging is an interesting cross-pollination from which both fields

can profit. While TADF emitters are generally not water soluble, several encapsulating strategies are known in literature and they have already been applied to the field of TADF imaging. Something that has not been investigated (to the best of my knowledge) is a phototherapeutic agent, such as the BODIPYs from Chapter 6, which has both TADF properties (which renders it suitable for time-resolved imaging) and the ability to generate singlet-oxygen. Computationally guided design could make this a reality and possibly some of the emitters presented in this thesis could exhibit the desired properties.

Despite the large amount of reports appearing in TADF literature, major breakthroughs have not been reported over the last years. As the field is maturing, the number of new TADF emitters will likely keep on expanding and it is only a matter of time until the next major breakthrough occurs. The most significant advances can maybe be made in the field of near-infrared (NIR) OLEDs, which has attracted only minor attention until recently.[5, 6] With potential applications in biological and biomedical fields, but also in telecommunication and security, there is enough motivation to explore this region of the electromagnetic spectrum. The task at hand is certainly not easy since, with increasingly red-shifted emission, the PLQY drops as a result of the energy gap law. Furthermore, detection of NIR wavelengths reaches beyond the specifications of traditional photoluminescence setups, often requiring the acquisition of new instruments. Another major breakthrough might come from a field where a combination of TADF and regular fluorescence emitters is utilized. Introduced by Adachi and coworkers in 2014,[7] this method relies on charge-recombination and ISC by a TADF emitter, after which electron transfer occurs to a regular fluorescent emitter. Doping of a small percentage of the fluorescent emitter is sufficient to dominate the emission if the energy transfer is efficient. This method has the ability to combine the best of TADF and fluorescent emitters as the TADF emitters provide up to 100% singlet excitons, while the fluorescent emitters provide a high radiative rate with minimal non-radiative losses and a narrow emission, leading to a high color purity. However, the addition of a second emissive material adds a whole new set of constraints to the design of these types of OLED devices as the efficient energy transfer between the TADF molecule and the fluorescent emitter becomes another factor to take into account.

Nonetheless, I believe the future for OLEDs is a bright one and more breakthroughs will follow in the coming years in this highly interesting and continuously evolving field.

7.3 Nederlandstalige samenvatting

Organische licht-emitterende dioden (OLEDs) hebben zich verankerd in ons dagelijks leven, waar we ze aantreffen in beeldschermen van moderne flatscreentelevisies en smartphones, maar ook in meer traditionele verlichting. Organische LEDs hebben zich ontwikkeld tot de meest succesvolle tak van de organische elektronica dankzij hun competitiviteit met alternatieve technologieën. OLEDs combineren immers een hoge efficiëntie (d.w.z. de lichtoutput versus de energie-input) met een goede zuiverheid en afstembaarheid van de kleur. Voor beeldschermen zijn het contrast en het kleurbereik ongeëvenaard.

De OLED-technologie heeft reeds een lange weg afgelegd sinds Pope *et al.* elektroluminescentie ontdekten in een antraceenkristal.[1] Verschillende klassen van organische verbindingen zijn sindsdien onderzocht, gaande van fluorescente moleculen (1ste generatie OLEDs) tot organometaalcomplexen (2de generatie OLEDs) en tenslotte materialen die thermisch geactiveerde uitgestelde fluorescentie (TADF) vertonen (3de generatie OLEDs). De 1ste generatie fluorescente OLED emitters waren beperkt in efficiëntie ten gevolge van de 25/75%-verdeling van singlet- en triplet-excitons die gevormd worden na elektrische excitatie, waarvan enkel de singlet-excitons radiatief verval vertonen. Organometaalcomplexen laten radiatief verval vanuit de triplettoestand toe door gebruik te maken van spin-orbitaal-koppeling (SOC). Deze tripletemissie, beter gekend als fosforescentie, maakt het mogelijk om 100% van de gevormde excitons te benutten voor emissie aangezien dezelfde SOC het ook mogelijk maakt om de 25% resterende singlet-excitons om te zetten naar de triplettoestand via intersysteemkruising (ISC). De huidige commerciële OLED-materialen komen grotendeels uit deze klasse van fosforescente emitters. Desalniettemin wordt het gebruik van 'zware' metalen, die tevens ook schaars en duur zijn, ontmoedigd omdat ze minder duurzaam zijn. TADF-emitters bieden hiervoor een oplossing. Door het nauwkeurig afstemmen van de moleculaire structuur van donor-acceptor (D-A) organische

verbindingen, kunnen de singlet- en triplet-energieniveaus dicht bij elkaar gebracht worden. Wanneer dit gebeurt, kan de resterende energiebarrière overwonnen worden door thermische energie en worden de 75% triplet-excitons omgezet naar de singlettoestand via omgekeerde intersysteemkruising (riSC), gevolgd door fluorescentie. Omdat deze overgang een relatief lange levensduur heeft, is ook de resulterende fluorescentie van deze excitons vertraagd in de tijd. De levensduur van vertraagde fluorescentie bevindt zich dan ook tussen die van de onmiddellijke fluorescentie en fosforescentie in.

Tegenwoordig ligt de focus van het OLED-onderzoek sterk op het emitterend materiaal aangezien er al veel vooruitgang is geboekt in de andere (technische) aspecten van OLEDs en deze vaak toepasbaar zijn op alle generaties van OLED-materialen. De meeste aandacht is uitgegaan naar het ontwerp van materialen die blauw licht uitzenden, omdat deze vaak onderhevig zijn aan stabiliteitsproblemen. Aan de andere kant van het zichtbaar spectrum blijken rode emitters echter ondervertegenwoordigd, hoewel er een toenemende interesse is in de wetenschappelijke literatuur voor rood- en nabij infrarood-emitterende materialen.

Het hoofddoel van deze doctoraatsthesis was om de gekende verzameling van donor- en acceptoreenheden voor TADF-emitters uit te breiden op basis van inzichten uit andere subdomeinen van de organische elektronica, met name organische zonnecellen (OPVs), door enkele van de daar gekende bouwstenen toe te passen in TADF-materialen. Kwantumchemische methoden zoals *density functional theory* (DFT) werden toegepast om op rationele wijze nieuwe moleculen te ontwerpen en ze te onderwerpen aan een computationele pre-screening.

Het tweede hoofdstuk van deze thesis omvat daarom de zoektocht naar de optimale *exchange-correlation functional* (XCF), die een cruciale rol speelt in het accuraat bepalen van de eigenschappen van organische moleculen in de aangeslagen toestand. Een reeks van 10 prototype D-A-verbindingen werd onderworpen aan een grondige analyse via DFT en tijdsafhankelijke DFT (TDDFT) om hun eigenschappen in de aangeslagen toestand te bepalen met 19 verschillende XCFs. Deze waarden werden dan vergeleken met waarden voor dezelfde eigenschappen bekomen via een golffunctiemethode genaamd "resolutie-van-de-identiteit tweede orde benadering van de gekoppelde cluster"

(riCC2). Daar waar sommige XCFs goede resultaten gaven voor het singlet-triplet energieverschil (ΔE_{ST}), bleken deze de individuele singlet- en tripletenergieën niet accuraat te voorspellen, waardoor de desbetreffende XCFs niet betrouwbaar zijn voor het screenen van onbekende moleculen. Uiteindelijk werd er gekozen voor XCFs met een gescheiden bereik van het percentage Hartree-Fock (HF) uitwisseling, d.w.z. de "range-separated XCFs", waarbij de HF-uitwisseling toeneemt met toenemende interelektronische afstand. Gepaste optimalisatie van de bereik-scheidende parameter (ω) zorgt voor een goede balans tussen de hoeveelheid HF-uitwisseling bij kleine en grote interelektronische afstanden en leidt tot de beste resultaten in vergelijking met de riCC2 methode. De meest performante XCFs waren LC-BLYP en LC-ωPBE, met een waarde voor ω van 0.17 $bohr^{-1}$. Bovendien gaf een globale hybride XCF, genaamd M06-2X, met een vast percentage HF-uitwisseling van 54% op alle interelektronische afstanden, vergelijkbare resultaten met deze van de range-separated XCFs. Toepassen van de Tamm-Dancoff-benadering voor TDDFT (die vaak gebruikt wordt om het triplet-instabiliteitsprobleem aan te pakken) gaf een verbetering van de fout op de triplet-excitatie-energieën ten opzichte van de riCC2-waarden, alsook in de fout op ΔE_{ST} voor de verschillende verbindingen.

Met de meeste performante functionaal op zak ben ik dan op zoek gegaan naar nieuwe ontwerpen voor D-A-D-moleculen die TADF kunnen vertonen. Benzo[1,2-*b*:4,5-*b*']dithiofeen (BDT) is een gekende vlakke, elektronenrijke bouwsteen die vaak gebruikt wordt in OPV-materialen, waarbij over het algemeen een hoge mobiliteit voor ladingdragers bereikt kan worden. Helaas zou conventionele koppeling van de BDT-eenheid via de α-posities van de thiofeeneenheden leiden tot vlakke D-A-verbindingen die meer dan waarschijnlijk geen TADF vertonen. Zodoende werd er een alternatief synthesepad ontwikkeld om de donor- en acceptoreenheden te koppelen via de benzeenkern van de BDT-eenheid. In hoofdstuk 3 werd de BDT-eenheid gekoppeld aan twee verschillende acceptoren, met name 9,9-dimethyl-9*H*-thioxantheen-10,10-dioxide (TXO2) en dibenzo[*a*,*c*]fenazine-11,12-dicarbonitrile (CNQxP). Om hun eigenschappen te kunnen vergelijken werden eveneens twee 9,9-dimethyl-9,10-dihydroacridine (DMAC) analoga gesynthetiseerd, waarvan de TADF-eigenschappen al gekend waren. Hoewel de TDDFT-berekeningen een relatief grote ΔE_{ST} voorspelden, werd op basis van de relatief goede scheiding van de HOMO- en LUMO-orbitalen

besloten om deze verbindingen toch aan te maken en hun fotofysische eigenschappen te bestuderen. De tijdsafhankelijke emissie in een zeonexfilm vertoonde zowel onmiddellijke als vertraagde fluorescentie voor alle 4 de verbindingen. De aard van de emissie verschilde echter. Daar waar de DMAC-verbindingen TADF-eigenschappen vertoonden, gaven de BDT-gebaseerde verbindingen fosforescentie bij kamertemperatuur (RTP) wanneer TXO2 als acceptor gebruikt werd en TADF voor CNQxP als acceptor. De RTP-eigenschappen van **TXO2-BDT-TIPS** zijn ongebruikelijk en werden toegeschreven aan de aanwezigheid van meerdere zwavelatomen in de BDT-eenheid. De BDT-TIPS-precursor werd daarop zelf onderzocht en bleek eveneens RTP te vertonen in film. **CNQxP-BDT-TIPS** en **CNQxP-DMAC** gaven langlevende TADF, met een kleine bijdrage van triplet-triplet annihilatie (TTA) bij zeer lang tijden. Het grote verschil tussen **TXO2-BDT-TIPS** en **CNQxP-BDT-TIPS** bevindt zich in de sterkte van de elektronenaccepterende eenheid. Daar waar de gelokaliseerde triplettoestand van BDT-TIPS, verantwoordelijk voor de RTP-eigenschappen, zich beneden de charge-transfer (CT) toestanden van **TXO2-BDT-TIPS** bevindt, is dit niet het geval voor **CNQxP-BDT-TIPS**. De kleinere experimentele ΔE_{ST} resulteert ook in de mogelijkheid om omgekeerde intersysteemkruising te krijgen voor **CNQxP-BDT-TIPS**, terwijl dit niet mogelijk is voor **TXO2-BDT-TIPS**.

In hoofdstuk 4 werd dan difluordithiëno[3,2-*a*:2',3'-*c*]fenazine (DTPz), opnieuw geïnspireerd door het OPV-veld, geïntroduceerd als een alternatieve acceptoreenheid om materialen met TADF-eigenschappen te ontwerpen. DTPz bezit een significant elektronenacceptor-karakter dat toelaat om rode fluoroforen te ontwikkelen. Twee donormaterialen, BDT-TIPS (reeds geïntroduceerd in hoofdstuk 3) en DMAC, werden gekoppeld aan de DTPz-acceptor, resulterend in D-A-D-verbindingen met CT-emissie. De berekende ΔE_{ST} was klein voor **DTPz-DMAC** (0.03 eV), terwijl deze voor **DTPz-BDT-TIPS** (0.43 eV) van dezelfde grootte-orde was als voor **CNQxP-BDT-TIPS** (uit hoofdstuk 3). Tijdsafhankelijke emissiemetingen in zeonex onthulden opnieuw een verschillend gedrag voor de DMAC- en BDT-TIPS-bevattende materialen. **DTPz-DMAC** vertoonde TADF, met een maximum bij 630 nm en een lange levensduur, terwijl **DTPz-BDT-TIPS** RTP vertoonde, met een energie gelijkaardig aan de fosforescentie van **DTPz-DMAC**. Dit suggereert dat de RTP-eigenschappen van

DTPz-BDT-TIPS niet afkomstig zijn van de BDT-TIPS-eenheid, maar van de DTPz-eenheid. Analyse van de DTPz-bouwsteen in zeonex onthulde ook RTP-eigenschappen voor deze acceptoreenheid.

Eén van de meest bestudeerde TADF-moleculen, **4CzIPN**, voor het eerst gepubliceerd door Adachi *et al.*,[2] werd verder in detail bestudeerd door Etherington *et al.*[3] nadat er een bathochrome verschuiving van de emissie werd vastgesteld in gedopeerde films met een toenemende concentratie van de emitter. Zij achterhaalden dat dimeer-emissie aan de basis lag van de bathochrome verschuiving in de gedopeerde OLEDs. Dimeer-emissie is echter ongewenst aangezien het de zuiverheid van de emissiekleur vermindert. De dimeren worden gevormd door niet-covalente interacties tussen de carbazooleenheden (Cz) van de verschillende **4CzIPN**-moleculen. Om deze interacties te vermijden werd in hoofdstuk 5 4*H*-dithiëno[3,2-*b*:2',3'-*d*]pyrrool (DTP) gekozen ter vervanging van 9*H*-carbazool. DTP is een gekende donorbouwsteen in het OPV-domein, waar het vaak gekoppeld wordt via de α-posities van de thiofeeneenheden en het centrale stikstofatoom gealkyleerd wordt om de oplosbaarheid te verbeteren. Synthese van DTP via een carbamaat-intermediair laat toe om het 'vrije-base' DTP te bekomen dat vervolgens via nucleofiele aromatische substitutie of Buchwald-Hartwig-koppeling aan een acceptoreenheid gehecht kan worden. **4DTP-IPN** werd in ons geval via nucleofiele aromatische substitutie bekomen, op basis van gelijkaardige omstandigheden als voor de synthese van **4CzIPN**. **4DTP-IPN** vertoonde een rood-verschoven emissie ten opzichte van **4CzIPN** en eveneens TADF in verschillende gedopeerde films. Door de zeer kleine theoretische en experimentele ΔE_{ST} bleek het moeilijk om onderscheid te maken tussen de vertraagde emissie en fosforescentie, zelfs bij 80 K. Het aggregatiegedrag van **4DTP-IPN** is zeker verschillend met dat van **4CzIPN**, maar de fotofysische metingen geven geen uitsluitsel of het nu meer of minder dimeervorming geeft en verdere experimenten zijn nodig om dit met zekerheid vast te stellen.

In het laatste hoofdstuk werden 4 bijkomende publicaties besproken waarin quantumchemische berekeningen toegepast werden om inzichten te verwerven in de experimentele eigenschappen van kleine moleculen of polymeren. De eerste publicatie ging over het ontwerp van boor-dipyrrometheen (BODIPY) fotosensibilisatoren, ontworpen voor fotodynamische therapie. (TD)DFT-

berekeningen gaven inzicht in de fotofysische eigenschappen van de BODIPY-moleculen en wezen indirect op de aanwezigheid van exciplex-emissie, die nadien ook experimenteel bevestigd kon worden. De aanwezigheid van de DMAC-eenheden in de BODIPY-chromoforen bleek essentieel voor de vorming van singletzuurstof en de exciplexvorming, die verwacht wordt verantwoordelijk te zijn voor de goede intersysteemkruising. De overige drie publicaties handelden allemaal over structuur-eigenschapsrelaties waarin oligomere verbindingen gebruikt werden om de eigenschappen van polymere materialen voor organische zonnecellen na te bootsen. Door de geoptimaliseerde structuren te analyseren, waren we in staat om de wisselwerking tussen de elektronische eigenschappen en de moleculaire orbitaal-delokalisaties te verklaren in specifieke reeksen van gelijkaardige polymeren.

7.4 Résumé en français

Les diodes électroluminescentes organiques (OLEDs) font aujourd'hui partie de notre vie quotidienne, puisqu'elles se retrouvent dans des applications d'affichage telles que les écrans de télévision ou de smartphone modernes et dans l'éclairage à semi-conducteurs. Les OLEDs constituent la branche la plus aboutie de l'électronique organique en raison de leur capacité à concurrencer d'autres technologies telles que les LEDs inorganiques, ce qui est lié à leur capacité à atteindre des rendements élevés (c'est-à-dire le rendement lumineux par rapport à la puissance absorbée), ainsi qu'à des pureté et accordabilité de couleurs élevées. Surtout pour les applications d'affichage, leur contraste et leur gamme de couleurs sont inégalés.

La technologie OLED a parcouru un long chemin depuis que Pope et collaborateurs ont découvert l'électroluminescence dans un cristal d'anthracène.[1] Plusieurs classes de composés ont été utilisées, passant des molécules fluorescentes (OLEDs de 1ère génération) aux complexes organométalliques contenant des métaux lourds (OLEDs de 2e génération) et, finalement, l'utilisation d'émetteurs affichant une fluorescence retardée activée thermiquement (TADF, OLEDs de 3e génération). Les émetteurs fluorescents de 1ère génération ont le désavantage de présenter une faible efficacité du dispositif car les états triplet agissent comme des voies sans issue pour 75% des excitons formés dans un processus de recombinaison de charge. Les complexes

organométalliques de métaux lourds ont permis de surmonter ce problème en utilisant l'état du triplet comme voie radiative principale. Cette émission, connue sous le nom de phosphorescence, a permis la conversion de jusqu'à 100% des excitons car les complexes de métaux lourds possèdent un couplage spin-orbite (SOC) significatif de sorte que les 25% d'excitons singulets restants passent à l'état triplet via le croisement intersystème (ISC). Ces émetteurs phosphorescents constituent la plupart des OLEDs commerciales actuelles. Cependant, l'utilisation d'atomes de métaux lourds, rares et coûteux, est découragée par la recherche permanente d'une société plus durable et plus respectueuse de l'environnement. Ici, les émetteurs TADF pourraient apporter une réponse. En accordant la structure moléculaire des composés de type donneur-accepteur, les niveaux d'énergie des états excités singulet et triplet peuvent être suffisamment proches pour que le croisement intersystème inverse (rISC) se produise. La barrière énergétique restante peut être surmontée par l'énergie thermique et la principale voie d'émission est la fluorescence. En raison du rISC activé thermiquement, pour les composés organiques, l'émission secondaire est retardée d'une durée de vie entre celle de la fluorescence rapide et de la phosphorescence.

De nos jours, l'objectif principal de la recherche sur les OLEDs est le matériau émissif, car de nombreuses avancées ont déjà été faites pour les autres composantes et celles-ci sont généralement applicables à toutes les générations. La plus grande attention a été accordée aux émetteurs bleus car ce sont les matériaux les plus difficiles à obtenir en raison de problèmes de stabilité. Au contraire, les investigations sur les émetteurs rouges sont à la traîne. Cependant, un intérêt croissant pour la gamme rouge et proche infrarouge (NIR) du spectre électromagnétique est apparent (apparu ?) dans la littérature récente.

Dans cette thèse de doctorat, l'objectif principal était d'élargir le pool connu des fragments donneurs et accepteurs qui peuvent être utilisés pour construire des matériaux émissifs de type D-A et D-A-D pour les OLED de 3ème génération. Pour y parvenir, différents domaines de l'électronique organique, notamment le domaine du photovoltaïque organique (OPV), ont inspiré la sélection de nouveaux blocs de construction qui n'avaient pas été utilisés auparavant dans le domaine des OLEDs. L'utilisation de méthodes de chimie quantique telles que la

théorie de la fonctionnelle de la densité (DFT) m'a permis de concevoir de manière rationnelle de nouveaux émetteurs sur la base des résultats des calculs. Le deuxième chapitre a donc traité de la recherche d'une fonctionnelle d'échange-corrélation (XCF) optimale, une partie cruciale des calculs DFT car elle détermine dans une large mesure la précision des propriétés obtenues. Une série de 10 composés prototypes donneurs-accepteurs ont été soumis à une investigation approfondie avec la DFT et la DFT dépendante du temps (TDDFT) et leurs propriétés d'état excité telles que les énergies d'excitation et les forces d'oscillateur ont été calculées en utilisant 19 XCF différentes avec des niveaux de complexité croissante. Ces valeurs ont été comparées à une méthode de fonction d'onde de haut niveau appelée méthode des agrégats couplés (coupled cluster) approximée au deuxième ordre et recourant à la résolution de l'identité (riCC2). Alors que certaines XCF se comportent bien pour estimer les différences entre les énergies singulet et triplet, les énergies individuelles singulet et triplet étaient fortement sur- ou sous-estimées, rendant ces fonctionnelles peu fiables. Enfin, nous avons opté pour des XCF à séparation de portée, qui incluent un pourcentage d'échange exact Hartree-Fock (HF) augmentant avec la distance interélectronique. Un réglage correct du paramètre de séparation de distance (ω) conduit à un équilibre correct entre une petite quantité d'échange HF à de petites distances et une grande quantité d'échange HF à de grandes distances et a donné les meilleurs résultats. Les fonctionnelles les plus notables étaient LC-BLYP et LC-ωPBE avec une valeur pour ω de 0,17 $bohr^{-1}$. En outre, une fonctionnelle hybride globale (M06-2X), avec un pourcentage fixe d'échange HF de 54% à toutes les distances, a donné des résultats comparables. L'application de l'approximation de Tamm-Dancoff (souvent utilisée pour surmonter les instabilités de type triplet) s'est avérée réduire l'erreur sur les énergies d'excitation des triplets par rapport à celles obtenues en utilisant riCC2, et a entraîné des erreurs encore plus petites pour les différences d'énergie singulet-triplet.

Avec la XCF la plus performante, je me suis engagé dans la conception de nouveaux émetteurs TADF. Le benzo[1,2-*b*:4,5-*b*']dithiophène (BDT) est une unité donneuse bien connue dans le domaine du photovoltaïque organique car il possède une force donneur d'électrons élevée, une planarité élevée et offre souvent une mobilité élevée des porteurs de charge. Malheureusement, un

couplage conventionnel via les positions α conduirait à des molécules D-A planaires, peu susceptibles de présenter des propriétés TADF. En tant que tel, une voie synthétique pour coupler les unités donneur et accepteur via le noyau benzénique du BDT a dû être développée. Dans le chapitre 3, l'unité BDT a été couplée à 2 accepteurs différents: le 9,9-diméthyl-9*H*-thioxanthène-10,10-dioxyde (TXO2) et le dibenzo[*a*,*c*]phénazine-11,12-dicarbonitrile (CNQxP). De plus, pour comparer leurs propriétés, deux analogues de la 9,9-diméthyl-9,10-dihydroacridine (DMAC) ont été conçus, car ils étaient connus pour présenter un comportement TADF. Bien que les calculs TDDFT prédisent un écart assez important pour les nouveaux composés BDT, la grande séparation spatiale HOMO / LUMO semble prometteuse et les composés ont été synthétisés afin d'étudier leurs propriétés photophysiques. La caractérisation photophysique des films zeonex a montré une émission rapide et retardée pour les 4 composés. Cependant, leur nature diffère. Les composés contenant du DMAC présentaient du TADF, tandis que les composés à base de BDT présentaient une phosphorescence à température ambiante (RTP) lorsque TXO2 était choisi comme accepteur et TADF lorsque CNQxP était choisi comme accepteur. Le comportement RTP du **TXO2-BDT-TIPS** est inhabituel et a été attribué à la présence de plusieurs atomes de soufre dans l'unité BDT. Par conséquent, nous avons étudié l'unité donneuse BDT-TIPS seule et avons trouvé un comportement RTP similaire dans le film zeonex. **CNQxP-BDT-TIPS** et **CNQxP-DMAC** ont montré un TADF à longue durée de vie avec une certaine contribution d'annihilation triplet-triplet (TTA) à des temps d'émission très longs. La principale différence entre **TXO2-BDT-TIPS** et **CNQxP-BDT-TIPS** est la force de l'accepteur. Alors que l'état du triplet localisé du groupe BDT-TIPS, responsable du comportement phosphorescent, est inférieur aux états à transfert de charge (CT) pour **TXO2-BDT-TIPS**, ce n'est pas le cas pour **CNQxP-BDT-TIPS**. La plus petite différence d'énergie singulet-triplet expérimentale a également entraîné la possibilité d'un rISC pour **CNQxP-BDT-TIPS**, alors que ce n'est pas possible pour **TXO2-BDT-TIPS**.

Dans le chapitre 4, l'entité difluorodithiéno[3,2-*a*:2',3'-*c*]phénazine (DTPz), connue dans le domaine OPV, a été utilisée comme unité accepteur pour construire des matériaux émissifs (TADF). Le DTPz possède une capacité à donner des électrons significative permettant le développement de matériaux

émettant dans le rouge. Deux matériaux donneurs, le BDT-TIP (présenté au chapitre 3) et le DMAC, ont été couplés à l'accepteur DTPz, ce qui a donné des composés de type D-A avec émission de CT. La différence d'énergie singulet-triplet calculée était faible pour le **DTPz-DMAC** (0,03 eV), tandis que pour le **DTPz-BDT-TIPS** (0,43 eV), elle était du même ordre de grandeur que pour le **CNQxP-BDT-TIPS** (chapitre 3). L'analyse de la succession des émissions résolues en temps dans le film zeonex a révélé un comportement différent pour les composés contenant du DMAC et du BDT-TIPS. Alors que le **DTPz-DMAC** a montré un comportement TADF avec une émission de longue durée et un pic maximum autour de 630 nm, le **DTPz-BDT-TIPS** a montré un comportement RTP avec un début similaire à la phosphorescence du **DTPz-DMAC**. Cela suggère une émission depuis le cœur DTPz au lieu de l'unité BDT-TIPS, comme indiqué dans le chapitre 3. Une analyse ultérieure de DTPz dans zeonex a montré que DTPz en lui-même montre en effet un comportement RTP similaire.
L'un des matériaux d'émetteur TADF les plus connus est le **4CzIPN**, initialement rapporté par Adachi et ses collègues.[2] Il a été étudié plus en détail par Etherington *et al.*[3] et s'est avéré conduire à la formation de dimères dans des films OLED dopés. Or, l'émission de dimères n'est pas souhaitée dans les dispositifs OLED car elle compromet la pureté de la couleur. Les dimères sont formés par des interactions entre les unités carbazole des molécules **4CzIPN**. Pour surmonter ces interactions, le 4*H*-dithiéno[3,2*b*:2',3'*d*]pyrrole (DTP) a été choisi comme unité donneuse pour remplacer le 9*H*-carbazole au chapitre 5. Le DTP est une unité donneuse bien connue dans le domaine de l'OPV, où il est généralement couplé via les positions α et l'atome d'azote central est alkylé pour une solubilité améliorée des polymères résultants. La synthèse via un intermédiaire carbamate permet d'obtenir le DTP sans chaîne alkyl après quoi il peut être utilisé dans des réactions de substitution nucléophile aromatique ou de type Buchwald-Hartwig. Le premier a été appliqué dans cette thèse pour préparer **4DTP-IPN**, en utilisant des conditions de réaction similaires à celles de la synthèse de **4CzIPN**. Le **4DTP-IPN** a montré une émission décalée vers le rouge par rapport à celle du **4CzIPN** et a présenté des propriétés TADF dans une variété de films. En raison des très petites valeurs, expérimentales et calculées, des différences d'énergie singulet-triplet, il était difficile de faire la distinction entre son émission retardée et sa phosphorescence, même à 80 K.

Bien que son comportement d'agrégation soit certainement différent de celui du **4CzIPN**, les mesures photophysiques du **4DTP-IPN** à diverses concentrations en solution et en couche mince donne lieu à des observations contradictoires et d'autres expériences sont nécessaires pour déterminer s'il est moins probable ou même plus susceptible de former des dimères.

Dans le dernier chapitre (chapitre 6), quatre publications supplémentaires ont été discutées dans lesquelles des calculs de chimie quantique ont été réalisés pour aider à l'interprétation des propriétés expérimentales de petites molécules ou de composés polymères. La première publication portait sur la conception de photosensibilisateurs au bore dipyrrométhène (BODIPY), développés pour former efficacement de l'oxygène singulet pour la thérapie photodynamique. Les calculs (TD)DFT conduisent à des informations sur la photophysique des molécules BODIPY et indiquent indirectement la présence d'une émission par des exciplex, ce qui a été confirmé expérimentalement. L'incorporation d'une unité DMAC s'est avérée cruciale pour la génération d'oxygène singulet et la formation d'exciplex et ce dernier devrait être responsable de l'ISC efficace. Les autres publications traitaient des relations structure-propriété dans lesquelles des espèces oligomères étaient utilisées pour imiter le comportement des chaînes polymères. En regardant leurs géométries optimisées, nous avons pu expliquer l'interaction entre les propriétés électroniques et les délocalisations des orbitales moléculaires dans des séries de polymères similaires.

7.5 References

1. M. Pope, H. P. Kallmann and P. Magnante, *J. Chem. Phys.*, 1963, **38**, 2042-2043.
2. H. Uoyama, K. Goushi, K. Shizu, H. Nomura and C. Adachi, *Nature*, 2012, **492**, 234-238.
3. M. K. Etherington, N. A. Kukhta, H. F. Higginbotham, A. Danos, A. N. Bismillah, D. R. Graves, P. R. McGonigal, N. Haase, A. Morherr, A. S. Batsanov, C. Pflumm, V. Bhalla, M. R. Bryce and A. P. Monkman, *The J. Phys. Chem. C*, 2019, **123**, 11109-11117.
4. C. Murawski, A. Graf, P. Liehm, A. Neferu, E. Zysman-Colman and M. C. Gather, *SID Symp. Dig. Tech. Pap.*, 2017, **48**, 742-745.
5. D. G. Congrave, B. H. Drummond, P. J. Conaghan, H. Francis, S. T. E. Jones, C. P. Grey, N. C. Greenham, D. Credgington and H. Bronstein, *J. Am. Chem. Soc.*, 2019, **141**, 18390-18394.
6. D.-H. Kim, A. D'Aléo, X.-K. Chen, A. D. S. Sandanayaka, D. Yao, L. Zhao, T. Komino, E. Zaborova, G. Canard, Y. Tsuchiya, E. Choi, J. W.

Wu, F. Fages, J.-L. Brédas, J.-C. Ribierre and C. Adachi, *Nat. Photon.*, 2018, **12**, 98-104.
7. H. Nakanotani, T. Higuchi, T. Furukawa, K. Masui, K. Morimoto, M. Numata, H. Tanaka, Y. Sagara, T. Yasuda and C. Adachi, *Nat. Commun.*, 2014, **5**, 4016.